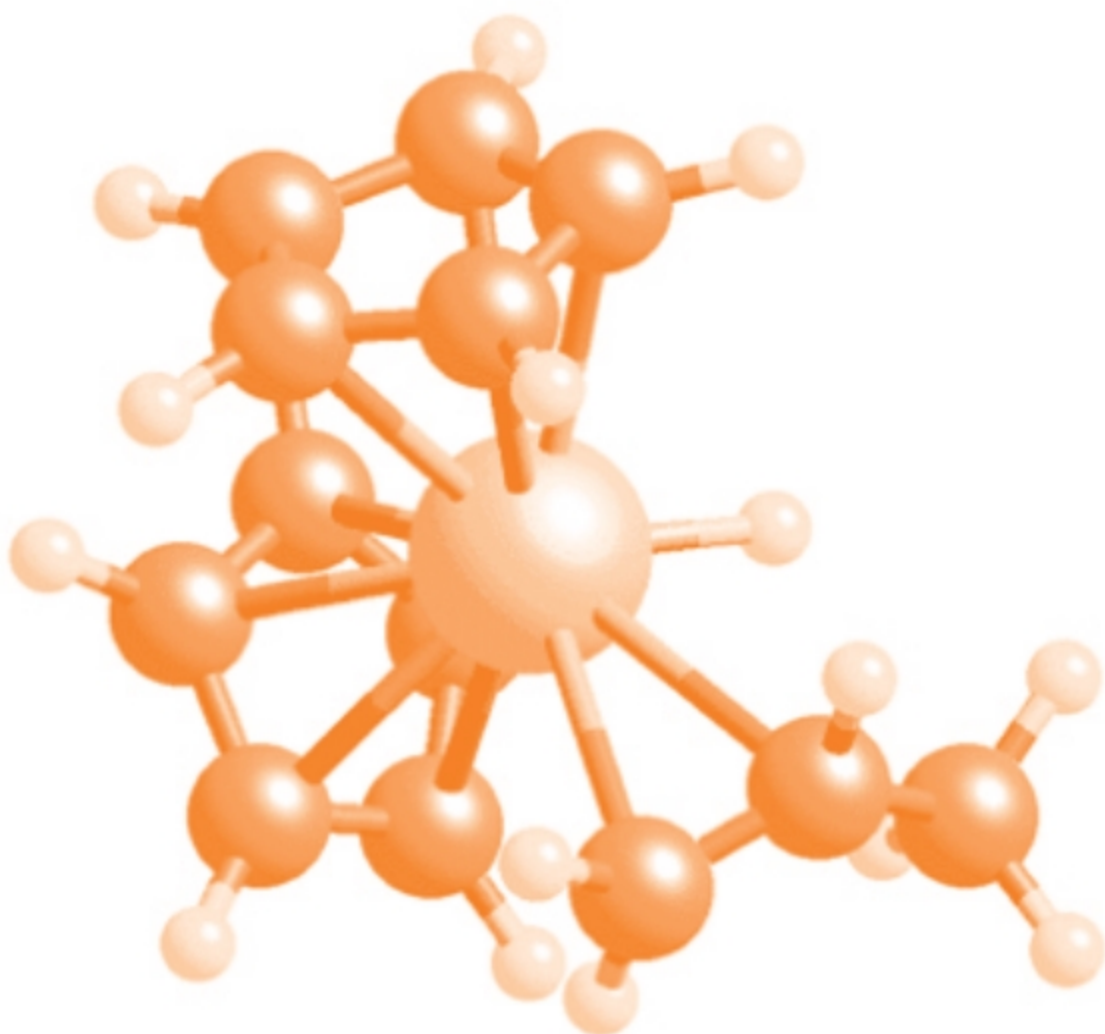




STUDIA UNIVERSITATIS
BABEȘ-BOLYAI



CHEMIA

3/2007

STUDIA

UNIVERSITATIS BABEȘ-BOLYAI

CHEMIA

3

Desktop Editing Office: 51st B.P.Hasdeu Street, Cluj-Napoca, Romania, phone + 40 264 405352

SUMAR - SOMMAIRE - CONTENTS - INHALT

IN MEMORIAM PROFESSOR EMIL CHIFU (1925-1997)	3
MARIA TOMOAI-COTISEL, EUGENIA GAVRILA, IOSIF ALBU AND IOAN- RĂDUCAN STAN, On the Dynamics of Free Drops.....	7
AURORA MOCANU, GHEORGHE TOMOAI, CRISTINA REJMERIAN, MARIA TOMOAI-COTISEL, OSSI HOROVITZ AND MARCELA TRIF, Atomic Force Microscopy Studies of Two Composites Based on Surface Active Glasses and Different Copolymers and Their Stability in Biologic Fluid.....	31
OSSI HOROVITZ, AURORA MOCANU, GHEORGHE TOMOAI, MARIA CRISAN, LIVIU-DOREL BOBOS, CSABA RACZ AND MARIA TOMOAI-COTISEL, Amino Acids Binding to Gold Nanoparticles	53
VASILE V. MORARIU, Short and Long Range Correlation in Fluctuating Phenomena..	73
IOAN PANEA, MARIA TOMOAI-COTISEL, OSSI HOROVITZ, COSTINELA LAURA GĂSPĂR, AURORA MOCANU, CSABA NAGY, Spectroscopic and Atomic Force Microscopy Study of a New Hemicyanine Dye.....	79
SIMONA ANTOANELA GAVAN AND DAN FLORIN ANGHEL, Investigation of Micellar Properties of Anionic Surfactants With the Aid of Pvc-Membrane Dodecyl Sulfate Electrode.....	87

LIANA MURESAN, MARIANA GHERMAN, IONUT ZAMBLAU, SIMONA VARVARA AND CAIUS BULEA, Corrosion Behavior of Electrochemically Deposited Zn-TiO ₂ Nanocomposite Coatings	97
A. PETER, I. C. POPESCU, E. INDREA, P. MARGINEAN AND V. DANCIU, The Influence of the Heat Treatment on the Photoactivity of the TiO ₂ -SiO ₂ Aerogels	105
ALEXANDRA CSAVDARI, IOAN BALDEA AND DANA-MARIA SABOU, Oxidation of DI-Methionine (2-Amino-4-Methylthiobutanoic Acid) by Chromate. Mechanistic Interpretation on the Base of an One-Plus Rate Equation.....	113
ELEONORA MARIA RUS, I. BÂLDEA, C. CĂLIN, Low Carbon Steels Corrosion in Different Aggressive Media	121
M. POPA, I.C. POPESCU, V. DANCIU, Photocatalytic Activity of Metal Doped TiO ₂ Aerogels Prepared by Sol-Gel Process.....	131
ELEONORA MARIA RUS, I. BÂLDEA, C. CĂLIN, Oit – 35 Low Carbon Steel Corrosion in Presence of Sulfate Ions	137
MIHAELA RALUCA CIUMAG, MARIA JITARU, Determination of Total Acid Content in Wine Based on the Voltammetric Reduction of 1,4-Benzoquinone....	147
SILVIA BURCĂ, GEORGE VERMESAN, CAIUS BULEA, MARIA STANCA, HOREA BEDELEAN, ANDRADA MĂICĂNEANU, Electroplating Wastewater Treatment Using a Romanian Bentonite.....	155
CAMELIA PUȘCAȘ, CLAUDIA LAR, SORIN MAGER, ELENA BOGDAN, ANAMARIA TERC, LUMINIȚA DAVID, ION GROSU, Synthesis and Stereochemistry of Some New 2,4,8,10-Tetraoxaspiro[5.5]Undecane Derivatives ...	165

IN MEMORIAM

PROFESSOR EMIL CHIFU (1925-1997)

Professor Emil Chifu was born on July 17, 1925 in Herta, county of Dorohoi, Romania (today, Ukraine). He died on April 1, 1997, in Cluj-Napoca.

He was a scientific personality of high professional standards, one of the creators of the modern science of the colloids, of the membrane surfaces and phenomena, fields in which his works brought him international recognition.

Born in a modest family of handicraftsmen, he graduated with "distinction" all school grades, completing his academic studies with «distinction and diploma of merit» at the Faculty of Science of the University of Cluj, department of Chemistry (1950). Appointed laboratory assistant as soon as 1949 at the same faculty, Emil Chifu dedicated himself to the didactic and scientific activity, which he combined in a creative manner, which allowed him to go through all the stages of the university career and, as a result of various exams, reached the position of outstanding university professor.

His didactic activity was reflected in the publishing of a series of textbooks and course books for students, as well as of the treatise "Colloidal Chemistry" (The Didactic and Pedagogic Publishing House, Bucharest, 1969). The new version of the book he left in the form of an unfinished manuscript, completed and finished by his collaborators, appeared under the title "Chemistry of the Colloids and of the Interfaces" (The University Press, Cluj-Napoca, 2000), after the author's death. Both editions of the treatise are addressed in a highly competent way, to chemists, physicists, biologists, engineers, biotechnologists, those working in industry, pharmaceuticals, nanomedicine, nanoscience, nanotechnology and to all those interested in the fundamental and applicative research of the physical chemistry of surfaces and interfacial phenomena.

He taught the courses of Chemical and Engineering Thermodynamics, Colloidal Chemistry, Chemistry of Colloids and of the Surfaces, Physical Chemistry. The scientific rigor of his lectures, the exigency towards the students, and last but not least, the propriety of the Romanian language spoken from the teaching desk, has brought him the respect of many generations of students. He coordinated over 80 diploma papers and more than 20 papers of specialization in Physical-Chemistry. Seven doctoral theses were drawn up and defended under his coordination. In 1967, as a token of the appreciation, the Ministry of Education awarded him the First

Prize for outstanding activity in the field of Chemistry and he concluded his career (he retired in 1990) with the title of outstanding university professor, working, even afterwards, as a consultant professor (1990-1997).

Between 1970 and 1991 he was the head of the department of Physical Chemistry at the Babes-Bolyai University in Cluj-Napoca.

The scientific activity of Professor Chifu was carried on based on his studies initiated with the drawing up of his doctoral thesis entitled "A Study on the Superficial Mobility of Solutions" (1965). The development and the thorough study of these were outlined in the publishing of over 160 scientific original papers. He published in national journals such as *The Chemistry Magazine* (Bucharest), *Revue Roumaine de Chimie*, *Studia Univ. Babes-Bolyai*, *J. Colloid & Surf. Chem. Assoc.*, but he also published more than 40 papers in prestigious publications from abroad, such as *Ann. Chim* (Rome), *Gazzetta Chim. Italiana*, *J. Colloid Interface Sci.*, (USA), *Biochim. Biophys. Acta*, *Chem. Phys Lipids*, *Langmuir* (USA), *Progr. Colloid Polym. Sci.*, *Colloids & Surfaces*, *Biochemical J.* The original research on the stability of thin films and on their properties in conditions of microgravity, the examination of the behavior of liquids under the action of superficial tension gradients caused by various surfactants or by differences in temperature, under normal conditions, or in conditions of microgravity have been nationally and internationally appreciated. Thus, in 1983, together with the research team, he was awarded the «Gheorghe Spacu» Prize of the Romanian Academy for the group of papers: «The Physical Chemistry of Interfacial Films», and in 1978, after a rigorous selection process, NASA of USA accepted to have the original research entitled: «Surface Flow of Liquids in the Absence of Gravity» tested in outer space. Professor Emil Chifu thus became the first Romanian whose proposal had been accepted and implemented on DDM (Drop Dynamic Module) in the 3rd mission of the Space Lab (1981). This spatial experiment opened the way to some important applications in the spatial technology of liquid behavior, as well as in the modeling of biological surfaces.

Researcher continuously animated by the aspiration to ever enlarged knowledge, Professor Chifu also initiated studies on the properties of active biologic compounds, such as: lecithins, fatty acids, carotenoids, vitamins, drugs, as well as on their interactions with the constituents of natural membranes. His research team, a real school created years ago, successfully develops and deepens these studies even now.

- M. Tomoaia-Cotisel, I. Zsakó, **E. Chifu**, A. Mocanu, P. T. Frangopol and P. J. Quinn, "Procaine binding to stearic acid monolayers spread at the air/buffer interface. The influence of pH and surface pressures", *J. Romanian Colloid and Surface Chem. Assoc.*, **2** (3-4), 30-36 (1997).
- J. Zsakó, M. Tomoaia-Cotisel, A. Mocanu, Cs. Racz and **E. Chifu**, "Thermodynamics of adsorption and micelle formation of sodium

cholate in two-phase systems", *J. Romanian Colloid and Surface Chem. Assoc.*, **2** (3-4), 37-40 (1997).

- M. Tomoaia-Cotisel, J. Zsako, A. Mocanu, **E. Chifu**, M. Salajan and S. Bran, "Adsorption kinetics of anaesthetics at the benzene/water interface", *J. Colloid and Surface Chem.*, **3** (2), 32-40 (1999).
- M. Tomoaia-Cotisel, L. C. Stewart, M. Kates, J. Zsakó, **E. Chifu**, A. Mocanu, P. T. Frangopol, L. J. Noe and P. J. Quinn, "Acid dissociation constants of diphytanyl glycerol phosphorylglycerol-methylphosphate, and diphytanyl glycerol phosphoryl glycerophosphate and its deoxy analog", *Chem. Phys. Lipids*, **100**, 41-54 (1999).
- **E. Chifu**, "*Chemistry of Colloids and Interfaces*", Editors: M. Tomoaia-Cotisel, I. Albu, A. Mocanu, M. Salajan, E. Gavrilă and Cs. Racz, *University Press, Cluj-Napoca*, **2000**, pp. 400.
- **E. Chifu**, M. Tomoaia-Cotisel, I. Albu, A. Mocanu, M.-I Salajan, Cs. Racz and D.-V. Pop, "*Experimental Methods in Chemistry and Biophysics of Colloids and Interfaces*", University Press, Cluj-Napoca, **2004**, pp. 175.
- **E. Chifu**, I. Stan and M. Tomoaia-Cotisel, "Marangoni flow and convective diffusion on a free drop", *Rev. Roum. Chim.*, **50** (4), 297-303 (2005).
- M. Tomoaia-Cotisel, I. Albu and **E. Chifu**, "*Chemical Thermodynamics*", University Press, Cluj-Napoca, **2007**, *in press*.

A brilliant professor and scientist, he was one of the creators of the modern science of colloids, surfaces, membrane and interfacial phenomena as well as of nanotechnology, hydrodynamics and nanostructured thin layers [see *Journal of Colloid and Interface Science*, **195**, 271 (1997)].

Not less important in his biography were the specializations abroad and the contacts with personalities of the international scientific life. A member of various Romanian and International scientific societies, he collaborated with scientists from the Universities of London, Moscow, Florence, Tübingen, Buffalo. He also took part with plenary conferences and communications to international workshops in his line of study (in Belgium at the Free University of Brussels, in France at the University of Provence, Marseille). At home, he organized and supervised conferences on Colloidal Chemistry, Physical Chemistry, Chemistry of Membranes and Interfacial Phenomena.

ON THE DYNAMICS OF FREE DROPS

MARIA TOMOAI-A-COTISEL^a, EUGENIA GAVRILA^a, IOSIF ALBU^a
AND IOAN-RĂDUCAN STAN^b

ABSTRACT. This is a review on the original work by *Chifu et al.* that explored the various movements of the free drops. This review also presents some theoretical models and experiments further developed by *the academic research group, established by him in the physical chemistry department*, to deeply investigate the free drop dynamics and related interfacial phenomena. The interfacial tension gradient caused by the surfactant adsorption at the surface of a free liquid drop gives rise to a surface flow (i.e. Marangoni interfacial flow) which causes the motion of the neighboring liquids by viscous traction, and generates a hydrodynamic pressure force, named Marangoni force, which acts on the drop surface. The effect of the surfactant adsorption and of Marangoni force on the dynamics of free liquid drops immersed in an unbounded liquid (the densities of the two bulk liquids are equal) is studied. Marangoni force was examined on several cases using non-deformable and deformable free drops. For a low value of the viscosity ratio of the two liquids (i.e., the drop liquid viscosity /unbounded liquid viscosity) at a high interfacial tension gradient, a dynamic instability of the drop was experimentally observed. This instability once triggered develops into the fragmentation of the drop into two droplets. For high values of the viscosity ratio of the two bulk liquids at a high interfacial tension gradient, only drop deformations appear. In the situation of a very high viscosity ratio and at a small interfacial tension gradient the drops are undeformable. The observed experimental data are in a substantial agreement with the results of our hydrodynamic theoretical model.

Keywords: Marangoni force, Marangoni effect, free drop deformations, interfacial tension gradient, drop dynamics, hydrodynamic model

INTRODUCTION

Since the original work by Chifu et al. [1-3] that describes the dynamics of a free liquid drop, immersed in an equal density bulk liquid, when a surface tension gradient is applied on the drop surface, some theoretical models and experiments were further developed to explore the drop dynamics [4-9]. To explain the drop dynamics, it was suggested that Marangoni instability, surface dilution, tip-stretching and capillary forces are important factors in drop movements and deformations.

^a Babes-Bolyai University of Cluj-Napoca, Department of Physical Chemistry, Arany Janos Str., No. 11, 400028 Cluj-Napoca, Romania;

^b Babes-Bolyai University of Cluj- Napoca, Department of Mechanics and Astronomy, Kogalniceanu Str., No. 1, 400084 Cluj-Napoca, Romania e-mail: mcotisel@yahoo.com, i_r_stan@yahoo.com

To determine which one from these is a major factor on the drop dynamics, in this work, we investigate experimentally and theoretically the effect of local changes in the surface tension, which are induced by the adsorption of a surfactant at the drop surface.

As a result of the adsorption of a surfactant (also called surface active compound), a surface tension gradient (Marangoni effect) appears, which generates a real surface flow, from low to high surface tension, called the Marangoni flow, and it is illustrated in Fig. 1. This Marangoni interfacial flow causes the motion of the neighboring liquids by viscous traction [3, 5], and generates the force of hydrodynamic pressure, named Marangoni force, which acts on the drop surface.

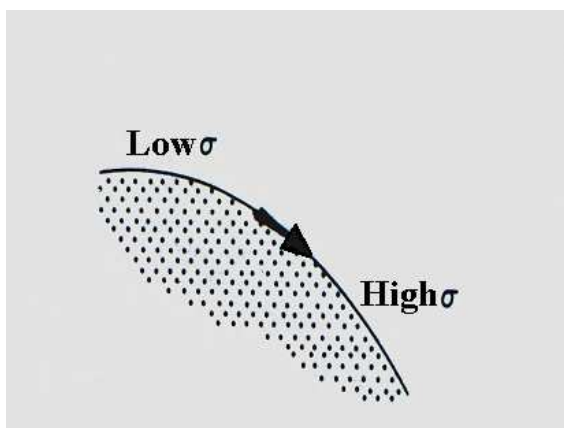


Fig.1. Marangoni interfacial flow resulting under a surface tension gradient

In this work, we have also developed a theoretical hydrodynamic model to calculate the Marangoni force. At the beginning of the interfacial flow, the Marangoni force acts like a “hammer” and modifies the shape of the drop. This force also generates other various factors, like the surface dilution, the tip-stretching, and the capillary forces, that might appear in the drop dynamics, depending on the working conditions. The results of our theoretical hydrodynamic model are in a substantial agreement with the observed experimental data.

THEORY

The investigation of the free drop dynamics is of a present interest, due to its appearance both in the industrial and biological processes, as well as in the space science and technology of liquids.

Hydrodynamic governing equations

We consider a viscous (L') liquid drop (with density ρ') immersed in an unbounded immiscible (L) liquid (of density ρ) at a constant temperature (T). The densities of the two bulk liquids are equal ($\rho = \rho'$) and initially the drop is motionless. Such a drop is also called free drop.

Further, we assume that both liquids (L and L') are incompressible and Newtonian. The drop has a viscosity μ' and the surrounding bulk fluid a viscosity μ , which are, in general, different. The surface between the two bulk fluids is characterized by an interfacial tension noted σ_0 .

Then, a small quantity of a surfactant (e.g. a droplet of 10^{-3} - 10^{-2} cm^3 , which is very small compared with the volume of the initial drop) is introduced on a well-chosen point (called also injection point) at the drop surface.

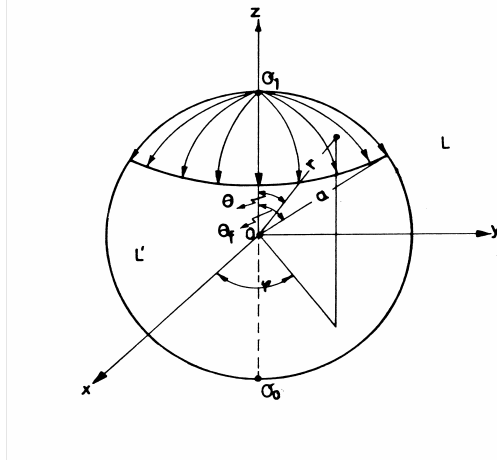


Fig. 2. The spreading and adsorption of a surfactant on the drop surface; the system of spherical coordinates (r, θ, ϕ); the θ_f angle characterizes the position of the surfactant front.

The surfactant, because of its molecular structure, is spread and simultaneously adsorbed at the liquid-liquid interface and it is continuously swept along the meridians of the drop by the convective transport (see, Fig. 2). In the injection point the interfacial tension is instantaneously lowered to σ_1 value. We mention that local changes in temperature [8] or the presence of surface chemical reactions might produce a similar effect.

Since the interfacial tension is a function of the surfactant concentration, a gradient of interfacial tension is established over the surface of the drop [3]. Consequently, the Marangoni spreading of the surfactant takes place from low surface tension to high surface tension (Fig. 1). As a result of the Marangoni surface flow, which causes the motion of the neighboring liquids by viscous traction, the Marangoni force of hydrodynamic pressure will appear acting on the

drop surface. Due to the drop symmetry, the Marangoni force has the application point in the injection point with surfactant at the drop surface.

This Marangoni force will determine all kinds of drop movements, especially deformations, rotations and oscillations of the whole drop, as well as surface waves and drop translational motions depending on the experimental working conditions.

The symmetry of the problem suggests a system of spherical coordinates (r, θ, φ) with the origin placed in the drop center and with the Oz axis passing through the sphere in the point of the minimum interfacial tension, i. e. the injection point of the surfactant.

We underline that the surfactant injection point at the drop surface may be taken anywhere, the drop being initially at rest. In the following theoretical model, we shall take it like it is shown in Fig. 2.

The surfactant front position, in this radial flow, is noted by the angle θ_f and the interfacial tension, σ , is considered a unique function of the angle θ . Within the surfactant invaded region, $(0 \leq \theta \leq \theta_f)$, for the variation of the interfacial tension [5] with θ , we take

$$\sigma(\theta) = \frac{\sigma_0 - \sigma_1}{1 - \cos\theta_f} (1 - \cos\theta) + \sigma_1 \quad (1)$$

where $\sigma_0 = \sigma(\theta_f)$ and $\sigma_1 = \sigma(0)$.

Derivation of Eq. (1) gives the interfacial tension gradient in the invaded drop region with surfactant

$$\frac{d\sigma}{d\theta} = \frac{\sigma_0 - \sigma_1}{1 - \cos\theta_f} \sin\theta, \quad (2)$$

where, the interfacial tension σ_0 is constant in any point of the uncovered surface, while the interfacial tension difference $\Pi = \sigma_0 - \sigma_1$ arises only in the invaded region. It is clear that only σ_1 and σ_0 , i. e. the minimum and the maximum values of the interfacial tension, can be experimentally measured.

From the theoretical point of view, the variation of the interfacial tension $\sigma(\theta)$ with the angle θ , inside the invaded region, is of the following form $\sigma(\theta) = \sigma_m + a_1 \cos\theta$ where σ_m and a_1 have different expressions. For the particular case when the surface of the entire drop is covered with surfactant $\theta_f = \pi$, the equation obtained is similar to that proposed by other authors [10].

The equations, governing the flow inside and outside the drop, are the continuity and Navier-Stokes equations [11-13]. The continuity equations for a Newtonian incompressible fluid are

$$\operatorname{div} \vec{v} = 0, \quad (3)$$

$$\operatorname{div} \vec{v}' = 0, \quad (4)$$

where \vec{v} is the velocity of the bulk liquid L and \vec{v}' represents the velocity of the liquid L' within the drop.

The Navier - Stokes equations for a steady flow are :

$$(\vec{v} \cdot \nabla) \vec{v} = - \frac{1}{\rho} \operatorname{grad} p + \nu \Delta \vec{v}, \quad (5)$$

$$(\vec{v}' \cdot \nabla) \vec{v}' = - \frac{1}{\rho} \operatorname{grad} p' + \nu' \Delta \vec{v}', \quad (6)$$

where p and p' are the pressures outside and inside of the drop; $\nu = \frac{\mu}{\rho}$ and

$\nu' = \frac{\mu'}{\rho}$ are the kinematic viscosities of continuous liquid and drop liquid, respectively. All these parameters are considered constants.

We give here some account on the equations governing fluid motion in a surface or in an interface, which is considered a two dimensional, incompressible Newtonian fluid, having surface density Γ and surface dilatational κ and shear ε viscosity. Even that we consider the interface like a two-dimensional geometrical surface, it has a thickness about $5 \cdot 10^{-10}$ cm.

The flow in a surface is not just a flow in a two-dimensional space whose governing equations will be immediate analogs of the three-dimensional ones. In contrast with the three- dimensional space, this surface is a two-dimensional space that moves within a three-dimensional space surrounding it. In our case, the interface is the region of contact of two liquids, i.e. drop liquid and bulk liquid. This is a new feature which oblige us to take account on the dynamical connection between the surface and its surroundings, namely on the traction exerted by the outer \vec{T} and inner \vec{T}' liquid upon the drop interface.

The equation of the interfacial flow [14 - 16] is

$$\Gamma (\vec{w} \cdot \nabla_S) \vec{w} = \vec{F} + \nabla_S \sigma + (\kappa + \varepsilon) \nabla_S (\nabla_S \cdot \vec{w}), \quad (7)$$

where $\vec{w} = \vec{v}_S$ is the interface velocity, $\vec{F} = \Gamma \vec{g} + \vec{T} - \vec{T}'$ is the external force acting on the drop surface, and ∇_S is the surface gradient operator.

Because the surface density [16] is very small ($\Gamma \approx 10^{-7} \text{g cm}^{-2}$) the inertial term can be neglected against the remainder terms.

It is significant to underline that equation (7) can be used in two ways: as the equation which describes the surface flow or as a dynamical boundary condition.

In order to find the distributions of the velocities \bar{v} and \bar{v}' and of the pressures p and p' , the system of equations (3)-(7) must be solved taking into account some appropriate boundary conditions [11- 13].

Thus, the velocities of the inner and outer liquid of the drop must satisfy the following conditions:

- the outer velocity must be zero far from the drop surface,

$$\bar{v} = 0 \text{ for } r \rightarrow \infty ;$$

- the normal component of the outer and the inner velocities must be zero on the surface of the drop

$$\bar{v}_n = \bar{v}'_n = 0, \text{ at } r = a;$$

- the tangential velocity components of the two liquids at the interface must be equals

$$\bar{v}_t = \bar{v}'_t \text{ at } r = a;$$

- the velocity \bar{v} within the drop must remain finite at all points, particularly at the centre of the drop ($r = 0$ the origin of the coordinates).

Since the Marangoni flow on the surface of the drop $r = a$ is symmetrical with respect to the Oz axis, the velocities of the inner and outer liquid flows are not functions of the angle φ , they will have only normal (radial) and tangential components $v_r(r, \theta)$, $v'_r(r, \theta)$, $v_\theta(r, \theta)$, $v'_\theta(r, \theta)$.

The continuity equation (3) for the outer flow in spherical coordinates is

$$\frac{\partial v_r}{\partial r} + \frac{1}{r} \frac{\partial v_\theta}{\partial \theta} + \frac{2v_r}{r} + \frac{v_\theta \text{ctg} \theta}{r} = 0, \quad (8)$$

while for the Navier-Stokes equation (5) we have

$$\frac{\partial p}{\partial r} = \mu \left(\frac{\partial^2 v_r}{\partial r^2} + \frac{1}{r^2} \frac{\partial^2 v_r}{\partial \theta^2} + \frac{2}{r} \frac{\partial v_r}{\partial r} + \frac{\text{ctg} \theta}{r^2} \frac{\partial v_r}{\partial \theta} - \frac{2}{r^2} \frac{\partial v_\theta}{\partial \theta} - \frac{2v_r}{r^2} - \frac{2\text{ctg} \theta}{r^2} v_\theta \right) \quad (9)$$

$$\frac{1}{r} \frac{\partial p}{\partial \theta} = \mu \left(\frac{\partial^2 v_\theta}{\partial r^2} + \frac{1}{r^2} \frac{\partial^2 v_\theta}{\partial \theta^2} + \frac{2}{r} \frac{\partial v_\theta}{\partial r} + \frac{\text{ctg } \theta}{r^2} \frac{\partial v_\theta}{\partial \theta} + \frac{2}{r^2} \frac{\partial v_r}{\partial \theta} - \frac{v_\theta}{r^2 \sin^2 \theta} \right) \quad (10)$$

It is to be noted that similar equations are obtained for the inner liquid motion.

The velocities of the inner and outer flow satisfy the following boundary conditions

$$v_r = v_\theta = 0 \quad \text{for } r \rightarrow \infty, \quad (11)$$

$$v_r = v_r' = 0 \quad \text{at } r = a, \quad (12)$$

$$v_\theta = v_\theta' \quad \text{at } r = a, \quad (13)$$

$$v_r' \text{ and } v_\theta' \text{ finite at } r = 0. \quad (14)$$

In addition to these kinematic conditions we also have, as we pointed before, a dynamic condition on the drop surface ($r = a$), obtained from the interface flow equation (7), which for small interfacial density Γ can be written in the following form [14, 15]:

$$\begin{aligned} \mu \left(\frac{1}{r} \frac{\partial v_r}{\partial \theta} + \frac{\partial v_\theta}{\partial r} - \frac{v_\theta}{r} \right)_{r=a} + \frac{1}{a} \frac{d\sigma}{d\theta} + (\kappa + \varepsilon) \left[\frac{1}{r} \frac{\partial}{\partial \theta} \left\{ \frac{1}{r \sin \theta} \frac{\partial}{\partial \theta} (v_\theta \sin \theta) \right\} \right]_{r=a} \\ + \varepsilon \frac{2(v_\theta)_{r=a}}{a^2} = \mu' \left(\frac{1}{r} \frac{\partial v_r'}{\partial \theta} + \frac{\partial v_\theta'}{\partial r} - \frac{v_\theta'}{r} \right)_{r=a} \end{aligned} \quad (15)$$

Solution of the flow equations

The solution of the flow equations (8-10) with the boundary conditions (11-15) can be obtained if we note that the surface flow gives rise to a current fluid directed to the drop along the Oz axis. This current fluid arises as a consequence of the continual replacement, by a ventilation effect, of that liquid layer which it was displaced by the interfacial flow. The profile of the flow indicates that a solution of the flow equations should be sought [13, 17] in the form

$$\begin{aligned} v_r(r, \theta) &= f(r) \cos \theta, \\ v_\theta(r, \theta) &= g(r) \sin \theta, \\ p(r, \theta) &= \mu h(r) \cos \theta, \end{aligned}$$

for the outer liquid L, and similar Eqs. are obtained for the inner liquid L'.

After well-known manipulations [17] we obtain for f, g, and h the following relations:

$$\begin{aligned} f(r) &= \frac{b_1}{r^3} + \frac{b_2}{r} + b_3 + b_4 r^2, \\ g(r) &= \frac{b_1}{2r^3} - \frac{b_2}{2r} - b_3 - 2b_4 r^2, \\ h(r) &= \frac{b_2}{r} + 10b_4 r, \end{aligned}$$

with b_1, b_2, b_3 and b_4 as constants. Also, equations of identical form for f', g' and h' are obtained with constants b'_1, b'_2, b'_3, b'_4 .

The eight b unknown constants will be determined from the boundary conditions (11-15). From (11) and (14) we have $b_3 = b_4 = b'_1 = b'_2 = 0$. For the outer liquid motion we obtain:

$$\begin{aligned} v_r(r, \theta) &= \left(\frac{b_1}{r^3} + \frac{b_2}{r} \right) \cos \theta, \\ v_\theta(r, \theta) &= \left(\frac{b_1}{2r^3} - \frac{b_2}{2r} \right) \sin \theta, \\ p(r, \theta) &= \mu \frac{b_2}{r^2} \cos \theta, \end{aligned}$$

and for the velocity and pressure distribution within the drop

$$\begin{aligned} v'_r(r, \theta) &= (b'_3 r^2 + b'_4) \cos \theta, \\ v'_\theta(r, \theta) &= -(2b'_3 r^2 + b'_4) \sin \theta, \\ p'(r, \theta) &= 10\mu b'_3 r \cos \theta. \end{aligned}$$

From (12) and (13) we have

$$b_2 = -\frac{b_1}{a^2}, \quad b'_3 = -\frac{b_1}{a^5}, \quad b'_4 = \frac{b_1}{a^3}.$$

Then, from equation (15), where for $\frac{d\sigma}{d\theta}$ we have used equation (2), the dependence of the constant b_1 as a function of the interfacial tension gradient $\Pi = \sigma_0 - \sigma_1$ is obtained:

$$b_1 = \frac{(\sigma_0 - \sigma_1)a^3}{3(\mu + \mu' + 2\kappa/3a)(1 - \cos\theta_f)}.$$

Thus, Eqs. (8-10) with the appropriate boundary conditions (11-15) lead to the distribution of the velocities \bar{v} , \bar{v}' and of the pressures p , p' outside and inside the drop:

$$v_r(r, \theta) = \frac{(\sigma_0 - \sigma_1)a^3}{3(\mu + \mu' + 2\kappa/3a)(1 - \cos\theta_f)} \left(\frac{1}{r^3} - \frac{1}{a^2 r} \right) \cos\theta, \quad (16)$$

$$v_\theta(r, \theta) = \frac{(\sigma_0 - \sigma_1)a^3}{3(\mu + \mu' + 2\kappa/3a)(1 - \cos\theta_f)} \left(\frac{1}{2r^3} + \frac{1}{2a^2 r} \right) \sin\theta, \quad (17)$$

$$p(r, \theta) = -\frac{\mu(\sigma_0 - \sigma_1)a}{3r^2(\mu + \mu' + 2\kappa/3a)(1 - \cos\theta_f)} \cos\theta, \quad (18)$$

for the outer flow, and

$$v'_r(r, \theta) = \frac{\sigma_0 - \sigma_1}{3(\mu + \mu' + 2\kappa/3a)(1 - \cos\theta_f)} \left(1 - \frac{r^2}{a^2} \right) \cos\theta \quad (19)$$

$$v'_\theta(r, \theta) = -\frac{\sigma_0 - \sigma_1}{3(\mu + \mu' + 2\kappa/3a)(1 - \cos\theta_f)} \left(1 - \frac{2r^2}{a^2} \right) \sin\theta \quad (20)$$

$$p'(r, \theta) = -\frac{10\mu'(\sigma_0 - \sigma_1)r}{3a^2(\mu + \mu' + 2\kappa/3a)(1 - \cos\theta_f)} \cos\theta \quad (21)$$

for the inner flow.

Marangoni force F_M exerted on the drop

Further, we describe the Marangoni force exerted on the free drop due to Marangoni flow. If we analyze the model of the Marangoni interfacial flow, we find that as the flow occurs with the driving by viscosity of the outer

liquid L, forces of hydrodynamic pressure will act on the drop L'. The resultant F_M , of the forces exerted by the fluid on the drop, due to the symmetry of the Marangoni flow, is oriented along the Oz axis. It has been computed by integrating the surface forces [11] acting along the drop surface:

$$F_M = \iint_S (p_{rr} \cos\theta - p_{r\theta} \sin\theta) ds \quad (22)$$

where, ds is the surface element covered with surfactant, and p_{rr} and $p_{r\theta}$ are the normal and tangential components [11-13], respectively, of the viscous stress tensor given by:

$$p_{rr}(r,\theta) = -p + 2\mu \frac{\partial v_r}{\partial r}, \quad (23)$$

$$p_{r\theta}(r,\theta) = \mu \left(\frac{1}{r} \frac{\partial v_r}{\partial \theta} + \frac{\partial v_\theta}{\partial r} - \frac{v_\theta}{r} \right). \quad (24)$$

The surface element in spherical coordinates on the drop ($r = a$) is

$$ds = 2\pi a^2 \sin\theta d\theta,$$

and, the force acting on the drop, given by (Eq. (22)), can then be rewritten as:

$$F_M(\theta_f) = 2\pi a^2 \int_0^{\theta_f} (p_{rr} \cos\theta - p_{r\theta} \sin\theta) \sin\theta d\theta. \quad (25)$$

Using Eqs. (16-18), one obtains for the normal (Eq. (23)) and tangential components (Eq. (24)) of the stress tensor, at the drop surface ($r = a$), the following expressions:

$$(p_{rr})_{r=a} = - \frac{\mu (\sigma_0 - \sigma_1)}{a (\mu + \mu' + 2\kappa/3a) (1 - \cos\theta_f)} \cos\theta, \quad (26)$$

$$(p_{r\theta})_{r=a} = - \frac{\mu (\sigma_0 - \sigma_1)}{a (\mu + \mu' + 2\kappa/3a) (1 - \cos\theta_f)} \sin\theta. \quad (27)$$

Introducing the viscosities ratio, $\lambda = \mu'/\mu$, the interfacial tension difference, $\Pi = \sigma_0 - \sigma_1$ and because $2\kappa/3a \approx 0$ as shown previously [5], after integration we have:

$$F_M(\theta_f) = A (1 - 2 \cos \theta_f - 2 \cos^2 \theta_f), \quad (28)$$

where A is given by

$$A = \frac{2\pi a \Pi}{1+\lambda}.$$

Thus, Eq. (28) represents the Marangoni force acting on the drop surface along the Oz axis. It can be seen that this force depends on the θ_f angle, namely, on the extent to which the drop surface is covered by the surfactant, as a function of the radial interfacial tension difference (Π), the ratio of the bulk viscosities (λ), as well as of the radius (a) of the drop.

Hammer Effect

For further discussions, it is useful to introduce a new function in Eq. (28), namely $f(\theta_f) = F_M(\theta_f) / A$, given by:

$$f(\theta_f) = 1 - 2 \cos \theta_f - 2 \cos^2 \theta_f \quad (29)$$

which is plotted in Fig. 3.

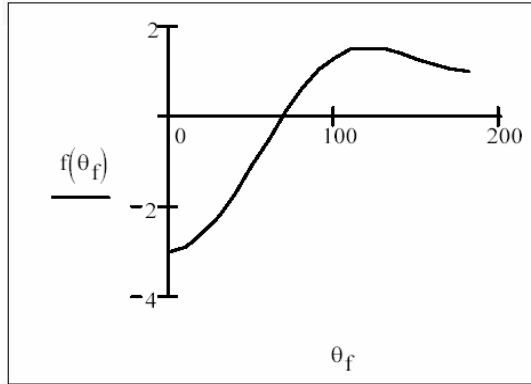


Fig. 3. The graphic of $f(\theta_f)$ as a function of θ_f angle

The value of θ_f , for which the force $F_M(\theta_f)$ cancels, $F_M(\theta_f) = 0$, is $\theta_0 \approx 68.53^\circ$. The value of θ_0 does not depend on the physical, chemical and geometric properties of the drop. Also, we see that for $\theta_f \in [0, \theta_0)$, the force is negative $F_M(\theta_f) < 0$, and for $\theta_f \in (\theta_0, 180^\circ]$ the force is positive, $F_M(\theta_f) > 0$, having the greatest value for $\theta_m = 120^\circ$.

From Eq. (28) it is found that for a coverage degree $\theta_f < \theta_0$ of the drop, with surfactant, as a result of the appearance of a radial interfacial tension gradient Π , the pressure force $F_M(\theta_f)$ exerted by the external liquid upon the drop is oriented toward the negative direction of the Oz axis (Fig. 3). This is similar with the application of a “hammer” knock on the drop in the injecting point of the surfactant. For a coverage degree θ_f greater than θ_0 , but less than 180° , the force $F_M(\theta_f)$ is oriented towards the positive direction of the Oz axis. The propulsive (lifting) force, $F_M(\theta_f) > 0$, responsible for the upward movement of the drop, appears only when the coverage of the drop with surfactant is greater than θ_0 .

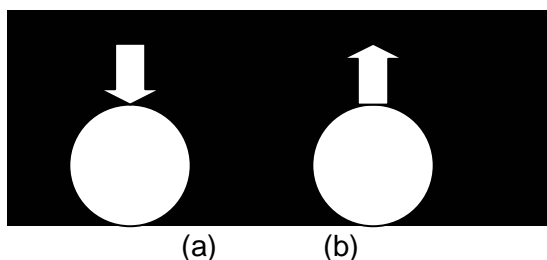


Fig. 4. The Marangoni force, F_M , acting on the free drop. a) Marangoni hammer force; b) Marangoni lifting force.

Therefore, the effect of coverage by the surfactant on the drop surface can be decomposed in two parts, the “hammer” effect for the coverage $0 \leq \theta_f < \theta_0$ and the “propulsive” effect for the coverage $\theta_0 < \theta_f \leq 180^\circ$ as shown in Fig.4a and 4b, respectively.

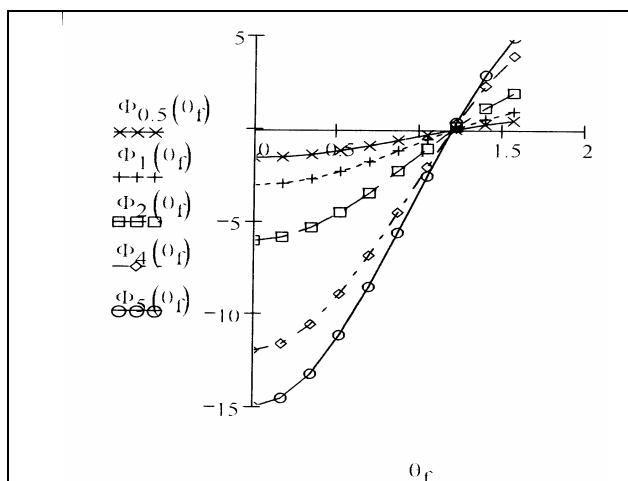


Fig.5. The plot of $\Phi_{\Pi}(\theta_f)$ versus θ_f , for $\theta_f < \theta_0$

To point out the role of the surface tension effects on the F_M force in the hammer case $\theta_f < \theta_0$ we introduce, in Eq. (28), another new function $\Phi_{\Pi} = \Pi f(\theta_f)$.

This Φ_{Π} function is a reduced Marangoni hydrodynamic force. Its graphic representation, Φ_{Π} versus θ_f , for various chosen values of Π (e.g., 0.5; 1; 2; 4; and 5 dyn/cm) is given in Fig.5.

It is observed that for high surface tension differences (e.g., 4 dyn/cm and 5 dyn/cm) the “hammer” effect is also high. For low surface tension differences (e.g. 0.5 dyn/cm, 1 dyn/cm and 2 dyn/cm), the hammer effect is small. This result is in good agreement with our previous work [3, 17], where the main goal was to maintain the drop non-deformable using high viscosity liquids and small surface tension gradients.

The $F_M(\theta_f)$ force reaches its maximum value at the spreading moment of the surfactant ($t=0$) for which $\theta_f \approx 0$ and is given by:

$$F(0) = \frac{6\pi a \Pi}{1+\lambda}, \quad (30)$$

where $F(0)$ represents the resultant force acting on the drop surface in the injecting point. For physical meanings, we can take the absolute value of this Marangoni hammer force.

Drop deformation

In our opinion, the Marangoni hammer force is the principal factor which can modify the shape of the drop, namely through deformations and break-ups of a drop. To see how this Marangoni force works, we give in Table 1 the values of the ratio $F_M(\theta_f) / A$ for different values of the θ_f .

Table 1.

The values of $F_M(\theta_f) / A$ are given versus θ_f :

θ_f	0^0	10^0	20^0	30^0	40^0	50^0	60^0	68.53^0
F_M/A	-3	-2.91	-2.65	-2.23	-1.70	-1.12	-0.50	0

In Fig. 6, we plotted the Marangoni hammer forces acting on the drop surface for different θ_f values, which are belonging to the interval of $[-\theta_0, +\theta_0]$.

Fig. 6 suggests that it is a direct connection between Marangoni hammer force $F_M(\theta_f)$ and the drop deformation, namely along the Oz axis. Our experiments confirmed this supposition in both cases, for the deformation and for break-up.

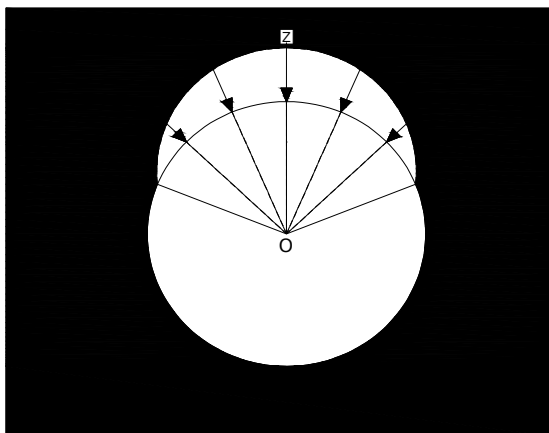


Fig. 6. Marangoni hammer forces acting on a free drop surface

We wish to point out the importance of this Marangoni hammer force, which is at the origin of other processes [18-23]. Indeed, the modification of the surface area of a drop, when the drop is deformed to a non-spherical shape, dilutes the surfactant surface concentration and the deformation of the drop is different from that expected one for the equilibrium σ_0 case. This is called the surface dilution effect.

Also, especially at the break-up process of the drop, surfactant molecules may accumulate at the tip of the drop due to the convection phenomenon. This phenomenon decreases the local interfacial tension and causes the tip to be overstretched. This process is called the tip-stretched effect. When during the deformations, a drop gets a concave surface, capillary forces appear, which tend to bring the drop in the initial spherical shape. All these effects appear, in our opinion, as a consequence of the Marangoni hammer force and of the real flow of the surfactant molecules within the drop surface.

Therefore, we suggest that the primary effect, due to a reduction of the equilibrium interfacial tension (σ_0) in the injection point of a free drop surface with a surfactant, at $t=0$, is the appearance of a Marangoni surface flow of the surfactant on the drop surface. This Marangoni flow of the surfactant modifies the equilibrium surface tension, σ_0 , and a Marangoni force $F_M(\theta_t)$ will act on the drop. At the beginning, it acts like a hammer which changes the shape of the drop, and consequently, several factors might appear, namely, the surface dilution and tip-stretching, as well as capillary forces.

Internal wave trains.

Further, we suggest that it is a direct connection between Marangoni force and the deformation of the drop, via the surface waves produced by the hammer effect.

Furthermore, we have considered that the surface waves, generated by the hammer effect, produce traveling periodic internal wave trains (Fig. 7). If these internal waves are absorbed by drop, the shape of the drop is not deformed. If these internal waves are not absorbed, the overlapping of the direct and reflected internal waves modifies the shape of the drop and causes deformations or even the break-up of the drop.

For small surface tension gradients, even in the case of the drop not deformable, there are different movements, first of all, the surface waves. We suggest that these surface waves are produced by the hammer effect described above. The surface waves generate a surface Marangoni instability of the drop. This instability was observed previously [23] but its cause was not discovered.

Our theoretical model can describe the surface instability due to the hammer effect. Further on, these surface waves will produce the internal waves (Fig. 7) which are generated by the surface tension gradients through hammer impact. As a consequence, traveling periodic internal wave trains are generated in the liquid drop after the adsorption and spreading of the surface-active compound on the surface of the drop, as illustrated latter on in the experimental work.

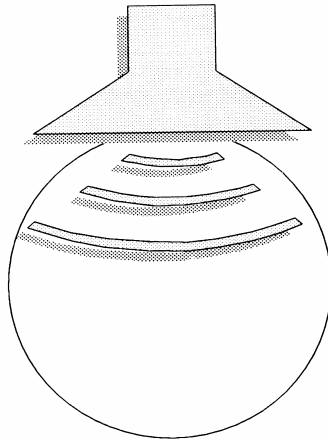


Fig. 7. Internal wave trains

- Further more, two possibilities can occur for the hammer effect ($\theta_f \leq \theta_0$):
1. If the drop viscosity μ' is large, then, the energy of the traveling periodic internal trains of waves are absorbed by the drop liquid and the drop is not deformable. Nevertheless, other movements might appear, like oscillations of the whole drop and rotations.
 2. When the drop viscosity μ' is small and the energy of the internal waves is not absorbed and the waves are reflected by the internal

drop surface. The superimposing of the direct internal waves with the reflected ones gives rise to a “resonant” effect, which generates the deformation and even break-up of the drop.

EXPERIMENTAL SECTION

The experimental work on drop dynamics and Marangoni instability was performed in liquid-liquid systems of equal densities presented in Tables 2 and 3. The densities of the liquids were determined picnometrically and the bulk viscosities by using an Ubbelohde viscometer. The surface dilatation viscosity at the liquid/liquid interface was not directly measured and only a few indications concerning this magnitude for the liquid/gas interface have been found [3].

The mixtures, making up the continuous L phase, were placed in a thermostated parallelepipedic vessel of 1 dm³, made of transparent glass. The drop (L') was made of various radii between 0.46 and 1.19 cm, by using the mixtures described in Table 2. The L' liquid was carefully submerged by using a pipette into the continuous L aqueous phase and the density of the latter was then adjusted by adding small quantities of water or alcohol until the buoyancy of the drop practically disappeared.

After the system was stabilized, a small quantity (10^{-3} - 10^{-2} cm³) of the surfactant solution (S) was injected with a micrometric syringe, in a point on the drop surface (injection point in Fig. 2). The injection was done either in a vertical direction (as in Fig. 8) or in different directions (Figs 9 and 10) and no influence of the mode of injection on the Marangoni flow or on the drop movements and deformations were observed.

The interfacial tension for the liquid/liquid systems, e.g. L/L' and L'/S, was determined by a method based on capillarity [3] and its value is given in Table 2. The measurement of the above parameters as well as the drop dynamics and surface flow experiments have been performed at constant temperature ($20 \pm 0.1^\circ\text{C}$). All chemicals were of analytical purity and used without further purification. In order to make visible the surface flow, the surfactant solution was intensely colored with methylene blue (0.28 g/100 cm³). We mention that we used surfactants which were soluble in the continuous phase L for systems 1 and 2. For the 3 – 6 systems, the surfactant was insoluble both in the L and L' liquid phases.

The movement of the surfactant front was followed by filming with a high speed camera (500 images/sec). A number of sequences, showing the surfactant front position at various moments t of the process, is presented in Fig. 8. It can be seen that the front position is easily distinguishable from the uncovered drop surface.

The positioning of the L' liquid drop in the continuous L liquid for a sufficiently long time as to perform the flow measurements raises difficulties. Although some authors pointed out that two drops never behave in the same manner under the action of interfacial tension differences, we have succeeded

in measuring the reproducible surface flow velocities as well as in evidencing the influence of several factors, like interfacial tension gradients and viscosities, on the drop deformations and movements. Several examples will be presented in the next section.

RESULTS AND DISCUSSION

Table 2.

Composition and physical characteristics of the liquid/liquid systems of equal densities.

For systems 3 to 5, the composition of phase L is given in (% of weight). For bulk viscosities μ and μ' , and interfacial tensions σ_0 and σ_1 , see the text. For systems 1 and 2, the drop radius is $a = 1.19$ cm and for systems 3 to 6, the drop radius is $a = 0.46$ cm.

System No.	Continuous Phase (L)			Drop Phase (L')		Surfactant Solution (S)	
	Composition (% vol)	μ (cP)	σ_0 L/L' (dyn/cm)	Composition (% vol)	μ' (cP)	Composition (% vol)	σ_1 L'/S (dyn/cm)
1	Ethanol 78.6 Water 21.4	2.26	7.9	Paraffin oil	80	Propanol 77.3 Water 22.7	3.5
2	Methanol 78 Water 22	1.33	10.2	Paraffin oil	80	Propanol 77.3 Water 22.7	3.5
3	NaNO ₃ 15.1 Water 84.9	1.1	28.7	Chlor benzene 40 Silicon oil 60	8.04	Benzylic alcohol 89 CCl ₄ 11	3.6
4	NaNO ₃ 15.1 Water 84.9	1.1	28.2	Chlor benzene 50 Silicon oil 50	5.46	Benzylic alcohol 89 CCl ₄ 11	3.6
5	NaNO ₃ 15 Water 85	1.1	25.6	Chlor benzene 85 Silicon oil 15	1.40	Benzylic alcohol 89 CCl ₄ 11	3.5
6	NaNO ₃ 14.9 Water 85.1	1.1	22.8	Chlor benzene 92 Silicon oil 8	1.03	Benzylic alcohol 89 CCl ₄ 11	3.6

In Table 2, we give the experimental parameters for three different cases of drop dynamics, under various surface tension gradients Π . The first case (systems 1 and 2) corresponds to the undeformable drops (Fig. 8). The second case (systems 3 and 4) represents the situation of the deformable drops (Fig. 9) and the third one (Fig. 10) describes the break-up of a drop.

Also, Table 2 gives the composition of the continuous (L) bulk and drop (L') phases, as well as the surfactant phase description and various phase physical characteristics. The continuous liquid bulk phase (μ) and drop phase (μ') viscosities and the interfacial tension, σ_0 and σ_1 , values are also given in Table 2. Investigated drops have the radius comprised between 0.46 and 1.19 cm.

Table 3.

Surface tension gradients, $\Pi = \sigma_0 - \sigma_1$, the ratio of the viscosities, λ , and the calculated values of Marangoni hammer force $F_M(0)$, for the six systems given in Table 2.

Sys-tem	Π (dyn/cm)	λ	$F_M(0)$, (dyn)	Remarks
1	4.4 ± 0.3	35.39	2.71	The free drop remains undeformable, having, at most, surface waves, as in Fig. 8.
2	6.7 ± 0.3	60.15	2.45	
3	25.1 ± 0.3	7.31	26.15	The free drop might have slight or big deformations, but after 0.6-0.8 sec., it returns to its initial form, as in Fig. 9.
4	24.6 ± 0.3	4.96	35.77	
5	22.1 ± 0.3	1.27	84.31	The free drop, after 0.3-0.4 sec., breaks up into two drops, as shown in Fig. 10.
6	19.2 ± 0.3	0.94	85.70	

The values of the surface tension gradient, Π , the ratio of the viscosities $\lambda = \mu' / \mu$ and the Marangoni hammer $F_M(0)$ force (see, equation 30) are given in Table 3.

Then, we compare the calculated values, obtained with our hydrodynamic theoretical model, with some experimental observations on the deformations and the break-ups of the drops under the surface tension gradient. The drops were visualized by filming with a high-speed camera

(500 images/sec). A number of image sequences illustrating the deformations of the drop at various moments (at different times, t) are presented in Figs. 9 and of the break-up in Figs. 10.

In Fig. 8, the filmed drop images, at different moments of time (t), are shown for the case of an undeformable free drop. In these images is possible to observe the motion of the surfactant front on the drop surface, easily distinguishable, by the contrast with the uncovered drop surface. Also, in Fig. 8, we can observe that the horizontal line, corresponding for the initial position of the free drop, is only slightly modified in time and the drop is not deformed or moved.

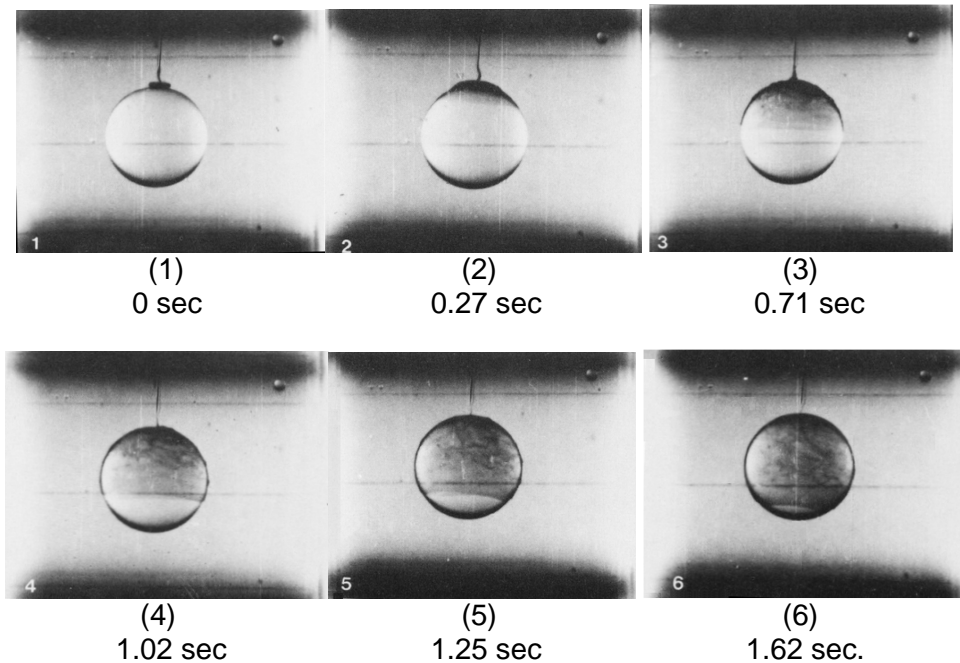


Fig. 8. Filmed pictures of an undeformable drop characterized by the system 2, given in Tables 2 and 3; the interfacial tension difference, $\Pi = \sigma_0 - \sigma_1 = 6.7$ dyn/cm, the viscosities ratio $\lambda = 60.15$ and the calculated Marangoni force $F_M(0) = 2.45$ dyn.

These findings are in substantial agreement with the data earlier published [3], for non-deformable free drops. For comparison, we have chosen similar experimental conditions given in Table 2, and therefore, we clearly demonstrated the reproducibility of these experiments. In plus, here, we calculated the Marangoni force $F_M(0)$, see Table 3.

Fig. 9 shows different shapes of a deformable free drop and its movement from the initial position (i.e. from the shown reference horizontal

line). In this case, for the system 4, given in Tables 2 and 3, due to the variation of the drop shape, besides the Marangoni force, the surface dilution and capillary forces will appear in the description of drop deformation.

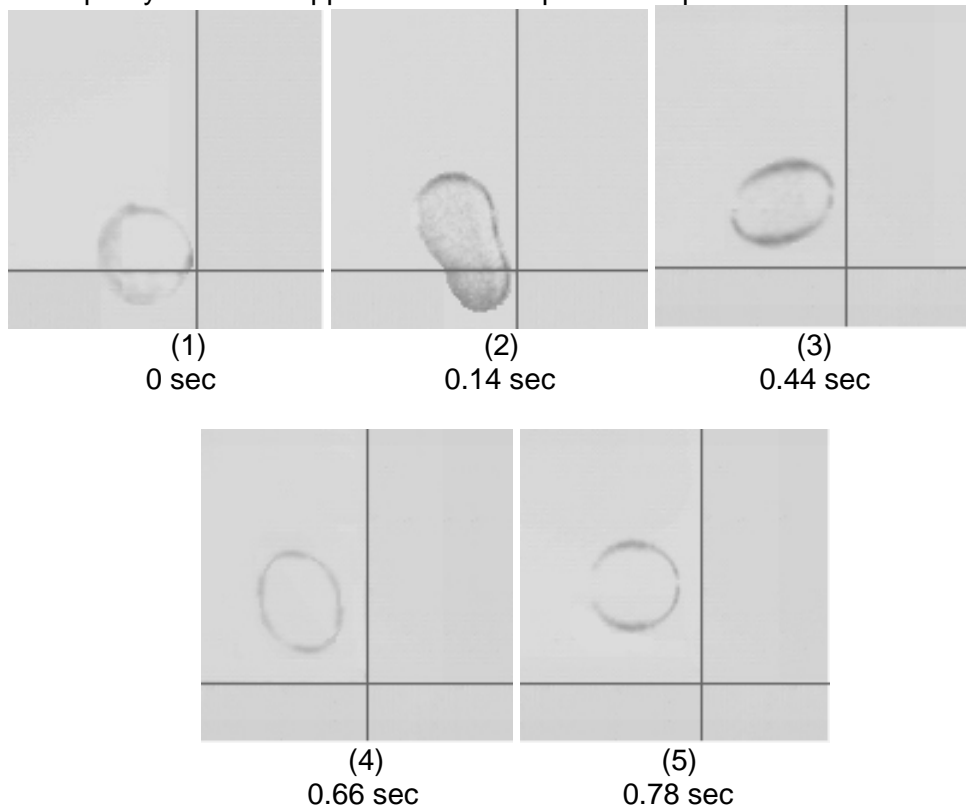


Fig. 9. Filmed pictures of drop deformations. The liquid-liquid system is characterized by the system 4 in Tables 2 and 3; $\Pi=24.6$ dyn/cm; $\lambda = 4.96$; $F_M(0) = 35.77$ dyn.

Fig. 10 illustrates the drop deformations (panels 1, 2 and 3), the drop movement and the break-up (panel 4, 5 and 6) of the drop into two parts. This is the third case of a deformable drop observed for the system 6, and its detailed characterization is given in Tables 2 and 3. It can be seen that at a certain moment in time (Fig. 10, panel 5) a tip in one of the drop compartments appears. Fig. 10, panel (5), might be an example of the tip-stretched effect.

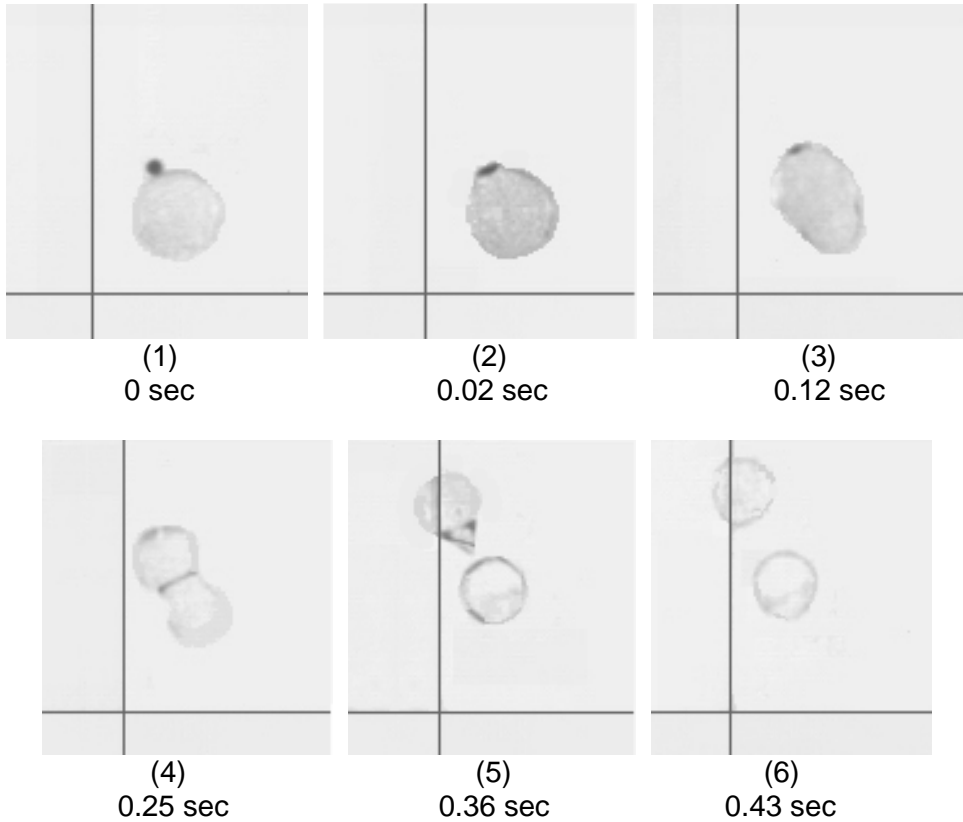


Fig.10. Filmed pictures of the initial free drop (a), the deformed drop (b) and the breakup drop (c). The liquid/liquid system is characterized by the system 6 given in Tables 2 and 3; $\Pi = 19.2 \text{ dyn/cm}$; $\lambda = 0.94$; $F_M(0) = 85.70 \text{ dyn}$.

As we can see, from Table 3, for systems 1 and 2, the values of viscosities ratio, $\lambda \gg 1$, are very large, and the values of the Marangoni force, $F_M(0)$, are slightly smaller than 3 dyn, and the drop is non deformable (Fig. 8). For systems 3 and 4, given in Table 3, the ratio values of the bulk viscosities are greater than unity $\lambda > 1$ (Table 3) and the Marangoni force is much higher than 1.

The Fig. 9 presents the different shapes of the free drop dynamics. Because there is a variation of the drop shape, in this case, the surface dilution and capillary forces will appear. This is the situation of a slightly viscous drop, when the Marangoni effect will provoke the drop deformations, which will generate the surface dilution in parallel with the appearance of capillary forces (Fig. 9, panel 2).

For the system 6, described in Tables 2 and 3, the viscosity of continuous bulk (μ) liquid and of the drop (μ') liquid are almost equal, $\lambda \approx 1$,

Table 3, but the Marangoni force $F_M(0)$ takes the highest value. In this situation, after a few moments (about 0.36 sec) the break-up of the drop appears (Fig. 10, panel 5), and the drop is divided into two parts (droplets).

This is the most complicated situation, when the Marangoni force will provoke the drop deformations, which will generate, in parallel, the surface dilution and the tip-stretching, until the drop is broken into two drops, as illustrated in Fig. 10, panel 5.

CONCLUSION

A hydrodynamic model has been developed in which the variable interfacial tension at the well defined free drop surface, caused by the addition of a surfactant, will generate a Marangoni force primarily responsible for the drop deformations and movements.

The drop deformation process is described and analyzed mathematically. It has been shown that it is a deep dependence of the absolute values of the Marangoni force $F_M(0)$ and the deformations of a free drop. In other words, a small Marangoni force will not cause the deformations of the viscous drop, but a large Marangoni force will provoke complicated deformations and movements of a free drop even the break-up of the drop. Thus, it is also shown experimentally and theoretically that the Marangoni force is a primary cause of the deformations of a drop. Surface dilution and tip-stretching effects, as well as the capillary forces, might appear as secondary factors in the drop deformation processes.

When a surface tension gradient appears at the free drop surface, the hammer Marangoni force $F_M(0)$ determines primarily the drop deformations and movements, taking into account the physical characteristics of the continuous liquid bulk phase and of the drop liquid phase, as well as those for the chosen surfactant solutions as indicated in Tables 2 and 3.

We can conclude that we explored six experimental systems that are classified into three important cases, in substantial agreement with the data given in Table 3. When the Marangoni hammer forces are small, the drop shape is not modified. For the intermediary values of the Marangoni hammer forces the drop is deformable. At the high values of Marangoni hammer forces the drop breaks up into two or more droplets.

Further, Marangoni hammer forces can also generate other different effects, like the surface dilution and the tip-stretching, as well as the capillary forces, that might appear in the drop dynamics, depending on the working conditions.

Finally, it is to be emphasized that such phenomena, generated by Marangoni force and Marangoni instability, are a result of the adsorption of a surfactant at the surface between the two liquid phases. These phenomena are of a major interest, both in industrial and biological

processes, in movements at biological membranes, as well as in the space science and technology of liquids.

REFERENCES

1. E. Chifu, "Surface flow of liquids in the absence of gravity", proposal selected by NASA's Office of Aeronautics and Space Technology, 1977, pp. 1-39.
2. E. Chifu and I. Stan, *Rev. Roum. Chim.*, **1980**, 25, 1449-1459.
3. E. Chifu, I. Stan, Z. Finta and E. Gavrilă, *J. Colloid Interface Sci.*, **1983**, 93, 140-150.
4. I. Stan, E. Chifu, Z. Finta and E. Gavrilă, *Rev. Roum. Chim.*, **1989**, 34, 603-615.
5. I. Stan, C.I. Gheorghiu and Z. Kása, *Studia Univ. Babeş-Bolyai, Math.*, **1993**, 38(2), 113-126.
6. E. Chifu, I. Albu, C. I. Gheorghiu, E. Gavrilă, M. Salajan and M. Tomoaia-Cotisel, *Rev. Roum. Chim.*, **1986**, 31, 105-112.
7. I. Stan, E. Chifu and Z. Kása, *ZAMM, Z. angew. Math. Mech.*, **1995**, 75, 369-370.
8. M. I. Salajan, A. Mocanu and M. Tomoaia-Cotisel, "Advances in Thermodynamics, Hydrodynamics and Biophysics of Thin Layers", University Press, Cluj-Napoca, **2004**, pp. 1-117.
9. E. Chifu, I. Stan and M. Tomoaia-Cotisel, *Rev. Roum. Chim.*, **2005**, 50, 297-303.
10. M. D. Levan, *J. Colloid Interface Sci.*, **1981**, 83, 11-17
11. L. Landau and E. Lifschitz, "Mécanique des fluides", **1971**, Ed. Mir, Moscou.
12. V. G. Levich, "Physicochemical Hydrodynamics", Chap. VIII. Prentice-Hall, Englewood Cliffs, New Jersey, **1962**.
13. T. Oroveanu, *Mecanica fluidelor vâscoase*, Ed. Acad., Bucharest, **1967**.
14. L. E. Scriven, *Chem. Eng. Sci.*, **1960**, 12, 98-108.
15. R. Aris, "Vectors, Tensors and the Basic Equations of Fluid Mechanics", Chap. X. Prentice-Hall, Englewood Cliffs, New Jersey, **1962**.
16. A. Sanfeld, in "Physical Chemistry Series", (W. Jost, Ed.), Vol. I, Acad. Press, New York, **1971**.
17. I.R. Stan, M. Tomoaia-Cotisel and A. Stan, *Bull. Transilvania Univ. Brasov*, **2006**, 13(48) 357-367
18. A. Wierschem, H. Linde and M. G. Velarde, *Phys. Rev. E.*, **2000**, 62, 6522-6531
19. Y. T. Hu and A. Lips, *Phys. Rev. Lett.*, **2003**, 91, 1- 4
20. H. A. Stone and L. G. Leal, *J. Fluid Mech.*, **1990**, 220, 161-186
21. W. J. Milliken, H. A. Stone and L. G. Leal, *Phys. Fluids*, A, **1993**, 5, 69-79
22. A.D. Eggleton and K. J. Stebe, *J. Colloid Interface Sci.*, **1998**, 208, 68-80.
23. R. Savino R. Monti, F. Nota, R. Fortezza, L. Carotenuto C. Picolo, *Acta Astronautica*, **2004**, 55(3), 169-179.

ATOMIC FORCE MICROSCOPY STUDIES OF TWO COMPOSITES BASED ON SURFACE ACTIVE GLASSES AND DIFFERENT COPOLYMERS AND THEIR STABILITY IN BIOLOGIC FLUID

AURORA MOCANU^a, GHEORGHE TOMOAI^b, CRISTINA PREJMEREAN^c,
MARIA TOMOAI-COTISEL^a, OSSY HOROVITZ^a AND MARCELA TRIF^c

ABSTRACT. The surface morphology of two composites (glass ionomer cements), and of their constituent inorganic and organic phases was investigated by atomic force microscopy (AFM), in tapping mode. The inorganic phase consists of a blend of inorganic powders, which was realized from surface active glasses. The organic phase contains either B1 copolymer or T1 copolymer, in the same weight percentage in water, with 3% tartaric acid. The two composites, noted B1 and T1, were made of the same inorganic powder blend, and the organic phase, containing either B1 or T1 copolymer. AFM imaging, namely height and phase-detection imaging with high resolution and contrast, was improved by monitoring the force of tapping of AFM probe on the sample surface. Morphological and structural analysis of investigated surfaces shows micro- and nanoparticles of inorganic powders embedded within the nano- and microdomains of copolymers. For B1 composite, it is observed a surface enrichment in B1 copolymer, against T1 composite. The surface of B1 and T1 composites was investigated both in native state and after polishing and glossing. The composites were measured in air and after 24 h or 7 days in artificial saliva. No essential topographical changes occurred to their surfaces, exposed about 24 h in saliva, independent of the used advanced processing methods for composite surfaces. The glossing leads to a stable surface of composites, both in air and after 24 h or even after 7 days exposed in saliva. However, after 7 days in saliva, the surface roughness is substantially increased for the T1 composite compared to B1 composite. Thus, B1 copolymer appears to be more stable in saliva than T1 copolymer. These data demonstrate that morphological and surface roughness analysis of both native surfaces and of enriched surfaces with polymers is important in determining the surface organization and the stability of composites in different environmental conditions.

Keywords: glass ionomer composites; AFM; biologic fluid; stability

Introduction

Composites include at least two categories of constituent materials: matrix and reinforcement (filling materials). The matrix material surrounds and supports the reinforcement materials by maintaining their relative

^a Babes-Bolyai University of Cluj-Napoca, Faculty of Chemistry and Chemical Engineering, 11 Arany J. Str., 400028 Cluj-Napoca, Romania;

^b Iuliu Hatieganu University of Medicine and Pharmacy, Department of Orthopedic Surgery, 47 Mosoiu Str., 400132 Cluj-Napoca, Romania;

^c Raluca Ripan Research Institute of Chemistry, 47 Fantanele Str., 400294 Cluj-Napoca, Romania
e-mail: horovitz@chem.ubbcluj.ro, mcotisel@yahoo.com

positions. The reinforcements impart their special mechanical and physical properties to enhance the matrix properties. A synergism produces material properties unavailable from the individual constituent materials [1, 2].

Polyacrylic acid-based glass-ionomer cements appeared in the 1960s. They include a basic component, a glass-like calcium aluminosilicate containing some fluoride, and an acidic polyelectrolyte, which is a homopolymer or a copolymer of unsaturated carboxylic acids. The glass-ionomer cement sets as a result of a reaction between an acid and a base. The product of the reaction, a hydrogel salt, acts as a binding matrix surrounding the silicate particles.

Among the key properties of the glass-ionomer cements are specific adhesion to enamel and dentine, aesthetic qualities and fluoride release, which inhibits secondary caries over a prolonged period. In the 1980s, resin modified systems have become available commercially. These materials involve the formation of an interpenetrating polymer network combining the acid-base cross-linking reaction of the metal ion-polyacid with the cross-linking polymerization of the monomer system or additive action of the polymers [3-5]. Methods were proposed both for the preparation of the glass component [6] and for the organic macromolecular component [7]. However, because of the mixing problems, these methods are generally accompanied by a number of disadvantages, such as the formation of aggregations of inorganic particles, irregularly coated by polymers, and the low efficiency of controlling the coating thickness of the composite surface.

In this study, we explore the importance of components organization at the surface of composite materials, in controlling both the surface chemistry and the morphology. In this respect, we developed new characterization methods for glass ionomer composites, owing to their potential applications in medicine, such as bone substitutes and dental biomaterials. These composites are made of inorganic phase, e.g. surface active glasses, and different copolymers, such as poly(alkenoic acids). Caution was taken to maintain a good homogenization so that no phase separation was observed.

Further, the structure control of the composite surface can be achieved, both by the preparation methods of the material and by surface engineering methods applied to the composite surface. Such methods comprise direct enrichment of the surface with one of the composite components or the application of thin films made of organic mixture, such as a gloss, with good adhesion on the composite surface.

On the other hand, the success of these methods, to form the composite or for the controlled enrichment of its surface with a polymer or a gloss depends on the accurate analysis of the final organization at the composite surface.

Physical chemistry of surfaces of composite materials offers diverse research methods, such as X-ray photoelectron spectroscopy (XPS), contact

angle analysis (CA) and secondary ion mass spectrometry (SIMS), which had proved their utility in chemical characterization of surfaces. XPS and SIMS can be used also for the visualization of surfaces, but the resolution offered by these techniques is not sufficient to make possible the determination of morphology of the composites at nanoscale.

Anyway, the characterization of surface organization can be achieved by scanning electron microscopy (SEM) [8]. Generally, SEM visualizes the morphology of the composite surface and to evidence the role of surface enrichment of the composite with polymer, only in the case where the enrichment generates significant topographical modifications between constituent domains. This limitation can be overcome by using the atomic force microscopy (AFM), in tapping mode. Moreover, the AFM technique offers the possibility to determine the surface roughness, an important parameter which can bring information on the changes in surface organization by advanced processing techniques as well as on the degradation of the composite surface, exposed to different environments. However, to the best of our knowledge, no report has been devoted to the AFM investigations on these type of glass ionomer composites.

In this work, for the first time, we explore AFM observations to describe the surface morphology and the surface roughness of the two composite materials and of their constituents, in native state as well as after their surface processing, and in different environmental conditions and at the chosen regular time.

Thus, in the following we determine the bidimensional (2D-) and three-dimensional (3D-) topographical AFM images and the phase images for the surface of inorganic phase, i.e. inorganic powder (IP), of the organic phase (B1 or T1 copolymer), and of the composite materials, labeled as B1 or T1 composite, polished or glossed, with the aim to decipher the surface structure of these materials. Then, the surface morphology and the surface organization, as well as the surface roughness for 17 samples were investigated.

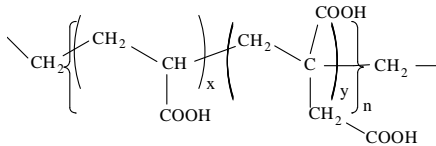
EXPERIMENTAL PART

Preparation of films made from inorganic powders or organic matter

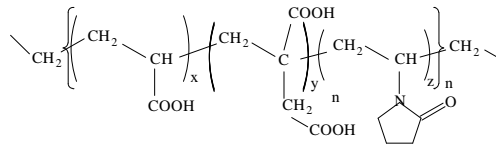
The *inorganic powder* (IP) was a blend of surface active glasses (glass ionomer products), viz. S1 and M glasses in the 7:1 mass ratio. The bulk composition of S1 glass is: SiO₂ (49%), Al₂O₃ (22%) and CaF₂ (29%): it is therefore a fluoro-aluminosilicate glass. The M glass has the following bulk composition: ZnO (16.72%), CaO (23.8%), Na₂O (9.33%) and SiO₂ (50.15%). These glasses were obtained from the corresponding oxides as described elsewhere [9-11]. After the raw materials were fused together, the melts were shock cooled in water. The glass fragments were ground and sifted to fine powders. Thin *films of this inorganic powder* were

assembled on adhesive tapes, by rotating the tape on the surface of the IP powder, lying on optically polished glass. This film was subsequently used for AFM investigations.

The *organic phase* contains either B1 copolymer (or T1 copolymer. The copolymers are both modified poly(alkenoic acids). Each copolymer was used as a 50% (weight/weight) aqueous solution. Finally tartaric acid was added to aqueous solution, resulting in a final composition of 48.5% copolymer (B1 or T1, respectively), 48.5% water and 3% tartaric acid.



Formula of B1 copolymer



Formula of T1 copolymer

Films for use as AFM samples were prepared from each of these copolymer solutions by casting 1 ml aliquot of solution onto mica (muscovite) substrates (1 cm x 1 cm squares) atomically plane and freshly cleaved. The films were dried at room temperature, in air environment, but protected against dust.

In all experiments, for the preparation of the organic phase deionized water, with resistivity of 18 MΩ·cm, was used. It was obtained from an Elgastat water purification system.

The glassware used in this research was washed and rinsed with ultra pure water before using. The B1 and T1 copolymer films, after drying, were observed by AFM.

Preparation of composite materials, B1 and T1 composite disks

The two kinds of composite specimens (glass ionomer cements), B1 and T1 composite, were made of the same inorganic powder blend (IP) described above in mixture with the organic phase, containing either B1 copolymer or T1 copolymer. The specimens were given the same labels as the copolymer, namely B1 or T1 composite. The inorganic phase constitutes the active filling (reinforcement material) of the composite, while the copolymers constitute the matrix material. In the preparation of both kinds of specimens, the same charging ratio was used: inorganic phase to organic phase 2.2:1 mass ratio.

The specimens were prepared, at 23°C from the aqueous solutions of the synthesized copolymers (polyalkenoic acids) and the superficially active glasses, by mechanical homogenization of the powders and liquids. The specimens, having the form of disks of 6 mm diameter and 1 mm height, were obtained by hardening of fresh mixed pastes in Teflon molds which were hermetically closed and stored in water at 37°C. After about 30

minutes, the specimens were taken out of the matrix and were immediately immersed in water at 37°C, for 24 hours [9].

AFM investigations

The AFM visualization of the surface of the investigated materials was executed using the scanning microscope, the AFM JEOL 4210 equipment, operating in the intermittent contact, known as tapping mode. The cantilever used was a triangular one, with a very pointed tip made from silicon nitride. The probe (tip) was on the cantilever, oscillating with a resonant frequency in the range of 200-300 kHz and with a spring constant of 17.5 N/m. Both a low scanning rate, 1Hz, and a higher rate, in the range 2-6 Hz were used, in order to detect possible scanning artifacts or those resulting from the sample preparation. The scanning angle was also modified on different directions, in order to distinguish between real images and those corresponding to artifacts. The AFM images consist of multiple scans displaced laterally from each other in y direction with 512 x 512 pixels. An adequate low pass filtering was performed to remove the statistical noise without loss in the structural features of the material. All AFM experiments were carried out under ambient laboratory temperature conditions (about 20°C) as previously reported [12-14]. AFM observations were repeated on different areas on the scanned surface (i.e. for different magnifications), resulting in scanned areas from 10 x 10 μm^2 to 1 x 1 μm^2 or scaled down even more (0.5 x 0.5 μm^2) for the same sample. The AFM images were obtained from at least five macroscopic zones separately identified on each sample. All the images were processed according to standard AFM proceeding.

For the beginning, the surface structure was investigated by AFM imaging separately for the films made from the inorganic phase, IP, i. e. a mixture of S1 and M glasses powder, or from the organic phase containing either B1 copolymer or T1 copolymer. In the following, the surface of the composite materials, B1 and T1 composite disks, was analyzed

- in their native, original state
- after mechanical polishing with a dental drill
- after application of a gloss on the composite disk surface.

The *polishing* was preceded by an initial smoothing of the surface with an extradure fraise with turbine E0130 (maillefer). The polishing was made with abrasive disks OptiDisc from KerrHawe and followed by a washing with water jet and drying.

The *finishing gloss* Vitremer™, manufactured by 3M-ESPE, is a resin without filling mass, based on bisGMA (Bisphenol-A-glycidyl dimethacrylate) and TEGDMA (triethylene glycol dimethacrylate). It was applied as a thin layer at the composite material surface and then cured by photopolymerization for 20 s using the curing light L.E.Demetrom II from SDS Kerr.

The AFM measurements were executed both in the air and in contact with artificial saliva as a simulation of the biological medium, versus time, after one day, and after 7 days, in order to evidence and control the releasing process of B1 or T1 copolymer from the composite material. The composition of the *artificial saliva* was: 50 mmol/l KCl, 1.5 mmol/l Ca^{2+} , 0.9 mmol/l PO_4^{3-} , 20 mmol/l trihydroxymethylaminomethane, buffer at pH 7.0 [15].

RESULTS AND DISCUSSION

Generally, the degradation or the releasing rate of the copolymer from the composite surface is mainly controlled by the polymer erosion in contact with saliva. From these studies, with B1 and T1 composite disks in their native state, the hydrolytic liability of the copolymers can be estimated and the polymer which suffers a faster degradation (dissolution) in contact with saliva can be established. A modality to control the degradation/modification of surface structure in B1 and T1 composites is to gloss the disk surface with a blend of components that generally increases the stability of the composite surface against the environment (saliva).

We used the topographical and phase AFM images for evidencing the surface characteristics of B1 and T1 composite disks, for the identification of surface components, for revealing the existence of inorganic micro- and nanoparticles associated with the copolymer matrix. Moreover, the AFM offers the possibility to determine the surface roughness, described by the rms value (root mean square) and calculated directly from the 2D topographical AFM images [12-14].

AFM investigations on the films made from inorganic material and from organic material

For the films made from the inorganic phase, the AFM images are shown in Figure 1, and for those of the organic phase in Figures 2 and 3: namely, in Figure 2 for the films containing B1 copolymer and in Figure 3 for films of T1 copolymer.

Figure 1 shows the morphology of the inorganic film surface. From the bidimensional (2D-) topographic AFM image (Fig. 1a), and from the three-dimensional (3D-) topographic image (Fig. 1c), as well as from the AFM phase image (Fig. 1b), the structuration of the inorganic powder into micro-agglomerates is seen (see, the arrow in panel a). From the cross section profile (Fig. 1d) we observe the microstructure of the inorganic film with particle sizes generally between 200 and 400 nm. In Fig. 1a it can be seen that the micro - agglomerates are formed from inorganic nano - powder

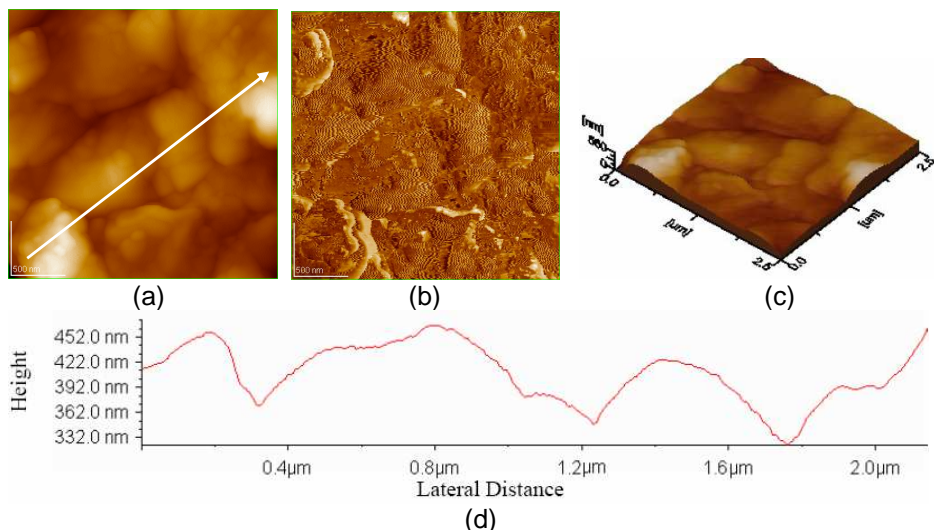


Fig. 1. AFM images of the film made from inorganic powder, deposited on adhesive tape. Scanned area: $2.5 \times 2.5 \mu\text{m}^2$. a) 2D topographic image; b) phase image c) 3D topographic image; d) cross section along the arrow in Fig. 1a.

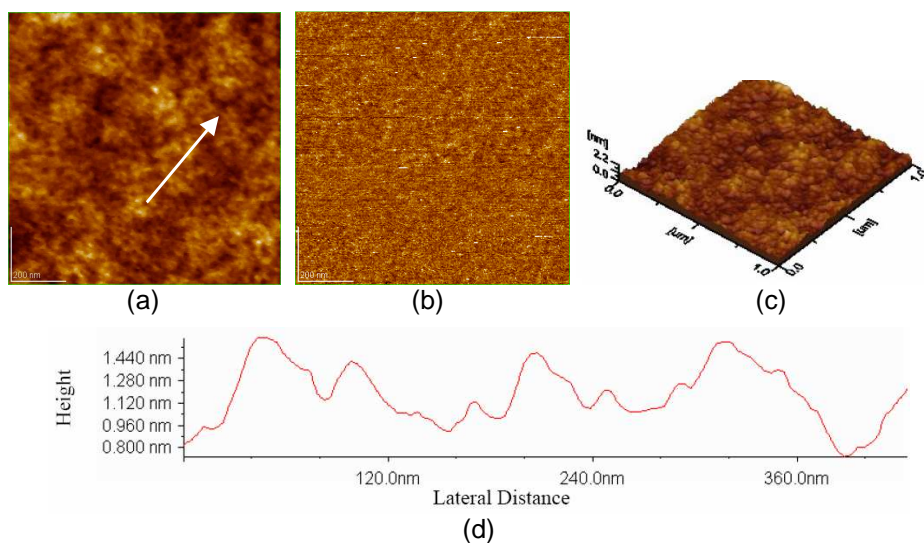


Fig. 2. AFM images of the organic film, containing B1 copolymer, deposited on mica support. Scanned area: $1 \times 1 \mu\text{m}^2$. a) 2D topographic image; b) phase image c) 3D topographic image; d) cross section along the arrow in Fig. 2a by association. The inorganic film is rough; the rms value showing the surface roughness is given in Table 1.

In Figure 2, we present the surface morphology of B1 copolymer films, containing tartaric acid, deposited on a mica substrate. From the

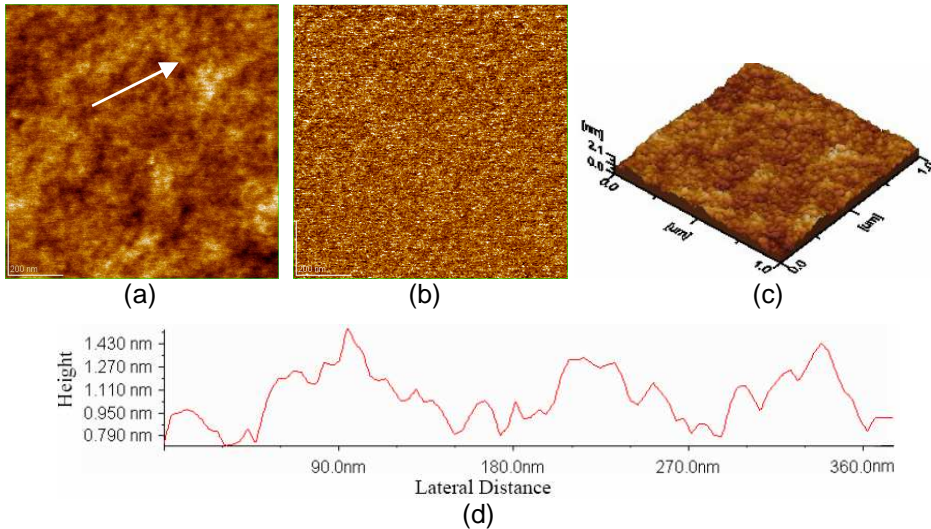


Fig. 3. AFM images of the organic film, containing T1 copolymer, deposited on mica support. Scanned area: $1 \times 1 \mu\text{m}^2$. a) 2D topographic image; b) phase image; c) 3D topographic image; d) cross section along the arrow in Fig. 3a

topographic AFM images (Figs. 2a, 2c) it is evident that the B1 copolymer forms nano domains, identified by their topographic characteristics. From the profile of the cross section (Fig. 2d), obtained along the direction given by the arrow in Fig. 2a, the dimensions of the nano domains are observed to be between 40 and 60 nm. The phase image (Fig. 2b) indicates the presence of a uniform film in every scanned area. The B1 copolymer film is smooth and the very low roughness of the B1 film is given in Table 1.

Figure 3 presents AFM images for the T1 copolymer film, deposited and oriented on the mica surface. The surface morphology (Figs. 3a, 3c) of the T1 copolymer film is similar to that characteristic to the B1 copolymer film (Fig. 2). The structuration of the T1 copolymer at the film surface results in nano domains situated in the range from 30 to 50 nm (Fig. 3d). The phase image (Fig. 3b) also indicates a T1 film smooth, with low roughness (Table 1).

From a comparison of Figures 2 and 3, a certain morphologic similarity is ascertained in the surface of B1 and T1 copolymers, which reflects a strong interaction between copolymer macromolecules, resulting in plane copolymer films. From this study it seems that both copolymers, B1 and T1, should be of interest in the realization of composite materials by individual mixing of their organic phases with the inorganic powder. As stated above, these composites (charging 2.2:1 ratio) were tableted, yielding B1 and T1 composite disk.

Surface morphology and characterization of B1 and T1 composites

In the following the bidimensional (2D-) and three-dimensional (3D-) topographical AFM images, as well as the phase images are presented, for the surface of the two composite materials, B1 and T1 composite disks, with the aim to decipher the surface morphology of the composites and the surface organization of their components, the inorganic and the organic phase.

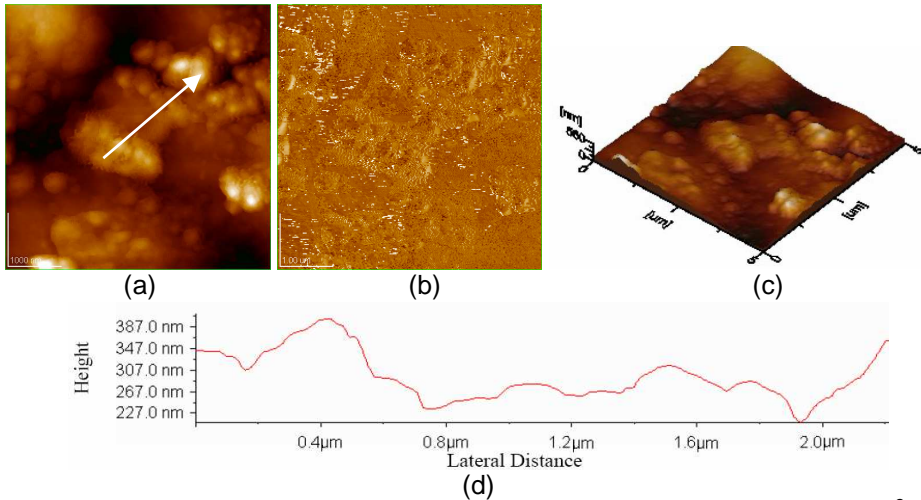


Fig. 4. AFM images of B1 composite disk surface. Scanned area: $5 \times 5 \mu\text{m}^2$. a) 2D topographic image; b) phase image; c) 3D topographic image; d) cross section along the arrow in panel 4a.

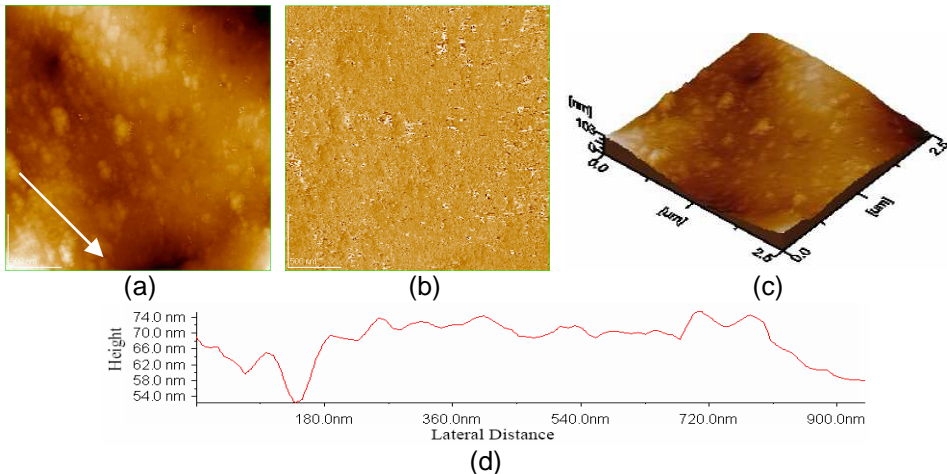


Fig. 5. AFM images of B1 composite disk surface. Scanned area: $2.5 \times 2.5 \mu\text{m}^2$. a) 2D topographic image; b) phase image; c) 3D topographic image; d) cross section along the arrow in panel 5a.

The measurements for the *B1* and *T1* composite disks, respectively, were carried out on native surfaces (Figs. 4-6) and after their advanced processing by mechanical polishing (Figs. 7, 8) and glossing (Figs. 9, 10), in air (Figs. 4 -10) and in saliva environment (Figs. 11-19), after 24 hours (Figs. 11-13, 16, 18) or 7 days (Figs. 14, 15, 17, 19).

From AFM images (Figs. 4, 5) one can observe the morphological and chemical organization of the *native B1* composite disk surface. Agglomerates of inorganic powder, also called clusters, are observed as high formations, light-colored in the 2D- (Figs. 4a, 5a) and 3D- topographical images (Figs. 4c, 5c), surrounded by the matrix of B1 copolymer (the lower, dark-colored zones). The associates of inorganic powder have the size in the range from 100 to 300 nm (Figs. 4d, 5d), comparable with their size visualized in the film made only from inorganic powder (Fig. 1). However, the undulation in the cross section profiles (Figs. 4d, 5d) indicate the existence of inorganic nano-powders associated as micro aggregates embedded in the B1 copolymer matrix. We also state the existence of both, heterogeneous (Fig. 4) and more homogeneous zones (Fig. 5), what should indicate that the B1 copolymer does strongly interact with the inorganic powder, which is embedded in its polymeric matrix (Figs. 4b, 5b). From cross section profiles (Figs. 4d, 5d), as compared with the profile of the inorganic powder film (Fig. 1d), it is evident that the inorganic particles are smaller in the B1 copolymer matrix, and are protected against the segregation existent in the native film of inorganic powder. The values for the surface roughness of B1 disk are given in Table 1 and reflect the significant diminution of the roughness in presence of B1 copolymer.

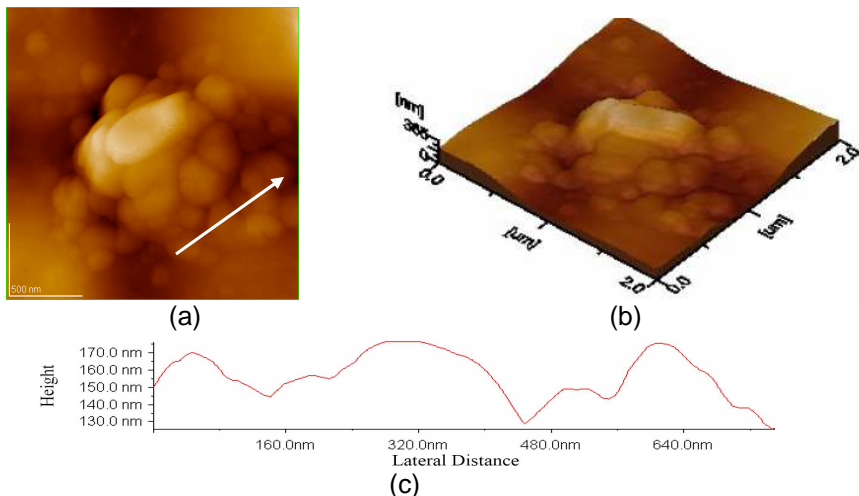


Fig. 6. AFM images of T1 composite disk surface. Scanned area: $2 \times 2 \mu\text{m}^2$. a) 2D topographic image; b) 3D topographic image; c) cross section along the arrow in panel 6a.

The AFM images for the surface (only one example is given in Fig. 6) of the original T1 composite disk are quite similar to those for B1 composite (Figs. 4 and 5). The size of the IP agglomerates is situated in the range from 150 to 300 nm. However, the surface roughness of the T1 composite disk (Table 1) is higher than that of the B1 composite disk. A possible explanation is the lower enrichment of the surface of the T1 composite in T1 copolymer, leaving the IP aggregates higher than in the matrix of B1 copolymer. This situation would also explain the lower stability of the T1 composite surface, particularly after 7 days exposure to saliva, against the better stability of the B1 composite in the same conditions.

Figure 7 shows AFM images for the surface of B1 composite disk, mechanically polished. In the same way with the morphology of the original B1 composite disk surface, here, also the existence of agglomerates of inorganic powder in the B1 copolymer matrix is observed. Thus, by the surface polishing of the B1 composite disk another plane from the bulk of the disk is evidenced and the AFM observations indicate a resemblance in the disposition of inorganic powder clusters both in the bulk and at the surface of B1 composite. Nevertheless, by a more thoroughly study of the cross section profiles, the existence of some larger agglomerates is ascertained in the polished surface (Fig. 7d) as compared to the original surface of B1 composite (Fig. 5d). This observation should indicate a trend to the surface enrichment in B1 copolymer during the fabrication process of B1 composite disk, having as the consequence a rather good protection of the IP particles against the tendency to segregation in the disk surface. The surface roughness (Table 1) is a little decreased by polishing, suggesting good mechanical properties for the B1 disk.

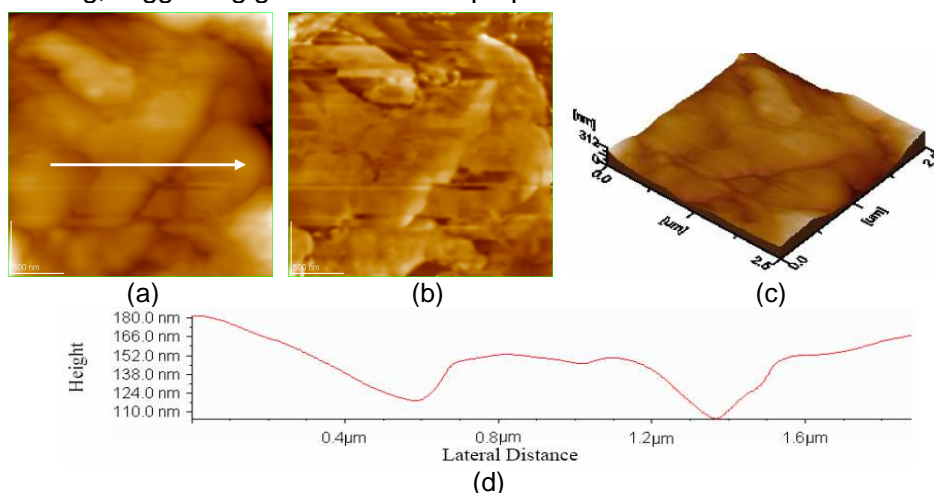


Fig. 7. AFM images of the polished B1 composite disk surface (B1p). Scanned area: $2.5 \times 2.5 \mu\text{m}^2$. a) 2D topographic image; b) phase image; c) 3D topographic image; d) cross section along the arrow in panel 7a.

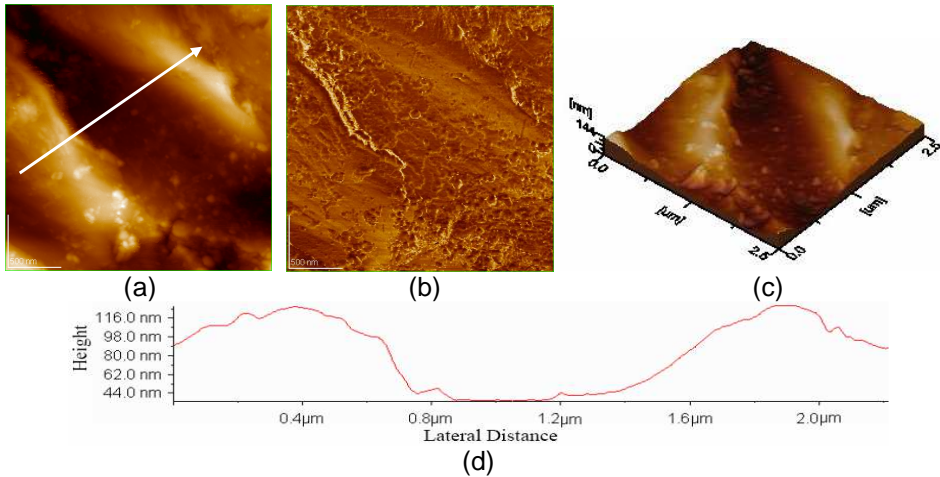


Fig. 8. AFM images of the polished T1 composite disk (T1p) surface Scanned area: $2.5 \times 2.5 \mu\text{m}^2$. a) 2D topographic image; b) phase image c) 3D topographic image; d) cross section along the arrow in Fig. 8a

At the surface of the T1 composite disk, mechanically polished (Fig. 8), the existence of IP agglomerates embedded in the copolymer matrix can be observed. A thorough analysis of topographic images (Figs. 8a, 8c) and particularly of the phase image (Fig. 8b) reveals the lamellar aspect of T1 copolymer. An arrangement in rows of the IP micro particles in the T1 copolymer matrix is observable (Figs. 8a, 8d). Therefore, we could infer that unlike B1 copolymer, the T1 copolymer does not homogenize (in bulk) sufficiently well the IP phase in the fabrication process of the disk. However, the surface roughness of the T1 disk, after polishing (Table 1), is lower than that of the native T1 disk, and comparable with that of the polished B1 composite disk, suggesting quite good (bulk) mechanical properties for the T1 composite.

The surface processing of B1 composite disk by glossing leads to a surface enrichment with a film made of an organic gloss, of polymeric nature. The gloss film gave AFM images shown in Fig. 9. From these images it can be seen that the gloss film follows the surface of the B1 disk, and the IP associates are still visualized both in the topographic images (Figs. 9a, 9c) and in the phase image (Fig. 9b). From the cross section profile (Fig. 9d) IP clusters are identified with a size of about 100 – 300 nm. The glossed surface of the B1 composite disk presents a much lower roughness versus the original disk (Table 1). This means that the gloss film fills the zones between the IP particles existent on the disk surface. Since the IP particles can still be visualized in the glossed surface, we can estimate that the gloss film is thin and presents a good adherence to the B1 composite disk.

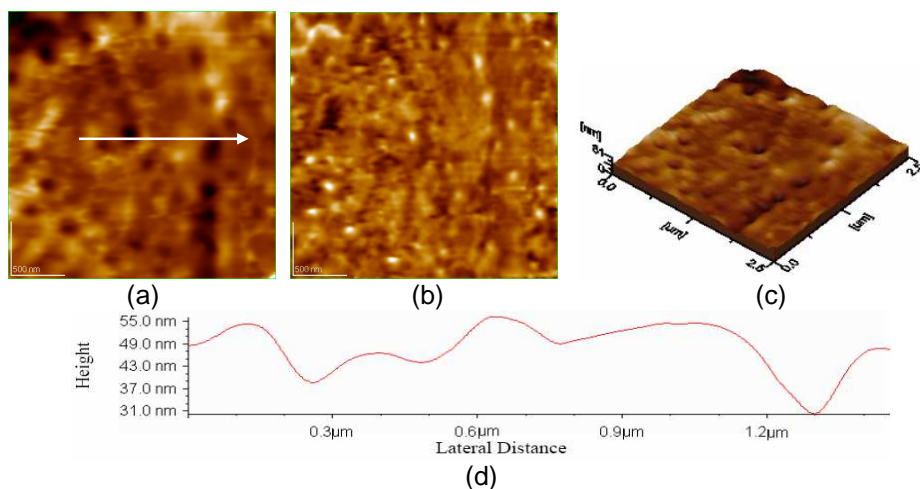


Fig. 9. AFM images of the glossed B1 composite disk (B1g) surface. Scanned area: $2.5 \times 2.5 \mu\text{m}^2$. a) 2D topographic image; b) phase image c) 3D topographic image; d) cross section along the arrow in Fig. 9a

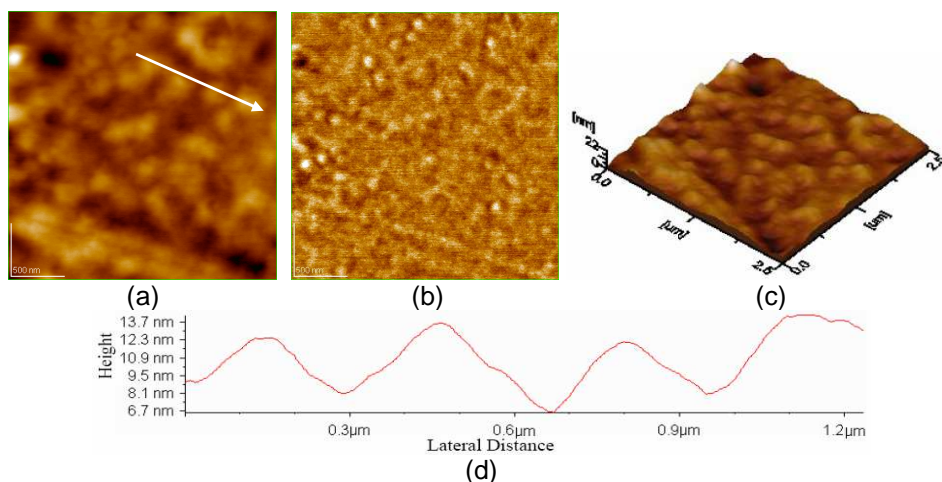


Fig. 10. AFM images of the glossed T1 composite disk (T1g) surface. Scanned area: $2.5 \times 2.5 \mu\text{m}^2$. a) 2D topographic image; b) phase image c) 3D topographic image; d) cross section along the arrow in Fig. 10a

The morphology of the gloss layer, deposited on the surface of the native T1 composite disk, was also visualized by AFM (Fig. 10), in the environment (air). From the analysis of these images, it results that the gloss layer is adherent to the disk surface, and the IP phase associates are evidenced both in topographic images (Figs. 10a, 10c) and in the phase image (Fig. 10b). From the cross section profiles (Fig. 10d), clusters of inorganic phase are identified, with sizes about 150 – 300 nm. The gloss layer presents a very low roughness against the

native T1 composite disk (see Table 1). This result is explained by the filling of the zones between the IP particles with gloss at the disk surface, similarly to the case of the glossed B1 disk (Fig. 9). Since the inorganic particles (ordered in rows) can still be visualized in the glossed surface of T1 composite disk, we can estimate that the gloss film is thin and adheres well to the disk.

In the following the behavior of B1 and T1 composite disks in saliva was investigated. After 24 hours in saliva, the morphologies of B1 composite disk (Figs. 11, 12) and of the T1 composite disk (Fig. 13) are similar to those observed in air after preparation (Figs. 4, 5, 6). The same heterogeneous zones (Fig. 11, with high rms values) or homogeneous (Fig. 12, with low rms values) are observed at the B1 composite surface. For the T1 disk, the rms values are slightly lower than for the native T1 disk in air (Table 1), but the values are comparable (within the limit of experimental errors) with those characteristic to the B1 disk surface, in similar conditions. We conclude that the original B1 and T1 disks present high stability in saliva for 24 hours.

After 7 days in saliva, the surface morphology of B1 disk (Fig. 14), as well as that of the T1 disk (Fig. 15) is still similar to that of the original disks (Figs. 5, 6) or to that of the disk after 24 hours in saliva (Figs. 12, 13).

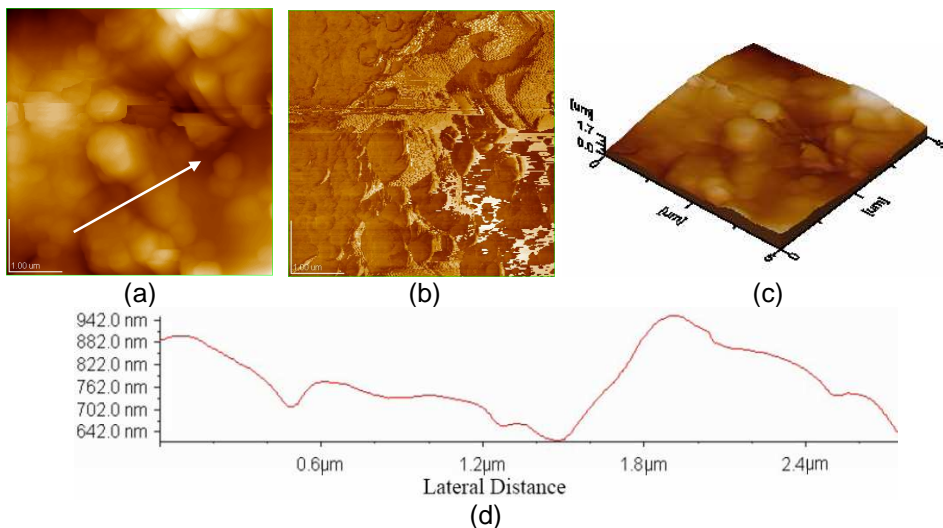


Fig. 11. AFM images of B1 composite disk surface after 24 h in saliva. Scanned area: $5 \times 5 \mu\text{m}^2$. a) 2D topographic image; b) phase image; c) 3D topographic image; d) cross section along the arrow in panel 11a.

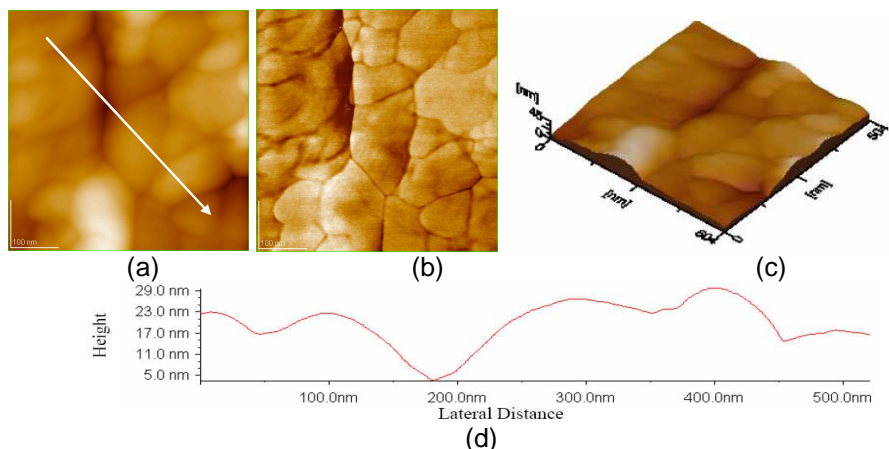


Fig. 12. AFM images of the B1 composite disk surface, after 24 h in saliva. Scanned area: $0.5 \times 0.5 \mu\text{m}^2$. a) 2D topographic image; b) phase image c) 3D topographic image; d) cross section along the arrow in Fig. 12a

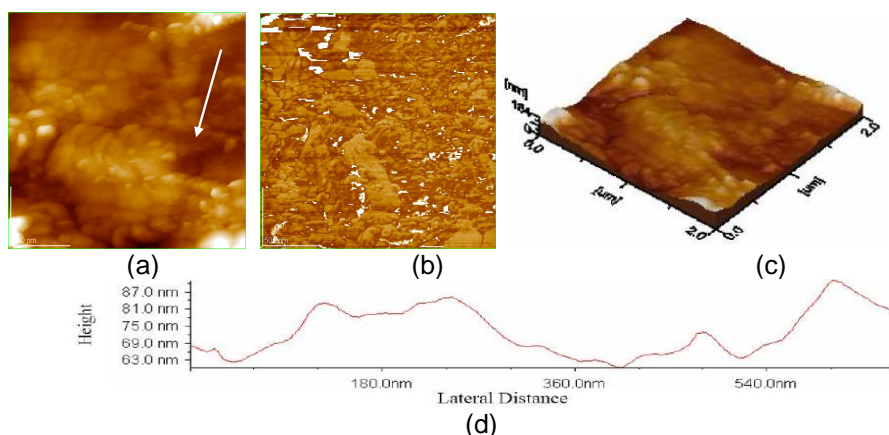


Fig. 13. AFM images of the T1 composite disk surface, after 24 h in saliva. Scanned area: $2 \times 2 \mu\text{m}^2$. a) 2D topographic image; b) phase image c) 3D topographic image; d) cross section along the arrow in Fig. 13a

However, a substantial increase of the surface roughness is to be seen, especially for the T1 composite (see Table 1). This should indicate a certain erosion of the T1 copolymer in the surface of the T1 disk, leaving the inorganic powder without coating layer as it had after the preparation or after 24 hours in saliva.

Further, the surface of the glossed B1 and T1 disks was visualized by AFM, also after 24 hours in saliva (Fig. 16, 18) and after 7 days in saliva (Figs. 17, 19). From the analysis of AFM images it results that the gloss layer does protect the B1 disk surface against the saliva fluid. Comparing

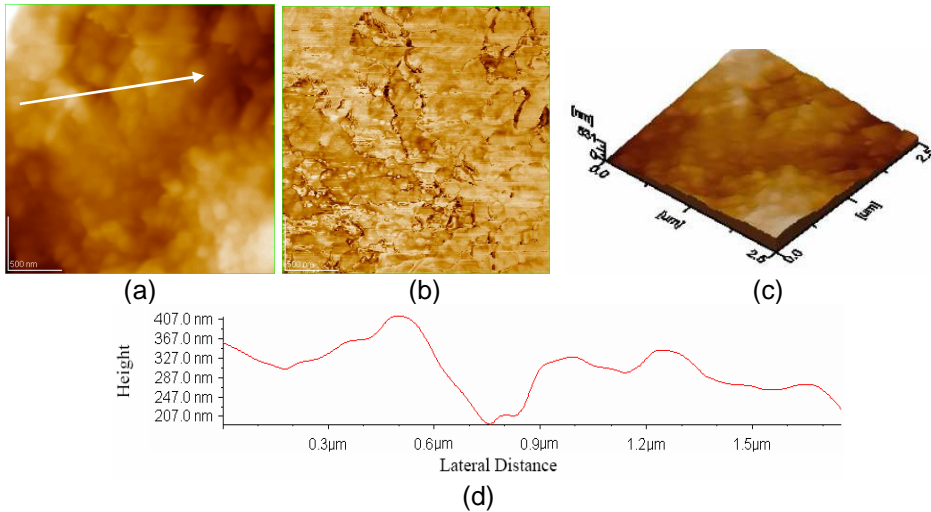


Fig. 14. AFM images of the B1 composite disk surface, after 7 days in saliva. Scanned area: $2.5 \times 2.5 \mu\text{m}^2$. a) 2D topographic image; b) phase image c) 3D topographic image; d) cross section along the arrow in Fig. 14a

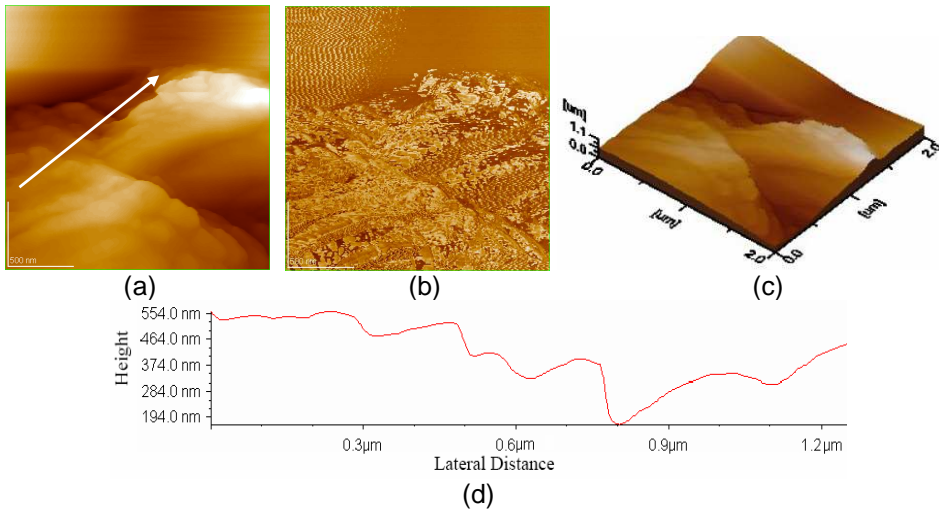


Fig. 15. AFM images of the T1 composite disk surface, after 7 days in saliva. Scanned area: $2 \times 2 \mu\text{m}^2$. a) 2D topographic image; b) phase image c) 3D topographic image; d) cross section along the arrow in Fig. 15a

the surface morphology of the glossed B1 disk measured in air (Fig. 9), and after exposure to saliva (Figs. 16, 17), the stability of the gloss film is evidenced, and its surface roughness remains practically constant. After 7 days of exposure to saliva, the morphologic texture of the disk surface

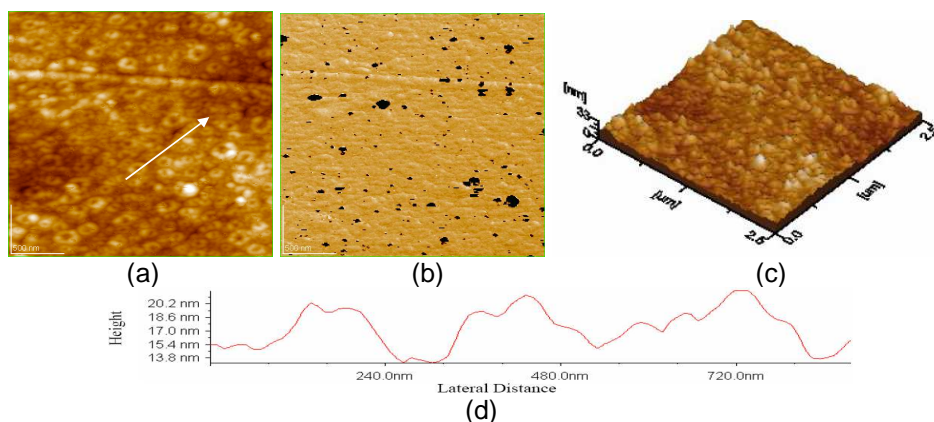


Fig. 16. AFM images of the glossed B1 composite disk (B1g) surface, after 24 h in saliva. Scanned area: $2.5 \times 2.5 \mu\text{m}^2$. a) 2D topographic image; b) phase image c) 3D topographic image; d) cross section along the arrow in Fig. 16a

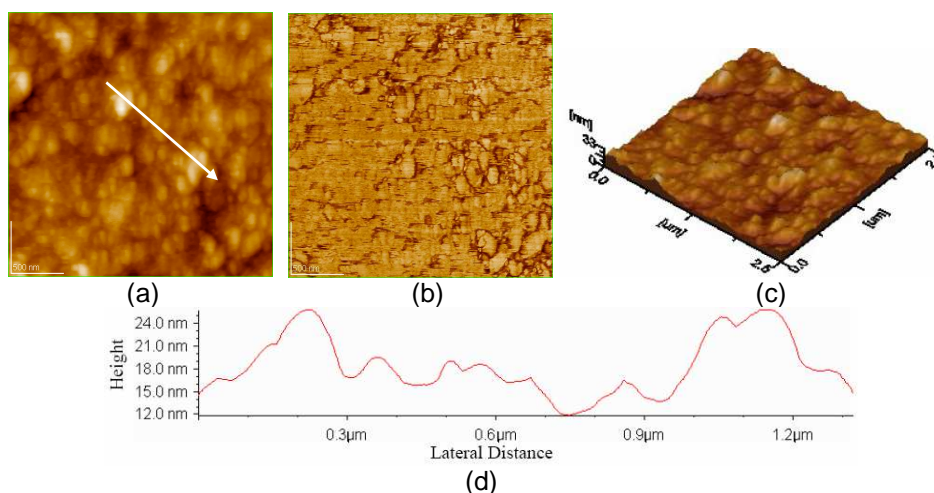


Fig. 17. AFM images of the glossed B1 composite disk (B1g) surface, after 7 days in saliva. Scanned area: $2.5 \times 2.5 \mu\text{m}^2$. a) 2D topographic image; b) phase image c) 3D topographic image; d) cross section along the arrow in Fig. 17a

begins to be more evidently outlined than after 24 hours in saliva. This could be explained either by a slight erosion of the gloss film, or by the fact that the thickness of the gloss film was not constant, rigorously controlled during its deposition process on the disk surface. Generally, the gloss film is fairly stable and its adhesion on the disk surface is quite good. It increases the surface stability of the disk, and this is also evidenced by the reduced surface roughness of the film (see Table 1). In the future, the long term stability (a month ore more) of the glossed disk in saliva will be investigated.

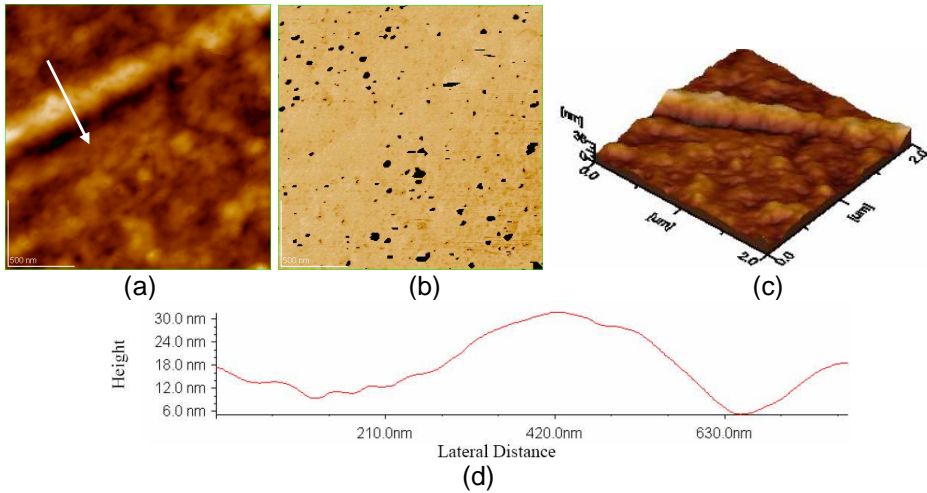


Fig. 18. AFM images of the glossed T1 composite disk (T1g) surface, after 24 h in saliva. Scanned area: $2 \times 2 \mu\text{m}^2$. a) 2D topographic image; b) phase image c) 3D topographic image; d) cross section along the arrow in Fig. 18a

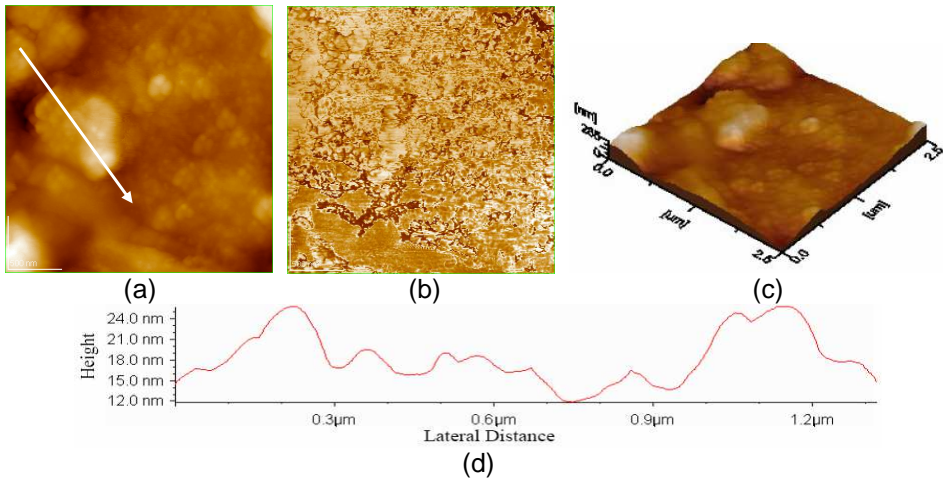


Fig. 19. AFM images of the glossed T1 composite disk surface (T1g), after 7 days in saliva. Scanned area: $2.5 \times 2.5 \mu\text{m}^2$. a) 2D topographic image; b) phase image c) 3D topographic image; d) cross section along the arrow in Fig. 19a

For the same tests in saliva with glossed T1 composite disks, the AFM images are given in Figure 18 (after 24 hours) and in Figure 19 (after 7 days in artificial saliva). From the comparison of surface morphology of the glossed T1 composite disk in air (Fig. 10), and after exposure to saliva, it results that here the gloss film is also stable, the surface roughness being practically constant (Table 1) after a 24 hours exposure to saliva.

After the 7 days exposure to saliva, the morphologic texture (Fig. 19) of the glossed T1 composite disk surface becomes more evidently outlined than after 24 hours. Its surface roughness (Table 1) increases much over its value in air, or in saliva for 24 hours.

Therefore, from the analysis of AFM images, it results that the gloss layer protects the surface of the T1 composite disk against saliva medium after a 24 hours exposure, but after 7 days in saliva the T1 copolymer presents striking erosion, reflected also by the increase of surface roughness. This could be explained by a pronounced erosion of the gloss layer, deposited on the T1 composite disk, after immersion for 7 days in saliva, assuming that the gloss film was uniformly deposited on the whole surface of the disk. It seems that the stability of the gloss film deposited on the surface of the composite from the T1 composite disk is lower than for its deposition on the B1 composite surface.

Table 1.

Surface roughness, determined by AFM, of the tested materials: inorganic powder (IP), B1 copolymer, T1 copolymer, composite materials: B1 and T1 composite specimen, for different kinds of processing, exposed to air or in saliva.

Sample Scanned areas (μm^2)		Surface roughness, nm				
		5 x 5	2.5x2.5	2 x 2	1 x 1	0.5x0.5
Sam- ple	Type of processing					
IP	Inorganic film	191	67.3			
B1	Organic film: B1 copolymer	0.28	0.26		0.23	
T1	Organic film: T1 copolymer	0.36	0.35		0.24	
B1	B1 composite disk	89.0	38.5	37.6	24.8	6.12
B1p	Polished B1 composite disk	70.0	35.0	32.8		
B1g	Glossed B1 composite disk	6.10	5.80	5.50	5.10	5.00
B1	B1 disk, 24 h in saliva	92.0	40.0	38.0	25.0	7.00
B1	B1 disk, 7 days in saliva	162	82.0	75.0		
B1g	Glossed B1 disk, 24 h in saliva	4.80	3.90	3.40		
B1g	Glossed B1 disk, 7 days in saliva	5.70	4.00			
T1	T1 composite disk	111	70.0	66.7	46.1	12.0
T1p	Polished T1 composite disk	95.0	31.4	30.5		
T1g	Glossed T1 composite disk	6.17	2.45	2.27	2.10	2.05
T1	T1 disk, 24 h in saliva	92.5	50.2	21.3	21.0	8.10
T1	T1 disk, 7 days in saliva	208	206	191		
T1g	Glossed T1 disk, 24 h in saliva	6.45	6.10	5.22		
T1g	Glossed T1 disk, 7 days in saliva	52.6	37.3			

The above mentioned investigations indicate that the composite material B1, presents some advantage over the T1 composite, as regards the homogeneity of the surface structure and the adhesion of the gloss film on the disk. This situation suggests the probability of a better mixture of the inorganic powder (IP) with the B1 copolymer (in bulk) and at the same time

indicates the existence of specific interactions between B1 copolymer and the polymers within the gloss film. Since the distinction between the two composites consists only in the used copolymer, we could conclude that the B1 copolymer presents more adequate characteristics than T1 copolymer for the realization of dental composites.

CONCLUSIONS

AFM observations make possible a profound analysis of the surface structure for the dental composites, as well as for the films made from the constituents of the composites: the inorganic phase (a mixture of surface active glasses) and the organic phase, differing only by the used copolymer (B1 or T1). The analysis of the surface structure for the films, made of the inorganic phase, and separately for the films made of the organic phase, indicates a micro and a nano structuration in the inorganic powder films and an advanced nano structuration of the B1 or T1 copolymer films.

B1 and T1 composite disks were prepared from the composite materials, formed from the inorganic phase and the organic phase (containing B1, respectively T1 copolymer) in the mass ratio of about 2.2:1. The surface morphology of the B1 and T1 composite disks, native, polished or glossed, was visualized by AFM, both in air environment and after 24 hours or after 7 days in saliva.

From the study of B1 and T1 composite disks, in their native state, in contact with saliva for 7 days, we estimate that the T1 copolymer presents a more pronounced hydrolytic lability than B1 copolymer, in fact T1 copolymer is degraded (dissolved) faster in saliva. Surface morphology and roughness of B1 and T1 composite disks are also comparatively discussed for different surface processing types, namely for the original, native disks and those mechanically polished. No significant topographic (morphologic) modifications of the surface for the two composites were observed for the samples polished in contact with air against the native disks evidencing quite good mechanical properties.

The morphologic organization differences in the surface of B1 and T1 composite disks, particularly after 7 days in saliva, lead to the following findings, the B1 copolymer seems to resist better than T1 copolymer to the erosion process in saliva, particularly for extended exposures (viz. 7 days). B1 copolymer seems to better homogenize the inorganic powder, insuring a better integration of organic and inorganic bulk phases, constituting the B1 composite.

Glossed B1 and T1 composite disks did not present a significant degradation of surface structure after 24 hours, or after 7 days of exposure to saliva. This means that the surface properties of the both composite materials can be improved and controlled by glossing the surface of the composites with a blend of polymeric components.

However, for the glossed T1 composite, after 7 days in saliva, an important increase of surface roughness is observed, which could be explained by a more pronounced degradation of the gloss on T1 composite, against that on the B1 composite. The higher stability of the gloss film applied on the B1 composite surface could be due to the better adhesion of the gloss on the B1 composite surface, due to the stronger specific interactions between the gloss components and the B1 copolymer.

On the basis of comparisons of B1 composite stability versus T1 composite, we can suggest that B1 composite is a better potential candidate for medical use.

ACKNOWLEDGEMENT

This research was realized having financial support from CEEEX project no.132/2006.

REFERENCES

1. V.Popescu, O.Horovitz, L.Damian, *Compozite cu matrice organică*, Ed. U.T.Press, Cluj-Napoca, **2001**.
2. O.Horovitz, V.Popescu, M.Moldovan, C.Prejmerean, *Macromolecule și compozite. Aplicații experimentale*, Ed. Mediamira, Cluj-Napoca, **2005**
3. D.C. Smith, *Biomaterials*, **1998**, *19*, 467-478.
4. R. Zimehl, M. Hannig, *Coll.Surf. A: Physicochem. Eng. Aspects*, **2000**, *163*, 55-62.
5. M. Darling, R. Hill, *Biomaterials*, **1994**, *15*, 299-306.
6. M.Taira, M.Yamaki, *J.Mater.Sci.:Mater.Med.*, 1995, *6*, 197-200.
7. M. H. Dotrong, W. M. Johnston, B. M. Culbertson, *J. Macromol.Sci.* 2000, *A37*, 911-926.
8. D. Xie, W. A. Brantley, B. M. Culbertson and G. Wang, *Dental Materials*, **2000**, *16*, 129-138.
9. C.Prejmerean, M.Moldovan, M.Brie, R.Grecu, M.Trif, M.Vezsenyi, O.Mușat, *Proc. Rom. Acad. SeriesB: Chemistry, Life Sciences and Geosciences*, **2000**, *2*, 117-125.
10. A.Puri, M. Georgescu, G. Voicu, *Rev. Roum.Chim.*, **2004**, *49*, 135-140.
11. G. Voicu, A. Puri, M. Georgescu, *Rev. Roum. Chim.*, **2005**, *50*, 713-716.
12. M. Tomoaia-Cotisel, Gh. Tomoaia, V. D. Pop, A. Mocanu, O. Cozar, N. Apetroaei and Gh. Popa, *Rev. Roum. Chim.*, **2005**, *50*, 471-478.
13. M. Tomoaia-Cotisel, "The nanostructure formation of the globular seed storage protein on different solid surfaces studied by atomic force microscopy", In *Convergence of Micro-Nano-Biotechnologies*, Series in *Micro and Nanoengineering*, **Volume 9**, Editors: Maria Zaharescu, Emil Burzo, Lucia Dumitru, Irina Kleps and Dan Dascalu, Romanian Academy Press, **2006**, Bucharest, pp. 147 - 161.
14. M. Tomoaia-Cotisel, A. Tomoaia-Cotisel, T. Yupsanis, Gh. Tomoaia, I. Balea, A. Mocanu and Cs. Racz, *Rev. Roum. Chim.*, **2006**, *51*,1181-1185.
15. M.C.Serra, J.A.Cury, *Quintessence Int.* **1992**, *23*, 143-7.

AMINO ACIDS BINDING TO GOLD NANOPARTICLES

OSSI HOROVITZ^a, AURORA MOCANU^a, GHEORGHE TOMOAI^b,
MARIA CRISAN^c, LIVIU-DOREL BOBOS^a, CSABA RACZ^a AND
MARIA TOMOAI-COTISEL^a

ABSTRACT. Gold nanoparticles capped with citrate anions were synthesized and characterized by UV-Vis spectroscopy; a strong absorption is identified at about 528 nm, corresponding to the surface plasmon resonance (SPR). The gold nanoparticles were analyzed by transmission electron microscopy (TEM) and TEM images indicate a mean gold nanoparticle size of 14 nm. The colloidal gold aqueous solution is stable in time, indicating a good electrostatic stabilization of gold nanoparticles through the adsorbed monolayer of citrate anions on gold nanoparticle surface. The interaction between the citrate capped gold nanoparticles in aqueous solution and various amino acids was investigated monitoring their UV-Vis spectra. Some of the tested amino acids, like glycine, isoleucine and asparagine, showed little interaction with gold nanoparticles. However, other amino acids, such as lysine, arginine, glutamic acid, histidine, cysteine and methionine, presented an absorption decrease of the colloidal gold solution at 528 nm and a bathochromic shift of the absorption maximum. At higher amino acid:gold molar ratios a new, large absorption band appears in the range of 600 to 700 nm, which increases in time. As a consequence of the assembly formation of gold nanoparticles, the color of the colloidal gold solution changes from red to blue. Further, TEM and atomic force microscopy (AFM) images evidenced the arrangements of gold nanoparticles mediated by amino acids. The analysis of AFM images indicate a close packed and an almost equidistant arrangement of gold nanoparticles coated by amino acids, especially for cysteine, arginine and lysine. These arrangements indicate a stabilization effect, mediated by these amino acids bonded to gold nanoparticle surface.

INTRODUCTION

There is increased current interest in the area of nanotechnology due to the outstanding physical and chemical properties of nanoparticles with potential applications in optoelectronic devices, non-linear optics and biosensors, just to name a few. One of the aims in nanotechnology is the organization of nanoparticles in thin films with the ability to modify and control the size and separation as well as the interactions between particles.

^a Babeș-Bolyai University of Cluj-Napoca, Faculty of Chemistry and Chemical Engineering, Arany J. Str., no 11, 400028 Cluj-Napoca, Romania

^b Iuliu Hațieganu University of Medicine and Pharmacy, Department of Orthopedic Surgery, Mosoiu Str., no. 47, 400132 Cluj-Napoca, Romania

^c Iuliu Hațieganu University of Medicine and Pharmacy, Department of Histology, Clinic of Dermatology, Clinicilor Str., no. 3, 400006 Cluj-Napoca, Romania;
e-mail: horovitz@chem.ubbcluj.ro, mcotisel@yahoo.com

Consequently, the optical and electronic properties of these assemblies can be tailored. Strategies are developed and explored for assembling metallic nanoparticles and biological molecules, in order to develop new materials for electronics and optics, and for biomedical and bioanalytical areas, such as controlled drug delivery, medical diagnosis and biosensors [1-6].

Among biological molecules, amino acids are important organic compounds to be used in biofunctionalization of gold nanoparticles, as protective layers and for their assembly in thin films. Functional groups such as -SH and -NH₂ present a high affinity for gold, and since amino acids contain some of these groups, they are expected to stabilize gold nanoparticles. Their capacity of generating structural diversity was recognized [7], and gold surfaces capped with amino acids are considered to represent the simplest models for protein surfaces [8].

There are relatively few reports on surface modifications of gold nanoparticles with amino acid molecules, and no systematic study of amino acid interactions with gold nanoparticles is available [9]. The binding of cysteine and lysine to gold nanoparticles was reported [10], and a review on amino acid interactions with metallic nanoparticles was given [11]. Some amino acids were used as reduction and capping agents for silver or gold nanoparticles, e.g. lysine [12-14], tryptophan [14, 15], aspartic acid [13, 16], tyrosine [14, 17], arginine [14, 17], cysteine, leucine and asparagine [18], and also the dipeptide glycyl-tyrosine [17]. The S-Au interaction in cysteine capped gold nanoparticles was discussed [18-21] and the binding of cysteine to Au was compared with that of leucine and asparagine [20]. Gold-silver nanocomposites were prepared from gold nanorod seeds in amino acid solutions: arginine, cysteine, glycine, glutamine, glutamate, histidine, lysine, and methionine [22].

Amino acids can be adsorbed on the particle surface already during the formation of particles, using the amino acid itself as reduction agent [14-18], or in a latter stage, by ligand exchange reactions or binding on the former adsorbed stabilizing molecules. In this way homogeneous monolayers or heterogeneous, mixed layers can be obtained. A pentapeptide was also used as a ligand on gold nanoparticles [23]. Cysteine adsorbed on a gold surface was used to immobilize protein molecules [24-26].

Previously, we have focused on the synthesis and physicochemical properties of citrate anions capped gold nanoparticles and on their organization in thin films on hydrophobic glass plates [27-30]. Surface functionalization of gold nanoparticles has been accomplished using a globular protein, extracted from aleurone cells of barley [27]. How citrate anions, capping agents of gold nanoparticles, are involved in the interaction between surface-modified gold nanoparticles and proteins is an important

question to be answered. An answer can be obtained by a systematic study of amino acids binding to gold nanoparticles.

This work is a follow-up to our ongoing research projects on the binding of amino acids and peptides to the gold colloidal nanoparticles. It deals with the synthesis of gold nanoparticles of controlled size and shape and with the functionalization of gold particles with different organic molecules, e.g. nine amino acids and two peptides. The interaction between gold nanoparticles and said organic molecules is observed by UV-Vis spectroscopy. Further, the deposition and organization of gold nanoparticle assemblies, in the presence of cysteine, arginine and lysine, are investigated by TEM and AFM.

EXPERIMENTAL PART

Materials

A colloidal gold solution was prepared by HAuCl_4 reduction with sodium citrate, in a variant of the Turkevich method, as adapted from [31]. The tetrachloroauric (III) acid was purchased from Merck (high purity above 99.5 %). The trisodium citrate dihydrate ($\text{Na}_3\text{C}_6\text{H}_5\text{O}_7 \cdot 2\text{H}_2\text{O}$) was obtained from Sigma Aldrich (high purity above 99%). All chemicals were used without further purification. Deionized water with resistivity of 18 $\text{M}\Omega\cdot\text{cm}$ was used in all experiments and it was obtained from an Elgastat water purification system. 200 mL 0.005% (w/w) $\text{HAuCl}_4 \cdot 3\text{H}_2\text{O}$ solution stirred vigorously was refluxed. To the boiling solution 15.3 mg trisodium citrate ($\text{Na}_3\text{C}_6\text{H}_5\text{O}_7 \cdot 2\text{H}_2\text{O}$), solved in a minimum amount of water, was added. After colour change, the heat was turned off and the solution was allowed to cool overnight to room temperature. The gold content in the final colloidal solution is 25 mg/L. The resulting solution of colloidal gold particles was stored in a brown bottle and kept at 4 °C.

The solid L-amino acids were purchased from Sigma and used without further purification. They were dissolved in deionized water. The amino acids used in this investigation, their three letter code, one letter code and the concentrations of their solutions (put in parentheses, in mol/L) were the following: L-glycine, Gly, G (0.41); L-isoleucine, Ile, I (0.1); L-glutamic acid, Glu, E (0.1); L-asparagine, Asn, N (0.5 M); L-cysteine, Cys, C (0.001; 0.01; 0.1); L-methionine, Met, M (0.2; 0.4); L-lysine, Lys, K (0.01; 0.1; 0.54); L-arginine, Arg, R (0.01; 0.1); L-histidine, His, H (0.01; 0.1).

Methods

The UV/VIS absorption spectrum of the solutions was studied using a Jasco UV/VIS V-530 spectrophotometer with 10 mm path length quartz cuvettes in the 190 – 900 nm wavelengths range.

The investigated mixtures were obtained from the gold colloidal solution (c_{Au}) and the amino acid solutions (concentration c_{AA}), by successive removal of

small amounts of the previous mixture and adding of equal amounts of amino acid solution. The gold and amino acid contents in the resulting mixtures and their ratios, used in most of the determinations, are given in Table 1.

Table 1.

Gold: amino acid ratios in the investigated mixtures. (c_{Au} = concentration of the gold colloidal solution; c_{AA} = concentration of the amino acid solution)

Gold content reported to c_{Au}	Amino acid content reported to c_{AA}	Content Au : AA ratio reported to (c_{Au}/c_{AA})
0.833	0.167	5 / 1
0.695	0.305	2.2 / 1
0.579	0.421	1.4 / 1
0.482	0.518	1 / 1.1
0.402	0.598	1 / 1.5
0.335	0.665	1 / 2
0.321	0.679	1 / 2.1
0.214	0.786	1 / 3.7

The colloidal gold nanoparticles suspension in the absence and in the presence of amino acids was deposited and air dried on the specimen grid and observed with a transmission electron microscope (TEM: JEOL – JEM 1010). TEM specimens consist of carbon or collodion coated copper grids. TEM images were recorded with a JEOL standard software.

Atomic force microscopy (AFM) investigations were executed on the gold nanostructured films made from gold nanoparticles functionalized with amino acids using a commercial AFM JEOL 4210 equipment with a 10 x 10 (x-y) μm scanner operating in tapping (noted *ac*) mode [32-34]. Standard cantilevers, non-contact conical shaped of silicon nitride coated with aluminum, were used. The tip was on a cantilever with a resonant frequency in the range of 200 - 300 kHz and with a spring constant of 17.5 N/m. AFM observations were repeated on different areas from 30 x 30 μm^2 to 250 x 250 nm^2 of the same gold film. The images were obtained from at least ten macroscopically separated areas on each sample. All images were processed using the standard procedures for AFM. The sizes of nanoparticles were measured directly from AFM 2D-topographic images and their 3D-views. The thickness (vertical distance) variations were estimated from vertical linear cross sections and height distributions on AFM images [32-34]. AFM images consist of multiple scans displaced laterally from each other in y direction with 512 x 512 pixels. Low pass filtering was performed to remove the statistical noise without to loose the features of the sample. All AFM experiments were carried out under ambient laboratory conditions (about 20 °C) as previously reported [34].

RESULTS AND DISCUSSION

Characterization of the colloidal gold solution

The visible absorption spectra of the gold colloidal aqueous solution presents a well-defined absorption band with a maximum at the wavelength $\lambda_{\max} = 527 - 528$ nm. This value is characteristic for plasmon absorbance for nanometric Au particles. The wavelength was not significantly modified, during a year after preparation, thus suggesting the stability of the colloidal solution.

The size of the gold colloid particles has been measured by TEM imaging. Two representative TEM images of these particles are given in Fig.1. The particles show mostly spherical or elliptical shape, just a few triangles, pentagons or hexagons are observed. From the sizes of a great number of particles, measured on the TEM images, an average size (diameter) of 14.2 nm with a standard deviation of 2.6 were calculated as well as the extreme values of the sizes, from 8.5 to 24 nm. From the average size, the approximate average mass of a particle (considered spherical) is estimated as $2.9 \cdot 10^{-17}$ g, the number of gold atoms in a particle

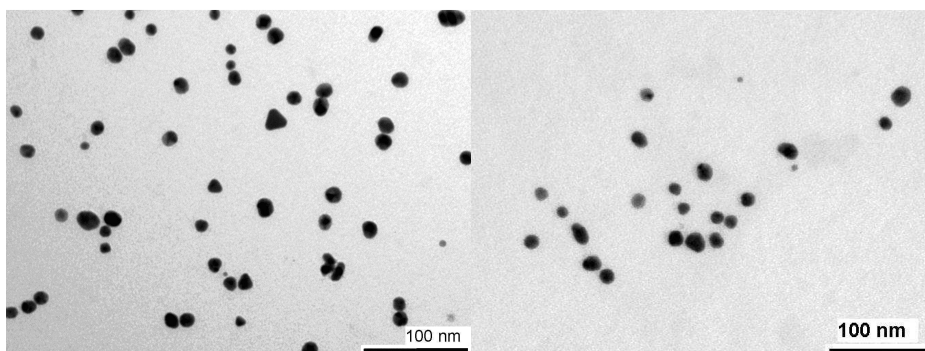


Fig.1. TEM images of gold nanoparticles

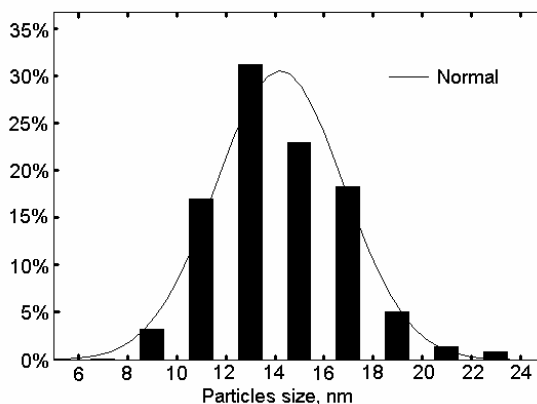


Fig.2. Histogram of size distribution for gold particles

is $8.8 \cdot 10^4$ and the number of particles per cm^3 of solution is $8.6 \cdot 10^{11}$. The histogram providing the size distribution of gold nanoparticles, obtained from TEM images is given in Figure 2. For comparison, the curve indicating the expected normal distribution was added.

The colloidal gold solution proved as very stable in time, without observable modifications in the UV-Vis spectrum for a year after preparation. This indicates electrostatic stabilization via citrate anions bonded on the gold nanoparticle surface. Therefore, the citrate capped gold nanoparticles are negatively charged.

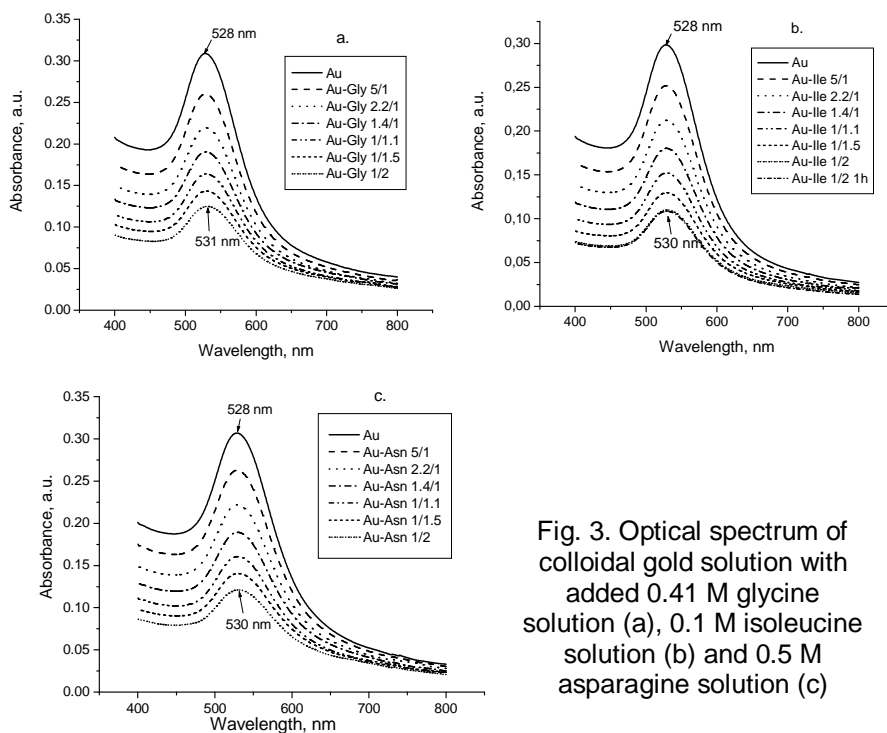


Fig. 3. Optical spectrum of colloidal gold solution with added 0.41 M glycine solution (a), 0.1 M isoleucine solution (b) and 0.5 M asparagine solution (c)

Interactions with amino acid solutions

The **UV-Vis spectra** of the amino acids present no adsorption bands in the range of wavelengths investigated here. For instance, the absorption maximum for arginine lies at 194 nm, for glycine under 190 nm, methionine presents a shoulder at 198 nm.

Adding of some of the amino acids produces no or little modification in the UV-Vis spectra of the gold colloidal solution. Besides the lowering of the absorbance due to the dilution of the gold solution, the absorption maxima are lightly shifted towards longer wavelength. This shift is due to

the change in the dielectric constant in the adsorption layer, the increase of the average refractive index of the environment surrounding the nanoparticles, and to the size increase of particles by the adsorbed layer [3]. For a *glycine* solution the maximum shift was 3 nm (Fig.3a), for an *isoleucine* solution 2 nm (Fig. 3b) and the same shift is observed for the *asparagine* solution (Fig. 3c). The shift does not change in time, i.e. the gold solutions with added amino acids remain stable in time (see, for instance Fig. 3b). We can assume the zwitterionic amino acid molecules to be settled by the $-\text{NH}_3^+$ group on the negative charged gold nanoparticle surface, while their $-\text{COO}^-$ group contributes further to the negative surface charge of the nanoparticles.

By adding the 0.2 M and 0.4 M *methionine* solution there are also only small shifts in the absorption maximum, but after four days a second absorption band appears at higher wavelengths, partially overlapped with the initial absorption band, with a shoulder at about 620 nm (Figs. 4a, b). For a higher colloidal gold concentration, the second band is more distinct, with a peak at 618 nm (Fig.4c). The new band is characteristic for the aggregation of nanoparticles. As a matter of fact, it is known that the apparition of the broad peak at longer wavelengths in the UV-Vis spectrum comes from the coupling of surface plasmon resonance (SPR) of two adjacent nanoparticles and it is an indication of the anisotropic optical properties of the gold nanoparticles aggregates [35].

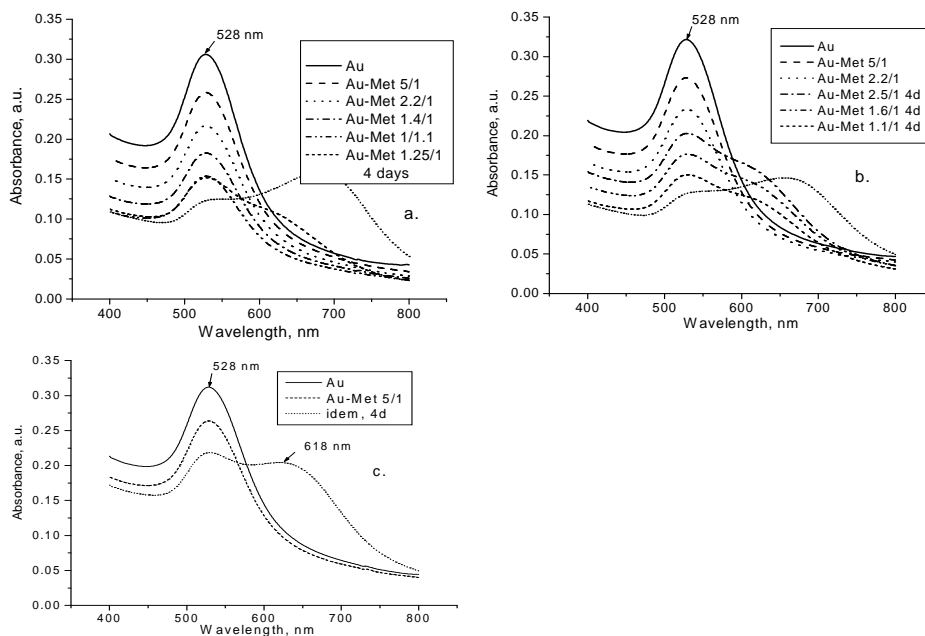


Fig.4. Optical spectrum of colloidal gold solution with added 0.2 M (a) and 0.4 M (b) methionine solution at different ratios and after 4 days, and for a higher gold content with 0.2 M methionine solution (c)

This tendency towards aggregation is much more pregnant when a sufficiently concentrated *lysine* solution is added (Fig.5). For a very diluted 0.01 M lysine solution (Fig. 5a) the plots look like those in Figure 3, with a small shift of the absorption band maximum. For a more concentrated 0.1 M solution (Fig. 5b) the shift towards higher wavelengths is much more important, and for higher quantities of lysine added the band becomes larger, suggesting an increasing aggregation of the nanoparticles. With a very concentrated (0.54 M) lysine solution, the band for aggregates appears at once (maximum at about 634 nm), while the 528 nm band for individual gold particles decreases and is observed only as a shoulder in the spectrum. The maximum of the broad absorption band continues its shift towards higher wavelengths in time (Fig. 5c). The color of the solution changed from reddish to blue. This kind of color change as an effect of aggregation is a well-understood phenomenon [36-38]. When the interparticle distance in the aggregates decreases to less than about the average particle diameter, the electric dipole-dipole interaction and coupling between the plasmons of neighboring particles in the aggregates results in the bathochromic shift of the absorption band. It has been used to study molecular recognition processes using gold nanoparticles in solution [39].

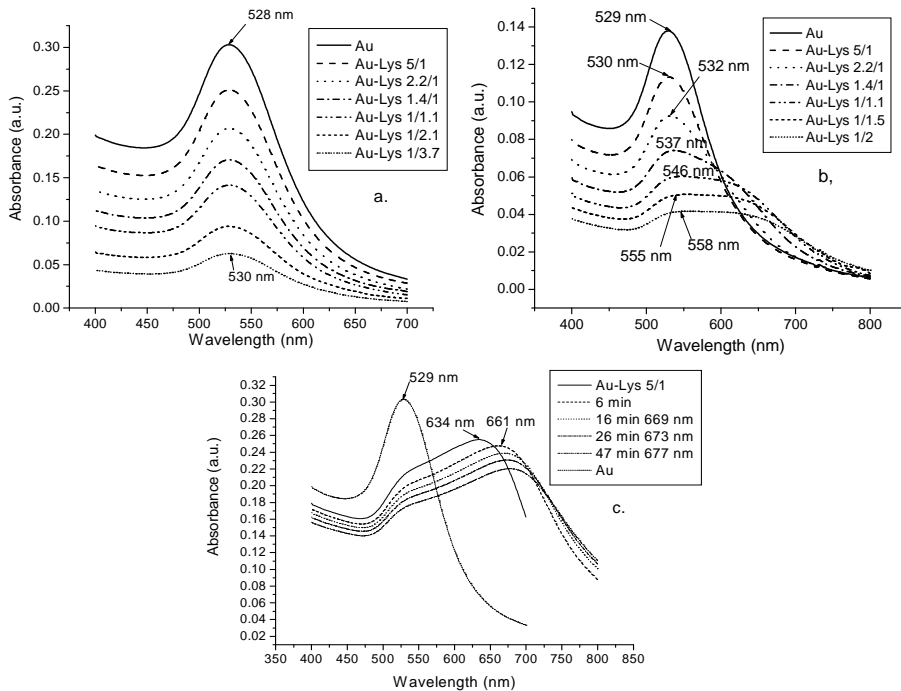


Fig.5. Optical spectrum of colloidal gold solution with added 0.01 M (a) and 0.1 M (b) lysine solution at different ratios, and with 0.54 M lysine solution in time (c)

Lysine adsorption on gold nanoparticles has been investigated [40], using 13 nm diameter gold particles and a $7 \cdot 10^{-4}$ M L-lysine solution at pH = 10.7. The UV-Vis spectrum showed a SPR peak at 520 nm, similar to that we found for citrate coated nanoparticles. The result is similar to our data, using the most diluted lysine solution (Fig. 5a). By adding a condensing agent, the authors [40] observed that particles aggregated by the formation of peptide bonds between two lysine molecules adsorbed on different nanoparticles. In the UV-Vis spectrum the SPR band of Au was shifted to 527 nm and a new broad peak appeared at 633 nm. The spectrum is similar to that obtained by us at high concentrations of the lysine solution.

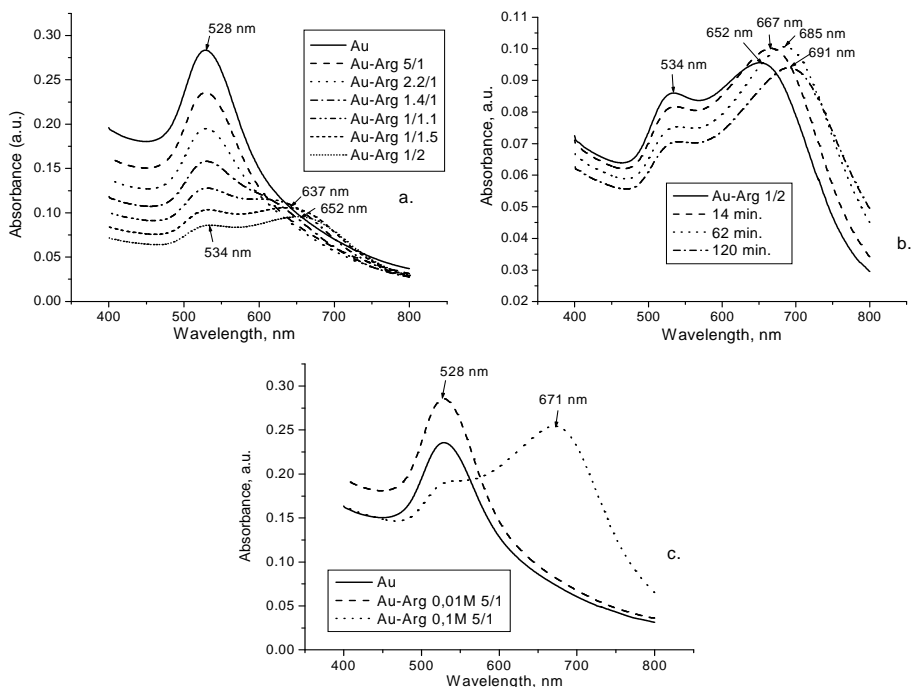


Fig.6. Optical spectrum of colloidal gold solution with 0.01 M arginine solution in different ratios (a) and time evolution (b) and with arginine solutions of different concentrations (c).

A similar behavior is observed in colloidal gold solutions with *arginine*. For a 0.01 M concentration of the arginine solutions and small added amounts, the maximum of the gold nanoparticles absorption is only slightly shifted, but at the 1.4:1 gold / arginine solution ratio the new band for particle aggregates appears, initially as a shoulder. By further adding arginine, the band broadens and its maximum shifts to 640-650 nm (Fig.6a). The time evolution of the aggregation is shown in Fig. 6b for the

colloidal Au / 0.01 M arginine solution ratio 1/2. The maximum is shifted further towards longer wavelengths. The adding of a more concentrated (0.1 M) arginine solution leads directly to the formation of the aggregates and to the colour change of the solution (Fig. 6c).

Likewise, a 0.01 M *histidine* solution leads to aggregation beyond a certain added quantity (Fig. 7a); the maxima of the new bands are in the wavelength range 670-690 nm. The 0.1 M histidine solution produces aggregation already at the first added amount (Fig. 7b); the maximum of the new band is found at about 700 nm.

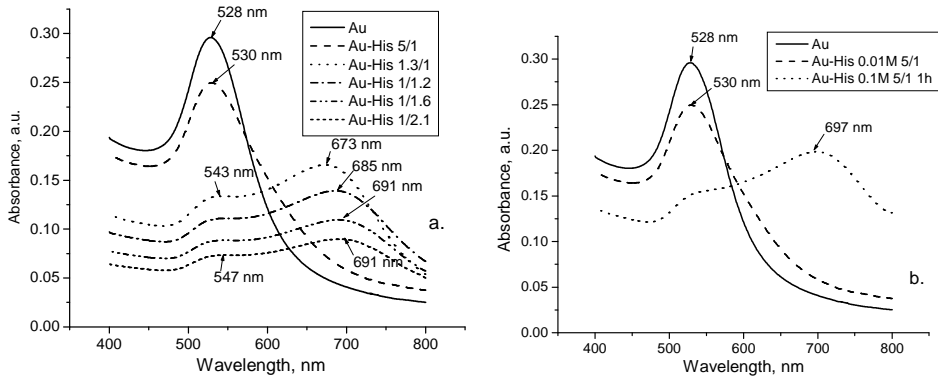


Fig.7. Optical spectrum of colloidal gold solution with 0.01 M histidine solution in different ratios (a) and with histidine solutions of different concentrations (b)

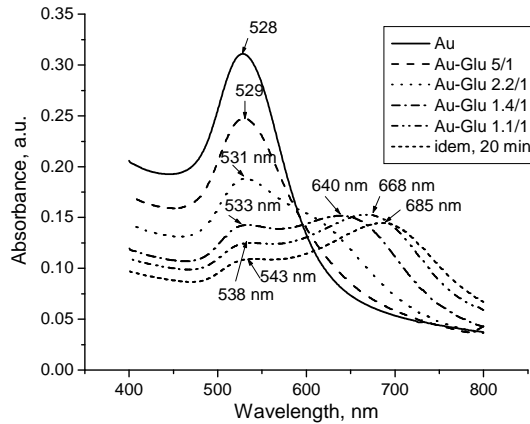


Fig.8. Optical spectrum of colloidal gold solution with 0.1 M glutamic acid solution in different ratios

Glutamic acid in a 0.1 M solution also initiates the aggregation of gold nanoparticles and the effect is increasing in time (Fig.8). It is interesting to mention that aspartic acid, closely related to glutamic acid, was used in the

reduction of chloroaurate ions and it was shown that this acid was strongly bonded to the nanoparticle surface and stabilized them efficiently [16].

Cysteine has the strongest effect from all the investigated amino acid solutions. Already a 10^{-3} M solution (Fig. 9a) added to the colloidal gold solution leads to a rapid aggregation, the peak for the broad band at longer wavelength surpasses rapidly the peak of the initial non-aggregated gold particles and the maximum wavelength goes above 700 nm. The 0.1 M cysteine solution (Fig. 9b) leads to the color change in blue of the gold solution at the first amount added. From Fig. 9b is also evident the time evolution of aggregation.

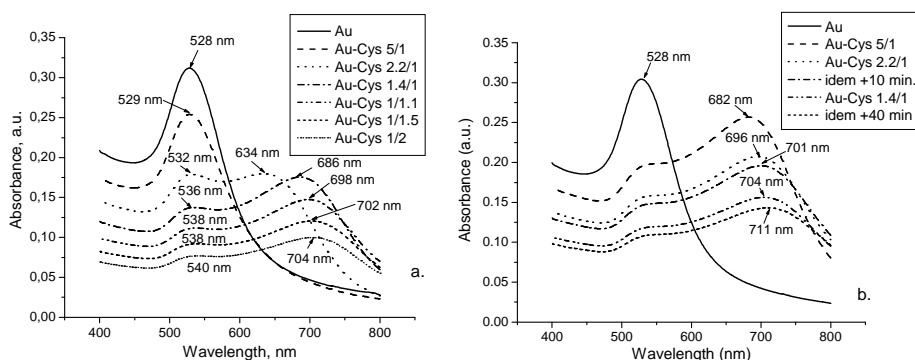


Fig.9. Optical spectrum of colloidal gold solution with 0.001 M (a) and 0.1 M (b) cysteine solution in different ratios.

These results support the observations about the interaction of cysteine with gold nanoparticles [19]; based on the analysis of FT-IR and Raman spectra, the authors affirm the existence of covalent interaction of sulphur and gold. The formation of a covalent bond Au-S is also assumed by other authors [21, 41]. It was suggested [38] that the positively charged amine group in cysteine ($-\text{NH}_3^+$) should interact with the negative charge on the surface of other gold nanoparticles through electrostatic binding, thus forming assemblies.

The band broadening and the shift of the surface plasmon band was shown to reflect the advanced aggregation of gold nanoparticles with decrease in pH and increase in electrolyte concentration [19].

The band broadening and the shift of the surface plasmon band was shown to reflect the advanced aggregation of gold nanoparticles with decrease in pH and increase in electrolyte concentration [19].

Further, we studied also the effect of two peptides on colloidal gold solutions. The dipeptide *glycyl-glycine* (GlyGly) was added as a 0.4 M aqueous solution to the colloidal gold solution. The UV-Vis spectra are shown in Fig. 10 for the wavelengths range 250-800 nm (a) and 400-800 nm (b). The dipeptide solutions present an increased absorbance toward

lower wavelengths, with a shoulder at about 320 nm. For this reason, unlike the other investigated systems, here the absorbance does not decrease continuously with diminishing of gold content and the absorption maximum is shifted towards lower wavelengths. The absorption band of gold nanoparticles is not affected and no aggregation takes place.

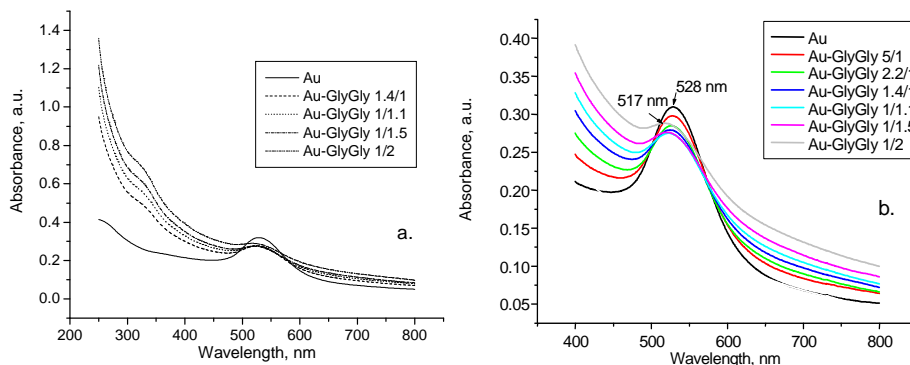


Fig.10. Optical spectrum of colloidal gold solution with 0.42 M glycylglycine (GlyGly) solution

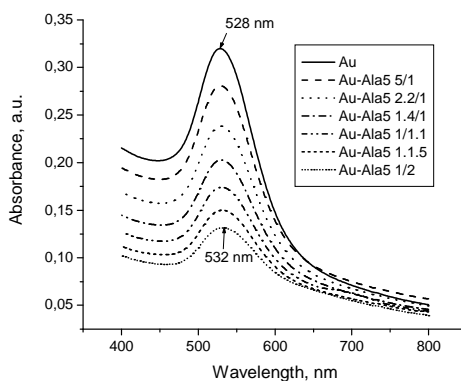


Fig.10c. Optical spectrum of colloidal gold solution with 0.007 M pentapeptide (Ala5) solution.

Similarly, a pentapeptide, *alanyl-alanyl-alanyl-alanyl-alanine* (Ala5) seems to have little effect on the gold nanoparticles (Fig. 10c); the plots are similar to those in Fig. 3.

The binding of amino acids with the gold nanoparticle interface may be achieved through the amine function. The binding could occur through the electrostatic interaction of the protonated amine group ($-NH_3^+$) with the surface bonded negatively charged citrate anions. On the other hand, a direct bonding of the amine group to the gold surface can not be excluded.

TEM images for gold nanoparticles with an 0.001 M cysteine solution show mostly linearly arranged assemblies of nanoparticles (Fig. 11), while for the nanoparticles with a 0.1 M lysine solution (Fig.12) and a 0.01 M arginine solution (Fig. 13) the assemblies are more complex.

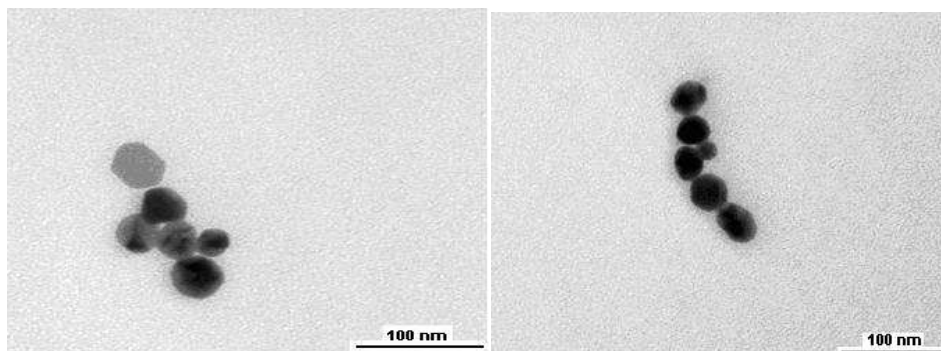


Fig. 11. TEM images of gold nanoparticles functionalized with 0.001 M cysteine solution

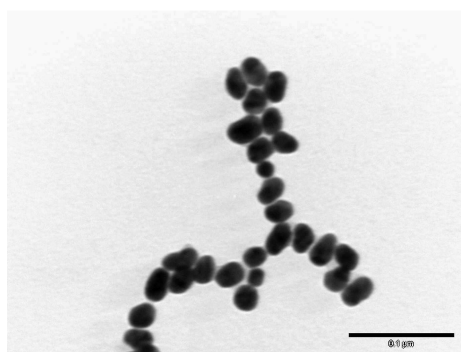


Fig.12. TEM image of gold nanoparticles capped with lysine (0.1 M), Au:Lys 1:1 ratio.

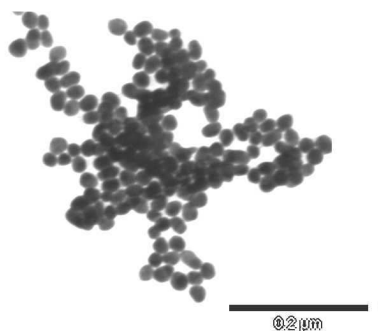


Fig. 13. TEM image of gold nanoparticles capped with arginine (0.01M), Au:Arg (1:1).

AFM images for assembled gold nanoparticles are shown in Fig. 14 with cysteine, in Fig. 15 with arginine, and in Fig. 16 with lysine. The atomic force microscope allows simultaneous acquisition of multiple images, such as topography and phase images, under tapping mode operation. The assembly of gold nanoparticles, mediated by the amino acid was deposited on planar hydrophobic glass or positively charged glass surfaces. Then, the assembly was observed by AFM under tapping mode and the structural features are visualized in Figs. 14-16. For instance the two-dimensional topographic image for lysine mediated gold nanoparticles assemblies (Fig. 16a) shows the

morphology of an almost ordered structure within domains, with small defects at domain boundaries. For the assembly of gold nanoparticles mediated by lysine,

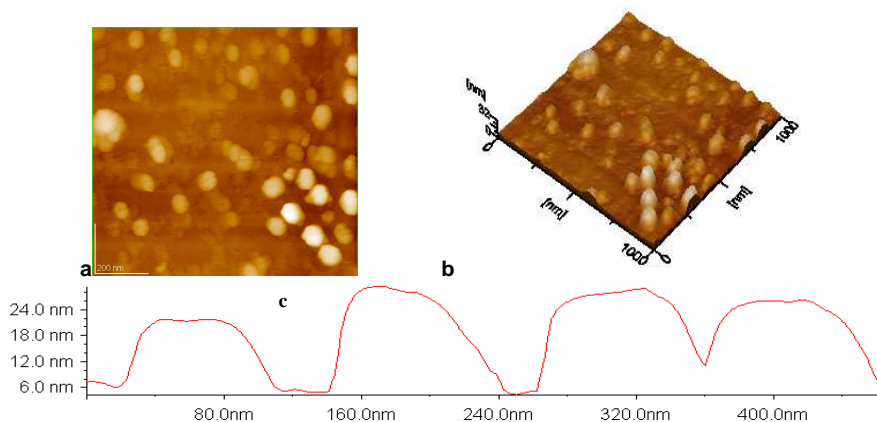


Fig.14. AFM images of the assembly of gold nanoparticles functionalized by cysteine. Scanned areas $1 \times 1 \mu\text{m}^2$. 2D-topography (a); 3D-view (b); cross section profile (c) along the arrow in panel a.

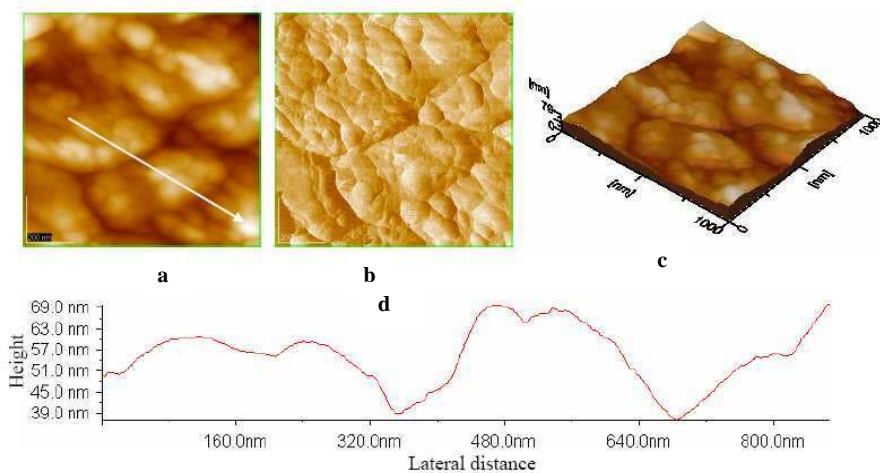


Fig. 15. AFM images of the assembly of gold nanoparticles functionalized by arginine. Scanned area $1 \times 1 \mu\text{m}^2$; 2D-topography (a); phase image (b); 3D-view (c); cross section profile (d) along the arrow in panel a.

immobilized on glass surface, individual gold nanoparticles are visible from 2D-topography (Fig. 16a) and 3D-view (Fig. 16c). The phase image (Fig. 16b) shows also that the assembly of gold nanoparticles mediated by lysine is almost compact. All AFM images were acquired with high resolution as described elsewhere [44].

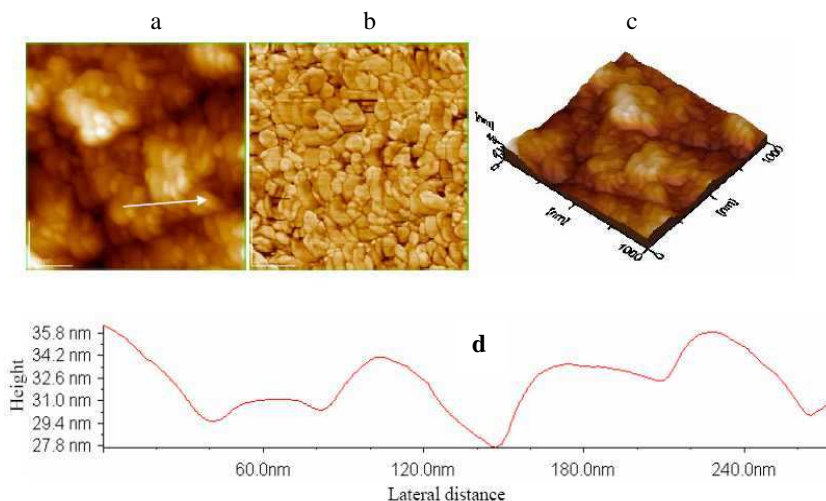


Fig.16. AFM images of the assembly of gold nanoparticles functionalized by lysine. Scanned area: $1 \times 1 \mu\text{m}^2$. 2D-topographic (a) and phase (b) and 3D-view (c); (d) cross section profile along the arrow in panel a.

The AFM images (Figs. 14-16) evidence the organization of gold nanoparticles functionalized with cysteine, arginine and lysine, respectively, within an almost compact network of aggregates, in substantial agreement with the UV-Vis spectroscopy. Also, the gold nanoparticles appear almost ordered both in AFM images and in cross section profile in substantial agreement with TEM images. For example, with cysteine (Fig. 14) it is observed a tendency of linear arrangements, in good agreement with TEM observations (Fig. 11).

In order to rationalize the behavior of the investigated amino acids versus gold nanoparticles we use a Venn diagram (Fig. 17), grouping amino acids according to their properties [45, 46]. The amino acids found to interact strongly with the gold nanoparticles and to initiate their aggregation were noted with “+”, and those which give only slight shifts of the UV-Vis absorption band with “-“. Most of the amino acids involved in the aggregation of gold nanoparticles fall in the class of “polar” amino acids, defined as those with side-chains that prefer to reside in an aqueous environment. For this reason, one generally finds these amino acids exposed on the surface of a protein [46]. All the “charged” amino acids present such strong interactions: both the amino acids that are usually *positive* (protonated) at physiological pH: lysine (K), arginine (R) and histidine (H), and those that are usually *negative* (i.e. de-protonated) at

physiological pH: glutamic acid (E) and aspartic acid (D). The last one was reported to bind also strongly to the gold nanoparticles [5]. Cysteine (C) is probably bonded to the gold nanoparticles by its thiol (-SH) group, as was

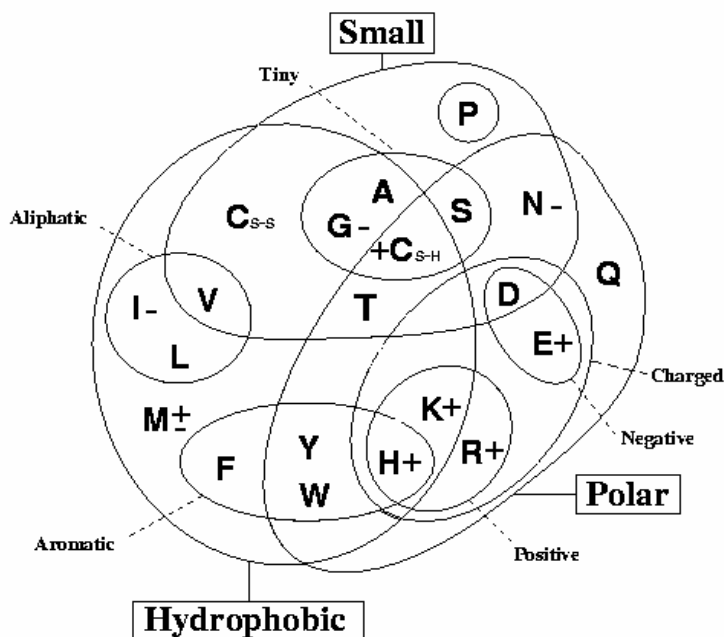


Fig. 17. Venn diagram grouping amino acids according to their properties (adapted from [45]) A – Alanine C_{S-H} – Cysteine C_{S-S} cystine D – Aspartic acid E – Glutamic acid F – Phenilalanine G – Glycine H – Histidine I – Isoleucine K – Lysine L – Leucine M – Methionine N – Asparagine P – Proline Q – Glutamine R – Arginine S – Serine T – Threonine V – Valine W – Tryptophan Y - Tirosine

suggested by the study of ¹H NMR spectra [19,20]. All these amino acids, after their adsorption on the gold particles, have still two functional groups free to form bonds between particles. A possible mechanism of amino acid bindings to gold nanoparticles and the formation of particle aggregates are shown for cysteine in Fig.18. Methionine was labeled as “±” in the Venn diagram because it leads to aggregation only in time (Fig.4). The S-atom seems to be responsible for this activity. Glycine (G), isoleucine (I) and probably alanine (A), having only two functional groups, are probably only adsorbed on the gold nanoparticles (by the amino group) and stabilize these gold nanoparticles. Asparagine (N), having one –COOH group blocked by formation of the amide group (CONH₂) has a similar behavior as the last ones.

AMINO ACIDS BINDING TO GOLD NANOPARTICLES

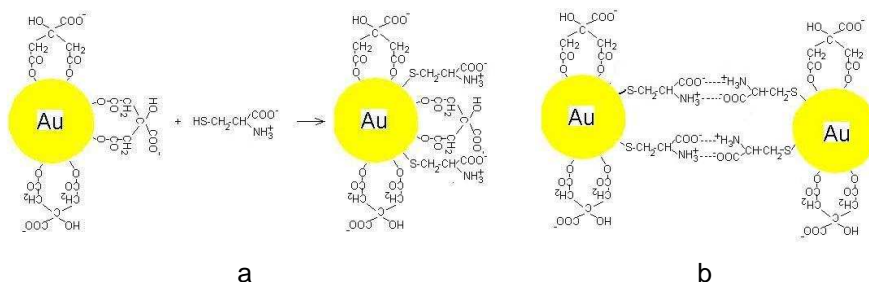


Fig. 18. A model of cysteine binding to citrate capped gold nanoparticles (a) and of bonds formation between gold nanoparticles (b)

CONCLUSIONS

These data indicate that the binding of amino acids to the gold nanoparticles can lead to the self-assemblies almost well organized, particularly for amino acids possessing additional functional groups, such as amine, imidazole, thiol or thioether besides the alpha-amine. The correlation between physical and chemical properties of amino acids, such as hydrophobicity and, acidity or basicity in various protolytic equilibria, and their molecular structure is in substantial agreement with their assembly effect on the gold nanoparticles. This effect could be explained primarily through the zwitterion-type electrostatic interactions between the charged amine and acid groups of the tested amino acid adsorbed/bound to different gold nanoparticles.

The affinity of gold nanoparticles towards amino acids can also lead to the development of new detection methods for analytical purposes, medical diagnostics and biosensors and to potential controlled drug delivery applications. On the other hand, the use of amino acids both in the functionalization of gold nanoparticles and in the cross-linking of amino acid capped gold nanoparticles leading to stable self-assemblies are promising ways to the synthesis of nanostructured biomaterials. The stabilization of gold nanoparticles through amino acids is also important for the understanding of complex phenomena involved in the formation of new biomaterials by binding of proteins with gold nanoparticles with important implications in nanoscience and nanotechnology. Another interesting possibility is covalent cross-linking of amino-acid capped nanoparticles by formation of amide bonds across nanoparticles. These types of studies are in progress in our laboratories.

ACKNOWLEDGEMENT

This research was financially supported by the Romanian Ministry of Education and Research (Scientific research project no.5/2005, within the Excellency Research Program).

REFERENCES

1. M.Zheng, X.Huang, In: *Biofunctionalization of Nanomaterials*, C.S.S.R. Kumar editor, Wiley-VCH, **2005**, 99-124
2. D.Fitzmaurice, S. Connolly, *Adv. Mater.*, **1999**, *11*, 1202-1205
3. S.Mann, W.Shenton, M.Li, S. Connolly, D.Fitzmaurice, *Adv. Mater.*, **2000**, *12*, 147-150
4. M.C. Daniel, D. Astruc, *Chem. Rev.* **2004**, *104*, 293-346
5. N.L. Rosi, C.A.Mirkin, *Chem.Rev.*, **2005**, *105*, 1547-1562
6. J.C.Love, L.A.Estroff, J.K.Knebel, R.G.Nuzzo, G.M.Whitesides, *Chem.Rev.*, **2005**, *105*, 1103-1170
7. G.M.Coppola, H.F.Schuster, *Asymmetric Synthesis. Construction of Chiral Molecules Using Amino Acids*, Wiley, New York, **1987**
8. C.C.You, M.De, G.Han, V.M.Rotello, *J. Am. Chem. Soc.*, **2005**, *127*, 12873-12881; C.C.You, M.De, V.M.Rotello, *Org.Lett.*, **2005**, *7*, 5685-5688
9. R.Levy, C.Doty, In: *Biofunctionalization of Nanomaterials*, C.S.S.R. Kumar editor, Wiley-VCH, **2005**, 235-269
10. J.Zsang, Q.Chi, J.U.Nielsen, E.P.Friis, J.E.T.Andersen, J.Ulstrup, *Langmuir*, **2000**, *16*, 7229-7237
11. S.Mandal, S.Phadtare, M.Sastry, *Curr. Appl. Phys.*, **2005**, *4*, 118-127
12. P.R. Selvakannan, S.Mandal, S.Phadtare, R.Pasricha, M. Sastry, *Langmuir*, **2003**, *19*, 3545-3549
13. H.Joshi, P.S.Shirude, V.Bansal, K.N.Ganeshand M. Sastry, *J. Phys. Chem. B*, **2004**, *108*, 11535-11540
14. Y. Shao, Y. Jin, S. Dong, *Chem. Commun.*, **2004**, 1104
15. P. Selvakannan, S.Mandal, S.Phadtare, A.Gole, R.Pasricha, S.D.Adyanthaya, M. Sastry, *J.Colloid Interf. Sci.*, **2004**, *269*, 97-102
16. S.Mandal, P.Selvakannan, S.Phadtare, R.Pasricha, M.Sastry, *Proc.Indian Acad.Sci. (Chem.Sci.)*, **2002**, *114*, 513-520
17. S.K.Bhargava, J.M.Booth, S.Agrawal, P.Coloe, G.Kar, *Langmuir*, **2005**, *32*, 5949-5956
18. S. Aryal, B.K. Remant, B. Narayan, C.K. Kim, H.G.Y. Kim, *J. Colloid Interf.Sci.*, **2006**, *299*, 191-197
19. S.Aryal, K.C.Remant Bahadur, N.Dharmaraj, N.Bhattacharai, C.H.Kim, H.Y.Kim, *Spectrochim. Acta, A*, **2006**, *63*, 160-163
20. S.Aryal, K.C.Remant Bahadur, N.Bhattacharai, C.H.Kim, H.Y.Kim, *J.Colloid Interf. Sci.*, **2006**, *299*, 191-197
21. Z.P.Li, X.R.Duan, C.H.Liu, B.A.Du, *Anal. Biochem.*, **2006**, *351*, 18-25
22. Y.F. Huang, Y.W. Lin, H.T. Chang, *Nanotechnology*, **2006**, *17*, 4885-4894
23. R.Levy, N.T.K. Thanh, R. C. Doty, I. Hussain, R. J. Nichols, D. J. Schiffrin, M. Brust, D.G. Fernig, *J.Am.Chem.Soc.*, **2004**, *40*, 3685-3688
24. P.Tengvall, M.Lestelius, B.Liedberg, I.Lundstroem, *Langmuir*, **1992**, *8*, 1236-1238
25. Y.C.Sasaki, K.Yasuda, Y.Susuki, T.Ishibashi, I.Satoh, Y.Fujiki, S.Ishiwata, *Biophys. J.*, **1997**, *72*, 1842-1848

26. I. Willner, E. Katz, B. Willner, R. Blonder, V. Heleg-Shabtai, A. F. Bückmann, , *Biosens. Bioelectron.*, **1997**, *12*, 337-356
27. O. Horovitz, Gh. Tomoaia, A. Mocanu, T. Yupsanis, Tomoaia-Cotisel, *Gold Bull.*, **2007**, *40*, 213-218
28. O. Horovitz, A. Mocanu, Gh. Tomoaia, L. Olenic, Gg. Mihăilescu, O. Borosțean, A. Popoviciu, C. Crăciun, T. Yupsanis, M. Tomoaia-Cotisel, In: "Convergence of micro-nano-biotechnologies", Series "Micro and Nanoengineering", Vol.9, Ed. Academiei, București, **2006**, 133-147
29. E. Indrea, S. Dreve, I. Bratu, Gh. Mihăilescu, L. Olenic, Gh. Tomoaia, A. Mocanu, O. Horovitz, M. Tomoaia-Cotisel, In "Technical Proceedings of the 2007 Nanotechnology Conference and Trade Show", NSTI-Nanotech, Santa Clara, **2007**, Vol. 4, 461-464
30. O. Horovitz, A. Mocanu, Gh. Tomoaia, L. Bobos, D. Dubert, I. Dăian, T. Yupsanis, M. Tomoaia-Cotisel, *Studia Univ. Babeș-Bolyai, Chem.*, **2007**, *52* (1), 97-108
31. S. Chah, M. R. Hammond, R. N. Zare, *Chem. Biol.*, **2005**, *12*, 323-328
32. J. A. DeRose, R. M. Leblanc, *Surf. Sci. Rep.*, **1995**, *22*, 73-77 ; Y. F. Dufrene, G. U. Lee, *Biochim. Biophys. Acta*, **2000**, *1509*, 14-17
33. K. S. Birdi, *Scanning Probe Microscopes. Applications in Science and Technology*, CRC Press, New York, **2003**
34. M. Tomoaia-Cotisel, Gh. Tomoaia, V. D. Pop, A. Mocanu, G. Cozar, N. Apetroaei and Gh. Popa, *Rev. Roum. Chim.*, **2005**, *50*, 471-478
35. N. R. Jana, L. Gearheart, S. O. Obare, C. J. Murphy, *Langmuir*, **2002**, *18*, 922-927
36. K. S. Mayya, V. Patil, M. Sastry, *Langmuir*, **1997**, *13*, 3944-3947
37. J. J. Storhoff, R. Elghanian, R. C. Mucic, C. A. Mirkin, R. L. Letsinger, *J. Am. Chem. Soc.*, **1998**, *120*, 1959-1964
38. U. Kreibitz, L. Genzel, *Surface Sci.*, **1985**, *156*, 678-700
39. C. A. Mirkin, R. L. Letsinger, R. C. Mucic, J. J. Storhoff, *Nature*, **1996**, *382*, 607-609
40. L. Xu, Y. Guo, R. Xie, J. Zhuang, W. Yang, *Nanotechnology*, **2002**, *13*, 725-728
41. P. K. Sudeep, S. T. S. Joseph, K. G. Thomas, *J. Am. Chem. Soc.*, **2002**, *127*, 6516-6517
42. I. S. Lim, W. Ip, E. Crew, P. N. Njoki, D. Mou, C. J. Zhong, Y. Pan, S. Zhou, *Langmuir*, **2007**, *23*, 826-833
43. C. Ku, Y. Zu, V. Wimg-Wah Yam, *Anal. Chem.* **2007**, *79*, 666-572
44. M. Tomoaia-Cotisel, In: "Convergence of Micro-Nano-Biotechnologies", Series "Micro and Nanoengineering", Vol.9, Ed. Academiei, **2006**, 147 - 161
45. C. D. Livingstone, G. J. Barton, *Comput. Appl. Biosci.*, **1993**, *9*, 745-756
46. M. J. Betts, R. B. Russell. In „*Bioinformatics for Geneticists*“, M. R. Barnes and I. C. Gray eds, Wiley, **2003**

SHORT AND LONG RANGE CORRELATION IN FLUCTUATING PHENOMENA

VASILE V. MORARIU*

ABSTRACT. Many natural phenomena from molecular to astrophysical processes may show a fluctuating behavior. Some of them are long-range correlated. However this paper reveals that just as many may show short-range behavior although they can be easily confounded with long-range correlation. The short-range memory of any complexity can be modeled by autoregressive processes.

INTRODUCTION

There are many natural phenomena which present fluctuating characteristics with apparent random properties [1]. The fluctuating characteristic may occur either in time or in space. For example the heart beating or human gating are not constant in time. The length of DNA coding sequences expressed as number of bases represents a fluctuating series along the genome etc. As a general rule we always search for order in such series of data which is not apparent to the naked eye. Order can be measured by investigating the correlation property of the data in the series. A correlation between two variables is a measure of the association or relationship between them. For example height and weight are related - taller people tend to be heavier than shorter people. An important point is that correlation does not always imply a causal relationship. However if correlation exists then research can be directed along specific lines such as to uncover causal relationships.

A fluctuating series of data may be attributed to two different kinds of processes: a) dynamic processes and b) stochastic processes. In the first case the source of fluctuation is a deterministic rule, described very often by a simple equation, which generates chaos. Stochastic processes means of, relating to, or characterized by conjecture and randomness. A stochastic process is one whose behavior is non-deterministic in that a state does not fully determine its next state. Here we distinguish uncorrelated (or random) fluctuation and correlated fluctuation respectively. They represent the subject of the present paper.

A classical example of correlated stochastic process is the so called $1/f$ noise where the amplitude of the noise is proportional to the inverse of

* National Institute of R&D for Isotopic and Molecular Technology, POBox 700, 400293 CLUJ-NAPOCA 5, ROMANIA

frequency [1]. This is also known as “pink” noise or flickering. Such a kind of noise is quite common in nature: from the flickering light of galaxies to the flickering of the red blood cells and many others. The present work started from the author’s earlier observation that a great deal of quite different fluctuating phenomena appeared to be fitted by the $1/f$ noise rule. This is generally associated to long range correlation or fractal like characteristics. However it became evident that quite often the $1/f$ characteristic revealed deviations from the rule of a power law. Evidence has accumulated in time until it was realized that deviations pointed to a significant qualitative difference from a $1/f$ behavior. These deviations were found to be due to short range correlation phenomena as opposed to the long range correlation of $1/f$ phenomena. The aim of this paper is to show how these distinctions can be made and to offer some examples from the field of molecular biology.

RESULTS AND DISCUSSION

We illustrate the case of the atomic mobility in the main chain of a protein (fig.1). The series of data were subjected to Fast Fourier Transform (FFT). Due to high dispersion of the data the spectrum can be easily approximated by a straight line and therefore by a $1/f$ spectrum. However, in this particular case it can be easily noticed that at low frequencies a plateau appears to be present and also at higher frequencies of the data. We found many similar cases which have been overlooked in the literature. Therefore this example shows how a non- $1/f$ spectrum can be easily confused by a $1/f$ spectrum.

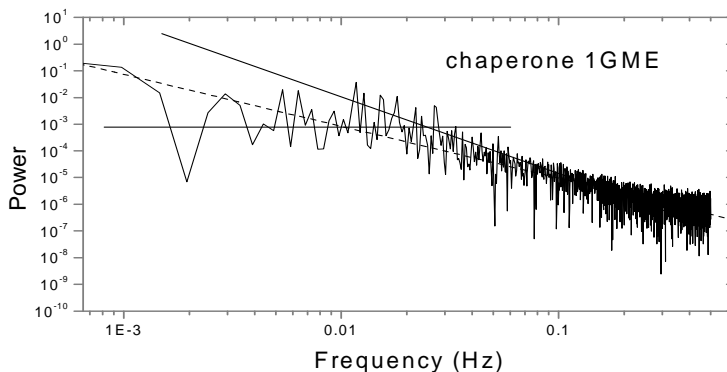


Fig.1. Non-averaged power spectrum for the atomic mobility in the backbone of a heat shock protein (Protein Data Bank code: 1gme). The linear fit (dashed line) of the spectrum may suggest a long-range correlation interpretation while the spectrum is non-linear with an evident plateau at low frequencies (continuous line) and a higher slope line at higher frequencies.

A main reason for this confusion is that the spectrum is quite noisy. Mandelbrot's recommendation that apparent $1/f$ spectra should be averaged before further interpretation has often been overlooked including in our own previous work [2-4]. Mandelbrot considers that non-averaged spectra lead to "unreliable and even meaningless results" [5]. An immediate consequence of the averaging procedure is that deviation from a power law description of the spectra can be easily disclosed otherwise remaining undetected. Sometimes such a deviation can be visible even if the spectrum is not averaged. On the other hand the non-averaged spectrum can be often reasonably fitted by a straight line, i.e. described by an apparent power law.

A further complication arises when the series has non-stationary character. The spectral analysis in fig. 1 is performed on the original series which is non-stationary as shown in fig. 2. The consequence is that the result is affected by the correlation introduced by the trend in the series (non-stationary character). Therefore the correlation described by the spectrum is in error. A simple procedure to avoid the non-stationary character is to define the trend by fitting the series with a higher degree polynomial. For example, in fig. 2, the trend can be described by a 10 degree polynomial. This can be subtracted from the series and the result is a detrended series (fig.3).

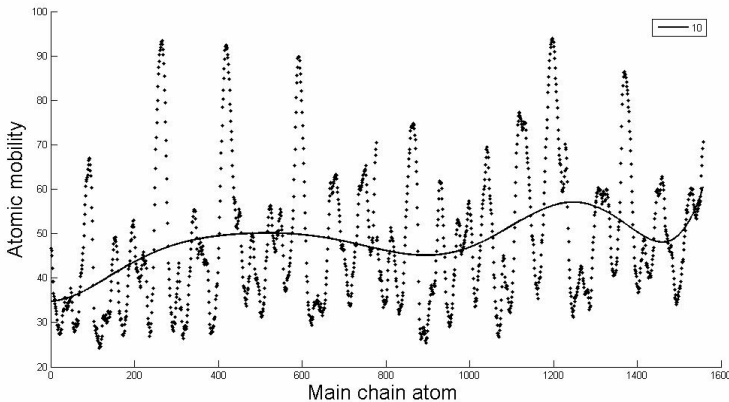


Fig.2. The series of the atomic mobility (crystallographic temperature factor) versus the main chain atom in the heat shock protein (PDB code: 1gme). The series is fitted by a 10 degree polynomial which describes the trend in the series.

It is on this detrended series that we performed Fourier Transform followed by averaging of the spectra. The true shape of the spectrum can be now revealed (fig.4).

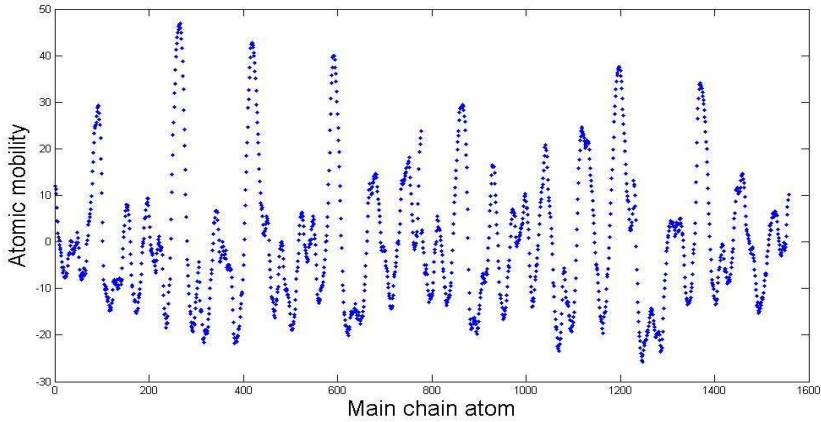


Fig.3. Detrended series shown in fig.2. This is done by subtracting the 10 degree polynomial from the original series.

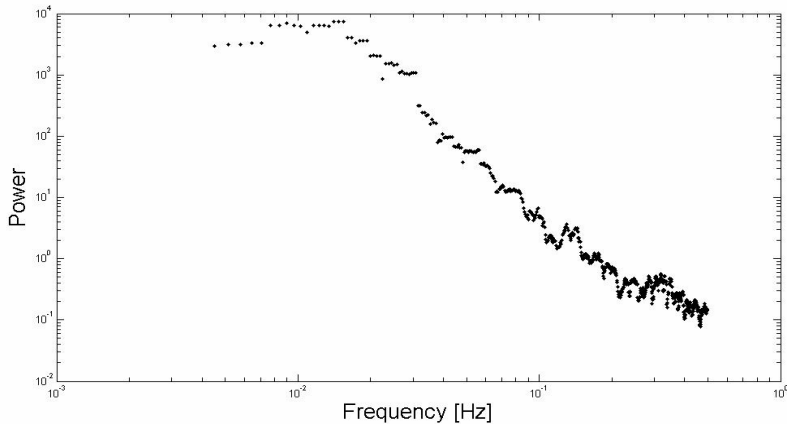


Fig.4. Averaged spectrum for the backbone atomic mobility of a heat shock protein (PDB code: 1gme). The number of averaged terms was $M=13$. The nonlinearity of the spectrum can be easily noticed. The averaging procedure was performed with a MATLAB program.

It can be noticed that the spectrum is non-linear, in other words it is not long-range correlated. A long-range correlation is visible on such double log plot as a linear dependence. Its slope represents the long-range correlation exponent β . However in this case long-range correlation is not operative therefore the spectrum cannot be described by a β exponent.

What can be done to characterize quantitatively such a spectrum? This is a more complicated question to answer in this limited space. The answer lays in the extreme large possibilities offered by autoregressive models [6-7]. Basically the most simple autoregressive model introduces an interaction between successive terms in a random series. Suppose $x_1, x_2, x_3 \dots$ is a random uncorrelated series. We can introduce a correlation in the series by constructing a new series following the simple rule [3]:

$$x_1, (x_1+x_2)0.5, [x_3+(x_1+x_2)0.5]0.5, \{x_4+[x_3+(x_1+x_2)/0.5]0.5\}0.5 \dots \quad (1)$$

It can be seen that each term contains some information about the previous term and the further are the following terms, the less memory about the initial terms in the series. The multiplying factor, in the above example is 0.5, is a kind of strength of interaction among the terms which may vary between $0 < \phi < 1$. If the factor $\phi=1$ the series represent the integral series of the initial random series (or random walk). The further the term in the new series the less correlated with the initial terms in the series. Obviously such a series is short-range correlated. The example above is known as autoregressive model of order one or AR(1). A more formal description of an AR(1) model is given by the equation:

$$X_t = \phi X_{t-1} + \varepsilon_t \quad (2)$$

where ε_t is a white noise process with zero mean and variance σ^2 , while ϕ is the interaction parameter [8]. The parameter values ϕ have to be restricted for the process to be stationary which means that $|\phi| < 1$. Examples of spectra for different values of ϕ for AR(1) processes are shown in fig. 5.

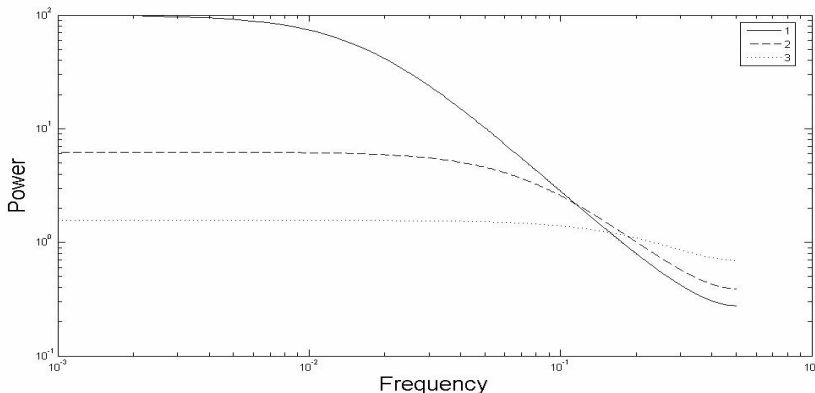


Fig. 5. Spectra of autoregressive models of first order, AR(1) for 1) $\phi=0.9$; 2) $\phi=0.6$; 3) $\phi=0.2$.

AR(1) spectra show features already encountered in the examples above: a plateau at lower frequencies and the beginning of a plateau at higher frequencies. The length of the plateau at lower frequencies is evident for longer series of data. Shorter and real series may miss the plateau and noise has high amplitude at higher frequencies. As a result the spectra can be reasonably fitted by a straight line and the false conclusion that the series is long-range correlated like in fig.1. We explored a large number of series not only for proteins but also for DNA, from cell biology (flickering of red blood cells) and cognitive psychology (generation of apparent random numbers by human subjects). We found that about a quarter of the cases can be described by AR(1) models. We also found that more complicated spectra can be described by higher order autoregressive models AR(p). The relevant parameter in case of AR(1) processes is the interaction constant ϕ , while for higher order autoregressive processes AR(p), several constants of interaction are operative. These interaction constants are sensitive to various characteristics and influence the system, so that they can be profitably used for comparative studies of various systems.

CONCLUSIONS

This work shows that spectral analysis of fluctuating phenomena should be carefully treated in order to reveal the long-range or short-range correlation property. It is necessary that the series should be first detrended, than subjected to spectral analysis and the spectra should be averaged by using a reasonably high number of terms. Spectra which are not of $1/f$ type, i.e. long-range correlated, are most likely short-range correlated. They can be modeled by autoregressive processes of first or higher order. While the long range correlated systems can be characterized by the correlation exponent, a short-range correlated systems is characterized by the values and numbers of interaction constant between the terms.

REFERENCES

1. E. Milotti, *arxiv preprint*, **2002** physics/0204033
2. V.V. Morariu, A. Coza, *Physica A* **320**, 461 (2003)
3. A. Coza and V.V. Morariu, *Physica A* **320**, 449 (2003)
4. V.V. Morariu, A. Isvoran, O. Zainea, *Chaos, Solitons and Fractals* **32**, 1305 (2007)
5. B.B. Mandelbrot, "Multifractals and $1/f$ noise" Springer, New York, **1998**
6. P.J. Brockwell and R.A. Davies, "Time Series: Theory and Methods" 2nd ed. Springer, New York, **1991**.
7. J.D. Hamilton, "Time Series Analysis", Princeton University Press, **1994**.
8. V.V.Morariu, L.Buimaga-Iarinca, C. Vamoş, Ş.Şoituz, *Fluctuation and Noise Letters* **7**, L249 (2007)

SPECTROSCOPIC AND ATOMIC FORCE MICROSCOPY STUDY OF A NEW HEMICYANINE DYE

IOAN PANEA^a, MARIA TOMOAI-COTISEL^b, OSSY HOROVITZ^b,
COSTINELA LAURA GÁSPÁR^c, AURORA MOCANU^b, CSABA NAGY^a

ABSTRACT. The new hemicyanine dye, named 1,3,3-trimethyl-2-[2-(4-florophenylamino) ethenyl]-3-H-indolium chloride **1**, was synthesized and characterized by spectroscopic methods (UV-VIS, IR, ¹H-NMR) and by atomic force microscopy (AFM). The AFM data, obtained on thin films deposited on solid substrates, glass and mica plates, indicated that the hemicyanine **1** is aggregated as clusters containing thousands of molecules. These data are in substantial agreement with UV-VIS absorption spectra, obtained both in solution and on films adsorbed on glass or mica plates, suggesting that hemicyanine **1** is aggregated both in bulk solution and in adsorbed films on solid substrates.

Keywords: hemicyanine dye, 1,3,3-trimethyl-2-[2-(4-florophenylamino) ethenyl]-3-H-indolium chloride, synthesis, spectroscopic characterization, AFM

INTRODUCTION

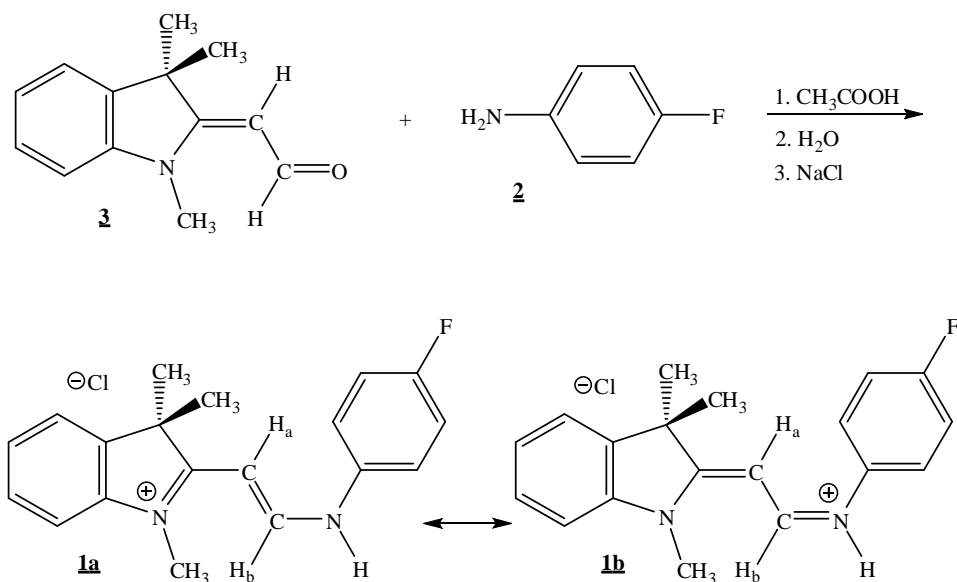
The hemicyanine dyes are widely used for dyeing textile fibers [1-4], as laser dyes and fluorescence probe [5], as well as in sensitization of silver halides in photography [1, 2, 6-8]. For such applications, spectroscopic and aggregation properties are important [1, 4, 5, 9]. Generally, the aggregation properties of dyes have been studied especially by UV-VIS spectroscopy [1, 9-19] and recently by atomic force microscopy [20].

Taking into account the large application potential of hemicyanine dyes and the influence of molecular aggregation on their properties we synthesised a new hemicyanine dye (noted compound **1**, in Scheme 1) and investigated its aggregation capability. The rational name for the new hemicyanine dye **1** is 1,3,3-trimethyl-2-[2-(4-florophenylamino)ethenyl]-3-H-indolium chloride.

^a "Babes-Bolyai" University of Cluj-Napoca, Faculty of Chemistry and Chemical Engineering, Department of Organic Chemistry, Arany J. Str., no. 11, 400028 Cluj-Napoca, Romania;

^b "Babes-Bolyai" University of Cluj-Napoca, Faculty of Chemistry and Chemical Engineering, Department of Physical Chemistry, Arany J. Str., no. 11, 400028 Cluj-Napoca, Romania;

^c S.C. Olchim S.A., Research Centre, Uzinei Str., no. 1, 240050 Râmnicu Vâlcea, Romania



Scheme 1. Synthesis of 1,3,3-trimethyl-2-[2-(4-florophenylamino)ethenyl]-3-H-indolium chloride (**1**)

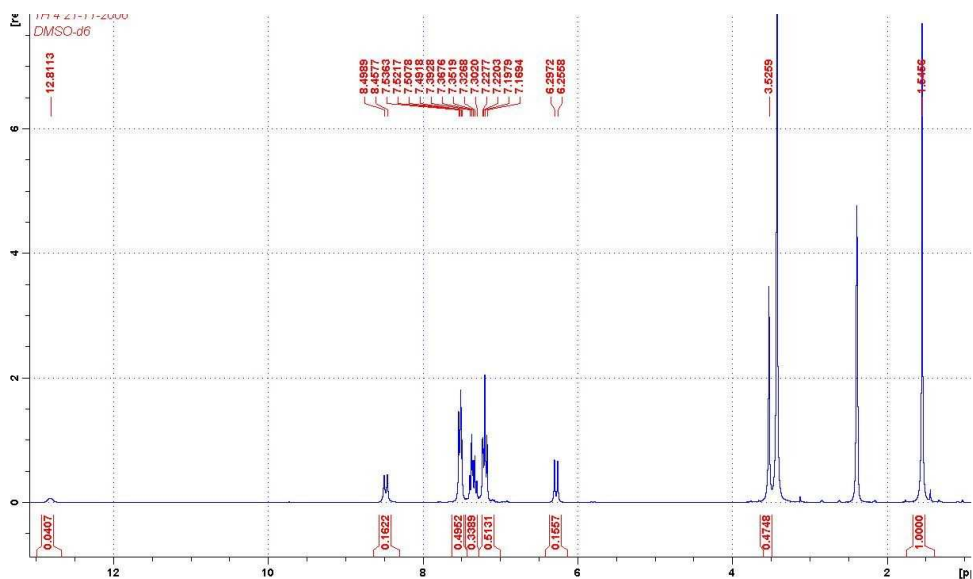


Fig. 1. The ¹H-NMR spectrum of hemicyanine dye, compound **1**.

EXPERIMENTAL PART

Materials

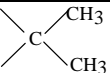
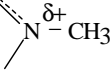
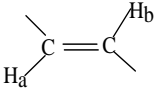
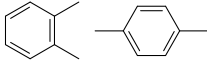
4-floroaniline (**2**) was purchased from Fluka (Buchs), glacial acetic acid, ethanol, methanol and diethylether from Chimopar (Bucharest) and hexadeuterated dimethylsulfoxid (CD_3SOCD_3) from INCDTIM (Cluj-Napoca). The aqueous solutions were prepared by using demineralized and twice distilled water. The 1,3,3-trimethylindolin-2-ylidene acetaldehyde (TIA), **3**, was synthesized as previously described [21].

Synthesis and characterization of hemicyanine **1**

The hemicyanine **1** was synthesized [2-4] by the condensation of TIA, **3** (0.01 mol) with 4-floroaniline (**2**) in glacial acetic acid (5 ml) (Scheme 1). The mixture was stirred at room temperature for 17 hours, then diluted with water (25 ml) and salted out with NaCl (5 g). The orange precipitate was filtered, washed with water, ethanol and finally with diethyl ether. After recrystallization from methanol: m.p. = 218 -221 °C, yield 40%, UV-VIS spectrum: λ_{max} (methanol) = 406 nm; ϵ_{max} = 43,000 L mol⁻¹ cm⁻¹; IR spectrum (KBr pellet) ν_{NH} = 3,384 cm⁻¹; $\delta_{\text{-CH=CH-}}$ (trans) = 931 cm⁻¹. The ¹H-NMR spectrum (300 MHz, in hexadeuterated dimethylsulfoxid) is given in Fig. 1. For each type of protons (Scheme 1), the chemical shift expressed in δ [ppm], using tetramethylsilane as internal standard, the multiplicity (s = singlet, d = doublet, m = complex multiplet), the number of protons and the coupling constant J [Hz] are given in Table 1. The presented spectroscopic data confirm the ascribed structure **1**.

Table 1.

¹H-NMR spectrum of hemicyanine **1**

Group	δ [ppm],	Multiplicity	Nr. of protons	J[Hz]
	1.55	s	6	
	3.53	s	3	
	H _a 6.28 H _b 8.48	d d	1 1	12.4 12.4
	7.1 – 7.6	m	8	
	12.81	s	1	

Instrumentation and measurements

The UV-VIS spectra were recorded on a Jasco spectrophotometer (V-530 and V-650 models) at 25 °C. The IR spectrum was registered as KBr pellet on a Nicolet Impact 410 FT-IR spectrometer. The $^1\text{H-NMR}$ spectrum was performed at room temperature using a FT-Bruker Avance 300 NMR spectrometer. The AFM measurements were carried out, as previously described [22-24], with an AFM-JEOL 4210 scanning microscope on samples of hemicyanine **1** as solid films deposited on glass and mica plates. The same samples were also used for the recording of UV-VIS spectra for **1** in solid state. The hemicyanine **1** solid films were obtained by application of drops of 10^{-4} M aqueous acidic (pH = 3.3) solution of **1** on glass or mica plates, followed by the complete evaporation of water at room temperature and atmospheric pressure. The size of the plates varied between 2.5 cm x 2.5 cm and 1 cm x 1 cm. The UV-VIS spectra in solution were measured on aqueous acidic (HCl) solution (pH = 3.3) in the range of about 10^{-5} M to 10^{-4} hemicyanine dye concentration.

RESULTS AND DISCUSSION

In the present paper the focus is on the examination of the capability of the hemicyanine **1** to aggregate, since aggregation properties of dyes are known [1, 5, 9, 19, 20] to be involved in many of their applications.

As the hemicyanine **1** in aqueous solution is implicated in an acid-base equilibrium [2, 3] it is very difficult to provide evidence on aggregation in solution [19, 25, 26]. Therefore we have tried to prove the capability of aggregation of **1** by comparing the UV-VIS absorption spectra of **1** in aqueous acidic solution (when the acid-base equilibrium is shifted towards form **1**) with that in solid films on mica (Fig. 2).

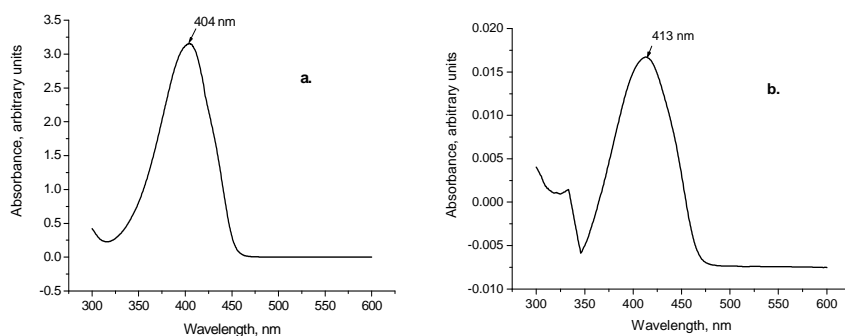


Fig. 2. UV-VIS absorption spectra of hemicyanine **1** in aqueous acidic solution (10^{-4} M, pH = 3.3) (a) and on solid film on mica (b).

As it can be seen (Fig. 2), the two spectra, both in solution (a) and in the solid state, adsorbed on mica (b), look very similar, although in the spectrum of the solid film (b) the absorption maximum is shifted bathochromically with 9 nm and the band width is slightly larger.

Since in solid state, both as crystals or adsorbed on solid substrates, as a rule dyes are considered to be aggregated [1, 9, 11, 13, 15, 16, 20, 27-30], the similar spectra obtained for hemicyanine **1** in solution (Fig. 2a) and in adsorbed solid state (Fig. 2b) could be an argument for the appearance of aggregation of **1** in bulk solution as well. The presence of hemicyanine **1** as aggregates in its solid films, adsorbed on glass or mica (having the UV-VIS absorption spectrum presented in Fig. 2b), has been also confirmed by AFM measurements (Figs. 3-6).

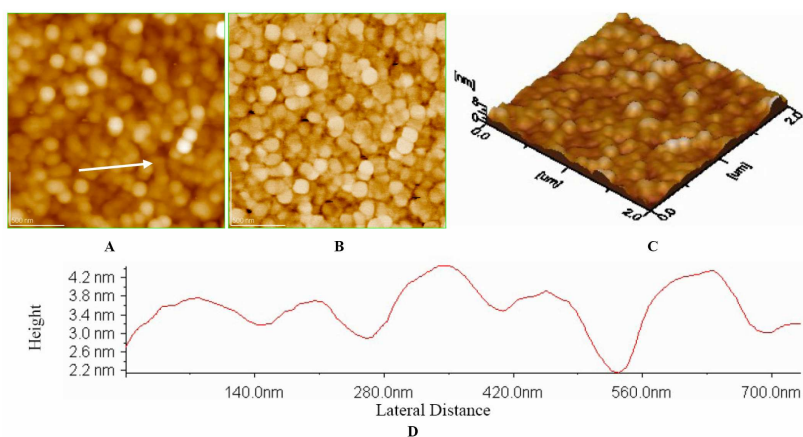


Fig. 3. AFM images of the hemicyanine **1** film deposited from aqueous solution (10^{-4} M, pH = 3.3) on optically polished glass. Scanned area: $2 \times 2 \mu\text{m}^2$. A) 2D- topographic image; B) phase image; C) 3D-topographic image; D) cross section profile along the arrow in Fig. 3A.

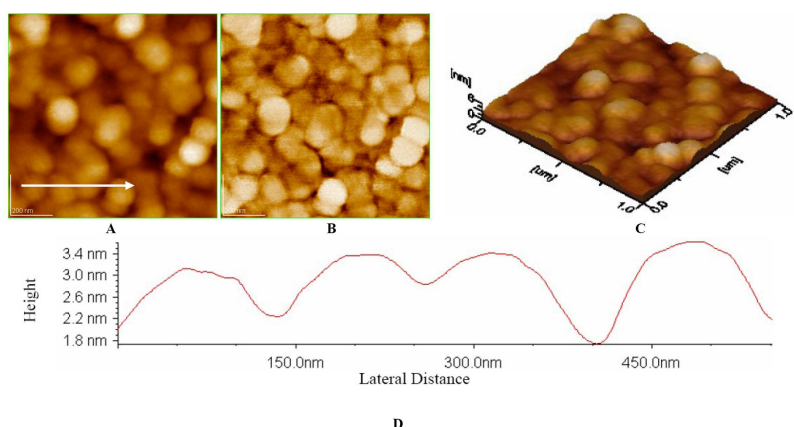


Fig. 4. AFM images of the hemicyanine **1** film on optically polished glass (see Fig. 3). Scanned area: $1 \times 1 \mu\text{m}^2$. A) 2D- topographic image; B) phase image; C) 3D-topographic image; D) cross section profile along the arrow in Fig. 4A.

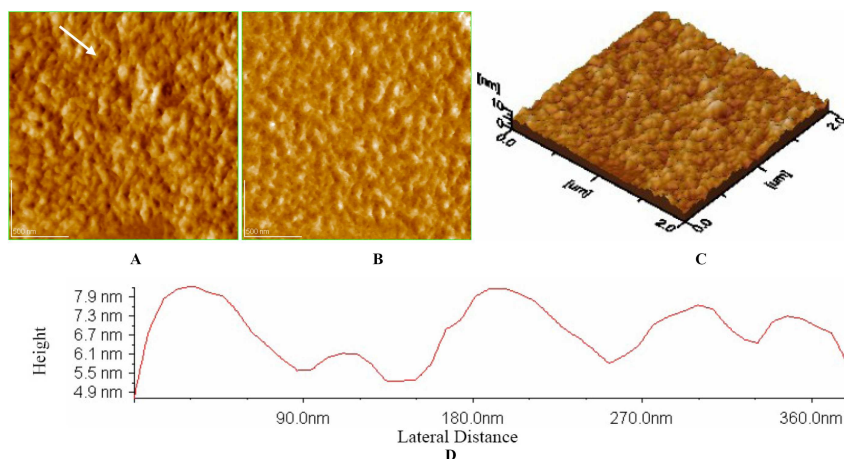


Fig. 5. AFM images of the hemicyanine **1** film deposited from aqueous solution (10^{-4} M, pH = 3.3) on mica. Scanned area: $2 \times 2 \mu\text{m}^2$. A) 2D- topographic image; B) phase image; C) 3D-topographic image; D) cross section profile along the arrow in Fig. 5A

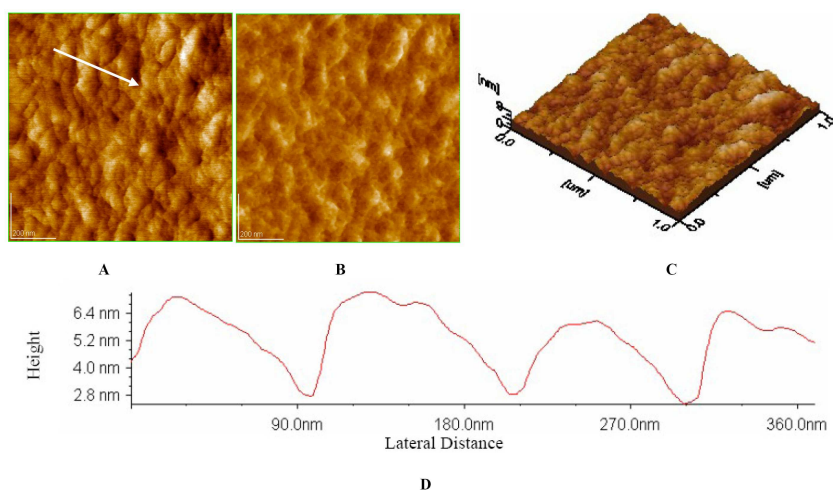


Fig. 6. AFM images of the hemicyanine **1** film on mica (see Fig. 5). Scanned area: $1 \times 1 \mu\text{m}^2$. A) 2D- topographic image; B) phase image; C) 3D-topographic image; D) cross section profile along the arrow in Fig. 6A

From Figs. 3-6, it is observed that the solid films of hemicyanine **1** adsorbed on glass (Figs. 3, 4) or on mica (Figs. 5, 6) appear as multilayers and have island structures. The clusters of hemicyanine **1** within these films correspond to supramolecular assemblies of approximately spherical shape, having a 70 ± 5 nm radius on glass (Figs. 3, 4) and about 45 ± 5 nm on mica.

A full geometry optimization was carried out using the *ab initio* Hartree-Fock 6-31G* level of theory implemented in the Gaussian 03. The

geometry of hemicyanine **1** molecule is given in Fig. 7. The van der Waals surface-bounded molecular volume is 946 \AA^3 , and the dimensions of the molecule are: length of about 14.2 \AA ; width of 4.3 \AA and height of 5.8 \AA .

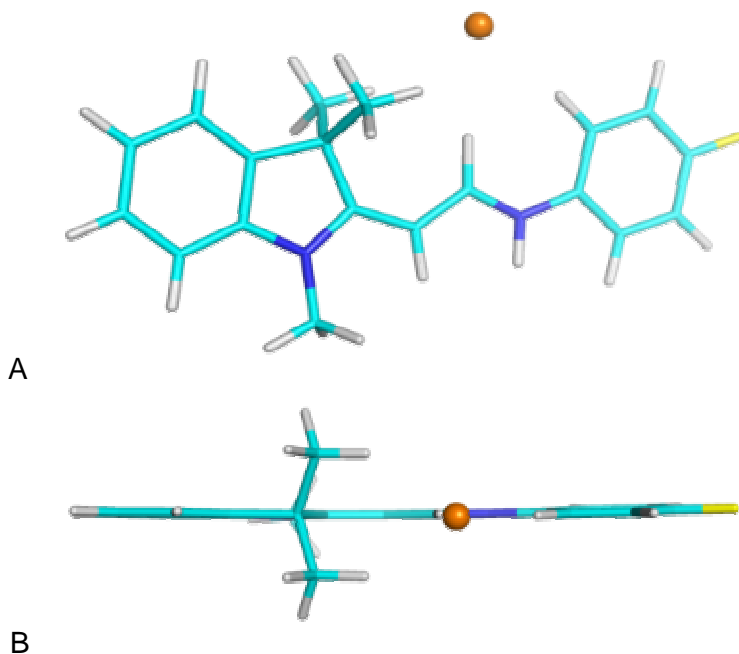


Fig.7. The hemicyanine **1** molecule represented in the plane of the first two inertial axes (A) and of the first and third inertial axes (B). The red ball represents the chloride anion.

Taking into account the estimated volume of a hemicyanine **1** molecule (about 1 nm^3), it might be concluded that the clusters of hemicyanine **1** adsorbed on glass or mica plates contain at least thousands of molecules.

CONCLUSIONS

The new hemicyanine dye **1** was synthesized and characterized by spectroscopic methods (UV-VIS, IR, $^1\text{H-NMR}$) and by atomic force microscopy. The obtained data show that in solid films deposited on glass or mica plates, the hemicyanine **1** appears as supramolecular clusters. These data suggest that the hemicyanine **1** might also build aggregates in bulk solutions.

ACKNOWLEDGEMENT

The financial support from CNCSIS Grant A -1347/2007 is gratefully acknowledged by the authors.

REFERENCES

1. R. Raue, In "Ullmann's Encyclopedia of Industrial Chemistry", Vol. A16, Wiley-VCH, **1990**, pp.487-534
2. C.L. Gáspár, Diss., Univ. Babes-Bolyai, Cluj-Napoca, **2007**.
3. C.L. Gáspár, I. Bâldea, I. Panea, *Dyes Pigm.*, **2006**, 69, 45-53.
4. C.L. Gáspár, I. Panea, I. Bâldea, *Dyes Pigm.*, **2007**, 74, 306-312; **2008**, 76, 455-462.
5. B. Jedrzejewska, J. Kabate, M. Pietrzak, J. Paczkowski, *Dyes Pigm.*, **2003**, 58, 47-58.
6. Y. Nakazawa, Y. Nakamura, T. Sueyoshi, A. Sato, U.S. Pat. 3,788,859, **1974**
7. K. Kameoka, Y. Miyota, M. Okazahi, S. Sasaoka, U.S. Pat. 4,725,532, **1978**.
8. K. Nobuaki, S. Takeshi, Jp. Pat. 6,161,013, **1994**; *Chem. Abstr.*, **1994**, 121, 241,669; Jp. Pat. 6,161,014, **1994**; *Chem. Abstr.*, **1994**, 121, 241,670.
9. H.Zollinger, *Colour Chemistry*, VCH, Basel, **1991**, pp. 289-291.
10. D.R.Lemin, T. Vickerstaff, *Trans. Faraday Soc.*, **1947**, 43, 491-502.
11. C.H. Giles, S.M.K. Rahman, D. Smith, *J.Chem.Soc.*, **1961**, 1209-1214.
12. D. Bârcă-Gălăţeanu, M. Giurgea, I. Iova, V. Sahini, A. Truţia, R. Ţiţeica, "Introducere în spectroscopia experimentală", Ed. Tehnică, Bucureşti, **1966**, pp. 244, 245, 266-268.
13. E.S.Emerson, M.A. Conlin, A.E. Rosenoff, K.S. Norland, H. Rodriguez, D. Chin, G.R. Bird, *J.Phys.Chem.*, **1967**, 71, 2396-2403.
14. E.H. Braswell, *J.Phys.Chem.*, **1968**, 72, 2477-2483; **1972**, 76, 4026-4030; **1984**, 88, 3653-3658.
15. R. Steiger, R. Kitzing, R. Hagen, H. Stoekli-Evans, *J.Photogr.Sci.*, **1974**, 22, 151-167.
16. B.R. Hsieh, D. Desilets, P. Kazmaier, *Dyes Pigm.*, **1990**, 14, 165-189.
17. M. Dakiki, K. Kanan, M. Khamis, *Dyes Pigm.*, **1999**, 41, 199-209.
18. M.R. Habibi, A. Hassanzadeh, A. Zeini-Isfahani, *Dyes Pigm.*, **2006**, 69, 111-117.
19. I. Panea, „Coloranţii organici“, Presa Univ. Clujeană, Cluj-Napoca, **2007**, pp. 65, 75, 84, 169, 170.
20. J.C. Horne, Y. Huang, G.-Y. Liu, G.J. Blanchard, *J. Amer. Chem. Soc.*, **1999**, 121, 4419-4426.
21. H. Fritz, *Chem. Ber.*, **1959**, 92, 1809-1817.
22. M. Tomoaia-Cotisel, Gh. Tomoaia, V. D. Pop, A. Mocanu, G.Cozar, N. Apetroaei and Gh. Popa, *Rev. Roum. Chim.*, **2005**, 50, 471-478.
23. M. Tomoaia-Cotisel, In: "Convergence of Micro-Nano-Biotechnologies", Series "Micro and Nanoengineering", Vol.9, Ed.Academiei, **2006**, 147 - 161.
24. M. Tomoaia-Cotisel, A. Tomoaia-Cotisel, T. Yupsanis, Gh. Tomoaia, I. Balea, A. Mocanu, Cs. Racz, *Rev. Roum. Chim.*, **2006**, 51, 1181-1185.
25. I. Panea, M. Pelea, I.A. Silberg, *Dyes Pigm.*, **2006**, 68, 165-176; **2007**, 74, 113-122.
26. M. Pelea, Diss., Univ. Babes-Bolyai, Cluj-Napoca, **2007**.
27. H. Daruwalla, In "The Chemistry of Synthetic Dyes", Vol. 7, Edit. K. Venkataraman, Academic Press, London, **1974**, pp.97-104.
28. L. Dähne, G. Reck, *Angew. Chem.*, **1995**, 107, 735-737.
29. J. Zgeng, D.-G. Wu, J. Zsai, C.H. Huang, W.W.Pei, X.C. Gao, *Phys. Chem. Chem. Phys.*, **1999**, 1, 2345-2349.
30. A.R. Kennedy, M.P. Hughes, M.L. Monaghan, E. Staunton, S.J. Teat, W.E.Smith, *J. Chem. Soc., Dalton Trans.*, **2001**, 2199-2205.

INVESTIGATION OF MICELLAR PROPERTIES OF ANIONIC SURFACTANTS WITH THE AID OF PVC-MEMBRANE DODECYL SULFATE ELECTRODE

SIMONA ANTOANELA GAVAN AND DAN FLORIN ANGHEL*

ABSTRACT. A polymer matrix electrode selective to anionic surfactants has been proposed. The active matter of the electrode was the dodecyltrimethylammonium dodecyl sulfate ion-pair. The matrix was made of high-molecular weight poly(vinyl chloride) (PVC) plastified with 2-nitrophenyl octyl ether. The electrode had Nernstian response with a slope of 57.3 ± 0.2 mV per decade over a range of dodecyl sulfate concentration from 3.5×10^{-6} to 6.0×10^{-3} M, and a detection limit of 2.2×10^{-6} M. The electrode was very selective towards inorganic interfering anions. Among the organic anions only those with surfactant properties did interfere. The working pH of the electrode was in the 3.0 - 13.0 range. The electrode was used to determine the critical micelle concentration (CMC) of sodium dodecyl sulfate (SDS) in the absence and presence of water-soluble organic additives and of inorganic electrolytes.

INTRODUCTION

Due to the amphiphilic character, the surfactants aggregate at a threshold value of their concentration in solution. This value is called the critical micelle concentration (CMC), and is a fundamental characteristic that depends on surfactant composition and the additives present in the system. CMC is determined by many of methods, such as: surface tension [1], electrical conductivity [2], dye solubilization [3], UV-Vis spectrometry [4], fluorescence [5], scattering techniques [6,7], FTIR [8], viscosity [9], osmometry [10], nuclear magnetic resonance [11], electron spin resonance [12], isothermal titration calorimetry [13], etc. There are also reports on measuring the CMC by potentiometry with surfactant-selective electrode (SSE). The technique was developed by our group more than 30 years ago, and we originally emphasized that the discontinuity in the calibration curve corresponds to the CMC [14,15]. Nowadays, potentiometry with SSE is barely used for CMC determination [16,17], being mainly applied in surfactant analysis [18-22].

In this work, we describe the construction and characterization of a new dodecyl sulfate selective electrode. The electrode was used to determine the CMC of sodium dodecyl sulfate (SDS) in aqueous solution in the absence and presence of inorganic electrolytes and organic additives.

* Romanian Academy, "Ilie Murgulescu" Institute of Physical Chemistry, Department of Colloids, Spl. Independentei 202, 060021 Bucharest, Romania

EXPERIMENTAL PART

Materials

All the chemicals were analytical grade reagents and were used as received. The surfactants were purchased from Serva (SDS), and Fluka (dodecyltrimethylammonium bromide, DTAB). The high molecular mass poly(vinyl chloride) and the plasticizer 2-nitrophenyl octyl ether (NPOE) were also Fluka products. Tetrahydrofuran was purchased from Merck. The water used to prepare the solutions was ultrapure water with a resistivity of 18.2 M Ω .cm at 25° C.

Apparatus

The potential measurements were made with a digital ORION pH-meter, model 420A (ATI ORION Boston, U.S.A.). The reference electrode was the Ag/AgCl model 900200 (ATI ORION, Boston, U.S.A.). The pH measurements were made with a glass electrode model P-05992-40, (COLE PARMER INSTRUMENT COMPANY, Vernon Hills, U.S.A.). The ultrapure water was prepared with the aid of Simplicity UV apparatus (MILLIPORE SAS, Molsheim, France).

Preparation of the ion-pair complex

The dodecyltrimethylammonium dodecyl sulfate ion-pair was obtained by drop-wise addition of 0.005 M SDS aqueous solution into 0.005 M DTAB aqueous solution. The ion-pair precipitate was extracted in chloroform. The organic layer was separated and dried over anhydrous sodium sulfate. The inorganic salt was removed by filtration, and the ion-pair was recovered by gentle evaporation of the organic solvent.

Membrane preparation

The ion-pair complex (10 mg) was mixed with 0.35 mL of 2-nitrophenyl octyl ether, 0.19 g of poly(vinyl chloride) powder and 5 mL of tetrahydrofuran. The solution was poured into a glass ring resting on a clean glass plate. A wad of filter papers, weighted down with a heavy weight, was placed on top of the ring and the whole assembly left at room temperature to evaporate the solvent.

Construction of electrode

Disks of 10 mm in diameter were cut from the master membrane with a cork borer and glued to the flat end of the hollow PVC support tube with an adhesive of PVC in tetrahydrofuran. The tube was filled with a 1:1 mixture of aqueous 10⁻³ M SDS and 10⁻³ M sodium chloride solutions and inserted into the inner reference saturated calomel electrode.

The electro-chemical cell contains the measuring solution, the surfactant selective electrode and the reference Ag/AgCl electrode.

RESULTS AND DISCUSSION

Electrode characterization

The procedure of electrode characterization consists of recording the calibration curve, response time, effect of pH and selectivity. All are important parameters in designing the electrode and estimating its performance.

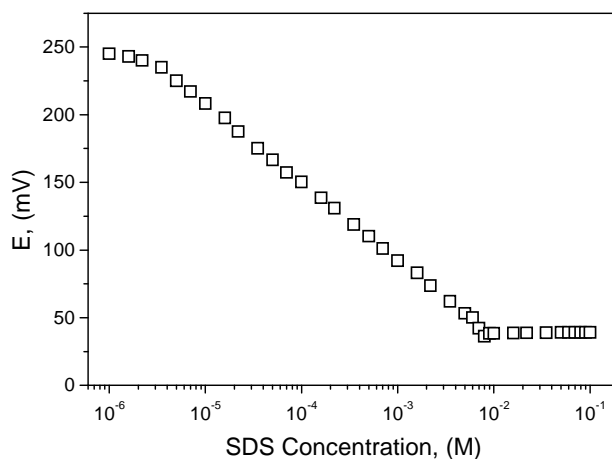


Figure 1. The calibration curve of DS-selective electrode at 25° C.

Figure 1 shows the results obtained at electrode calibration in SDS solutions at 25° C. The curve is linear in-between 3.5×10^{-6} and 6.0×10^{-3} M SDS. At 8.0×10^{-3} M, the calibration curve has a breaking point assigned by us to the formation of surfactant micelles into solution. The figure is within the range of values $(7.1 - 8.3) \times 10^{-3}$ M reported in literature [23-25]. After CMC, the recorded potential is practically constant. This is in accord with the theory of surfactant micellization which predicts that all the surfactant introduced into the system above CMC forms micelles, and the concentration of free surfactant is constant.

The linear fit of potential values within the linear range of electrode response resulted in a slope of 57.3 ± 0.22 mV/decade of SDS concentration and a regression coefficient of 0,99986. Both the slope and the regression coefficient prove the good performance and quality of the electrode and allowed us to consider it for further steps of characterization.

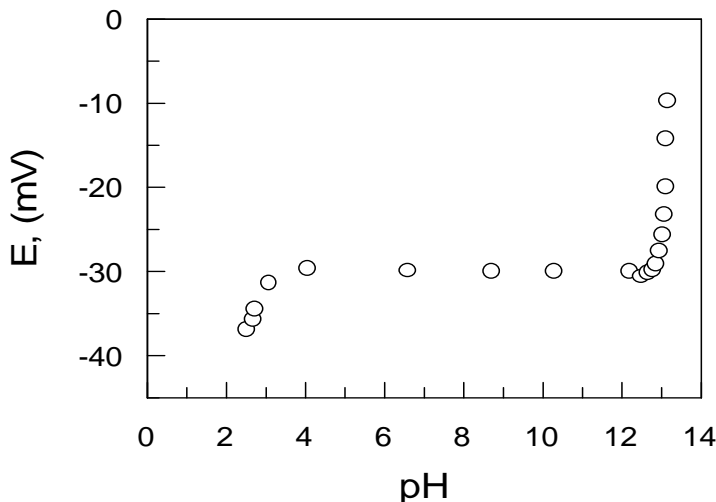


Figure 2. The influence of pH upon the SD-selective electrode.

Time of response and lifetime

The response time is the period elapsed between the moment when the DS-selective electrode and the reference electrode are brought into contact with a sample solution (or at which the activity of the ion of interest in solution is changed) and the first instant at which the slope of the cell potential vs. time plot ($\Delta E/\Delta t$) becomes equal to a limiting value selected to be of 0.6 mV/min [25]. The response of electrode was very fast. Within the linear range of the calibration curve, the elapse time was of maximum 5 seconds within the range of linear response. Within the same range, a set of 10 calibrations gave reproducible potentials with an error of ± 2.0 mV/day. At very low surfactant levels, the lapse time increased to 2 - 5 minutes.

The lifetime of the electrode was of four months. After that it had erratic response, the membrane lost elasticity and became opaque. We suspect responsible for this behavior the loss of plasticizer by diffusion.

Effect of pH

The influence of hydrogen ions on the electrode was determined at a constant surfactant concentration of 1.0×10^{-3} M SDS. The pH was changed by means of minute amounts of concentrated hydrochloric acid and sodium hydroxide solutions. The modification of pH was monitored with the glass electrode. After every pH change, it was waited until the surfactant selective electrode stabilized its reading. Figure 3 illustrates the results obtained. One may observe that the electrode potential is not affected by pH

in the 3.0 -13.0 range. This large pH working range will allow to use the electrode both in surfactant and soap titrations.

Selectivity of electrode

Electrode selectivity is defined by means of the potentiometric selectivity coefficients and it is an important parameter in designing a suitable electrode. The selectivity coefficient, $K_{i,j}^{\text{pot}}$, defines the ability of an ion-selective electrode to distinguish a particular ion, i , from others, j [26]. Usually $K_{i,j}^{\text{pot}}$, has values in-between 10^{-4} and 10^4 , but it may fall outside this range. The smaller the value of $K_{i,j}^{\text{pot}}$, the greater the preference of the electrode for the principal ion.

In our case, the selectivity coefficient, $K_{\text{DS},j}^{\text{pot}}$, was evaluated by measuring the electromotive force (EMF) of ion-selective electrode in separate solutions of principal ion, DS, and interfering ion, j . For a solution containing only the primary ion, the electrode potential is given by equation (1):

$$E_1 = E^{01} + (RT/F)\ln a_{\text{DS}} \quad (1)$$

In a solution of only the interfering ion the electrode potential is:

$$E_2 = E^{02} + (RT/F)\ln a_{\text{DS}} + (RT/F)\ln K_{\text{DS},j}^{\text{pot}} \quad (2)$$

If $a_{\text{DS}} = a_j$, by converting to decimal logarithm, one obtains:

$$\lg K_{\text{DS},j}^{\text{pot}} = (E_2 - E_1) F / (2.303 RT) \quad (3)$$

Relation (3) permits to determine the potentiometric selectivity coefficients from the recorded values of the E_1 and E_2 . The values obtained by us for $K_{\text{DS},j}^{\text{pot}}$ are given in Table 1. The selectivity coefficient values show that the electrode has excellent selectivity for the DS ion over inorganic anions. The same holds true for organic anions like formate, acetate and propionate, and for short-chain alkyl sulfates and sulfonates. For sulfates and sulfonates, the interference increases with the length of the alkyl chain. However, this apparent disadvantage offers the possibility of using the electrode as end-point detector in potentiometric titration of anionic surfactants, irrespective of their alkyl chain length.

Table 1.

Selectivity coefficients of dodecyl sulfate electrode

Interferent anion, j	a_j (M)	$K_{DS,j}^{pot}$
Cl^-	10^{-3}	4.07×10^{-4}
Br^-	10^{-3}	5.25×10^{-4}
I^-	10^{-3}	5.74×10^{-4}
SO_4^{2-}	10^{-3}	2.63×10^{-7}
$HCOO^-$	10^{-3}	6.33×10^{-5}
CH_3COO^-	10^{-3}	9.12×10^{-4}
$C_2H_5COO^-$	10^{-3}	1.27×10^{-3}
$C_5H_{11}SO_4^-$	10^{-3}	1.40×10^{-3}
$C_8H_{17}SO_4^-$	10^{-3}	0.01
$C_{10}H_{21}SO_4^-$	10^{-3}	0.33
$C_{12}H_{25}SO_4^-$	10^{-3}	1.00
$C_{14}H_{29}SO_4^-$	10^{-3}	65.1
$C_{16}H_{33}SO_4^-$	5×10^{-4}	113.2
$C_5H_{11}SO_3^-$	10^{-3}	0.94×10^{-4}
$C_8H_{17}SO_4^-$	10^{-3}	0.011
$C_{12}H_{25}SO_3^-$	10^{-3}	0.96
$C_{14}H_{29}SO_3^-$	10^{-3}	58.3
$C_{12}H_{25}C_6H_4SO_3^-$	10^{-3}	105.6

Determination of CMC

Micelles that form in dilute aqueous solutions are affected by the additives present in the system. Previous works have demonstrated that electrolytes usually decrease the CMC [27-29], whereas hydrophobic solubilizates entail the increase of spherical micelles to ellipsoids and rods [30,31].

The data in Table 2 show that CMC decreases by increasing the electrolyte concentration. The result can be explained taking into account the attraction and adsorption of counterions at the ionic micelle surface. The phenomenon stabilizes the micelle surface in an extent that depends on the micelle charge density. At the same time, there is a gradual change in the counterion-micelle interaction as the electrolyte concentration increases. The higher is the electrolyte concentration, the higher is the adsorption of counterions and the lower is the CMC.

Table 2.

Effect of electrolytes on the CMC of SDS at 298 K

Electrolyte	Concentration (M)	CMC Electrode (M)	CMC Literature (M)	Reference
-	-	8.0×10^{-3}	$(7.1-8.3) \times 10^{-3}$	24,25
NaCl	10^{-3}	7.0×10^{-3}	6.90×10^{-3}	23
	10^{-2}	5.6×10^{-3}	5.62×10^{-3}	23
	10^{-1}	1.5×10^{-3}	1.49×10^{-3}	23
NaBr	10^{-1}	1.4×10^{-3}	1.42×10^{-3}	23
NaF	10^{-1}	1.6×10^{-3}	1.45×10^{-3}	23
IaI	10^{-1}	1.3×10^{-3}	1.38×10^{-3}	23

Table 3.

Effect of organic additives on the CMC of SDS at 298 K

Organic Additive	Concentration (wt. %)	CMC Electrode (M)	CMC Literature (M)	Reference
-	-	8.0×10^{-3}	$(7.1-8.3) \times 10^{-3}$	24, 25
Methanol	25.0	9.0×10^{-3}	-	This work-
Ethanol	5.0	5.5×10^{-3}	1.07×10^{-2}	23
	10.0	6.5×10^{-3}	5.96×10^{-3}	23
	25.0	1.1×10^{-2}	1.07×10^{-2}	23
	30.0	2.0×10^{-2}	1.90×10^{-2}	16
	40.0	4.0×10^{-2}	4.20×10^{-2}	16
1-Propanol	5.0	4.0×10^{-3}	4.40×10^{-3}	16
	10.0	5.0×10^{-3}	5.20×10^{-3}	16
	20.0	1.3×10^{-2}	1.35×10^{-2}	16
2-Propanol	5.0	4.0×10^{-3}	4.3×10^{-3}	23
Dioxane	5.0	8.0×10^{-3}	7.7×10^{-3}	23
	10.0	1.0×10^{-2}	9.0×10^{-3}	23
	20.0	2.0×10^{-2}	2.12×10^{-2}	23

The aggregation of SDS in ethanol- and *n*-propanol-water mixtures was formerly investigated with the aid of a dodecyl sulfate selective electrode [16]. A decrease of CMC at low and moderate alcohol content and an increase at high additive levels was observed, the effect being more evident for *n*-propanol. Table 3 presents the data obtained by us for short alkyl chain alcohols and dioxane. The trend is similar to that previously observed [16]. The results might be explained by the ability of alcohols to adsorb near the head group region of surfactant micelle, with the alcohol groups in between the ionic groups. The process reduces the electrical repulsion and lowers the CMC. High concentrations of short-chain alcohols influence the solvent characteristics of water, improve the surfactant solubility and therefore increase the CMC.

CONCLUSIONS AND PERSPECTIVES

A new, easy to construct, and reliable dodecyl sulfate-selective electrode is described. The electrode has Nernstian slope, instantaneous

response, good stability in time and a working pH range in-between 3.0 and 13.0. The electrode is characterized by good selectivity towards inorganic anions. Among the organic interferents tested, only those having surface-active properties do interfere, and the interference rises with the hydrophobic character of the surfactant. The electrode performs well in measuring the critical micelle concentration of SDS both in the absence and presence of inorganic electrolytes and organic water-miscible additives.

Work is in progress now in our laboratory to improve the electrode lifetime by using polymeric plasticizers that diffuse slowly, or not at all, from membrane. We also undertake a study on systems of water-soluble polymers and anionic surfactants. It aims to construct the binding isotherms, to obtain the binding parameters and to determine the effect of additives on them.

ACKNOWLEDGMENT

We thank CNCSIS for financial support (Grant No. 201/2006).

REFERENCES

1. B. Z. Putlitz, H. P. Hentze, K. Landfester, M. Antonietti, *Langmuir* **2000**, *16*, 3214-3220.
2. N. Jiang, P. Li, Y. Wang, J. Wang, H. Yan, R. K. Thomas, *J. Colloid. Interface. Sci.*, **2005**, *286*, 755-760.
3. N. Zhang, S. R. Guo, H. Q. Li, L. Liu, Z. H. Li, J. R. Gu, *Macromol. Chem. Phys.*, **2006**, *207*, 1359-1367.
4. J. Zhang, B. Dong, L. Q. Zheng, G. Z. Li, *Colloid. Surf. A*, **2006**, *290*, 157-163.
5. C. Q. Zhu, Y. Q. Wu, H. Zheng, J. L. Chen, S. J. Zhuo, Y. X. Li, *Anal. Bioanal. Chem.*, **2004**, *379*, 730-734.
6. P. C. Griffiths, M. L. Whatton, R. J. Abbott, W. Kwan, A. R. Pitt, A. M. Howe, S. M. King, R. K. Heenan, *Journal Colloid Interface Sci.*, **1999**, *215*, 114-123.
7. L. T. Okano, F. H. Quina, O. A. El Seoud, *Langmuir* **2000**, *16*, 3119-3123.
8. L. Carolei, I. G. R. Gutz, *Talanta*, **2005**, *66*, 118-124.
9. S. Shirai, S. Yoshimura, Y. Einaga, *Polym. J.*, **2006**, *38*, 37-43.
10. V. B. Wagle, V. G. Gaikar, *J. Chem. Engn. Data*, **2006**, *51*, 886-891.
11. P. C. Griffiths, E. Pettersson, P. Stilbs, A. Y. F. Cheung, A. M. Howe, A. R. Pitt, *Langmuir* **2001**, *17*, 7178-7181.
12. M. A. Bahri, M. Höbeke, A. Grammenos, L. Delanaye, N. Vandewalle, A. Seret, *Colloid. Surf. A*, **2006**, *290*, 206-212.
13. M. Prasad, I. Chakraborty, A.R. Rakshit, S. P. Moulik, *J. Phys. Chem. B*, **2006**, *110*, 9815-9821.
14. D. F. Anghel, N. Ciocan, *Colloid Polym. Sci.*, **1976**, *254*, 114-115.
15. N. Ciocan, D. F. Anghel, *Tenside Deterg.*, **1976**, *13*, 188-192.
16. A. A. Rafati, H. Gharibi, M. Rezaie-Sameti, *J. Mol. Liq.*, **2004**, *111*, 109-116.
17. K. Nesmerak, I Nemcova, *Anal. Lett.*, **2006**, *39*, 1023-1040.

18. G. A. E. Mostafa, *J. Pharm. Biomed. Anal.*, **2006**, *41*, 1110-1115.
19. T. Masadome, K. Yada, S. I. Wakida, *Anal. Sci.*, **2006**, *22*, 1065-1069.
20. M. A. Plesha, B. J. van Wie, J. M. Mullin, D. A. Kidwell, *Anal. Chim. Acta*, **2006**, *570*, 186-194.
21. S. Martinez Barrachina, M. del Valle, *Microchem. J.*, **2006**, *83*, 48-54.
22. M. Sak-Bosnar, D. Madunic-Cacic, R. Matesic-Puac, Z. Grabaric, *Anal. Chim. Acta*, **2007**, *581*, 355-363.
23. P. Mukerjee, K. J. Mysels, "Critical Micelle Concentrations of Aqueous Surfactant Systems", Nat. Stand. Ref. Data Ser., Nat. Bur. Stand. (U. S.), Washington, D.C., **1971**.
24. M. N. van Oss, J. R. Haak, L. A. M. Rupert, "Physico-Chemical Properties of Selected Anionic, Cationic and Nonionic Surfactants", Elsevier, Amsterdam, **1993**.
25. B. Antalek, J. Kowalczyk, C. Krishnan, *Langmuir*, **2004**, *20*, 11818-11820.
26. R. P. Buck, E. Lindner, *Pure Appl. Chem.*, **1994**, *66*, 2527-2536.
27. M. Pisarcik, F. Devinsky, I. Lacko, *Colloids Surf. A*, **2000**, *172*, 139-144.
28. S. S. Shah, N. U. Jamroz, Q. M. Sharif, *Colloids Surf. A*, **2001**, *178*, 199-206.
29. S. Miyagishi, N. Takeuchi, T. Asakawa, M. Inoh, *Colloids Surf. A*, **2002**, *197*, 125-132.
30. I. Johnson, G. Olofsson, M. Landgren, B. Jonsson, *J. Chem. Soc., Faraday Trans. 1*, **1989**, *85*, 4211-4226.
31. R. De Lisi, S. Milioto, R. E. Verral, *J. Solut. Chem.*, **1990**, *19*, 639-664.

CORROSION BEHAVIOR OF ELECTROCHEMICALLY DEPOSITED Zn-TiO₂ NANOCOMPOSITE COATINGS

LIANA MURESAN^{1*}, MARIANA GHERMAN¹, IONUT ZAMBLAU¹,
SIMONA VARVARA² AND CAIUS BULEA³

ABSTRACT. Zn-TiO₂ nanocomposite films were successfully formed on carbon steel by rapid plating from a ZnSO₄-based bath ($i = 10 \text{ A dm}^{-2}$). The corrosion resistance of the composite coatings was studied by polarization and electrochemical impedance spectroscopy measurements. In the presence of TiO₂, simultaneously with the negative shift of the corrosion potential, a decrease of the corrosion current density was observed as compared to pure zinc coatings, reflecting the beneficial effect of TiO₂ nanoparticles on the corrosion resistance of zinc coatings.

Keywords: nanocomposite coatings, zinc, titanium oxide, corrosion

1. INTRODUCTION

Electrodeposition of Zn films on steel is widely practiced for corrosion resistance increase. However, the life span of such coatings is limited due to the aggressive nature of some environments, particularly those containing industrial pollutants. Consequently, considerable efforts are being made to improve their corrosion resistance [1].

TiO₂ can reinforce metallic coatings including zinc electroplate to improve corrosion and wear resistance, hardness and other properties of the coating such as semiconductor and magnetic properties, lubricity etc. [2-5].

One of the methods used for entrapment of TiO₂ micro- or nanoparticles in the metallic matrix is the electrolytic co-deposition. The main advantages of this method over other coating methods are the uniformity of deposition for complex shapes, reduction of waste encountered in dipping or spraying techniques, low level of contamination, high production rates, low initial capital investment requirements and easy transfer from the research laboratory to existing infrastructure in electroplating and electroforming industries [6].

¹ "Babes-Bolyai" University, Department of Physical Chemistry, 11 Arany Janos St., 400028 Cluj-Napoca, ROMANIA.

* E-mail: limur@chem.ubbcluj.ro

² "1 Decembrie 1918" University, Department of Topography, 11-13 Nicolae Iorga St., 510009 Alba-Iulia, ROMANIA

³ BETAK S.A., 4 Industriilor St., 420063 Bistrița, ROMANIA

The present paper seeks to investigate the corrosion behavior of Zn-TiO₂ coatings obtained by electrolytic co-deposition of zinc with TiO₂ nanoparticles, on steel substrate (OL 37 / Zn-TiO₂). The investigation methods were open circuit potential measurements, hydrodynamic voltammetry and electrochemical impedance spectroscopy.

2. EXPERIMENTAL

Materials

TiO₂ aerogel (surface area 305 m²/g) was obtained by the sol-gel method and was a kind gift from Dr. Virginia Danciu (Laboratory of Electrochemical Research, Faculty of Chemistry and Chemical Engineering Cluj-Napoca).

Zn and Zn-TiO₂ films were co-deposited on OL 37 steel substrate (S = 0.78 cm²) using a rotating disc electrode (1000 rpm) from solutions containing 350 g/l ZnSO₄·7 H₂O and 30 g/l (NH₄)₂SO₄ (pH 4) without or with 20 g/l TiO₂, at a current density of 100 mA/cm², during 30 minutes.

Corrosion experiments were carried out in 0.2 g/l aerated Na₂SO₄ solution (pH 3), at room temperature.

Methods

Potentiodynamic polarization measurements were conducted using an electrochemical analyzer (PARSTAT 2273, USA) connected to a PC for potential control and data acquisition. Open-circuit potential (*ocp*) measurements were performed as a function of time.

The electrochemical experiments were performed in a three-electrode cell with a separate compartment for the reference electrode connected with the main compartment *via* a Luggin capillary. The working electrode was a rotating disc, the reference electrode was a saturated calomel electrode (SCE) and the counter electrode was a platinum foil.

Anodic and cathodic polarization curves were recorded in a potential range of $E = E_{\text{corr}} \pm 200$ mV with a scan rate of 0.25 mV s⁻¹. The rotation speed of the working electrode was fixed at 1000 rpm.

Impedance measurements were performed at the open circuit potential in the moment of immersion of the samples in the Na₂SO₄ solution during 30 h from this moment. The impedance spectra were acquired in the frequency range 10 kHz to 10 mHz at 10 points per hertz decade with an AC voltage amplitude of ± 10 mV.

3. RESULTS AND DISCUSSION

3.1. Open-circuit potential (*ocp*) measurements

The open-circuit potentials evolution in time for OL 37/Zn and OL 37/Zn-TiO₂ electrodes, recorded immediately after 60 minutes immersion in the corrosive medium is presented in Figure 1.

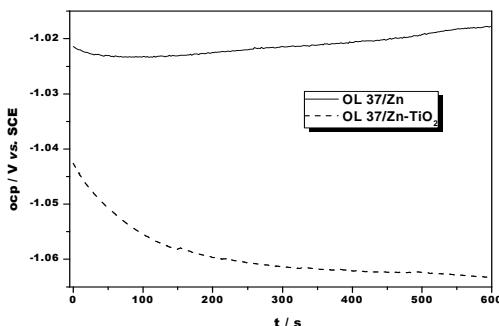


Figure 1. Open-circuit potentials evolution for the OL37/Zn and OL37/Zn-TiO₂ electrodes immersed in 0.2 g/l Na₂SO₄ (pH 3).

In the case of OL 37/Zn-TiO₂ electrode, the *ocp* values gradually increase in the negative direction during the first minutes to reach a stationary state characterized by -1.065 V vs. SCE. This evolution of the potential toward more negative values with the increase of immersion time can be explained by taking into account the growth of a corrosion products layer. According to this growth, the cathodic reaction is hindered and consequently the corrosion potential becomes more negative [7]. The *ocp* value is more negative in the presence of TiO₂ in the zinc deposit than in its absence, suggesting an intervention of these particles in the cathodic process (oxygen reduction).

3.2. Potentiodynamic polarization measurements

The cathodic and anodic polarization curves of OL 37/Zn and OL 37/Zn-TiO₂ electrodes recorded after their immersion during 60 minutes in Na₂SO₄ solution are shown in Figure 2.

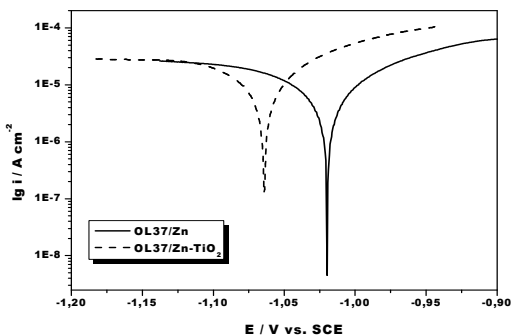


Figure 2. Influence of TiO₂ presence in the zinc deposit on the anodic and cathodic polarization curves.

The same shift of the corrosion potential towards more negative values is noticed in the case of OL 37/Zn-TiO₂ electrode as compared to OL37/Zn electrode. A similar behavior was reported in the case of Cu-ZrO₂ composite films immersed in 0.5 M H₂SO₄ solution [8], when the oxide nanoparticles were proved to retard or inhibit the oxygen reduction on the composite surface.

The corrosion parameters were calculated from the potentiodynamic polarization curves on the basis of the Tafel extrapolation, according to the equation:

$$i = i_0 \exp\left[\frac{2,303}{b_a}(E - E_{corr})\right] - \exp\left[-\frac{2,303}{b_c}(E - E_{corr})\right]$$

where b_a and b_c are anodic and cathodic Tafel slopes, E_{corr} is the corrosion potential and the other parameters have their usual meaning.

Table 1.

Electrochemical parameters of the corrosion process determined by Tafel method

Electrode	E_{corr} (mV vs. ESC)	i_{corr} ($\mu\text{A}/\text{cm}^2$)	$-b_c$ (mV/dec)	b_a (mV/dec)
OL37/Zn (0h)	-1025	15,96	240	153
OL37/Zn-TiO ₂ (0h)	-1063	15,20	155	84

As can be seen, the presence of TiO₂ in the zinc deposit gives rise to decreases of corrosion current densities and of the Tafel coefficients as compared to the pure zinc coating.

3.3. Electrochemical impedance spectroscopy

The Nyquist impedance diagrams recorded on OL 37/Zn and OL 37/Zn-TiO₂ electrodes are presented in Figure 3.

The impedance spectra recorded in the absence and in the presence of TiO₂ nanoparticles in the zinc coatings exhibit a predominant capacitive behavior. The low frequency loop is characteristic of convective diffusion impedance. In agreement with the polarization measurements, it is necessary to consider that this loop is representative of the diffusion process in the electrolyte and through the porous layer [7].

The polarization resistance R_p corresponding to the lower frequency limit of the impedance spectra increases in parallel with the thickness of the corrosion products layer. The increase of R_p can be explained by a limitation of the active area by this layer, more important when the layer is more developed (thicker and/or more compact) [7]. As can be seen from figure 3, in the moment of immersion, the highest value of R_p is noticed in the case of pure zinc coating, while after 12 h of immersion, R_p is higher in the case of the composite layer.

This behavior suggests a different evolution of the corrosion products layer in the two cases. Further work will address the chemical composition of these layers.

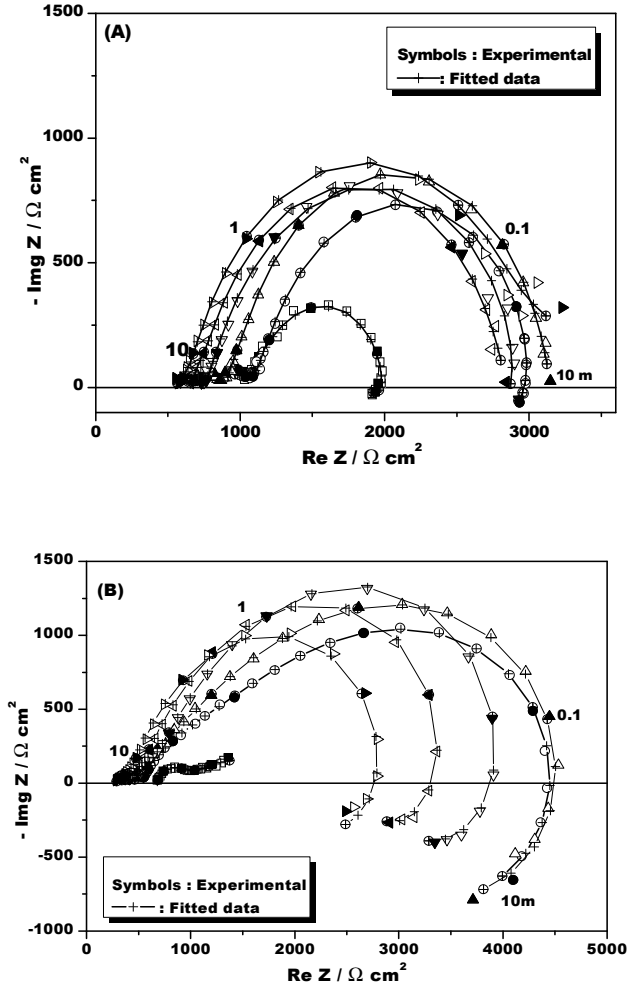


Figure 3. Nyquist impedance diagrams for OL 37/Zn (A) and OL 37/Zn-TiO₂ (B) electrodes in 0.2 g/l Na₂SO₄ solution (pH 3) at different immersion times: (■) 0 h; (●) 6h; (▲) 12h; (▼) 18h; (◄) 24h; (►) 30h.

The inductive behavior is almost inexistent in the case of pure Zn coating and more pronounced in the case of Zn-TiO₂ nanocomposite film. It should be mentioned that this behavior becomes more important with the increase of immersion time, suggesting that the inductive loop could be due

to the potential dependence of some inhibiting species present on the electrode surface (hydrogen or corrosion products involving metal ions) [9].

The equivalent electrical circuits used for non-linear regression calculations with a simplex method are presented in Figure 4.

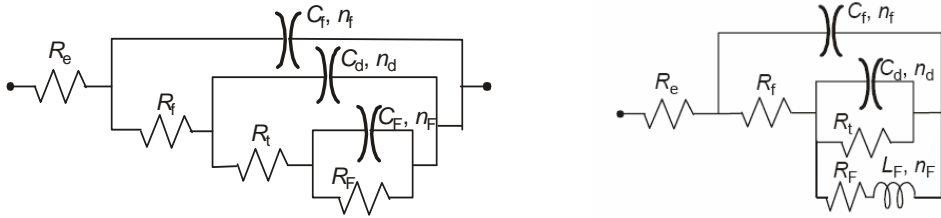


Figure 4. The equivalent electrical circuits used for computer fitting of the experimental data

When the impedance spectra contained only capacitive loops, the fitting was performed using a 3RC equivalent circuit, while when an inductive loop was present, an equivalent 2RC-LC circuit was used. The significance of the different variables is the following [10]:

- R_e : Electrolyte resistance
- C_f : Capacitance due to the dielectric nature of surface film (corrosion products)
- R_f : Resistance representing the ionic leakage through pores of the dielectric film
- C_d : Double layer capacitance at the zinc / electrolyte interface
- R_t : Charge transfer resistance
- C_F : Faradic capacitance due to an oxidation - reduction process taking place at the electrode surface, probably involving the corrosion products.
- R_F : Faradic resistance of the corrosion products accumulated at the interface.
- n_f , n_d , and n_F : Coefficients representing the depressed characteristic of the three capacitive loops in the Nyquist diagrams.

The values of the corrosion parameters obtained by fitting of the experimental impedance data are presented in Table 2.

Table 2.

Parameter values for OL 37/Zn and OL 37/Zn-TiO₂ electrodes corrosion calculated by non-linear regression of the impedance data from figure 3 using the 3RC or 2RC-LC models

Electrode	Immers. time (h)	R _f (Ω cm ²)	C _f (μF cm ⁻²)	n _f	R _t (Ω cm ²)	C _d (μF cm ⁻²)	n _d
OL 37/Zn	0	152.48	2.10	0.75	1164.3	17.24	0.75
	6	194.94	3.02	0.59	4052.2	113.77	0.80
	12	346.25	73	0.88	1731.3	103.24	0.86
	18	124.94	29.65	0.85	983.4	96.62	0.85
	24	462.01	89.4	0.84	1470.9	117.74	0.87
	30	197.65	49	0.84	1777.4	129.65	0.83
OL 37/ Zn-TiO ₂	0	290.61	15.36	0.76	454.33	3430	0.51
	6	1277.1	5.04	0.63	3840.7	70.45	0.58
	12	1493.9	10.87	0.55	4365.7	20.67	0.61
	18	377.53	4.11	0.68	3537.6	62.12	0.80
	24	252.04	5.35	0.71	3017.1	105.62	0.83
	30	196.43	7.48	0.69	2579.3	141.32	0.83

As can be observed from figure 3, between the experimental and the calculated regression data exists a good accordance. The analysis of the results presented in table 2 led to the following conclusions:

(i) The charge transfer resistance R_t (of 10³ Ω cm² order of magnitude) suggests that the layer of corrosion products is not very compact [11]. Generally, if the composition of the corrosion products does not change during the experiments, an increase of R_t values can be correlated with an increase of the thickness of non-conductive corrosion products layer. Thus, the higher R_t values in the presence of TiO₂ nanoparticles than in their absence suggests a better corrosion resistance in the first case. The decrease of R_t during long-term measurements could be attributed to the formation of less protective corrosion products.

(ii) The double layer capacitance values of the corrosion products layer C_f are also characteristic to a porous layer (10⁻⁴ F/cm²). In the case of OL 37/Zn electrode, the relative constancy of C_f after 12 h of immersion points to a certain stabilization of the composition of the corrosion products layer. The decrease of C_f in the case of OL 37/Zn-TiO₂ electrodes could be attributed to the thickening of the corrosion products layer, which leads to a change of permittivity of the environment [11].

4. CONCLUSIONS

The electrochemical measurements showed that the corrosion process on zinc-titania composite surface is slower than on pure zinc surface, because of oxide particles embedded in the zinc matrix.

The titanium oxide particles retard or inhibit the oxygen reduction on the composite surface.

ACKNOWLEDGEMENTS

The authors thank Dr. Virginia Danciu and Dr. Veronica Coşoveanu, from the Laboratory of Electrochemical Research, Faculty of Chemistry and Chemical Engineering Cluj-Napoca for supplying the TiO₂ aerogel. The financial support within the Project INOVARE No. 97/28.09.2007 is gratefully acknowledged.

REFERENCES

1. N.R. Short, A. Abibsi, J.K. Dennis, *Trans. Inst. Met. Finish*, **1991**, 67, 73 - 79.
2. C. Jakob, F. Erler, R. Nutsch, S. Steinhäuser, B. Wielage, A. Zschunke, *Metallobenflaeche*, **2000**, 54, 52-58.
3. A. Gomes, M. I. da Silva Pereira, M. H. Mendonça, F. M. Costa, *J. Solid State Electrochem.*, **2005**, 9, 190 – 196.
4. S.M.A. Shibli, V.S. Dilimon, Smitha P. Antony, R. Manu, *Surface & Coatings Technology*, **2006**, 200, 4791- 4796.
5. T. Deguchi, K. Imai, H. Matsui, M. Iwasaki, H. Tada, S. Ito, *J. Mat. Sci.*, **2001**, 36, 4723 – 4729.
6. J. T. Tuaweri, G.D. Wilcox, *Surface & Coatings Technology*, **2006**, 200, 5921 - 5930.
7. L. Bousselmi, C. Fiaud, B. Tribollet, E. Triki, *Corr. Sci.*, **1997**, 39, 1711 – 1724.
8. L. Benea, O. Mitoseriu, J. Galland, F. Weniger, P. Ponthiaux, *Materials and Corrosion*, **2000**, 51, 491 - 495.
9. C. Gabrielli, *Identification of Electrochemical Processes by Frequency Response Analysis*, Monograph designed by Solartron Instrumentation Group, Ref. No. 004/**1983**.
10. B. Trachli, M. Keddou, A. Srhiri, H. Takenouti, *Corros. Sci.*, **2002**, 44, 997-1008.
11. J.J. Santana Rodriguez, C. Motesdeoca Alvarez, J.E. Gonzalez Gonzalez, *Materials and Corrosion*, **2006**, 57, 350 -356.

THE INFLUENCE OF THE HEAT TREATMENT ON THE PHOTOACTIVITY OF THE TiO₂-SiO₂ AEROGELS

A. PETER^a, I. C. POPESCU^a, E. INDREA^b, P. MARGINEAN^b
AND V. DANCIU^a

ABSTRACT. TiO₂-SiO₂ aerogels were prepared by sol-gel method followed by supercritical drying with liquid CO₂ and heat treatment. The structural and morphological particularities of the prepared TiO₂-SiO₂ aerogels were studied by means of X-ray diffraction and BET analysis. The photocatalytic activity of the TiO₂-SiO₂ aerogels was determined by monitoring the degradation rate of the salicylic acid. It was found that the efficiency of the TiO₂-SiO₂ catalyst strongly depends upon the heat treatment temperature and also on the silica content. The larger specific surface area has been achieved for the sample with the higher Si content. The heat treatment performed at 600^oC and 700^oC allowed the formation of anatase phase, as well as the meso- to micropore transformation. The TiO₂-SiO₂ (1:1 molar ratio) aerogel, heat treated at 500^oC has the highest photocatalytic activity.

KEYWORDS: TiO₂-SiO₂ aerogels, photocatalyst, sol-gel method, BET analysis, X-ray diffraction.

INTRODUCTION

TiO₂-SiO₂ binary materials have been attracting the interests of many researchers [1-8]. One of the outstanding features commonly attributed to the sol-gel processing of the multicomponent materials is the high degree of homogeneity at molecular scale. One of the most studied systems was TiO₂-SiO₂, especially because glasses of this system have a low thermal expansion coefficient and aerogels can be used as photocatalysts [9]. The photocatalytic activity of TiO₂-SiO₂ aerogels is due to their larger specific surface areas and higher porosities in comparison with conventional TiO₂-SiO₂. These solids combine the mechanical properties of silica with the chemical and catalytic properties of titania.

Anderson and Bard [10, 11] have demonstrated that a mixed oxide of TiO₂ and SiO₂ produced by a sol-gel method was a more efficient photocatalyst for the photodecomposition of rhodamine-6G than TiO₂ alone. The increase in efficiency was attributed to the presence of SiO₂ as adsorbent, which enhances the concentration of the organic material near to the TiO₂ sites.

^a Babes-Bolyai University, Faculty of Chemistry and Chemical Engineering, 400028, Cluj-Napoca, Romania

^b National Institute for Research and Development of Isotopic and Molecular Technologies, 400293 Cluj-Napoca, Romania

The heat treatment temperature influences the structure of the TiO_2 - SiO_2 aerogels and also their photoactivity. Annealing at 500-600°C determines the anatase phase obtaining, the structure of TiO_2 with the most intense photocatalytic activity. The aerogels annealed at temperatures above 700°C contain rutil phase, which doesn't manifest photoactivity [12]. In contrast, Choi and coworkers [13] obtained TiO_2 - SiO_2 aerogels which remain amorphous even after heat treatment at 1000°C. This behavior is explained by the small amount and very good dispersion of TiO_2 (Si :Ti = 1:0.05 molar ratio) into SiO_2 network.

In this work, we prepared TiO_2 - SiO_2 aerogels with different contents of Ti and Si, which are subsequently heat treated at different temperatures. Our interest was also focused on determining the photocatalytic activity of the prepared samples and on finding the role played by both the SiO_2 presence, besides TiO_2 , and the heat treatment effect on the salicylic acid photodegradation rate. The photocatalytic activity of the as prepared aerogels in the salicylic acid decomposition process is influenced by the Si content and also by the heat treatment temperature.

EXPERIMENTAL PART

The sols were prepared from Ti(IV) isopropoxide (Merck), tetramethoxysilane (Merck), anhydrous ethanol (Fluka), water and nitric acid reagent (Aldrich). The molar ratio of reactants was: $[\text{Ti}/\text{Si}]:[\text{H}_2\text{O}] = 1:3.5$, $[\text{Ti}/\text{Si}]:[\text{C}_2\text{H}_5\text{OH}] = 1:23.33$, $[\text{Ti}/\text{Si}]:[\text{HNO}_3] = 1:0.08$.

The as prepared gels were kept for 4 weeks in closed vessels and than were dried using supercritical CO_2 in a SAMDRI – 790 A (Tousimis) critical point dryer. Annealing, at 500°C, 600°C and 700°C for 2 h was performed to obtain crystalline phases of TiO_2 and to remove residues of organic substances.

The X-ray diffraction patterns were obtained using a standard BRUKER D8 Advance X-Ray Diffractometer, working at 45 kV and 30mA. The Cu K_α radiation, Ni filtered, was collimated with Soller slits. The data of the X-ray diffraction patterns were collected in a step-scanning mode with $\Delta 2\theta = 0.02^\circ$ steps. Pure silicon powder standard sample was used to correct the data for instrumental broadening.

The X-ray diffraction patterns were obtained also by using a standard DRON-3M powder diffractometer, working at 35 kV and 25 mA, and equipped with scintillation counter with single channel pulse height discriminator counting circuitry. The Co K_α ($\lambda_{\text{CuK}} = 1.54178 \text{ \AA}$) radiation, Fe filtered, was collimated with Soller slits. The data of the X-ray diffraction patterns were collected in a step-scanning mode with $\Delta 2\theta = 0.05^\circ$ steps and then transferred to a PC for processing.

The specific surface area of the as prepared samples was determined using Brunauer-Emmett-Teller (BET) method, in a partial pressure range of $0.05 < P/P_0 < 0.3$. Krypton adsorption was carried out at 77 K. Before each measurement, the samples were heat-cleaned at 333 K for 2h.

Studies of photocatalytic activity of the TiO₂-SiO₂ aerogels were performed measuring the degradation rate of salicylic acid. The decrease in time of the salicylic acid concentration ($C_0 = 3,38 \times 10^{-4}$ M) was measured by spectrophotometry ($\lambda = 297$ nm). The aerogels immersed in salicylic acid solution were irradiated with UV light. The experimental setup contains: a medium pressure Hg lamp (500 W) as UV source; polyethylene photochemical 8 ml capacity cell with quartz window ($S=12$ cm²); working temperature: 20-22°C, solution pH = 5.3. Before UV irradiation as well as before spectrophotometric measurements, the cell with the sample was kept in dark for 15 minutes in order to achieve the equilibrium of the adsorption-desorption process.

RESULTS AND DISCUSSION

In table 1 are presented the Ti composition, the specific surface area and the salicylic acid photodecomposition apparent rate constants of the TiO₂-SiO₂ aerogels.

The specific BET surface area decreases with heat treatment temperature, due to the meso- to micropores transformation. For aerogels heat treated at 500°C, the specific BET surface area increases with Si content. This behavior can be explained by the high porosity of silica. The salicylic acid photodecomposition apparent rate constants decreased with heat treatment temperature, with exception of A1 sample. On this aerogel type, thermal treated at 500°C, the rate constant is much smaller than the one obtained for the aerogels heat treated at 600 and 700°C. This behavior could be explained by the amorphous structure of this sample.

In figure 1 are presented the X-ray diffraction patterns obtained using Co radiation and Fe filter, of the aerogels heat treated at 600 and 700°C. The greater rate constant value observed for the A1 (600) sample is due to the formation of the anatase phase (figure 1), which has photocatalytic activity [14]. The very small rate constant value of the A1 (700) sample is mainly caused by the change in the structure from meso- to micropores. The microporous structure inhibits the diffusion of various gaseous reactants and products during photocatalytic reaction, and those decrease the photocatalytic activity.

Table 1.

The Ti molar percentage content of the TiO₂-SiO₂ aerogels, the specific surface area and the salicylic acid photodecomposition apparent rate constants

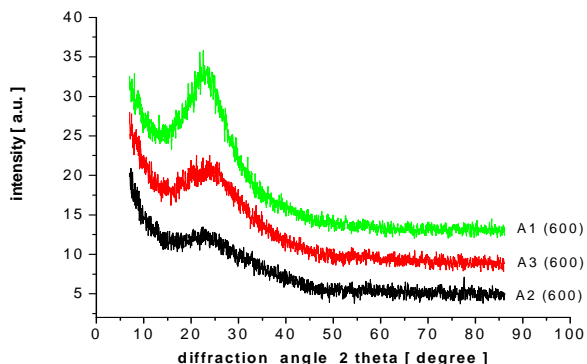
	Sample cod	Sample type	Ti [% mol.]	S_{BET} [m²/g]	k_{app} × 10⁻³ [min⁻¹]
Sample A 1	A 1 (500)	TiO ₂ -SiO ₂ heat treated for 2 h, at 500 ⁰ C	75	62	0.3481
	A 1 (600)	TiO ₂ -SiO ₂ heat treated for 2 h, at 600 ⁰ C	75	52	1.13
	A 1 (700)	TiO ₂ -SiO ₂ heat treated for 2 h, at 700 ⁰ C	75	44	0.2152
Sample A 2	A 2 (500)	TiO ₂ -SiO ₂ heat treated for 2 h, at 500 ⁰ C	50	384	3.97
	A 2 (600)	TiO ₂ -SiO ₂ heat treated for 2 h, at 600 ⁰ C	50	327	1.65
	A 2 (700)	TiO ₂ -SiO ₂ heat treated for 2 h, at 700 ⁰ C	50	273	1.42
Sample A 3	A 3 (500)	TiO ₂ -SiO ₂ heat treated for 2 h, at 500 ⁰ C	25	457	2.34
	A 3 (600)	TiO ₂ -SiO ₂ heat treated for 2 h, at 600 ⁰ C	25	293	1.71
	A 3 (700)	TiO ₂ -SiO ₂ heat treated for 2 h, at 700 ⁰ C	25	265	1.38

It can be observed (figure 1 a, b) that the A1 samples presents the highest peak, fact that indicates a greater local ordination degree. This could be explained by the present of the highest content of Ti (75%), which promotes the crystalline phase formation.

In figure 2 are presented the X-ray diffraction patterns realized with Cu radiation and Ni filter, of the A1 sample heat treated at 500⁰, 600⁰ and 700⁰C. The X-ray diffraction patterns of the A1(500) sample is typical for an amorphous titania structure. The X-ray diffraction pattern of the A1 (600) sample presents a very large X-ray diffraction line at 2θ = 25.30 degree, typical for the most intense anatase (101) diffraction line, indicating the beginning of the crystallization of the anatase structure. This crystallization process is continued for the A1(700) sample but, at this temperature, a new TiO₂-SiO₂

crystallized system has been formed. The presence of a new TiO₂-SiO₂ crystallized system is indicated by the existence of a large X-ray diffraction maxima that is situated at $2\theta = 22.30$ degree in the diffraction pattern [15-19].

a)



b)

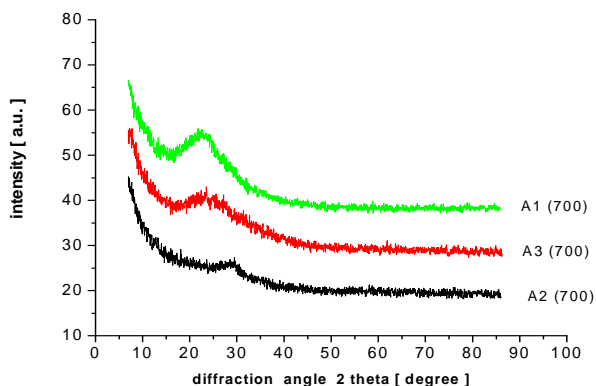


Figure 1. X-ray diffraction patterns of the TiO₂-SiO₂ aerogels heat treated at (a) 600°C and (b) 700°C, Co K_α ($\lambda_{CuK} = 1.54178 \text{ \AA}$) radiation, Fe filter.

The microstructural parameters of the A1 samples after heating at 600°C and 700°C showed an average size of $D_{eff} = 25 \text{ \AA}$ for the TiO₂ nanocrystallites and a large value of the lattice microstrain $\langle \epsilon^2 \rangle^{1/2} (L) = 5\div 6 \times$ that suggests an important TiO₂ – Si intercrystallites interaction

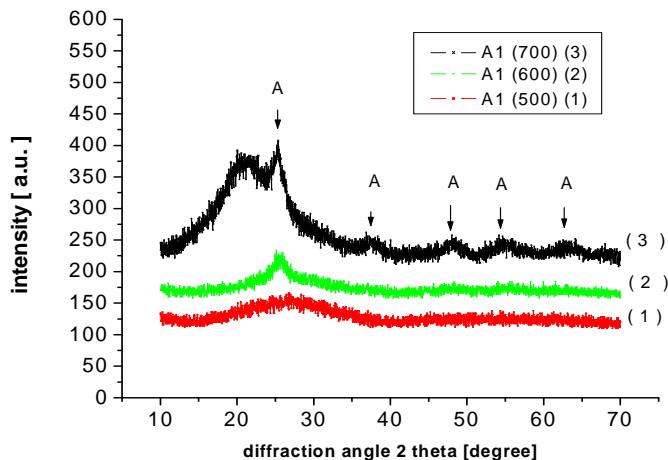


Figure 2. X-ray diffraction pattern for the samples A 1, heat treated at 500⁰, 600⁰ and 700⁰C, Cu K_α radiation, Ni filter.

The new TiO₂-SiO₂ crystallized system formed after heat treatment at 700⁰C of the sample A1 has the lowest photocatalytic activity. In contrast, the salicylic acid decomposition rate constant of the A1(600) sample was for three times greater than for the A1(500) sample (Table 1), due to the anatase formed after heat treatment at 600⁰C.

CONCLUSIONS

In this work, we prepared TiO₂-SiO₂ aerogels with different contents of Si, which are subsequently heat treated at different temperatures. The morpho-structure of the as obtained silica – titania aerogels was studied by X-ray diffraction and specific surface area measurements. The photocatalytic activity of the SiO₂-TiO₂ aerogels was determined by measuring the degradation rate of the salicylic acid used as reference organic material. The anatase phase is formed after heat treatment at 600⁰C in case of A1 aerogels, which forms a new TiO₂-SiO₂ crystallized system after heat treatment at the 700⁰C. This new crystallized system manifests low photocatalytic activity. The larger specific surface area has been determined for the sample A3 (500) with the higher Si content. The heat treatment performed at 600⁰C and 700⁰C allowed the formation of anatase phase, as well as the meso- to micropore transformation. The TiO₂-SiO₂ (1:1 molar ratio) aerogel, heat treated at 500⁰C has the highest photocatalytic activity.

REFERENCES

1. J.K. Walters, J.S. Rigden, P.J. Dirken, M.E. Smith, W.S. Howells, and R.J. Newport, *Chem. Phys. Lett.*, **1997**, 264, 539.
2. H. Yamashita, S. Kawasaki, Y. Ichihara, M. Harada, M. Takeuchi, M. Anpo, G. Stewart, M.A. Fox, C. Louis, and M. Che, *J. Phys. Chem. B*, **1998**, 102, 5870.
3. K. Kosuge and P.S. Singh, *J. Phys. Chem. B*, **1999**, 103, 3563.
4. M. Hori and M. Toki, *J. Sol-Gel Sci. Technol.*, **2000**, 19, 349.
5. M. Jung, *J. Sol-Gel Sci. Technol.*, **2000**, 19, 563.
6. W. Que, Y. Zhou, Y.L. Lam, Y. C. Chan, Z. Sun, S.D. Chen, H.P. Li, and C.H. Kam, *J. Mater. Sci. Lett.*, **2000**, 19, 1247.
7. W. Que, Z. Sun, Y.L. Lam, Y.C. Chan, and C.H. Kam, *J. Phys. D: Appl. Phys.*, **2001**, 34, 471.
8. J.E. Goncalves, S.C. Castro, A.Y. Ramos, M.C.M. Alves, and Y. Gushikem, *J. Elec. Spec.*, **2001**, 114–116, 307.
9. L. Esquivias, M. Ramirez del Solar, *J. of Non-Cryst. Solids*, 220, 1997, 45-51
10. C. Anderson, A.J. Bart, *J. Phys. Chem. B*, **1997**, 101, 2611.
11. C. Anderson, A.J. Bart, *J. Phys. Chem. B*, **1995**, 99.
12. L. Baia, M. Baia, A. Peter, V. Cosoveanu, V. Danciu, *J. Opt. and Adv. Mat.*, **2007**, 9(3), 668
13. S.S. Choi, *J. of Sol-Gel Science and Technology*, **2004**, 30, 215-221.
14. J. Yu, J. C. Yu, W. Ho, Z. Jiang, *New J. Chem.*, **2002**, 26, 607-613.
15. P. McMillan, *American Mineralogist*, **1984**, 69, 622.
16. J.G.M. van Bercum, A.C. Vermeulen, R. Delhez, T.H. de Keijser and E.M. Mittemeijer, *J. Appl. Phys.*, **1994**, 27, 345.
17. E. Indrea and Adriana Barbu, *Appl. Surf. Sci.*, **1996**, 106, 498.
18. N. Aldea and E. Indrea, *Comput. Phys. Commun.*, **1990**, 60, 155.
19. W. Kraus, and G. Nolze, G. "PowderCell for Windows", Version 2.3, Federal Institute for Materials Research and Testing, Berlin, Germany, **1999**.

OXIDATION OF DL-METHIONINE (2-AMINO-4-METHYLTHIOBUTANOIC ACID) BY CHROMATE. MECHANISTIC INTERPRETATION ON THE BASE OF AN ONE-PLUS RATE EQUATION

ALEXANDRA CSAVDARI*, IOAN BALDEA AND DANA-MARIA SABOU

ABSTRACT. The “one-plus” rate equation is an useful tool for interpreting reaction mechanisms. The kinetic study of the oxidation of 2-amino-4-methylthiobutanoic acid (methionine) by chromate has been undertaken. The reaction obeys a “one-plus” rate law. In order to suggest a reaction mechanism, the interference of kinetic along with extra-kinetic proofs was taken into consideration. The reaction starts with a pre-equilibrium to form an intermediate from the substrate and the reactant. This step is followed by the rate determining electron-transfer process. The influence of the organic substrate and hydrogen ion concentrations was deduced from the kinetic data.

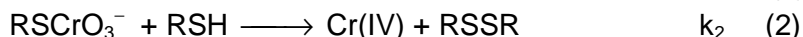
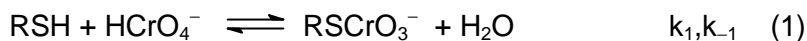
Keywords: one-plus rate law, chromate, methionine, reaction mechanism

Introduction

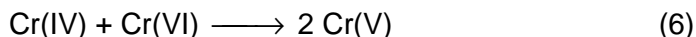
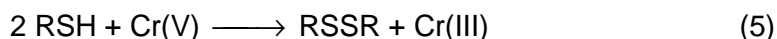
Each kinetic study implies the measurement of reaction rates as well as the compilation of an *empirical power-law rate equation* from extensive experimental results over a wide range of conditions. Most reactions of practical interest are multistep processes and therefore do not proceed by simple pathways. They do not obey always power-law rate equations and thus have no exact and constant reaction orders¹⁻⁵. Hence, a traditional power-law with empirical fractional exponents cannot be expected to result from combinations of elementary steps. In contrast, “one-plus” rate equations may result from step combinations; they contain integer exponents and are therefore more likely to reflect the true mechanism¹. Therefore, the phenomenological rate coefficients are combinations of those of the elementary steps involved in the network¹⁻⁵.

An example (see equations 1 to 7), based on literature survey as well as on experimental studies of our group, concerns the oxidation of inorganic and organic thio-derivatives by chromate⁶⁻¹². A general mechanism for the reaction of chromium(VI) with thiols involves the formation of a chromium(VI)-thioester (reaction step 1) followed either by the redox decomposition of this intermediate (an uni-equivalent step – see process 3) or its redox reaction with a second molecule of thiocompound (a bi-equivalent step – see process 2):

* Babeș-Bolyai University, Faculty of Chemistry and Chemical Engineering, 11 Arany Janos Street, Cluj-Napoca, 400028, Romania. e-mail: acsavidari@chem.ubbcluj.ro



These are followed by several potentially fast steps:



These processes were assumed on the base of extra-kinetic proofs (free-radical and Cr(V) identification)⁶⁻⁸ as well as to justify the reaction stoichiometry. Cr(V) seems to be a tetra-coordinated (or even a penta- or hexa-coordinated) species, that is a hypochromic acid reacting likewise to Cr(VI). On the other hand, Cr(IV) is a labile hexa-coordinated compound^{13,14}. When the thioester is formed rapidly and in significant concentration in the pre-equilibrium (1) than: $[\text{RSCrO}_3^-]/[\text{Cr}^{\text{VI}}]_t = K[\text{RSH}]/(1 + K[\text{RSH}])$, where $K = k_1/k_{-1}$. Hence, the overall rate law will be of the "one-plus" form below:

$$-\frac{d[\text{Cr}^{\text{VI}}]}{dt} = \frac{k_2 K [\text{RSH}]^2 + k_3 K [\text{RSCrO}_3^-]}{1 + K [\text{RSH}]} [\text{Cr}^{\text{VI}}] \quad (8)$$

It has two limiting forms corresponding to the cases when either the second-order (k_2) or the first-order (k_3) process prevails. In such cases substantial spectral evidence has been found to support the assumption of the thioester formation⁵⁻¹². The latter situation has been found in the case of benzene-thiol and α -toluenethiol oxidation in acetic acid¹¹. Here the uniequivalent step prevails, yet the rate law is still of the "one-plus" form:

$$-\frac{d[\text{Cr}^{\text{VI}}]}{dt} = \frac{k_3 K [\text{RSH}]}{1 + K [\text{RSH}]} [\text{Cr}^{\text{VI}}] \quad (9)$$

In the case of S-methylcysteine or other disulphides, the bi-equivalent oxidation yields sulfoxide and the rate law is also of the form (8)¹⁵⁻¹⁶.

EXPERIMENTAL

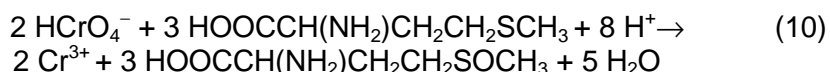
Employed chemicals were of guaranteed reagent grade purity, purchased from commercial sources (*Merck, Aldrich, Fluka* and *Reanal*) and used without further purification. All solutions were prepared in demineralised and tetra-distilled water.

The advance of the reaction was followed by spectrophotometrical means at 350 nm, a wavelength at which the oxidizing agent exhibits a characteristic absorption band in acidic solutions. A Jasco V-530 spectrophotometer (Japan) with a controlled-temperature cell holder as well as computerised kinetic data acquisition has been used. The reaction was initiated directly in the measurement cell by injecting the chromate solution over a mixture of the other reactants. Absorbance was recorded as a function of reaction time. The acidity and ionic strength were maintained constant by means of HClO₄ excess and NaClO₄, respectively. The temperature was controlled by means of a Lauda M-20 circulation bath. Other experimental details are also presented elsewhere¹⁷. At least three replicate runs were performed for each set of experimental conditions.

RESULTS AND DISCUSSION

The stoichiometry of the reaction was established by colorimetric measurements. Various reaction mixtures in acidic media, having increasing molar ratios, were allowed to react to completion (for at least 10 half times) and the remaining absorbance due to unreacted chromate was recorded at 350 nm. At excess concentration of methionine, larger than 1.5 times that of Cr(VI), the entire amount of the oxidising agent Cr(VI) is completely consumed and residual absorbencies remain small and constant. This fact suggests that the oxidised product is the corresponding sulfoxide. Even with strong oxidizing agents as peroxyanions (peroxydisulfate and peroxydihosphate), the oxidation product was sulfoxide in the case of alkyl aryl sulphide¹⁸ or diphenylsulfide¹⁹.

Hence, we concluded that Cr(VI) and methionine react by a ratio of 1/1.5, so that we assumed the following overall reaction:



Kinetic experiments were carried out at various concentrations of methionine (always in large excess), at constant acidity as well as at various HClO₄ concentrations and constant excess of methionine. These conditions ensure pseudo-first order rate laws with respect to the coloured species. Therefore, plots of $\ln(A - A_\infty)$ vs reaction time were linear over a large degree of reaction extent with very good correlation coefficients (0.9935 - 0.9999). A_∞ stands for the remaining absorbance at completion. Both the linearity of the plots and the identical first-order rate constants we have obtained with three different initial chromate concentrations (as limiting reagent) confirm the first-order dependence with respect to the oxidizing coloured species.

The apparent first-order rate coefficient (k_{obs}) depends upon the substrate and mineral acid concentration. By increasing the concentration

of the substrate, increased first-order rate constants were measured as the slopes of semi-logarithmic plots (see results in Table 1). By plotting $\lg k_{obs}$ vs $\lg [\text{Meth}]$ to determine the reaction order with respect to methionine, a line ($R = 0.9914$) with a slope of 0.85 was found. This fractional order can be rationalised by the following rate equation (similar to 9):

$$-\frac{d[\text{Cr}^{\text{VI}}]}{dt} = \frac{k'[\text{Meth}]}{1 + k''[\text{Meth}]}[\text{HCrO}_4^-] \quad (11)$$

Table 1.

First-order rate constants as a function of methionine concentration at $298 \pm 0.1\text{K}$, $\mu = 0.34$, $[\text{HCrO}_4^-] = 1.00 \times 10^{-4}$ and $[\text{HClO}_4] = 8.50 \times 10^{-2}$ and as a function of the acid concentration at $[\text{Meth}] = 7.50 \times 10^{-2}$, respectively. Each listed value is the mean of three replicate runs.

$10^2[\text{Meth}]$	$10^3 k_{obs} (\text{s}^{-1})$	$[\text{H}^+]$	$10^3 k_{obs} (\text{s}^{-1})$
0.38	0.76	0.042	0.59
0.56	1.12	0.085	1.23
0.75	1.23	0.128	1.69
0.94	1.83	0.170	3.11
1.13	2.02	0.191	3.45
1.50	2.31	0.213	3.73
1.88	2.97	0.255	4.73
2.25	3.57	0.298	6.62
2.50	3.75		

Rate equation (11) is similar to equation (9) that is of the “one-plus” form. If a linearization of the type (4) is used with all the data, such as follows,

$$\frac{1}{k_{obs}} = \frac{k''}{k'} + \frac{1}{k'} \frac{1}{[\text{Meth}]} ; \quad \frac{1}{k_{obs}} = (90 \pm 16) + (4.7 \pm 0.2) \frac{1}{[\text{Meth}]} \quad (12)$$

a good fit has been obtained ($R = 0.9917$). On the other hand, the reaction order with respect to hydrogen ions is of 1.22 ($R = 0.9908$). It may be interpreted in two ways: either by a parabolic dependence corresponding to two parallel reaction paths in which one is of first-order and the other of second-order with respect of $[\text{H}^+]$ (see equation 13a), or by a dependence of the “one-plus” form (13b):

$$(a) k_{obs} = a[\text{H}^+] + b[\text{H}^+]^2 ; \quad (b) k_{obs} = \frac{c[\text{H}^+]^2}{1 + d[\text{H}^+]} \quad (13)$$

Where a, b, c and d stand for some constants. If the first alternative were true, than, according to the linear form of equation (13a) $k_{obs}/[\text{H}^+] = a + b[\text{H}^+]$, the plot $k_{obs}/[\text{H}^+]$ vs $[\text{H}^+]$ should result in line with

good correlation coefficients. The results were: $a = 12.1 \text{ L mole}^{-1}\text{s}^{-1}$, $b = 29.2 \text{ L}^2 \text{ mole}^{-2}\text{s}^{-1}$ and $R = 0.8360$. This correlation coefficient is quite poor. On the other hand, the second alternative can be proved by its linear form that gave a better fit ($R = 0.9536$):

$$\frac{[\text{H}^+]^2}{k_{\text{obs}}} = \frac{1}{c} + \frac{d}{c}[\text{H}^+] \quad \frac{[\text{H}^+]^2}{k_{\text{obs}}} = (2.6 \pm 0.5) + (42 \pm 3)[\text{H}^+] \quad (14)$$

The intercept $1/c$ (see equation 14) is expressed in $\text{L}^2\text{mole}^{-2}\text{s}$ and the slope d/c in $\text{L}^3\text{mole}^{-3}\text{s}$, respectively. Therefore, we assume that the second alternative describes adequately the involvement of the hydrogen ion concentration. By taking into consideration both the influences of methionine and hydrogen ion concentrations, two rate laws may be written: one that contains separate terms for $[\text{Meth}]$ and $[\text{H}^+]$ (see equation 15) and another that depends on the product $[\text{Meth}][\text{H}^+]$ (see equation 16):

$$-\frac{d[\text{Cr}^{\text{VI}}]}{dt} = \frac{k_a [\text{Meth}][\text{H}^+]^2 [\text{HCrO}_4^-]}{1 + k_b [\text{Meth}] + k_c [\text{H}^+]} \quad (15)$$

$$-\frac{d[\text{Cr}^{\text{VI}}]}{dt} = \frac{k_a' [\text{Meth}][\text{H}^+]^2 [\text{HCrO}_4^-]}{1 + k_b' [\text{Meth}][\text{H}^+]} \quad (16)$$

Rate law (15) would correspond to two independent pre-equilibria, while rate law (16) to two coupled equilibria or an overall equilibrium involving chromate, methionine as well as the hydrogen ion. The apparent first-order rate coefficient in equations (15) and (16) can be transposed into linear forms by taking the reciprocals and should therefore hold with both series of measurements. If the linear form of the apparent first-order rate coefficient of law (15) is considered while either $[\text{Meth}]$ or $[\text{H}^+]$ are held at constant values, the plots do not fit a line although the reproducibility of the experiments is quite good. This is true especially when $[\text{H}^+]/k_{\text{obs}}$ is plotted as a function of $1/[\text{H}^+]$. On the other hand, if we assumed that a coupled equilibria takes place, the linear form of k_{obs} as expressed from rate law (16) – see equations (17) – has a good correlation coefficient of 0.9917. Figure 1 presents the plot of equation (17) and proves the statement above.

$$\frac{[\text{H}^+]}{k_{\text{obs}}} = \frac{k_b'}{k_a'} + \frac{1}{k_a'} \frac{1}{[\text{Meth}][\text{H}^+]}; \quad \frac{[\text{H}^+]}{k_{\text{obs}}} = (7.6 \pm 1.3) + \frac{(3.4 \pm 0.1)10^{-2}}{[\text{Meth}][\text{H}^+]} \quad (17)$$

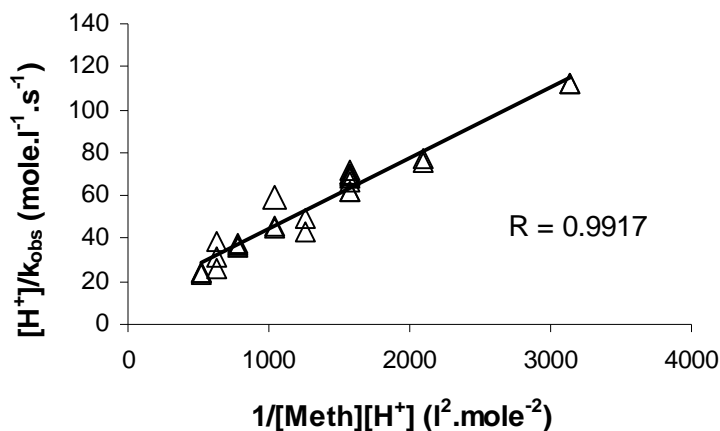


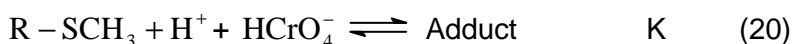
Figure 1. The plot of equation (17) with data presented in table 1.

An attempt to use this reaction system to initiate polymerization of ethylacrylate failed. This fact suggests that the reaction mechanism does not involve free radicals.

In view of the above discussion, the reaction scheme for the Cr(VI) oxidation of methionine involves the formation of an adduct by hydrogen ion. The adduct further suffers the electron and atom redistribution to yield sulfoxide and Cr(IV) during the rate determining step. This step also occurs with the assistance of hydrogen ions. Either the chromate acid or a conjugated acid of methionine will further react with the partner to form the intermediate adduct. No discrimination by kinetic experiments is possible between the two alternative pre-equilibria (18) and (19):



The two coupled equilibria can be written as an overall one with $K = K_1' K_2'$ (or $K_1'' K_2''$):



This will be followed by the electron transfer and the S=O double bond formation in the rate determining step:



The process continues by potentially rapid steps of the type (6) and (7). With other words, Cr(V) may be obtained. It can also oxidize methionine to the corresponding sulfoxide.

The rate law deduced from this reaction scheme - by using the pre-equilibrium assumption - is of the form (16) in which $k'_a = kK = (29.4 \pm 0.8) \text{ L}^3 \text{ mol}^{-3} \text{ s}^{-1}$ and $k'_b = K = (2.24 \pm 0.45) \cdot 10^2 \text{ L}^2 \text{ mole}^{-2}$. A second-order rate constant $k = (1.31 \pm 0.23) \cdot 10^{-1} \text{ L mole}^{-1} \text{ s}^{-1}$ for the rate determining step was computed under the employed experimental conditions.

CONCLUSIONS

The experimental kinetic data obey a typical "one-plus" rate law, with integer exponents. A pre-equilibrium involving the oxidant and the organic substrate is present. The bi-equivalent electron-transfer is the rate-determining step. In acidic media, the involvement of hydrogen ion favours the redox reaction. Phenomenological rate coefficients and some intermediate formation constants could be calculated. The data fit well with the rate law expressed from the proposed reaction scheme, thus supporting the suggested mechanism.

REFERENCES

1. F. P. Helfferlch, *Kinetics of multistep reactions*, 2-nd Ed., in *Comprehensive Chemical Kinetics*, Vol 40, N.J.B. Green, Elsevier, Amsterdam, 2004, p.53-159; 178-206.
2. R. G. Wilkins, *The study of kinetics and mechanism of reactions of transition metal complexes*, Allyn and Bacon Inc., Boston, 1974, p.60-117
3. J. H. Espenson *Chemical kinetics and reaction mechanisms*, McGraw-Hill Book Co., New-York, 1981, p. 89-115
4. J. W. Moore and R. G. Pearson, *Kinetics and Mechanisms*, 3-rd Ed., J. Wiley and Sons, New-York, 1981, p.192-283
5. I. Baldea, *Cinetica chimica si mecanisme de reactie. Baze teoretice si aplicatii*, Presa Univ. Clujeana, Cluj-Napoca, 2002, p. 358-379
6. I. Baldea, G. Niac, *Inorg. Chem.* 9 (1970) 110
7. P. H. Connert, K. E. Wetterhahn, *J. Am. Chem. Soc.* 107 (1985) 4282
8. D. A. Dixon, T. P. Dasgupta and N P. Sadler, *Inorg. Reaction Mech.*, 1 (1998) 41; D. C. Ramdon, D. A. Dixon, and T. P. Dasgupta, *Inorg. Reaction Mech.*, 5 (2005)
9. I. Baldea, G. Niac, *Studia Univ Babeş-Bolyai, Chem.* 31(2) (1986) 41
10. Baldea, *Studia Univ Babeş-Bolyai, Chem.* 33(2) (1987) 42
11. I. Baldea and Dana M. Sabou, *Rev. Roum. Chim.* 45 (2000) 537

12. Dana M. Sabou, I. Baldea, *Studia Univ. Babeş-Bolyai, Chem.* 45(1,2) (2001) 17
13. J. H. Espenson, *Accounts Chem. Rev.* 3 (1970) 347; A. Levina, L. Zhang, P. A. Lay, *Inorg. Chem.* 42 (2003) 767 and reference therein.
14. E. Huss, W. Klem, *Angew. Chem.* 66 (1954) 468; K.A. Wilhelm, O. Jonsson, E. Lagerwall, *Acta Chem. Scand.* 23 (1969) 1074
15. I. Baldea, Dana M. Sabou, Alexandra Csavdari, *Studia Univ. Babeş-Bolyai, Chem.* 52(1) (2007) 19
16. I. Baldea, Dana M. Sabou and Alexandra Csavdari. *Rev Chim* to be published.
17. Alexandra Rustoiu–Csavdari, D. Mihai, I. Baldea, *Anal. Bioanal. Chem.* 381 (2005) 1373; Gabriela C. Bucşa,
18. I. Baldea, *Studia Univ. Babeş-Bolyai, Chem.* 50(1) (2005) 157
19. N. Arumugam, C. Srinivasan, P. Kuthalingam, *Indian J. Chem.* 16A (1978) 478; C. Srinivasan, P. Kuthalingam,
20. Arumugam, *Can. J. Chem.* 56 (1978) 3043; *idem*, *J. Chem. Soc. Perkin Trans. 2*, (1980) 170; C. Srinivasan, P.
21. Kuthalingam, N. Arumugam, *Int. J. Chem. Kinet.* 14 (1982) 1139.
22. D. Kolp, H C. Thomas, *J. Am. Chem. Soc.* 71 (1949) 3047; G. Calvaruso, F. P. Cavalino, C. Sbrizlolo, *Int. J. Chem. Kinet.* 13 (1981) 135; V. K. Grover, S. K. Mishra, Y. K.
23. Gupta, *J. Inorg. Nucl. Chem.* 32 (1970) 267

LOW CARBON STEELS CORROSION IN DIFFERENT AGGRESSIVE MEDIA

ELEONORA MARIA RUS*, I. BÂLDEA*, C. CĂLIN**

ABSTRACT. Electrochemical methods have been used to obtain details on the corrosion behaviour of the following carbon steels:OLT – 35, OL 37, OL 44, OL 60 in different electrolytic environments (neutral aqueous solutions, salty, swamp and normal soils). Corrosion parameters of electrochemical reactions at the steel/environment interface as: corrosion potential (E_{corr}) and current density (i_{corr}), was determined using steady state polarization curves method. The results were compared with corrosion rates values obtained by gravimetric measurements. OLT 35 carbon steel was found as the most corroded related to the other studied steels.

Keywords: carbon steel, underground electrochemical corrosion, soil, polarization curves.

1. INTRODUCTION

The corrosion process is quite complexes and depends on the alloy nature and the corrosion environment. From a practical point of view, the underground corrosion of metallic networks is wary important, especially in the presence of the dispersion currents. The simultaneously action of corrosion environment and the dispersion currents bring about much damage on the underground networks [1- 4]. The underground corrosion is the determining factor on the life service of the pipe system. The soil where the pipes are buried has numerous corrosion agents as the oxygen dissolved in water, acid or basic compounds, salts, microorganisms and stray currents [5-6]. The aggressivity of the environment is much enhanced in the soil of the industrialized cyties, where the corrosion processes take place either electrochemically or electrolytically due to stray currents. In the neutral media the corrosion takes place mainly by depolarization with dissolved oxygen.

In order to study the corrosion of gas buried pipes we have taken advantage of recoding the open circuit potential, E_{OCP} .

Low carbon steels OLT-35, that is used at medium and low pressure (up to 60Kgf/cm²) [7-8], has been undertaken for corrosion study and compared with other carbon steels for general usage as OL-37, OL-44, and OL-60.

* Babeș-Bolyai University, Faculty of Chemistry and Chemical Engineering, 11 Arany. Janos St. Cluj-Napoca,400024, Romania, e-mail norus@chem.ubbcluj.ro

** S.C.Distrigaz-Nord S.A. Tg-Mures, ROMANIA

2. EXPERIMENTAL

The chemical composition of the studied steels is given in Table1. Eprouvettes of cylindrical or paralelipipedic forms having the aria of 1 cm^2 were obtain from carbon steel sorts in the study and used in the corrosion experiments. Before tested, the samples were carefully cleaned mechanically and chemically [9-10]. Various soils, where the gas pipes are buried, as well as salts solutions to simulate natural conditions were employed as electrolytes [11-12]. Their characteristics are contained in table 2.

All potential values were measured and presented in the diagrams as compared to saturated calomel electrode ($E = 0.242 \text{ V}$ versus ENH) as reference.

Table1.

The content of various elements in the alloys

% of	OLT-35	OL-37	OL-44	OL-60
C	0.17	0.22	0.22	0.40
Si	<0.35	0.07	0.50	0.40
Mn	<0.40	0.56	0.95	0.66
P	<0.05	0.055	0.055	0.055
S	<0.05	0.055	0.055	0.055
Fe	Up to 100 %			

In order to record polarization curves, a graphite electrode (made of spectral graphite) was used as counter-electrode. The open circuit electrode potential, E_{OCP} , against time has been measured periodically. The time exposure to the corrosive environment was varied within 0 and 144 hours.

Table 2.

Some characteristics of used electrolytes

Electrolyte	Provenience	pH	Conductivity (mS)
NaCl 1.5%	Laboratory	5.5	12
NaCl 3%	Laboratory	5.5	28
NaCl 1,5% + Na ₂ SO ₄ 1,5%	Laboratory	5.5	17
Salty soil	Ocna Dej, salt mine zone	6.7	3.5
Marshy soil	Cluj-Napoca Intre Lacuri district	7.0	10.2
Normal(ordinary) soil	Cluj-Napoca rail station , zone	6.5	0.6

3. RESULTS AND DISCUSSIONS

3.1. Time change of the rest potential (open cell). As literature stipulates, an increase of negative potential in an open cell during time is

associated with metal corrosion, while its positive tendency is associated with a decrease of the corrosion rate or its inhibition by formation of a protecting oxide film at the surface. An oscillating behavior during time is rationalized by a localized corrosion, especially pitting [13].

3.1.1. The effect of chloride on E_{OCP} -time curves. Figures 1.a and b show the E_{OCP} -time diagrams of studied carbon steels in solutions with sodium chloride. For both the concentrations the corrosion process proceeds quite rapidly within the first hours of exposure. In the case of 3% NaCl solution all the samples of OLT-35, OL-37 and OL-44 suffers a steep increase of negative rest potential within the first five hours of exposure. In the case of OLT-35 steel, a change from -505 mV to -635 mV takes place. After that, the change of the potential during time is quite minor. In the case of OL-37 steel after 35 hours a new increase of negative potential is noticed. On the contrary, in the case of OL-60 steel the increase of negative potential is not as steep as for the other two within the first 5 hours of exposure and a slight shift towards positive values. This behavior can be explained by a passivation of this sort of steel.

3.1.2 The effect of sulphate ions on E_{OCP} -time curves. In 1, 5% NaCl and 1, 5% Na_2SO_4 solution a similar pattern of rest potential variation has been found. Within 5 hours an important increase of the negative values has been noticed. In the case of OLT-35 steel, the potential E_{OCP} varied from -521mV to -619mV. After that the change is almost imperceptible. In the case of OLT-35 steel, after 20 hours a slight tendency towards positive value appears (fig. 1.c).

3.1.3 The effect of salt concentration and bacteria content on the corrosion rate. The change of rest potential E_{OCP} during time of the steel samples put in the mud of various soils is presented in figure 2. Within first two hours a similar pattern of dependence was found with ordinary and marshy soil, with a steep increase of negative values. Then, the potential maintains almost constant during time (see figures 2a and 2c)

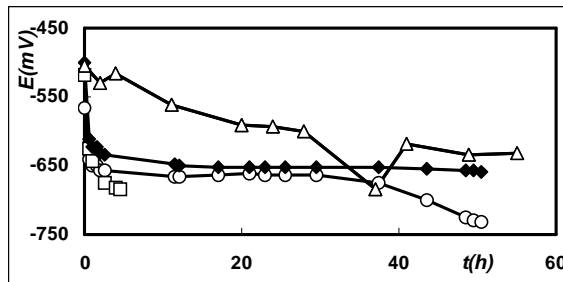
In the case of OLT-35 steel, the salty soil is more aggressive soil exhibiting a continuous increase of negative potential, more pronounced within the first three hours of exposure and a small variation after that. (Figure 2b). When the sample exposure exceeds 28 hours, the rest potential maintains constant, due to passivation. A similar behaviour was noticed with OL-37 steel. When samples were introduced into marshy soil, the negative potential varies less steeply in the beginning period of exposure. After three hours a tendency towards positive values was noticed, indicating some passivation. After 38 hours, the corrosion starts again, due to the destruction of the protective film at the surface [14]. All the sorts of steel exhibits different behaviour in the marshy soil, the passive film at the surface lasts longer than in the salty soil.

Table 3 presents the order of aggressivity of the corrosive tested media on the low carbon steels.

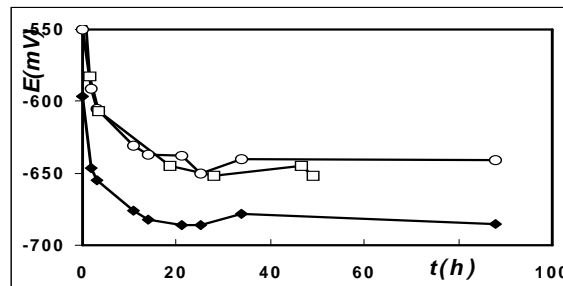
Table 3

Corrosive aggressivity order of used media

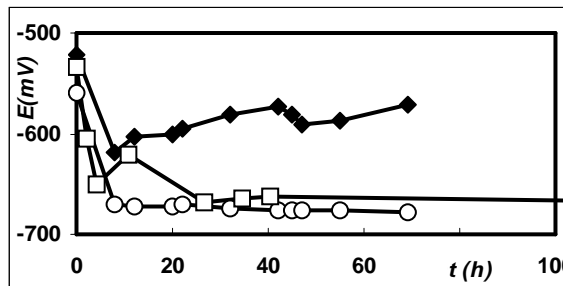
Electrolyte	aggressivity order
NaCl 1.5%	OLT-35 > OL-37 > OL-44 > OL-60
NaCl 3%	OLT-35 > OL-37 > OL-44 > OL-60
NaCl 1,5% and Na ₂ SO ₄ 1,5%	OL-44 > OL-60 > OL-37 > OLT-35
Salty soil	OLT-35 > OL-37 > OL-44 > OL-60
Marshy soil	OL-37 > OLT-35 > OL-60 > OL-44



a)



b)



c)

Fig. 1. E_{ocp} -time diagram for studied steels (---◇--- OL 37; ---□--- OL 44; ---■--- OLT 35; ---△--- OL 60) in: a) NaCl 3%, b) NaCl 1.5%, c) NaCl 1.5% + Na₂SO₄ 1.5% solutions

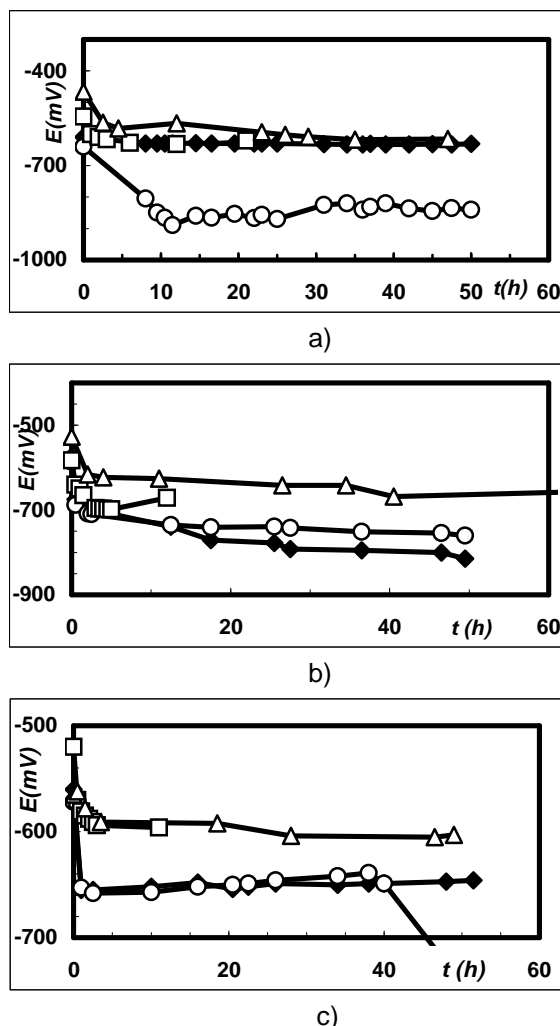


Fig. 2. E_{OCP} -time diagram for studied steels (--◇-- OL 37; --□-- OL 44 ; --■-- OLT 35; --△-- OL 60) in: a) normal(ordinary) soil; b) salty soil c) marshy soil.

3.2. Determination of kinetic parameters. The corrosion mechanism of the various electrolytic media on OLT-35 steel, aiming to determine kinetic parameters of electrochemical surface reactions (corrosion potential (E_{corr}), corrosion current density (i_{corr}) and the corrosion rate) has been obtained from polarization curves [15]. The corrosion current and potential were obtained by the extrapolation of Tafel curves. The corrosion parameters, as obtained from polarization curves are presented in table 4. The gravimetric index, V_{corr} [g/m^2h] has been calculated by means of the relationship:

$$v_{\text{corr}} = \frac{i_{\text{corr}} \cdot A}{26,8 \cdot z} \quad (1)$$

where: v_{corr} -the corrosion rate is expressed as gravimetric index, $[\text{g}/\text{m}^2\text{h}]$, i_{corr} -stands for the current density $[\text{A}/\text{m}^2]$, z - the number of electrons exchanged in the corrosion process and A stands for the atomic mass of the metal element.

Table 4.

Corrosion parameters

The alloy type	Electrolyte	ϵ_{corr} [mV]	i_{corr} [mA/m ²]	V_{corr} [g/m ² h]
OLT-35	NaCl 3%	-825	870	0.908
	NaCl 1.5%	-790	691	0.721
	Normal (ordinary) soil	-594	301	0.314
	Salty soil	-825	812	0.847
	Marshy soil	-901	933	0.974
OL-37	NaCl 3%	-771	501	0.523
	Normal(ordinary) soil	-660	295	0.307
	Salty soil	-749	805	0.840
	Marshy soil	-813	1000	1.044
OL-44	NaCl 3%	-722	512	0.534
	NaCl 1,5%	-812	436	0.455
	Normal(ordinary)soil	-455	407	0.424
	Salty soil	-800	602	0.628
	Marshy soil	-830	912	0.952
OL-60	NaCl 3%	-843	630	0.657
	NaCl 1.5%	-853	436	0.455
	Normal(ordinary) soil	-583	398	0.415
	Salty soil	-705	810	0.845
	Marshy soil	-763	1112	1.160

The polarization curves for OLT-35 steel in solution are presented in figure 3. The results presented in table 4 shows a decrease of corrosion rate of OLT-35 with the decrease of NaCl concentration and a change of potential towards positive values.

The effect on corrosion of the soils containing salt or bacteria is shown in figure 4. It can be found out that the most aggressive is the marshy soil, having a corrosion rate as much as 3.09 the ordinary soil. The salty soil brings about a

corrosion rate of 1.15 times faster than the ordinary soil. It results from the increase of the mixed corrosion potential towards its negative values.

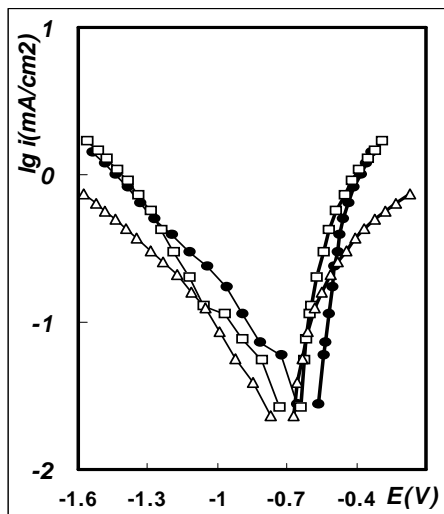


Figure 3. Polarization curves of OLT-35 in : -□- NaCl 3%; -■- NaCl 1.5%; -△- NaCl 1.5% + Na₂SO₄ 1.5% solutions.

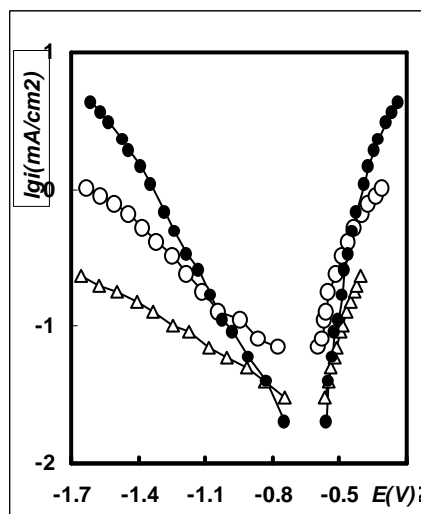


Figure 4. Polarization curves of OLT-35 -△- normal; -□- salty; -■- marshy soils.

The corrosion rate for the sample buried in salty or marshy soil is comparable or even higher than the one in 3% NaCl solution. Concerning the OLT-35 steel, the order of aggressivity is:

Marshy soil > 3% NaCl solution > salty soil > 1,5% NaCl solution > ordinary soil

From the polarization curves recorded with 3% NaCl for all the steel types undertaken in the study (figure 5) it has been found out the faster corrosion rate in the case of OLT-35.

A comparison of the corrosion rate reveals that OL-37, exhibits a value as 1.73 as the one of OLT-35 in 3% NaCl and comparable with that in the marshy soil. The OL-37 steel exhibits a corrosion rate in marshy soil as much as 1.24 as compared to salty soil, and as much as 3.9 as compared to ordinary soil. For all the steels tested, marshy soil is the most aggressive, followed by salty soil. Always when the corrosion rate decreases, the potential shifts towards positive values. Table 4 reveals also that the OL-44 steel in 3% NaCl solution has a smaller corrosion rate (1.69 times slower) as compared to OLT-35 steel. The

same behavior has been noticed with 1.5 % NaCl solution (Figure 6). The OL-60 alloy has identical corrosion pattern as OL-44 one.

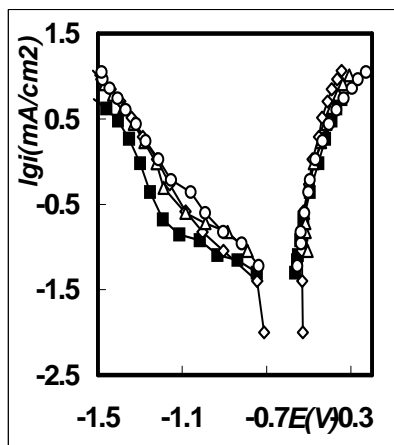


Figure 5. Polarization curves recorded in 3% NaCl solution: --■-- OLT 35; --◇-- OL 37; --□-- OL 44 ; --△-- OL 60.

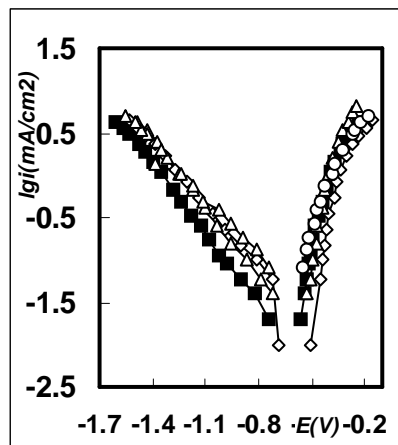


Figure 6. Polarization curves recorded in 1,5% NaCl solution: --■--OLT 35; --◇-- OL 37; --□-- OL 44 ; --△-- OL 60

CONCLUSIONS

The corrosion rate of OLT-35 steel increases as the salt concentration of the solution increases. The addition of sodium sulphate to 1.5 % NaCl solution has an enhancing effect on corrosion rate of OLT-35. Also, it transforms the generalized corrosion into a localized one during time. The localized and well defined attacks on the alloys were not noticed, the corrosion being mainly uniform with un-adherent and soluble products.

In the cases studied, the tendency of corrosion of OLT-35 is greater than the one of OL-37, with a few exceptions. This behavior is caused by the chemical composition of the two steels (larger content of C, Mn, Si, P of OL-37).

OLT-35 alloy is attacked especially in the salty or marsh soils and less in the ordinary. In the case of OL-37 the corrosion susceptibility is enhanced in marshy soil and ordinary soils.

The corrosion rate is greater when a mixture of salts was used indicating the acceleration character of sodium sulphate. In ordinary soil a smaller corrosion rate has been noticed, as corrosion potential becomes more positive. Because of the generation of corrosive substances by bacteria, all tested alloys were significantly corroded in this sort of soils, even more than the salty soils.

REFERENCES

1. I.Lingvai, N. Secreteanu, «Coroziunea retelelor de transport și distribuție a gazelor naturale», Bucuresti, Ed. ICPE Bucuresti, **2000**
2. I. Lingvai, C. Lingvai, G. Rus, L. Ancas, «Protectia anticoroziva a conductelor metalice subterane», Ed. Electra, Bucuresti, **2002**
3. H. Vermesan, „Coroziunea si protectia anticoroziva”, Ed. Risoprint, Cluj-Napoca, **2002**
4. T.Visan, M.Buda, N.Ibris, «Metode electrochimice de cercetare in electrochimie si coroziune-principii teoretice», Litografia U.P.B., **1999**
5. A.W. Peabody, M.E.Parker, "Corrosion Basics", *An Introduction*, NACE, **1984** 179-200.
6. G. Beizadea, E. Roman, *Revista de Chimie*, (34) **1983**, 350-355.
7. J.R.Scully, "Electrochemical", in *Corrosion Tests and Standards Manual*, edited by G.S. Haynes, ASM International, New York, **1993**, 75-90.
8. J.J.Lamoureaux, «Precis de corrosion», *Science des materiaux*, Ed. Masson, Beauchemin, **1987**,127-154.
9. C. Calin, E.M. Rus, I. Baldea, "Analele Universitatii din Oradea," Fascicola chimie, VIII, **2004**, 32-40.
10. C. Calin, E.M. Rus, I. Baldea, "Analele Universitatii din Oradea," Fascicola chimie, VIII, **2001**, 5-10.
11. C.Calin, I.Lingvai, Georgeta Rus, I.Baldea, Eleonora Maria Rus, "Study on corrosion behaviour of carbon steel in salted media", *The 1st International Corrosion Conference-Study and Control of Corrosion in the Perspective of Sustainable Development of Urban Distribution Grid*, Constanta, June 6-8, **2002**, 96-101.
12. C. Calin, I. Baldea, I.Lingvai, E.M. Rus, G. Rus, "Corrosion behaviour of OLT 35 steel in neutral soils," *The 15th International Corrosion Congress-Frontiers in Corrosion Science and Technology*, September, 15-21, Granada, Spain **2002**, CD
13. C. Calin, I. Baldea, E. M. Rus," Steel corrosion and its control in neutral media", *The 2nd International Corrosion Conference-Study and Control of Corrosion in the Perspective of Sustainable Development of Urban Distribution Grid*, M. Ciuc, june 19-21, **2003**,138-144.
14. C. Calin, I. Baldea, E.M. Rus, "Annals of West University of Timisoara", *Series Chemistry*, 12(3), **2003**, 747-756.
15. C. Calin, I. Baldea, E.M. Rus, "Determination the corrosion rate and corrosion prevention for underground metallic structures", *The 3rd International Conference-Study and Control of Corrosion in the Perspective of Sustainable Development of Urban Distribution Grid*, July 1-3, Petrosani, Romania, **2004**, 91-97.

PHOTOCATALYTIC ACTIVITY OF METAL DOPED TiO₂ AEROGELS PREPARED BY SOL-GEL PROCESS

M. POPA*, I.C. POPESCU, V. DANCIU

ABSTRACT. Oxide semiconductor photocatalyst based on TiO₂ is normally used in UV photodegradation of different organic pollutants. This paper is focused on preparation of 1at%Cu, 1at%Ce, 1at%Fe doped and undoped TiO₂ aerogels and their application in photodegradation of an organic compound. The aerogels were obtained by sol-gel process in acid catalysis, followed by supercritical drying with liquid CO₂. The preparation process involved a single precursor based on Ti(OPr)₄ and doping was made by using ethanolic solutions of metal nitrates. The obtained aerogels were analyzed by BET method, determining the specific surface area (S_{BET}). Photocatalytic behavior of the obtained aerogels was tested by the decomposition of salicylic acid, under UV light. The photocatalytic activity of doped aerogels was compared with the undoped one and with the reference Degussa P25 TiO₂.

Keywords: Ce doped TiO₂, Cu doped TiO₂, Fe doped TiO₂, salicylic acid, photodegradation

INTRODUCTION

The concern for the environmental pollution made the society to reconsider the old path and to create new technologies, less expensive and less polluting.

In the last years the interest for using TiO₂ as a catalyst in photodegradation of organic compounds became wildly spread. It is a stable, non toxic material and is a 3.2 eV band gap semiconductor with attractive photoabsorbtion properties [1]. Under UV light, with wavelength shorter than 380 nm, the electrons from the valence band are excited and jump in the conduction band. The electron-hole pairs thus generated serve as the oxidizing and reducing agents. The photodegradation of pollutants in water takes place due to the OH• radicals, which are formed either through the interaction of water molecules with a hole or through the interaction of oxygen molecules with a hot electron, and which are the key active species [2]. Doping TiO₂ with transition metals (Me) was thought to increase the absorption of TiO₂ to the visible light of solar spectrum [3] and especially to inhibit the recombination of the electron-hole pair photogenerated [3-5] and thus, to increase the photocatalytic activity of TiO₂. Some authors agree the increasing of photocatalytic activity by doping TiO₂ with transition metals [5] while others deny it [6]. Many authors confirmed that the best dopping results are obtained for a concentration of 0.5-1at% metal dopant [4, 5]. Nevertheless the efficiency

* Babes-Bolyai University, Faculty of Chemistry and Chemical Engineering, Cluj-Napoca, Romania

of TiO₂ photoactivity is depending on many factors such as: the chosen metal dopant, crystallinity, particles size, specific surface area, surface OH groups of TiO₂, time of recombination between the electron-hole pair etc [7].

This aim of this paper is to present the preparation of 1at% cerium, 1at% copper and 1at% iron doped TiO₂ photocatalyst and some photocatalytic results obtained in degradation of salicylic acid.

EXPERIMENTAL

Sample preparation

Iron, copper and cerium doped and undoped TiO₂ were prepared by sol-gel method in acid catalysis, followed by supercritical drying with liquid CO₂. The acid catalyzed sol-gel process was carried out under normal conditions. Two different solutions were prepared: the first one contained 5 ml tetra-iso-propyl ortotitanate - TIP (Merck; >98%) in 10 ml ethanol and the second one 0.049M Fe (NO₃)₃·9H₂O (Aldrich) or 0.098M Ce(NO₃)₂·6H₂O (Aldrich), or 0.052M Cu(NO₃)₂·3H₂O (Aldrich) dissolved in ethanol, doubly distilled water, nitric acid and 10 ml ethanol. After homogenizing, the first solution was quickly added to the second one under vigorous stirring. The corresponding molar ratios of Me(NO₃)₃/TIP are presented in Table 1. The EtOH/H₂O and H₂O/HNO₃ molar ratios were 4.89 and 31.59, respectively. The resulting gels were covered and allowed to age for several weeks at room temperature. The solvent was then removed by low-temperature supercritical drying with liquid CO₂, using homemade equipment. The aerogels obtained in this way were calcined at 773 K for 2h in air, using a CARBOLITE furnace, and subsequently characterized.

Sample characterization

The BET surface areas (S_{BET}) were derived from krypton physisorption measurements at 77 K using a home-made installation. Prior to measurements, the samples were degassed to 0.001 Pa at 448 K. S_{BET} was calculated in the relative pressure range of 0.05-0.3, assuming a cross-sectional area of 0.195 nm² for the krypton molecule.

Photocatalytic activity

The photocatalytic activity of the doped and undoped TiO₂ aerogels was determined by observing the photodegradation of the salicylic acid. Photodecomposition experiments were performed in a Teflon cell with a quartz window for UV illumination using a 250 W high pressure Hg lamp. The photodegradation profile was obtained by observing the concentration of salicylic acid, measured with a Jasco V-530 spectrophotometer. The cell was kept for 15 min in the dark before the degradation experiment and spectra measurements. The absorbance of the aliquots, withdrawn at every 30 min of the irradiation time, was recorded at 295 nm.

RESULTS AND DISCUSSIONS

Table 1 lists the specific surface area (S_{BET}) of different transition metal doped TiO₂ aerogels, calcined at 2h at 773 K. The biggest specific surface area is obtained for the undoped TiO₂. Cu doped TiO₂ seems to have the biggest S_{BET} , between the transition metal doped TiO₂ aerogels.

Table 1.

Specific surface area (S_{BET}), and apparent rate constant for the transition metal doped and undoped TiO₂ aerogel and TiO₂ Degussa P25, calcined at 773 K for 2h

Me-TiO ₂ Sample	Me(NO ₃) _x /TIP (molar ratio)	S_{BET} [m ² g ⁻¹]	$10^3 \times k_{app}$ [min ⁻¹]
Fe-TiO ₂	1.031	65	4.16
Ce-TiO ₂	0.575	63	9.75
Cu-TiO ₂	0.618	80.5	6.89
Undoped TiO ₂	0	131	12.9
P25 Degussa	0	53	2.5

The evolution of the salicylic acid concentration in time for both doped TiO₂ aerogels and TiO₂ Degussa can be closely described by exponential curves (Fig. 1). Thus, an apparent rate constant k_{app} (Tabel 1) derived from the expression:

$$C = C_0 \exp(-k_{app} t) \tag{1}$$

can be determined. This behavior is generally found in the photocatalytic degradation of organic pollutants in water. A Langmuir-Hinschelwood mechanism [7] with the rate proportional to the surface coverage combined with a low initial concentration of the pollutant leads to a pseudo first-order kinetic law [9, 10].

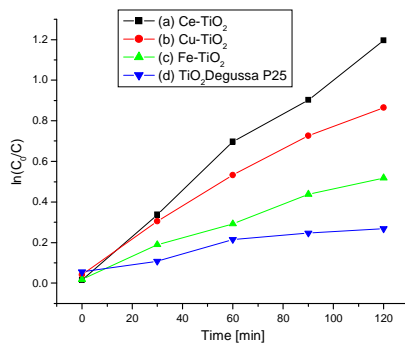


Fig.1. Salicylic acid degradation on different photocatalysts: (a)Ce-TiO₂, (b) Cu-TiO₂, (c) Fe-TiO₂, (d) TiO₂ Degussa P25

It is known that photodegradation is depending on photogenerated OH• radicals. The Ti⁴⁺-OH• entity is formed by a hydroxyl group which traps a hole [7]. The goal of doping with transition metal was for increasing the time of recombination between electrons and holes photogenerated. The place of metal ions in the TiO₂ lattice can have different effects. A substitution position of a titanium ion with a metal ion in the TiO₂ lattice is desired in order to reach this goal. In this case metal ion is capable to create traps in the band gape of TiO₂ (Fig.2) and thus, the time of recombination of the electron hole pair is increased. Experimentally was revealed that metal dopants can take different forms in TiO₂ matrix: substitution, interstitial position and/or especially as metal oxides [7, 11].

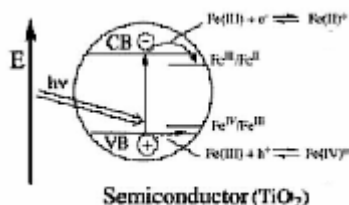
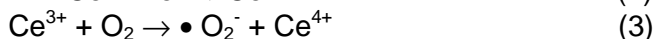


Fig.2. Photocatalytic mechanism of doped TiO₂, in the presence of iron doping ions [4]

All doped samples reveal a lower photocatalytic activity (table 1) comparing with the undoped TiO₂. One possible explanation, as Coronade et al. [12] remarked on Ce doped TiO₂ compared with the undoped one, is that the photogenerated holes are stabilized as Ti⁴⁺-O⁻ radicals due to CeO₂ presence, which might exist in Ce-TiO₂. In addition, the presence of the metal oxide in the transition metal doped TiO₂ can be an impediment not only for OH groups that form on the TiO₂ surface but also for the adsorption sites of TiO₂ destined to the organic pollutants. In doped samples can exist a partial blockage on the surface sites available for organic pollutant.

However, comparing Ce-TiO₂ with the undoped one, can be observed that S_{BET} of Ce-TiO₂ is smaller than the undoped one. This could lead to the conclusion that the k_{app} of photodegradation process of the Ce doped TiO₂ could be only due to its small S_{BET} and not necessary due to CeO₂. In this case Ce ions could be incorporated in the TiO₂ lattice and thus, the increasing time of recombination of the electron – hole pair by Ce doping could be considered. Ce⁴⁺ is a scavenger of electrons and the electron trapped in Ce⁴/Ce³⁺ is transferred to the surrounding adsorbed O₂, increasing the photocatalytic activity of TiO₂ on organic compounds. The process is described below [13]:



Fe doped TiO₂ has almost the same S_{BET} with Ce doped TiO₂ but its photocatalytic activity is the smallest. This result is in accordance with the literature [3], where Fe doped TiO₂ was found to have low photocatalytic activity. Cu doped TiO₂ presents the biggest S_{BET}, comparing with the other doped samples but its photocatalytic activity is lower than that of Ce doped TiO₂. However, all obtained TiO₂ aerogels present a better photocatalytic activity comparing with Degussa P25 TiO₂.

Further studies are necessary to clarify the effects of surface area, microstructure, doping, UV-VIS absorption, presence of OH groups on TiO₂ surface, crystalline structure on photocatalytic activity of doped and undoped TiO₂.

CONCLUSIONS

1at% Ce, 1at% Cu, 1at% Fe doped and undoped TiO₂ aerogels were prepared by sol-gel method. The photodegradation process of salicylic acid on doped and undoped TiO₂ aerogels shows a better photocatalytic activity for the undoped TiO₂. One possible explanation is the partial blockage created on TiO₂ surface due to the formation of metal oxides during doping. However, further research has to be done in order to clarify the causes that determined the lower photocatalytic activity of the doped samples comparing with the undoped one. All obtained samples have a better photocatalytic activity comparing with the reference Degussa P25 TiO₂.

REFERENCES

1. Ulrike Diebold, *Appl. Phys. A*, **2003**, 76, 681-687
2. Al-Ekabi H., Sperpone N., Pelizzetti E., Minero C., Fox M. A. and Draper, R.B.
3. *Langmuir*, **1989**, 5, 250-255.
4. P.N. Kapoor, S.Uma, S. Rodriguez, K.J. Klabunde, *J. Molec. Catalysis A: Chem.*, **2005**, 229 145-150
5. Lopez T, Moreno J.A, Gomez R, Bokhimi X., Wang J.A. Pecchi G, *J. Mater. Sci.*, **2002**, 12, 714-718
6. C. M. Whang, J. G. Kim, E. Y. Kim, Y. H. Kim, and W. I. Lee, *Glass Phys Chem.*, **2005**, 31, 390-395
7. C.D. Valentin, E. Finazzi, G. Pacchioni, A. Selloni, S.Livracchi, M.C. Paganini, E. Giamello, *Chem. Phys*, **2007**, 339, 44-46
8. J. Xiao, T. Peng, Ran Li, Z. Peng, Ch. Yan, *J. Solid State Chem.*, **2006**, 179, 1161-1170
9. Herrmann J. -M., Tahiri H., Ait-Ichou Y., Lassaletta G., González-Elipse A. R.,

10. Fernández A, *Appl. Catalysis B: Environ.* **1997**, 13(3-4), 219-228
11. Lee W., Shen H-S., Dwight K, Wold A, *J. Solid State Chem.*, **1993**, 106 (2), 288-294
12. Papp J., Shen H. S., Kershaw R., Dwight K., Wold A, *Chemi. Mater*, **1993**, 5(3) 284– 288
13. W.Li, A.j.Ferenkel, J.C. Woicik, C.Ni, S.Ismat Shah, *Phys. Rev.*, B, **2005**, 72, 155315
14. J.M. Coronado, A.J. Maira, A. Martinez-Arias, J.C.Conesa, J.Soria, *J. Photochem. Photobiol.*, **2005**, 150, 2002 213-221
15. Y. Xu, H. Chen, Z. Zeng, B. Lei, *Appl. Surface Sci.*, **2006**, 252, 8565-8570

OLT – 35 LOW CARBON STEEL CORROSION IN PRESENCE OF SULFATE IONS

ELEONORA MARIA RUS*, I. BÂLDEA*, C. CĂLIN**

ABSTRACT.The OLT-35 low carbon steel corrosion in aqueous NaCl solutions in the absence and the presence of sulfate ions by electrochemical methods (cyclic voltammetry and polarization curves) and metallographic microscopy has been investigated. From the corrosion parameters values, of the studied steel/electrolytic systems, and the analyzed micrographs results that the OLT –35 low carbon steel is most susceptible for corrosion in 1.5% NaCl + 1.5% Na₂SO₄ solution than in 3% NaCl due to the decreasing of polarization resistance.

Key words: carbon steel, sulfate ions, electrochemical corrosion, polarization curves, cyclic voltammetry, metallographic microscopy.

INTRODUCTION

The study of electrochemical behavior of an alloy, such as low carbon steel OLT – 35, may give relevant information about the corrosion of buried steel pipes or storage tanks in various media. Such studies serve as a rational basis for evaluation of coating performance and determination of controlling parameters.

The complexity of the corrosion processes of buried metallic structures results at first because of the multitude of metallic underground networks placed in the same environment, networks that can galvanically interact. Another factor in emphasizing the complexity of this problem is represented by chemical, electrochemical, biochemical, electromagnetic (stray currents) high pollution of the soil. The soil is a corrosive environment that has special characteristics from one place to another because of the variable humidity, the different percent of dissolved salts, various pH, the presence of microorganisms, the variable quantity of oxygen and stray currents presence.

In urban areas, residual wasters, containing carbonate, chloride and possibly sulfate ions, may be in contact with underground pipelines, made from mild steel bitumen coated, electrically insulating with paint and, sometime, cathodically protected. Any defects on these insulations permit corrosion. Depending on the ion concentration, potential, pH and temperature each ionic

* Babeș-Bolyai University, Faculty of Chemistry and Chemical Engineering, 11 Arany Janos St. Cluj-Napoca, 400024, Romania, e-mail norus@chem.ubbcluj.ro

** S.C. Distrigaz-Nord S.A. Tg-Mures, ROMANIA

species has a different effect on the electrochemical behavior of mild low carbon steel. Studies of the corrosion of iron and its alloys are mainly focused on the effect of chloride ions [1-10]. By contrast, the literature for corrosion by sulfate ions is scarce [11-15]. The objective of this research was to investigate the electrochemical behaviour of low carbon steel OLT – 35 , in the range of anodic active potential of iron, in salted aqueous solutions containing Na_2SO_4 .

EXPERIMENTAL

Electrochemical measurements were all carried out in a three-electrode type cell with separate compartments for reference electrode. The counter electrode, separated from the main compartment of the cell by a Nafion membrane, was a platinum sheet of 5 cm^2 in area. The working electrode was a disk of OLT – 35 steel (whose composition is (wt%): C 0.17, Si <0.35, Mn <0.4, P <0.05, S <0.05, Fe 98.98) with a surface area of 0.154 cm^2 . Surface of the working electrode was prepared by grinding abrasive paper 400 – 1200 gradation. Next they were rinsed with distilled water and degreased with acetone. Before each experiment the OLT-35 steel electrode was cathodically polarized (for 5 minutes i.e.) in the range of hydrogen evolution potential, to provide a reproducible electroreduced steel surface.

The experiments were carried out at room temperature and quiescent solutions. The volume of the used experimental cell was quite large ($\sim 0.35 \text{ l}$) so that the concentration of eventually dissolved iron compound in the bulk of the solution could be neglected

Potentials were measured vs. saturated calomel electrode (SCE) as reference. This was connected to the main compartment of the cell by a salt bridge and a Lugging capillary.

Aqueous solution of 3% NaCl, 1.5% NaCl, a mixture of 1.5% NaCl and 1.5% Na_2SO_4 were used as electrolyte. The electrolytes solution was prepared from analytical grade reagents using double distilled water.

The voltammograms at different scanning rate: 500mV/s, 200mV/s, 100mV/s, 50mV/s in the potential range between -1.8 and -0.25 V/SCE with an Autolab PGSTAT 10 system were recorded.

The instantaneous corrosion potential (ϵ_{corr}), the corrosion current density (i_{corr}) and polarization resistance (R_p) were determined from the Tafel plot using the Resistance Polarization measurement techniques developed by Stern et al [16]. A polarization sweep from -10 to 10 mV around the corrosion potential (in anodic and cathodic direction) at the scan rate of 1 mV s^{-1} was applied to OLT-35 steel electrode in studied electrolytes. The measurements were performed by using a SYCOPEL SCIENTIFIC – SCANING MINISTAT.

Metallographic microscopy was used to examine the morphology and the nature of corrosion on the OLT-35 steel surface after immersion, for 36 months, in

various test solutions. The metallographic microscopy was performed with a NEOPHOT 21- CARL ZEISS JENA microscope with incorporated camera.

RESULTS AND DISCUSSION

Cyclic Voltammetry

Figure 1 shows typical cyclic voltammograms for OLT –35 steel recorded at different scan rates in: a) NaCl 3%, b) NaCl 1.5% and c) NaCl 1.5% + Na₂SO₄ 1.5% solutions. Such voltammograms in steady state could be obtained after a few cycles (20) over the whole potential range (–1.8 and –0.25V/SCE), Fig.1 d). The voltammetric profile changes with the number of sweeps in this range of potentials and well-defined anodic and cathodic peaks appear. All voltammograms shows two anodic (A₁ and A₂) and two cathodic (C₁ and C₂) peaks. Table 1 presents the values of the main electrochemical parameters.

Table 1.

Electrochemical parameters for OLT 35 in studied solutions

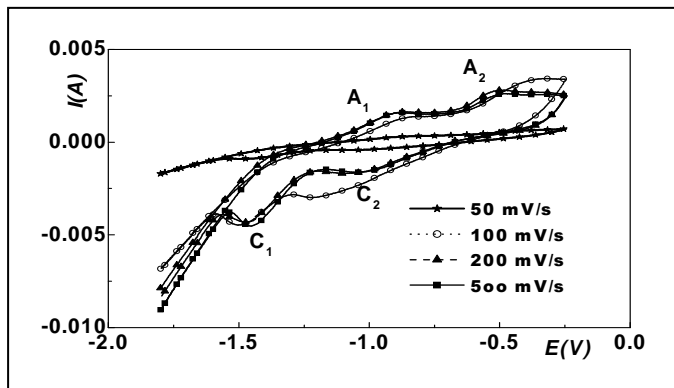
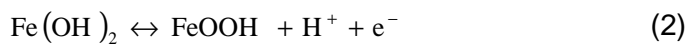
Electrolyte /Parameters	3% NaCl	1,5% NaCl	1,5%Na ₂ SO ₄	1,5% NaCl + 1,5%Na ₂ SO ₄
ε _{A1} (V)	-0.910	-0.939	-0.951	-0.918
I _{A1} (A)10 ⁴	7.190	3.290	1.870	4.240
ε _{A2} (V)	-0.515	-0.535	-0.486	-0.515
I _{A2} (A)10 ⁴	8.140	2.710	4.180	5.020
I _{A1} /I _{C1}	0.580	0.650	-	0.490
I _{A2} /I _{C2}	0.960	0.930	1.130	1.000

According to peaks potential values, there two processes can be identified [3-4]:

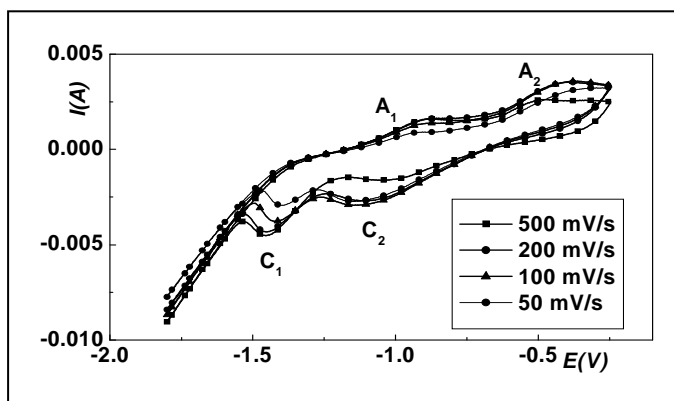
Process I – corresponding to oxidation of Fe(0) to Fe(II), peak A₁, coupled with the reduction of Fe(II) to Fe(0), peak C₁:



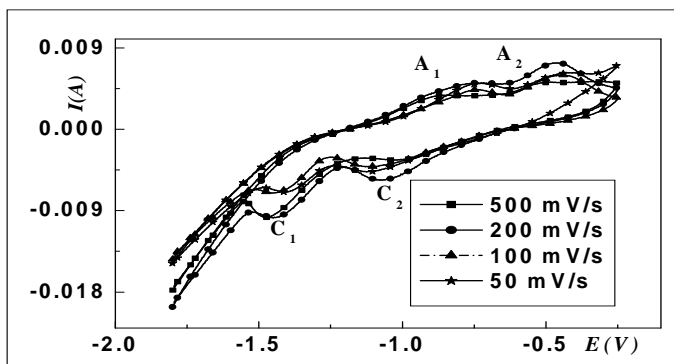
Process II – corresponding to oxidation of Fe(II) to Fe(III), peak A₂, and to reduction of Fe(III) to Fe(II), peak C₂:



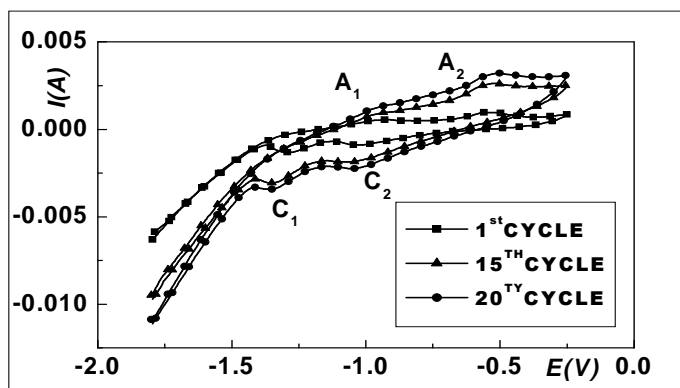
a)



b)



c)



d)

Figure 1. Voltammograms recorded for OLT 35 steel in a) 3% NaCl .b) 1.5% NaCl and c) 1.5% NaCl +1.5 Na₂SO₄ solutions; d) influence of cycles number (3% NaCl)

In anodic scan direction three domains can be identified: a) the active zone of corrosion where the anodic peak A₁ can be pointed out; b) a relative passive zone, between -0.6 and -0.9V/ECS where appears a slow increase of current, so a reduced corrosion rate; c) a transpassive zone, over the potential value of -0.6V/ECS where the oxidation of Fe (II) to Fe (III) take place (peak A₂) followed by the oxygen evolution.

The increase of the scanning rate brings about an increase of the peak currents intensity in all three cases. A higher effect in the case of solution of 3% NaCl was observed. It results from the above figures that the cycle's number not influences the voltammograms shape.

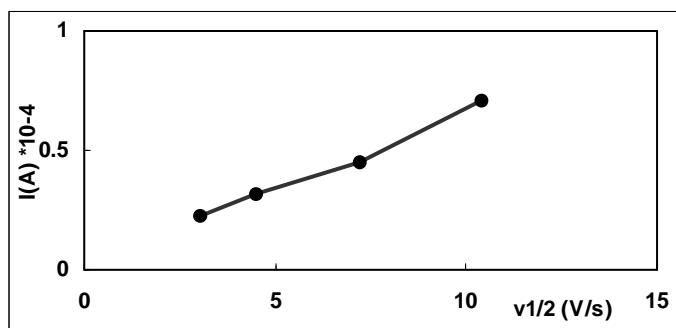


Figure 2. The peak current vs. (scan rate)^{1/2} relations for the anodic peak A₁ for OLT 35/3% NaCl system

In the present experiments, all anodic observed peaks exhibited a relative linear relationship between the peak current and the square root of the scan rate (figure 2). This suggests that the processes are diffusion rather than kinetically limited.

Adding sodium sulphate to NaCl 1.5% solution produces an increase of A_1 and A_2 anodic peaks intensity of 1.3 and 1.85 fold respectively.

Polarization measurements

The ϵ_{corr} , i_{corr} and Tafel slops were determined from the Tafel plots of potentiodynamic measurements by extrapolation.

The polarization resistance (R_p) was calculated using the Stern–Geary equation:

$$i_{\text{corr}} = \frac{1}{2.303} \frac{b_a \cdot b_c}{(b_a + b_c)} \frac{1}{R_p} = \frac{B}{R_p} \quad (3)$$

where b_a and b_c are the Tafel slopes.

The corrosion rate, v_{corr} ($\text{mg}/\text{cm}^2 \cdot \text{h}$), was also calculated from the corrosion current, i_{corr} (A/dm^2), using Faraday's law:

$$v_{\text{corr}} = \frac{i_{\text{corr}} \cdot A}{26,8 \cdot z} \quad (4)$$

where 26.8 is the Faraday constant, A the average atomic weight of steel, z the number of electrons exchanged by metal ion ($z = 2$).

Figure 3 shows Tafel plots of OLT –35 steel in studied electrolytes.

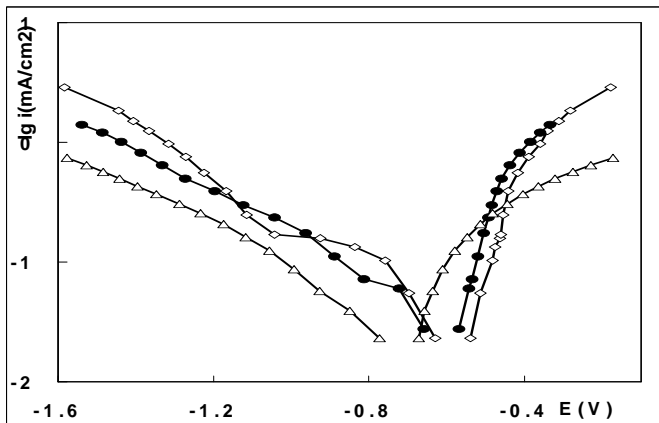


Figure 3. Polarization curves of OLT- 35 steel in: NaCl 3% (-○-); NaCl 1.5% (-●-) and NaCl 1,5% + Na₂SO₄ 1,5% (- △ -)

On the polarization curves of OLT- 35 in 3% NaCl solutions as well as in chloride and sulphate mixture, linear domains on the anodic and cathodic branches can be observed. The analysis of these curves reveals that, in all studied electrolytes, the corrosion of OLT –35 steel takes place by a kinetic control by the charge transfer typical reaction [5].

Table 2.

Corrosion parameters for OLT 35 in studied solutions

Electrolyte /Parameters	3% NaCl	1.5%NaCl	1.5% NaCl + 1.5% Na ₂ SO ₄
$I_{corr} \times 10^2$ [mA/cm ²]	2.63	2.18	7.07
E_{corr} [mV/ECS]	-620	-555	-580
b_a [mV/dec]	190	185	180
b_c [mV/dec]	160	195	280
R_p (k Ω cm ²)	1.424	1.890	0.673
$V_{corr} \times 10^2$ [mg/cm ² h]	2.74	2.27	7.38

The polarization parameters (table 2) shows that the OLT –35 steel is more corrodible in 1.5% NaCl + 1.5% Na₂SO₄ solution than in 3% NaCl due to the decreasing of polarization resistance.

The higher corrosion rate in the mixture of salts, in our experiments, suggests that Na₂SO₄ acts as a corrosion accelerator.

Metallographic microscopy

Samples surfaces aspects obtained by metallographic microscopy are presented in the figure 4.

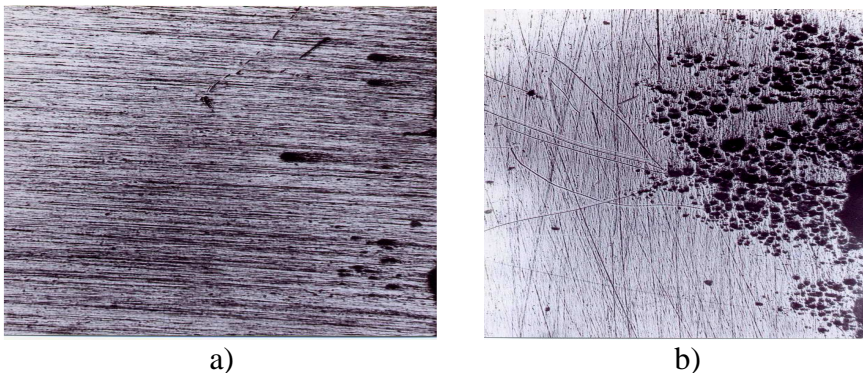
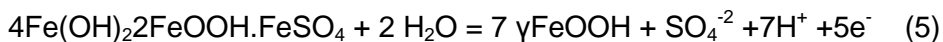


Fig.4. Micrographs of the corroded surface of the OLT- 35 steel in the presence of a) NaCl 3%, b) mixture of NaCl 1,5% + Na₂SO₄ 1,5%

The metallographic microscopy observations confirms, by the higher localized attack of the metal surface (Fig.4 b) that NaCl 1,5% + Na₂SO₄ 1,5% mixture solution is more aggressive than NaCl 3%.

Micrographs recorded for OLT- 35 steel in NaCl 3% solution denote a relative generalized corrosion, with a thickness of the corrosion products layers around 0, 2 mm. No rusts are seen from the micrograph. The surface morphology of the samples immersed in mixture of NaCl 1, 5% + Na₂SO₄ 1, 5% solution is different. Localized corrosion takes place, in the plague forms, with larger depth and diameters, on the most of the surface. Dark green rust was observed on the electrode surface.

According to Genin et al. [17] the green rust may be a transient compound with the following formula: 4Fe(OH)₂2FeOOH.FeSO₄.nH₂O, with *n* of probable 4 value. The formation of a passive layer may be considered according to:



Although the surface oxidation in the presence of sulfate ions induces the formation of a passive film, the precipitation of a sulfate product alone can not protect the steel against localized attack or uniform dissolution.

These are confirmed by the surfaces aspect of the samples macroscopically analyzed with the help of a magnifier [18], Fig. 5.

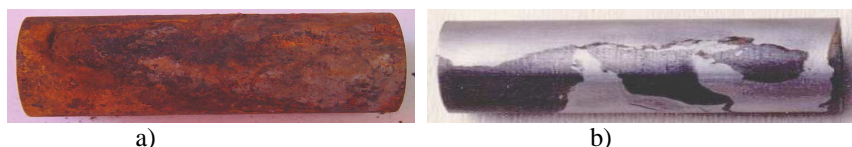


Fig.5. The aspect of the corrosion products formed on the OLT 35 carbon steel in 1.5 % NaCl + 1.5% Na₂SO₄: a) before and b) after removing the corrosion products

CONCLUSIONS

Results of this investigation showed that buried pipeline systems made from OLT – 35 low carbons steel in presence of sulfate ions will develop surface corrosion problems.

By analyzing the corrosion parameters values, obtained from electrochemical measurements, a greater susceptibility for corrosion of OLT – 35 low carbons steel in presence of sulfate ions was demonstrated.

A good agreement between electrochemical measurements results and surface morphological studies was observed.

A relatively uniform corrosion for samples immersed in NaCl solutions was observed in comparison with those exposed in a mixture of NaCl + Na₂SO₄ where the localized corrosion is predominant.

The metallographic microscopy shows that a NaCl + Na₂SO₄ mixture solution is more aggressive than NaCl solution. This fact is confirmed by the higher localized attack of the metallic surface which is covered by corrosion defects (pitting and plague type with higher depth and diameters).

REFERENCES

1. Daksh Baweja, Harold Roper, and Vute Sirivivatnanon, *Materials Journal*, **2003**, 100, 228-238.
2. C. Calin, I. Lingvay, Georgeta Rus, I. Baldea, Eleonora Maria Rus, "Study on corrosion behaviour of carbon steel in salted media", *The 1st International Corrosion Conference-Study and Control of Corrosion in the Perspective of Sustainable Development of Urban Distribution Grid*, Constanta, June 6-8, **2002**, 96-101
3. M. Fathy, W. Bayoumi, A. Ghanem and B. G. Ateya, *Int. J. Electrochem. Sci.*, **2006**, 1, 258-267.
4. Eleonora Maria Rus, Georgeta Țarălungă, Delia Maria Constantin, *Studia Universitatis Babeș-Bolyai, Chemia L(1)*, **2005**, 261 – 270.
5. C. Calin, I. Baldea, Eleonora Maria Rus, " Steel corrosion and its control in neutral media", *The 2nd International Corrosion Conference-Study and Control of Corrosion in the Perspective of Sustainable Development of Urban Distribution Grid*, M. Ciuc, June 19-21, **2003**, 138-144
6. C. Calin, I. Baldea, Eleonora Maria Rus, "Annals of West University of Timisoara", *Series Chemistry*, 12(3), **2003**, 747-756
7. Gui-Fang Huang, Wei-Qing Huang, Ling-Ling Wang, Bing-Suo Zou, Di-Ping Chen, De-Yi Li, Jia-Mou Wei, Jian-Hui Zhang, *Int. J. Electrochem. Sci.*, **2007**, 2, 321 - 328
8. Y. M. Liou, S. Y. Chiu and C. L. Lee, *J. Appl. Electrochem.*, **1999**, 29, 1977 – 1981
9. J. A. Bardwell, J. W. Fraser, B. MacDougall and M. J. Graham, *J. Electrochem. Soc.*, **1992**, 139, 366 - 375.
10. Dae-Kyeong Kim, J. D. Scantlebury, Srinivasan Muralidharan, Tae-Hyun Ha, Jeong-Hyo Bae, Yoon-Cheol Ha and Hyun-Goo Lee, (<http://www.umist.ac.uk/corrosion/jcse>) *Journal of Corrosion Science and Engineering*, **2004**, 9 – 14.
11. G. Vatankhah, M. Drogowska, H. Menard and L. Brossard, *J. Appl. Electrochem.*, **1998**, 28, 173 - 183.
12. Bore Jegdič, Dragutin Dražič and Jovan P. Popič, *J. Serb. Chem. Soc.*, **2006**, 71 (5) 543–551.
13. C. Calin, Eleonora Maria Rus, I. Baldea, *Analele Universitatii Oradea, Fascicola Chimie*, **2001**, VIII, 5 – 10.
14. M. Drogowska, H. Menard and L. Brossard, *J. Appl. Electrochem.*, **1996**, 26, 217 - 225.

15. M. Drogowska, L. Brossard and H. Menard, *J. Appl. Electrochem.*, **1998**, 28, 491 - 501.
16. M. Stern and A. L. Geary, *J. Electrochem. Soc.*, **1957**, 104, 56.
17. Ph. Refait, M. Abdelmoula and M. R. Genin, *Corrosion Science*, **1994**, 36,55-63.
18. C. Calin, I. Baldea, Eleonora Maria Rus, "Analysis of underground gas pipelines corrosion by optical methods. Corrosion control and its efficiency", *The 4th International Conference URB-CORR- Study and Control of Corrosion in the Perspective of Sustainable Development of Urban Distribution Grid*, Sibiu, Romania, June, 9-11, **2005**, 182-194.

DETERMINATION OF TOTAL ACID CONTENT IN WINE BASED ON THE VOLTAMMETRIC REDUCTION OF 1,4-BENZOQUINONE

MIHAELA RALUCA CIUMAG, MARIA JITARU*

ABSTRACT. In this work, voltammetric determination of the total acid content in wine was made, by measuring the reduction prepeak current of p-benzoquinone (BQ). This prepeak is due to the presence of acids in unbuffered ethanol medium. The simple system of p-benzoquinone was found to be suitable for this determination, because of its reduction potential, stability and solubility in ethanol containing organic acids. On the voltammograms of BQ, obtained in standard synthetic ethanolic solutions of organic acids, such as tartaric, citric and acetic, a well-defined single prepeak appeared during the cathodic potential scan. Its height was proportional to the total acid concentration. The values of total acid content of 5 wine samples and of a vinegar sample were determined by the present method, which is superior in sensitivity and requires a very small volume of wine sample compared to the conventional potentiometric titration method.

Keywords: voltammetry, total acid determination, wine, quinone

Introduction

In wines are present various organic acids, such as tartaric, malic, citric and acetic acid. Acid content doesn't rest unchanged in time, it changes during the fermentation of grape juice. Total acid content is expressed in terms of "total acidity" or "total acid" and serves as an indicator of wine taste and aroma. Total acid determination is essential for the control of fermentation and quality of wine.

Titration with NaOH using phenolphthalein as an indicator is the official method for total acid determination in wine [1]. But the results are not always satisfactory owing to vagueness of the indicator colour change, especially for the red and rose wines. Potentiometry is thus strongly recommended as an alternative method, in which the end point is defined as alkali consumption up to a given pH, e.g., pH 7 in the European standard method. The acidity corresponding to the alkaline consumption is called "titratable acidity". Though, pH values at the end points differ from wine to wine and so, the accuracy of the results may be affected. Thus it was needed a more sensitive, simple and rapid method to be found for the total acidity of wines determination.

S. Ohtsuki and Co. developed a new voltammetric method for determining the total acid content in wine, based on the fact that acids in

* Faculty of Chemistry and Chemical Engineering, Babes-Bolyai University, 11, Arany Janos, 400028, Cluj-Napoca, Romania mjitaru@chem.ubbcluj.ro

unbuffered ethanol solutions of 3,5-di-t-butyl-1,2-benzoquinone (DBBQ) gave rise to a new peak (termed the prepeak) on a voltammogram at more positive potentials than that corresponding to the normal reduction peak of DBBQ. The total acid content of wines was determined from the prepeak height [2].

Same as wines, vinegar also contains various organic acids and acidity quality control is necessary in order to produce vinegar. Normally, the titratable acidity of vinegar is to be around 9% in Romania. Therefore, an acidity determination is essential to control the fermentation and quality of vinegar.

The same team of researchers established also a new method for the determination of titratable acidity in vinegar, based on the same principle like the determination of wines total acidity: the reduction prepeak of 3,5-di-t-butyl-1,2-benzoquinone due to the presence of acids in unbuffered solution [3].

The previous studies made by Ohtsuki et al involved a quinone with a complicated structure, and therefore not advantageous economically (expensive enough). In the present study, the total acid content determination was made by voltametry using one of the most common quinones: 1,4-benzoquinone and a classic three-electrode electrochemical cell.

Experimental

Reagents and solution preparation

Red and white wines examined were obtained from commercial sources. 1,4-Benzoquinone (BQ, 98%) was from Merck.

Ethanol (95%, Reagents SRL) solution containing 0,1 M LiClO₄ (98%, Fluka) was used as the supporting electrolyte. BQ solution was prepared by dissolving an appropriate amount of BQ (98%, Merck) in the supporting electrolyte to a concentration of 3×10^{-3} M. Test solutions were made by adding 500 μ L of wine to the BQ solution (40 mL).

Reagent grade tartaric acid, citric acid (anhydrous, >98 %) and acetic acid (99, 8%, Primexchim) were used to prepare standard acid solutions by diluting with the BQ solution.

Apparatus

Voltammetric measurements were made using a potentiostat-galvanostat system – BAS 100B (Bioanalytical Systems, USA) with the specific software BAS 100W and a classic three-electrode electrochemical cell. The electrochemical cell is comprised of a cell bottom of 20 mL capacity and a plastic cell top. A working electrode of vitreous carbon (2 mm diameter), an Ag/AgCl reference electrode and a platinum plate auxiliary electrode were inserted through the cell top into the cell. The pH measurements for the wines were made with a pH-meter Basic 20 from Crison.

Procedure

Cyclic voltammetry and linear sweep potential voltammetry were performed in the usual way with a potential sweep rate of 5 mV/s at 25° C. The sensitivity is 10 μ A/V and the domain of potential was established after several determinations: -400 to 400 mV vs. Ag/AgCl. During the voltammetry determination, a salt bridge for the protection of the reference electrode Ag/AgCl was used.

RESULTS AND DISCUSSIONS***Choice of quinone reagent***

In the study of Ohtsuki [2] a substituted quinone has been used, 3, 5-di-*t*-butyl-1, 2-benzoquinone (DBBQ). This quinone gave a well-defined reduction prepeak and it proved a good stability in ethanol solution in time, but we supposed that the simple benzoquinones can be used too. We choose the 1, 4-benzoquinone, one of the most simple quinone systems, for the present study, for economical reasons for the study of a cheaper way to apply this method of total acid content determination.

To avoid overlap of the prepeak and the reduction peak of dissolved oxygen in the solution, use of quinones reduced at potentials more positive than -0,4 V (vs. Ag/AgCl) is desirable. *p*-Benzoquinone reduces at a potential more positive than -0,4 V vs. Ag/AgCl, so that dissolved oxygen causes no interference in measuring the prepeak height. The stability of BQ in ethanol was demonstrated by time-course measurements of absorption UV-Vis spectrum ($\lambda_1 = 244$ nm, $\log \epsilon_1 = 4.3$; $\lambda_2 = 279$ nm, $\log \epsilon_2 = 2.8$; $\lambda_3 = 430$ nm, $\log \epsilon_3 = 1.3$).

Acid determination in synthetic solutions, based on the voltammetric reduction of BQ

Following the addition of tartaric acid into the BQ solution, a prepeak appeared at a potential more positive than that corresponding to the original reduction peak, as shown in figure 1 and 2. The prepeak of benzoquinone reduction in presence of tartaric acid occurs at 0.1 V vs. Ag/AgCl.

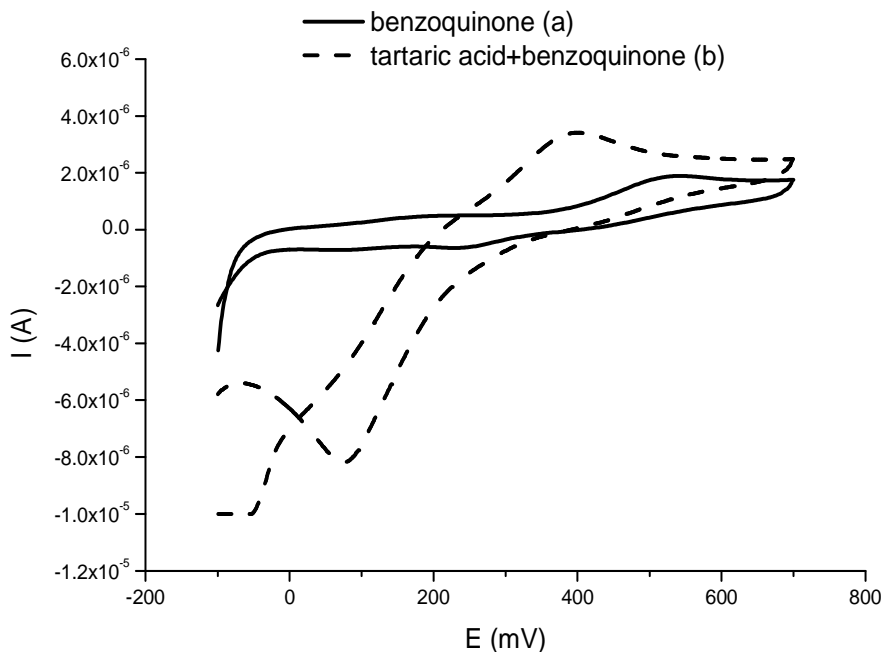


Fig.1. Cyclic voltammograms of 3×10^{-3} M 1,4-benzoquinone in absence (a) and in presence (b) of $1,2 \times 10^{-3}$ tartaric acid in ethanol containing 0,1 M LiClO_4 . WE: VC, RE: Ag/AgCl, CE: platinum plate; scan rate: 5mV/s

The prepeak height was found to be proportional to the tartaric acid concentration from 5×10^{-4} M to 1.5×10^{-2} M with a correlation coefficient of 0,996. The relative standard deviation (RSD) of the prepeak height obtained with 5×10^{-4} M tartaric acid was 2% ($n = 5$).

Electrochemical reduction of quinone in amphiprotic solvents is known to involve a two-electron transfer coupled with a two-proton transfer to form the corresponding hydroquinone. In previous studies of proton donor effects on the voltammetric reduction of quinone in an unbuffered solution [2], the prepeak current was found to be controlled by the diffusion of the acid in the electrolyte solution to the electrode surface.

DETERMINATION OF TOTAL ACID CONTENT IN WINE BASED

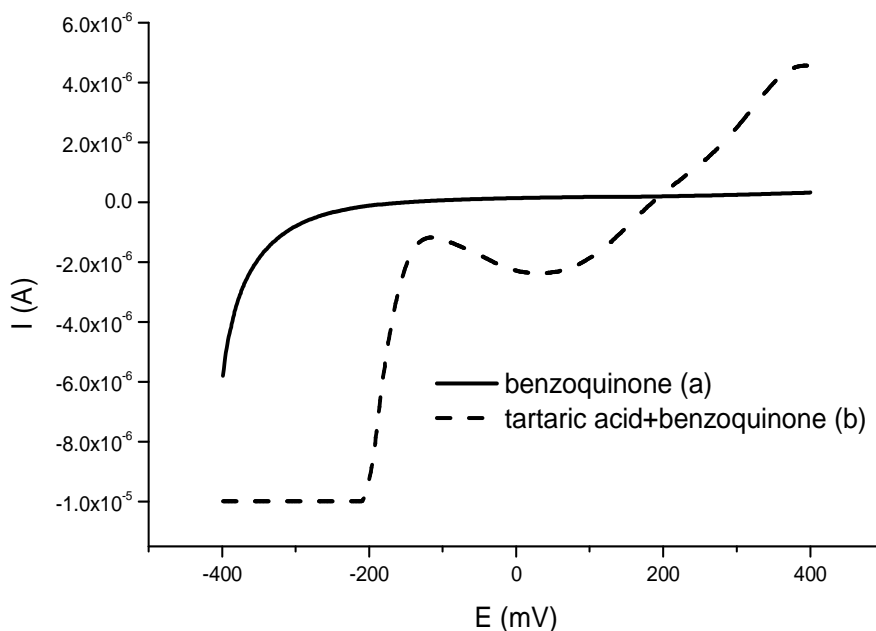


Fig.2. Linear sweep voltammograms of 3×10^{-3} M 1, 4-benzoquinone in absence (a) and in presence (b) of 1.2×10^{-3} tartaric acid in ethanol containing 0.1 M LiClO_4 . WE: VC, RE: Ag/AgCl, CE: platinum plate; scan rate: 5mV/s

The electrolysis of quinone at the prepeak potential demonstrated that hydroquinone was likewise produced through a two-electron reduction process, although the electrolysis potential was more positive than the normal reduction potential [4]. Based on this fact, the occurrence of the prepeak can be ascribed in the increased availability of protons from the added acid compared to solvent molecules. This results in a lowering of the free energy for the reduction process, leading to a reduction potential shift in the positive direction depending on the acid strength [4 – 6].

Addition of various carboxylic acids to individual BQ ethanol solutions gave rise to a single prepeak at -0.22 to 0.05 V (vs. Ag/AgCl), as shown in figure 3 and 4. In all cases, each acid concentration was the same, but the prepeak height differed according to the number of protons available for the transfer. For the citric acid, the prepeak occurs at -0.2 V vs. Ag/AgCl and for the acetic acid, the reduction prepeak occurs at 0.05 V vs. Ag/AgCl. The prepeak of BQ in presence of acetic acid is less visible,

probably due to the more reduced electrosorption of acetic acid at the surface of the electrode, compared to the tartaric and citric acid.

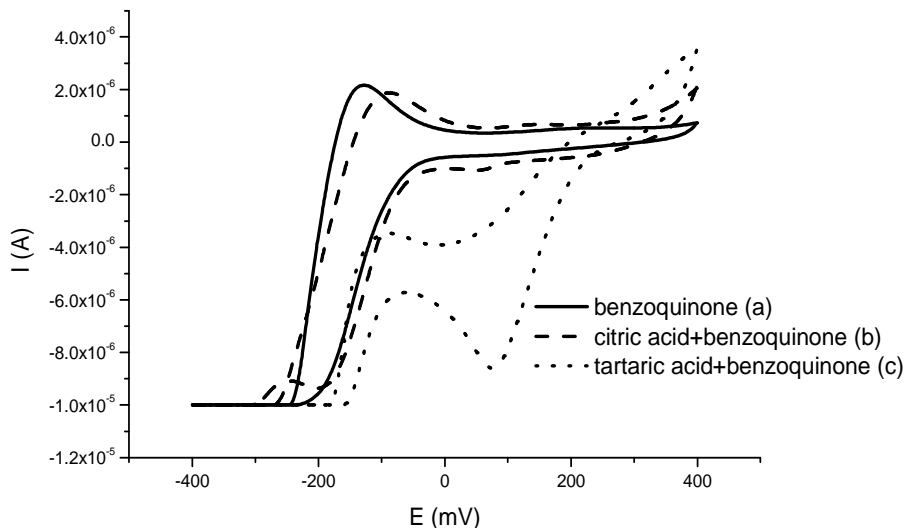


Fig.3. Cyclic voltammograms of 3×10^{-3} M 1,4-benzoquinone in absence (a) and presence of $1,2 \times 10^{-3}$ citric acid (b) and $1,2 \times 10^{-3}$ tartaric acid (c) in ethanol containing 0.1 M LiClO_4 . WE: VC, RE: Ag/AgCl, CE: platinum plate; scan rate: 5mV/s

The prepeak height was found to be linearly related to the equivalent concentration for the acetic acid ranging from 5×10^{-5} M to $2,5 \times 10^{-3}$ M, with a correlation coefficient of 0,998. The equation of the calibration curve for tartaric acid is: $y = -3,7107x - 0,571$. The relative standard deviation (RSD) of the prepeak height obtained with 5×10^{-4} M acetic acid was 1,6% ($n = 5$).

The occurrence of a prepeak current in the case of benzoquinone reduction in an unbuffered medium in presence of an organic acid does not depend on the nature of the acid. Though, the nature of the acid can influence the position and the prepeak form. The prepeak current has a linear variation with the acid's concentration for a domain of concentrations large enough. These concentrations are to be found within the limits of the acid's usual concentrations in wines. In this case, the calibration curve found for the tartaric acid can be used successfully for determining the acidity of real wine samples. The calibration curve for the acetic acid can be also successfully used for determining the acidity of vinegar.

DETERMINATION OF TOTAL ACID CONTENT IN WINE BASED

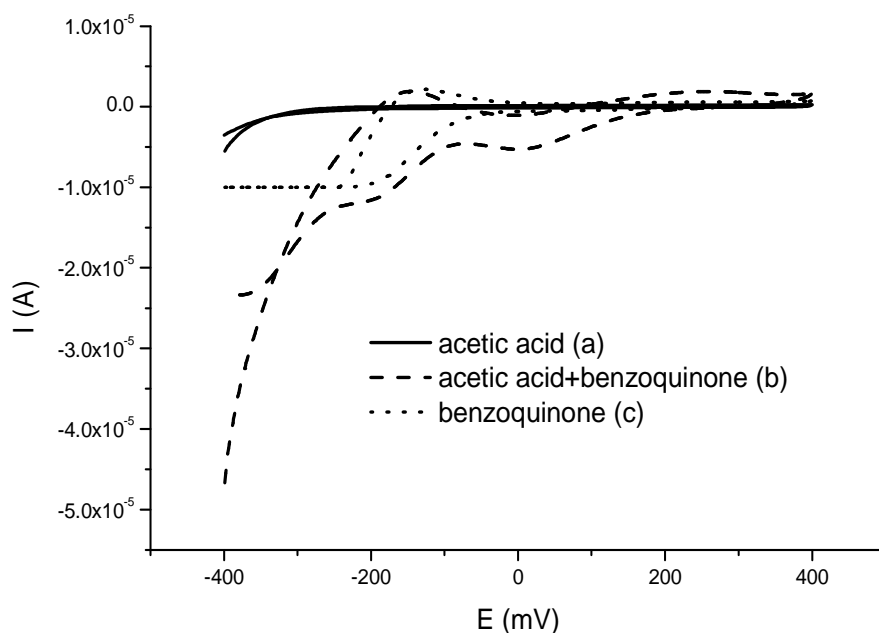


Fig.4. Cyclic voltammograms of 1.2×10^{-3} acetic acid in absence (a) and in presence of 3×10^{-3} M 1,4-benzoquinone (b) in ethanol containing 0.1 M LiClO_4 . WE: VC, RE: Ag/AgCl, CE: platinum plate; scan rate: 5mV/s

Total acid determination of wine

Various acids contained in wine gave rise to a prepeak on the voltammogram of BQ. By the addition of 500 μL of wine to 40 mL of the BQ solution, a prepeak occurred. The total acid content in wine is calculated, based on the calibration curve obtained for the tartaric acid. The total acid content should be converted to the concentration of tartaric acid (g/10 mL), according to the definition of the total acidity of wine in the official analytical methods.

The present method was applied to the total acid determination of 5 different kinds of wines, and the results are listed in table 1. For each kind of wine 5 determination were performed and the RSD is for all of them under 2%. For comparison pH measurement is showed also (table 1). However, total acid content may not always be closely related with pH values, since the latter reflects the hydrogen ion activity in the acid mixture solution.

Table 1.

Total acid content in wine, as tartaric acid

Wine	pH	Total acid content ($\times 10^{-2}$ g/10 mL)
Red, Pinot Noir, 2006	3,35	5,78
Red, Pinot Noir, 2003	3,55	5,53
Red, Feteasca Neagra, 1999	3,30	6,22
White, Chardonnay Koşer Pesah, 2003	3,18	6,19
White, Aiud producer, 2006	3,25	7,09

The concentration of acetic acid in 9% vinegar was also verified, based on the calibration curve of acetic acid. The concentration value for the acetic acid found by voltammetric determination is 9,08%, value very close to the real one (known). The relative standard deviation (RSD) of the prepeak height obtained was 1,62% ($n = 5$).

CONCLUSIONS

The present method was shown to be practically useful for determining the total acid content in wine and vinegar. The method is straight forward and simple to use. Dissolved oxygen in the test solution has no effect on the measurement of the prepeak height, leading to a considerable reduction of the operation time. Also, sample colour and turbidity cause no interference on the analytical results. This methods is sensitive and accurate, it requires small sample volumes (500 μ L) and the RSD values are less than 2 %. Determination of total acid content of wines and vinegar by electrochemical reduction of quinones has the advantage of the electrochemical methods – rapidity, sensitivity, precision and not last – it is an environmental friendly method.

As perspectives, it is envisaged to use this method as a suitable alternative for titratable acidity determination, not only in wine and vinegar, but also in food, fruit, alcoholic and non-alcoholic beverages.

REFERENCES

1. *Official Methods of Analysis*, National Tax Administration, Japan
2. S. Ohtsuki, N. Kunimatsu, K. Takamura, F. Kusu, *Electroanalysis*, **2001**, 13, 404
3. A. Kotani, Y. Miyaguchi, D. Harada, F. Kusu, *Anal. Sciences*, **2003**, 19, 1473
4. K. Takamura, Y. Hayakawa, *J. Electroanal. Chem.*, **1971**, 31, 225
5. O. H. Müller, *J. Am. Chem. Soc.*, **1940**, 62, 2434
6. B. R. Egings, J. Q. Chambers, *J. Electrochem. Soc.*, **1970**, 117, 186

ELECTROPLATING WASTEWATER TREATMENT USING A ROMANIAN BENTONITE

SILVIA BURCĂ^a, GEORGE VERMESAN^b, CAIUS BULEA^c, MARIA STANCA^a, HOREA BEDELEAN^d, ANDRADA MĂICĂNEANU^{a,*}

ABSTRACT. In this study we considered the possibility to remove iron and zinc ions from electroplating wastewaters using a clay mineral (bentonite). We worked with a bentonite cropped from Valea Chioarului, Maramures County, Romania, deposit. The bentonite sample was characterised by means of surface specific area (BET), chemical analysis, X-ray diffraction, scanning electron microscopy (SEM), energy dispersive X-ray spectroscopy (EDS) and Fourier transformed infrared (FTIR) spectroscopy. Electroplating wastewaters provided by SC BETAK SA Bistrita, with an initial iron and zinc content of 1100.7 g Fe_{total}/dm³ and 126.8 g Zn²⁺/dm³ respectively, and a pH of 0.5, were used. The heavy metal ions removal process was realised in a batch reactor (static regime) using a micronised bentonite sample ($d < 4.5 \mu\text{m}$). This type of bentonite proved to be efficient in the iron and zinc ions removal (100% removal efficiency).

Keywords: Clay mineral, bentonite, montmorillonite, electroplating wastewaters, zinc ions, iron ions.

1. INTRODUCTION

Galvanic plating workshops consume a great amount of water in the technological process (plating, acid treatment) as well as in the plated pieces washing process. The most important wastewaters containing heavy metal ions resulted in the technological process are used electrolytes (concentrated solutions) and acid washing solutions (semi-concentrated solutions).^{1,2} These waters will have a high content of heavy metal ions and low pH values.¹ In the last years, the problem of re-utilisation of these waters, after a proper treatment, became an important issue.² The classical technology applied in the majority of the industrial units, is dilution until the maximum allowable concentration is reached. Taking in account the increasing number of galvanic plating workshops, this classical technology reached its limits.

^a Department of Chemical Technology, "Babes-Bolyai" University, 11 Arany Janos st., RO-400028 Cluj-Napoca

^b Department of Materials Science and Environmental Protection, Technical University, 103-105 Muncii bd, RO-400641, Cluj-Napoca

^c S.C. BETAK S.A., 4 Industriei st., RO-420063, Bistrița

^d Department of Geology, "Babes-Bolyai" University, Cluj-Napoca, 1 Mihail Kogălniceanu st., RO-400084 Cluj-Napoca

* Corresponding author; e-mail: andrada@chem.ubbcluj.ro

Heavy metal ions can be removed from wastewaters using physical, chemical and electrochemical methods. A variety of methods such as precipitation, solvent extraction, vacuum evaporation, membrane technologies (microfiltration, ultrafiltration, reverse osmosis), adsorption and ionic exchange, electrolysis, or electrodialysis are available.³⁻¹⁴

Due to the high toxicity of the heavy metal ions (zinc, lead, cadmium, etc.) maximum allowable concentrations for discharging in surface water streams are very small.¹⁵ In order to achieve the maximum allowable concentrations imposed for discharged waters according to specific legislation, combined methods are frequently used.

The usage of natural mineral raw materials (zeolitic volcanic tuffs, clays, porous silicatic rocks etc), even if feasible, is still approached only as research proposals, as a result of the incomplete knowledge on their amounts, quality and behavior, and especially on the possibilities of their regeneration after technological usage.

On a global scale, clays (clay minerals), besides the zeolites proved to be very suitable materials for various industrial activities (special building materials, ceramics, etc.).

Clay minerals are aluminium hydrosilicates, crystallized in monoclinic system, characterized by planar reticular structures. Stratified structure of mineral clays is determined by the combination in one reticular plan (structural unit) of two cationic layers, one layer in which silicon is coordinated tetrahedric with O·OH (tetrahedric level Te) and one layer in which aluminium is coordinated octahedric with O·OH (octahedric level Oc). These layers are bonded between them with van der Waals bonds forming the structural unit. According to the numbers of Te and Oc layers, clay minerals are classified in 1Te:1Oc (eg. kaolinite), 2Te:1Oc (eg. montmorillonite) and 2Te:2Oc (eg. chlorite). The layered structure of the clay minerals and presence of isomorphous replacement of Si⁴⁺ with Al³⁺ (negative charge compensated by Na⁺, K⁺, Ca²⁺ and/or Mg²⁺) determines their main properties: hydration, swelling, water and organic compounds adsorption and ionic exchange capacity.^{1,16} Clays have been found a large applicability also in depollution processes, purification of urban and industrial residual waters, protection of waste disposal areas or purification of industrial gases.¹⁷⁻¹⁹

Clay minerals of different types and with different modifications (organic modified, immobilised) were widely studied in the heavy metal ions removal processes from wastewaters. Between the clay minerals used to remove heavy metal ions from wastewaters, bentonite (Ca-, Na- or organic modified bentonite) and kaolin were mainly studied.^{9-11,20-29}

Bentonite is a material composed of clay minerals, predominantly montmorillonite with minor amounts of other smectite group minerals,

commonly used in drilling mud. Montmorillonite forms from weathering of volcanic ash, most often in the presence of water.

Montmorillonite is a phyllosilicate mineral, member of the smectite family, consisting of two tetrahedral layers and one octahedral layer (2Te:1Oc). The silicate tetrahedral layers have a slight negative charge (due to replacement of silicon atoms with Al, Mg and sometimes with Fe atoms) that is compensated by exchangeable ions in the intercrystallite region. The charge is so weak that the cations (in natural form, predominantly Ca^{2+} , Mg^{2+} or Na^+ ions) can be adsorbed in this region with their hydrated shell. The extent of hydration produces intercrystalline swelling. Bentonite presents strong colloidal properties and its volume increases several times when coming into contact with water, creating a gelatinous and viscous fluid. The special properties of bentonite, with its main component smectite, hydration, swelling, water absorption, viscosity, tixotropy, make it a valuable material for a wide range of applications. Worldwide complex research work on clays evidenced a large range of usages based on the specific properties of clay minerals. The most important properties of bentonites are adsorption and ionic exchange capacity, properties which gives them exceptional qualities related to environmental protection technologies.³⁰⁻⁴⁵

In Romania, large bentonite deposits are known from the Transylvanian Depression or the extra-Carpathian area.

This paper presents the results obtained using a Valea Chioarului (Maramures County) bentonite sample, within the framework of an ample study regarding the uses of some clay minerals (different occurrences) from Romania, in wastewaters treatment. This bentonite sample was characterized and used to remove iron and zinc from wastewaters.

2. EXPERIMENTAL

2.1. Bentonite compositional and structural investigations

A representative sample of crude bentonite, ($d < 4.5 \mu\text{m}$), from Valea Chioarului (Maramures county) deposit was characterised by means of surface specific area (BET), X-ray diffraction, chemical analysis, scanning electron microscopy (SEM), energy dispersive X-ray spectroscopy (EDS) and Fourier transformed infrared (FTIR) spectroscopy.

2.2. Operating conditions

For the iron and zinc removal study we used electroplating wastewaters from SC BETAK SA Bistrita with an initial iron and zinc content of $1100.7 \text{ g Fe}_{\text{total}}/\text{dm}^3$ and $126.8 \text{ g Zn}^{2+}/\text{dm}^3$ respectively and a pH of 0.5. These waters were neutralised (from pH = 0.5 to 7.3), filtered and diluted hundred times. After these procedures the concentrations of the water sample (the initial concentration for the removal process) were $636.8 \text{ mg Fe}_{\text{total}}/\text{dm}^3$ and $833.3 \text{ mg Zn}^{2+}/\text{dm}^3$. Determination

of zinc and iron ions in wastewaters was realised using a Jenway 6305 UV/VIS spectrophotometer after a prior centrifugation. Zinc determination was made at 420 nm (potassium ferrocyanide), while for iron we worked at 510 nm (ortho-phenantroline), according to Romanian standards.^{46,47} The concentration and efficiency values calculated in this paper have to be looked as according to the precision limits of the determination methods. Experiments were carried out without any modification of temperature (room temperature).

The heavy metal ions removal process was realised in a batch reactor in static regime using 20 g of bentonite ($d < 4.5\mu\text{m}$) and 100 ml wastewater (bentonite : solution ration, 2:10).

The evolution of the wastewater treatment process was followed by means of variation of ions concentration in time, heavy metal ions removal efficiency (calculated from values of ions concentration at a moment t and initial concentration) and adsorption capacity (iron and zinc uptake).

3. RESULTS AND DISCUSSIONS

3.1. Petrographic results

The bentonite from Valea Chioarului (VCh) is usually greasy and has grey-greenish colour, and locally could be whitish or yellowish. The bentonite formed by hydrothermal alteration of an acid rock (rhyolite). Relicts of primary rhyolite structure are often present. From mineralogical point of view, the bentonite from Valea Chioarului ore contains montmorillonite (72-80%) and feldspar, micas, quartz and opaque minerals in lower quantities. The colloidal fraction contains 97-98.5% montmorillonite and 1.5-2.5% cristobalite.^{17,48,49}

BET specific surface area was determined to be 57.6 m²/g.

The X-ray diffraction diagram performed on random powder (Siemens Bruker, Cu K α anticathode, 10° to 70° 2 θ , 2 degrees step) of the whole material indicated the massive presence of Na-montmorillonite, characterised by a (001) reflect at about 12.5 Å associated with a few percents of halloysite and/or kaolinite (in $< 2\mu$ fraction), and cristobalite, quartz and feldspar in bulk sample (figure 1). Cristobalite generation was caused by the excess of silica resulted from the montmorillonitization process of the volcanic glass.

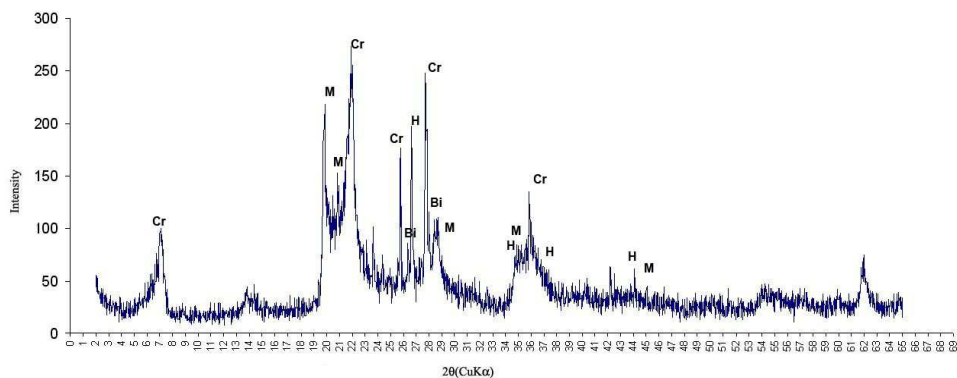


Figure 1. Powder X-ray diffractogram of a bentonite sample from Valea Chioarului (Maramures County); M=montmorillonit, Cr=cristobalit (silice), Bi=biotit, H=haloysit.

Surface morphology and local composition were established using SEM images, recorded with a scanning electron microscope JSM-5600 LV (JEOL), and EDS graphs, recorded with an Oxfrod Instruments EDS spectrometer. SEM images of the bentonite sample, figure 2, points out a gradual devitrification of the ground mass and the neoformation of smectite minerals. On the EDS spectra of the bentonite, figure 3, we could identify the elements forming the main structure of the clay mineral – Si, Al, Na and O – and also the accompanying elements – K, Ca, Mg, Fe, Ti, confirming the Na-montmorillonite type for our sample.

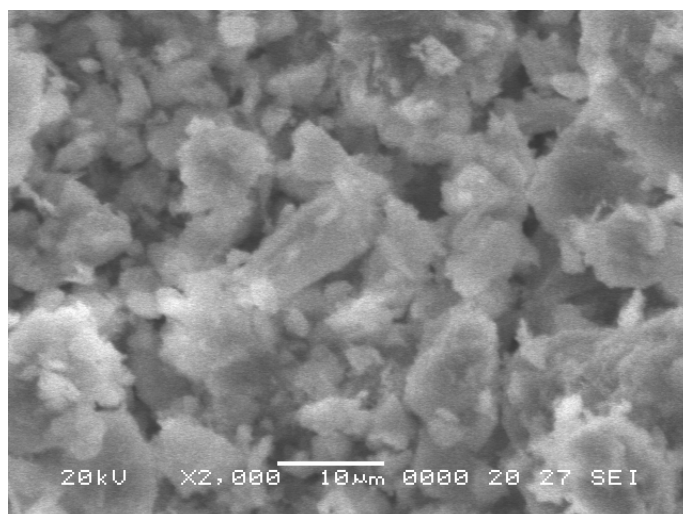


Figure 2. SEM image of a Valea Chioarului (Maramures County) bentonite sample.

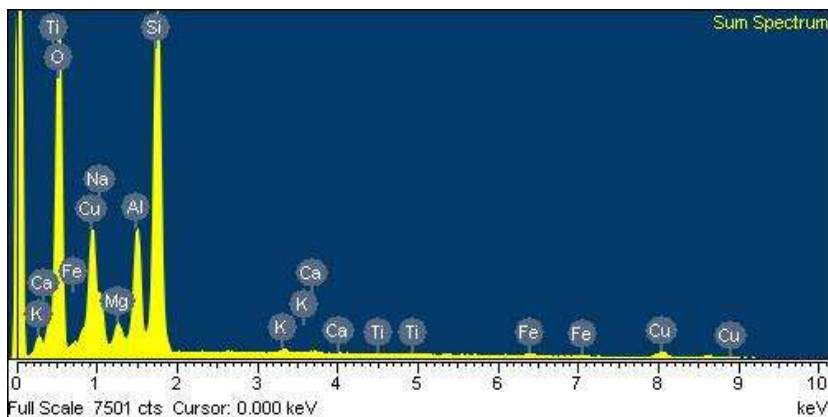


Figure 3. EDS spectra of a Valea Chioarului (Maramures County) bentonite sample.

The bulk chemical composition of the bentonite, table 1, indicates a very high content of silica, a low content of iron oxide and a higher content of Na as compared with other bentonite occurrences from Romania.

Table 1.

Chemical composition of the bentonite sample from Valea Chioarului (Maramures County).

Oxides, [%]	SiO ₂	TiO ₂	Al ₂ O ₃	Fe ₂ O ₃	CaO	MgO	Na ₂ O	K ₂ O	L.O.I.
VCh	70.71	0.31	13.90	1.48	3.35	0.60	2.20	0.55	6.90

Examination of the infrared spectra, recorded with a FTIR Jasco 6100, resolution 2 cm⁻¹, of the bentonite sample, figure 4, indicates the presence of specific bentonite peaks,⁵⁰⁻⁵⁴ as follows: 3620.21 cm⁻¹ – stretching vibrations of isolate hydroxyls and OH less firmly bond to the tetrahedral outer layer, 3435.08 cm⁻¹ – stretching vibrations of the structural OH and also the hydration water, 1632.45 cm⁻¹ – angular deformation of hydroxyls from adsorbed water molecules (held in interlayers), 1089.58/1037.51 cm⁻¹ – main bands corresponding to the stretching vibrations of Si,Al-O and 467.17/520.68 cm⁻¹ angular deformations of Si-O-M bonds (M can be Al, Na, Fe).

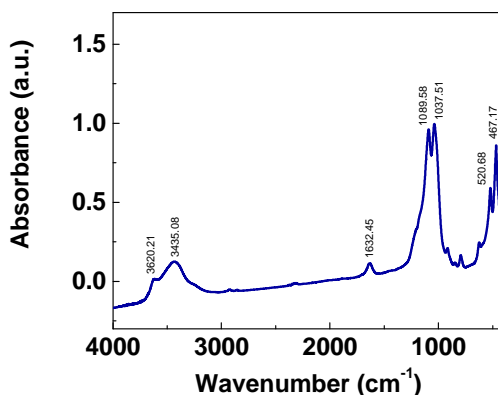


Figure 4. FTIR spectra of a Valea Chioarului (Maramures County) bentonite sample.

3.2. Heavy metal ions removal results

Evolutions of iron and zinc concentrations in static regime on the bentonite sample are presented in figure 5.

The heavy metal ions concentration drastically drops from the initial 636.80 mg Fe_{total}/dm³ and 833.33 mg Zn²⁺/dm³, to 46.88 mg Fe_{total}/dm³ and 2.68 mg Zn²⁺/dm³ respectively during the first 24 hours. After 48 hours zinc concentration drops to 0, while in case of iron the same thing happened after 72 hours. Therefore the values for removal efficiency are 100% in both cases. Evolution of the removal efficiencies values during the removal of heavy metal ions process is presented in figure 6. The efficiencies increase from 0 to 99.68% and 92.64% in 24 hours for zinc and iron respectively, reaching 100% after 48 hours for zinc and 98.17% for iron. After 72 hours the removal efficiency reached 100% for iron also.

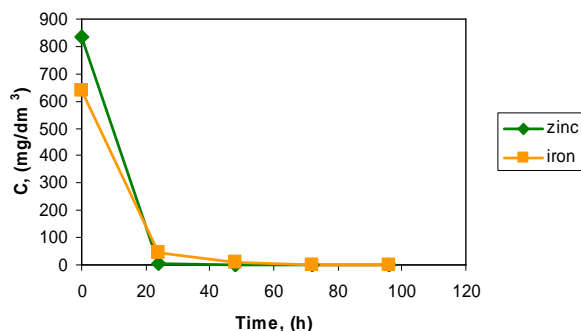


Figure 5. Concentration of zinc and iron ions as a function of time during the removal process.

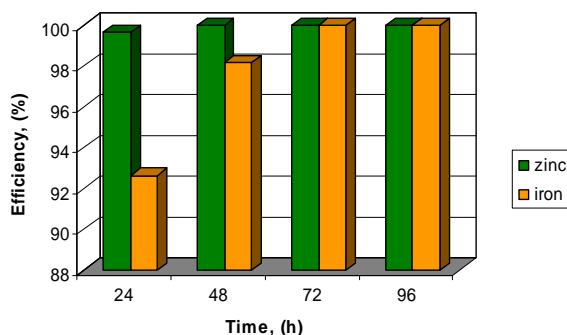


Figure 6. Variation of the removal efficiency during the zinc and iron ions adsorption process.

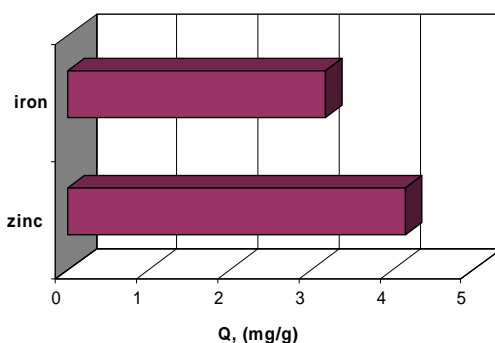


Figure 7. Maximum zinc and iron uptake on a bentonite sample from Valea Chioarului (Maramures County); static regime, 2:10.

If we compare the ionic uptake for iron and zinc, figure 7, it is easy to observe that zinc ions are adsorbed in a higher quantity, respecting the rule according to which, when two ions with similar charges exist in a solution, the one with the highest concentration will be adsorbed preferentially. The maximum values calculated for the ionic uptake are 4.17 mg Zn^{2+} /g solid and 3.18 mg Fe_{total} /g solid.

4. CONCLUSIONS

The heavy metal ions removal process took place with good results on the Valea Chioarului (Maramures county), Romanian bentonite sample, therefore the natural material (clay mineral) is considered to be an appropriate material to remove iron and zinc ions from electroplating wastewaters.

The ionic exchange experiments in static regime demonstrate that iron and zinc ions are hindered with high efficiencies. The ionic exchange efficiencies reached 100% value for both ions, faced to the initial concentration, in 48 and 72 hours for zinc and iron respectively.

ACKNOWLEDGMENT

This material is based upon work supported by CNCSIS grant 1334/2007.

REFERENCES

1. M. Macoveanu, D. Bilba, N. Bilba, M. Gavrilesco, G. Soreanu, "Procese de schimb ionic în protectia mediului", Matrixrom, Bucuresti, 2002.
2. A. Gherghely, E. Bay, M. Dumitrescu, „Tratarea apelor reziduale si recuperarea electrolitilor in galvanotehnica”, Bucuresti, Romania, 1992.
3. J.C. Crittenden, R.R. Trussel, D.W. Hand, K.J. Howe, G. Tchobanoglous, „Water Treatment: Principles and Design”, Willey, New-York, 2005.
4. O. Ianculescu, G. Ionescu, R. RacoviTeanu, „Epurarea apelor uzate” Bucuresti, Romania, 2001.
5. E. Alvarez-Ayuso, A. Garcia-Sanchez, X. Querol, *Water Res.*, **2003**, *37*, 4855-4862.
6. V. Badillo-Almaraz, P. Trocellier, I. Davila-Rangel, *Nuclear Instr. Methods Phys. Res.*, **2003**, *B210*, 424-428.
7. V.M. Palacios, I. Caro and L. Perez, *Adsorption*, **2001**, *7*, 131-138.
8. M.M. Abou Mesalam, *J. Radioanal. Nuclear Chem.*, **2002**, *252*, 579-583.
9. E. Alvarez-Ayuso, A. Garcia-Sanchez, *Clay and Clay Min.*, **2003**, *51*, 475-480.
10. V.J. Inglezakis, H. Grigoropoulou, *J. Hazardous Mat.*, **2004**, *B112*, 37-43.
11. V. Chantawong, N.W. Harvey, V.N. Bashkin, *Water, Air, Soil Poll.*, **2003**, *148*, 111-125.
12. J.S. Kim, J.C. Park, J. Yi, *Separation Sci. Technol.*, **2000**, *35*, 1901-1916.
13. E. Erdem, N. Karapinar, R. Donat, *J. Colloidal Interface Sci.*, **2004**, *280*, 309-314.
14. S.K. Ouki, M. Kavannagh, *Waste Management Res.*, **1997**, *15*, 383-394.
15. A. Pfeinninger, "Manufacture and Use of Zeolites for Adsorption Processes. Molecular Sieves", Berlin, Germany, 1999.
16. D. Radulescu, N. Anastasiu, "Petrologia rocilor sedimentare", Editura Didactica si Pedagogica, Bucuresti, 1979.
17. www.ima-eu.org
18. V. Brana, C. Avramescu, I. Călugăru, "Substanțe minerale nemetalifere", Editura Tehnica, Bucuresti, 1986.
19. G. Alther, *Environ. Eng. Geosci.*, **2004**, *X(4)*, 347-359.
20. U. Ulusoy, S. Simsek, O. Ceyhan, *Adsorption*, **2003**, *9*, 165-175.
21. A.R. Usman, Y. Kuzuyakov, K. Stahr, *Chemistry and Ecology*, **2004**, *20*, 123-135.
22. A. Kapoor, T. Viraraghavan, *J. Environ. Eng.*, **1998**, *124*, 1020-1024.
23. A. Dimirkou, A. Ioannou, P. Papadopoulos, C. Paschalidou, *Commun. in Soil Sci. Plant Analysis*, **2002**, *33*, 2917-2934.
24. V.R. Ambikadevi, M. Lalithambika, *Appl. Clay Sci.*, **2000**, *16*, 133-145.

25. H. Hongping, G. Jiugao, X. Xiande, P. Jinlian, *Chinese J. Geochem.*, **2000**, 19, 105-109.
26. R.P.T. Janssen, M.G.M. Bruggenwert, W.H. Van Riemsdijk, *European J. Soil Science*, **2003**, 54, 347–355.
27. K. Kayabali, H. Kezer, *Environ. Geology*, **1998**, 34, 95-102.
28. L.Y. Li, F. Li, *J. Environ. Eng.*, **2001**, 5, 420-429.
29. F.D. Tillman, S.L. Bartelt-Hunt, J.A. Smith, G.R. Alther, *Bull. Environ. Contam. Toxicol.*, **2004**, 72, 1134–1141.
30. T.K. Gale, J.O.L. Wendt, *Aerosol Sci. Technol.*, **2003**, 37, 865-876.
31. M. Rozic, S. Cerjan-Stefanovic, L. Jurcovic, *Croatica Chemica Acta*, **2002**, 75, 255-269.
32. M. Rozic, S. Cerjan-Stefanovic, S. Kurajica, V. Vancina, E. Hodzica, *Wat. Res.*, **2000**, 34, 3675-3681.
33. S. Balci, *Wat. Res.*, **2004**, 38, 1129-1138.
34. D. Bahulayan, G. Narayan, V. Sreekumar, M. Lalithambika, *Synthetic Comun.*, **2002**, 32, 3565–3574.
35. G. Song, B. Wang, G. Wang, Y. Kang, T. Yang, L. Yang, *Synthetic Comun.*, **2005**, 35, 1051-1057.
36. C. Catrinescu, C. Teodosiu, M. Macoveanu, J. Miehe-Brendle, R. Le Dred, *Water Res.*, **2003**, 37, 1154-1160.
37. J.-M. Tatiboue, E. Guelou, J. Fournier, *Topics in Catalysis*, **2005**, 33, 225-232.
38. E.E. Kiss, J.G. Ranogajec, R.P. Marinkovic-Neducin, T.J. Vulic, *React. Kinet. Catal. Lett.*, **2003**, 80, 255-260.
39. J. Guo, M. Al-Dahhan, *Chem. Eng. Sci.*, **2005**, 60, 735-746.
40. E. Guelou, J. Barrault, J. Fournier, J.-M. Tatibouet, *Appl. Catal. B: Environ.*, **2003**, 44, 1-8.
41. J. Barrault, C. Bouchoule, K. Echachoui, N. Frini-Srasra, M. Trabelsi, F. Bergaya, *Appl. Catal. B: Environ.*, **1998**, 15, 269-274.
42. M. Barhoumi, I. Beurroies, R. Denoyel, H. Said, K. Hanna, *Colloids Surfaces A: Physicochem. Eng. Aspects*, **2003**, 223, 63-72.
43. M. Barhoumi, I. Beurroies, R. Denoyel, H. Said, K. Hanna, *Colloids Surfaces A: Physicochem. Eng. Aspects*, **2003**, 219, 25-33.
44. S. Al-Asheh, F. Banat, L. Abu-Aitah, *Separation Purif. Technol.*, **2003**, 33, 1-10.
45. A. Pusino, I. Braschi, C. Gessa, *Clay Clay Miner.*, **2004**, 8, 19-25.
46. *** STAS 6327-81
47. *** STAS 8634-70
48. I. Kalmar, *St. cerc. geol., geofiz., geogr., Ser. geol.*, **1975**, 20, 187-202.
49. I. Marza, L. Ghergari, L., *Anal. Univ. Bucuresti, Ser. st. nat., geol.-geogr.*, **1967**, XVI, 31-45.
50. F.D. Iacomi, "Zeoliti Naturali. Structura, Proprietati, Utilizare", Editura Universitatii Aurel Vlaicu, Arad, 2001.
51. A.T. Balaban, M. Banciu, I. Pogany, "Aplicatii ale metodelor fizice in chimia organica", Editura Stiintifica si Enciclopedica, Bucuresti, 1983.
52. D. Haffad, A. Chambellan, J.C. Lavalley, *Catal. Lett.*, **1998**, 54, 227-233.
53. R.-J. Hu, B.-G. Li, *Catal. Lett.*, **2004**, 98, 43-47.
54. A. Bakhti, Z. Derriche, A. Iddou, M. Larid, *European J. Soil Sci.*, **2001**, 52, 683-692.

In memoriam Professor Emil Chifu

SYNTHESIS AND STEREOCHEMISTRY OF SOME NEW 2,4,8,10-TETRAOXASPIRO[5.5]UNDECANE DERIVATIVES

**CAMELIA PUȘCAȘ, CLAUDIA LAR, SORIN MAGER, ELENA BOGDAN,
ANAMARIA TERC, LUMINIȚA DAVID*, ION GROSU**

ABSTRACT. The synthesis and the stereochemistry of some new 2,4,8,10-tetraoxaspiro[5.5]undecane derivatives are reported. The structural analysis carried out using NMR investigations revealed the anancomeric structure of the compounds and the influence of the chirality of the spirane skeleton.

INTRODUCTION

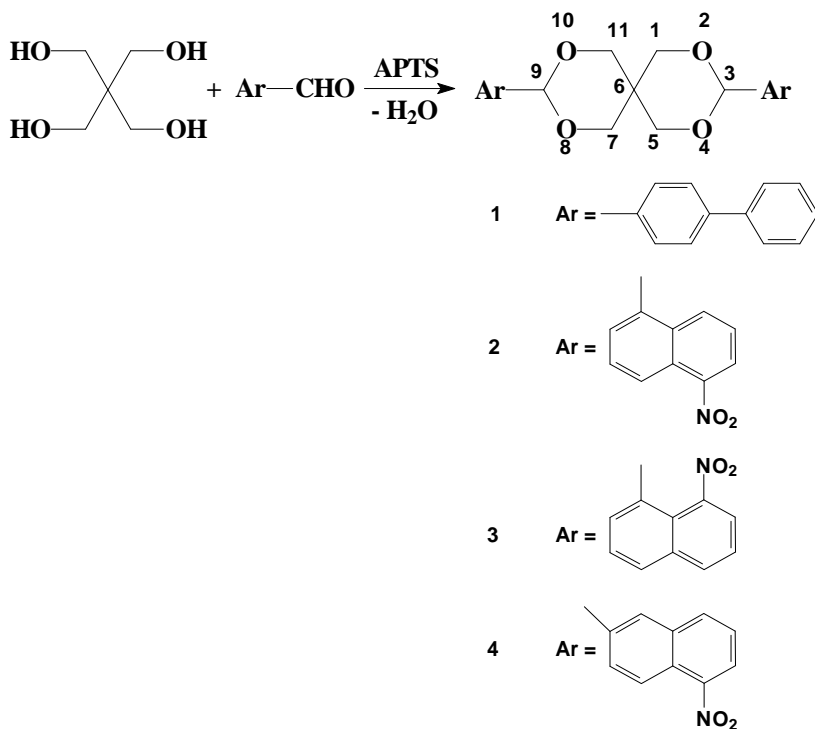
Many spiro and polispiro compounds with saturated six-membered rings were studied in connection with their structural behavior.¹⁻¹⁰ The investigations of these compounds revealed the helical chirality of the spirane skeleton and the anancomeric or flipping conformational behavior of the compounds in correlation with the nature of the substituents located at the extremity of the spirane skeleton.^{1-4,10} In polyspirane the helix turns identical with itself after each fourth six-membered ring. Many spiro 1,3-dioxane compounds, derivatives of pentaerythritol were synthesized for various applications in material sciences,¹¹ as chiral reagents,¹² and drugs¹³.

We considered of interest to obtain new derivatives with larger aromatic moieties and to investigate the influence of the aromatic part on the stereochemistry of the heterocyclic compounds.

RESULTS AND DISCUSSIONS

New 2,4,8,10-tetraoxaspiro[5.5]undecane derivatives were obtained by the condensation reaction of pentaerythritol with appropriate aromatic aldehydes (Scheme 1).

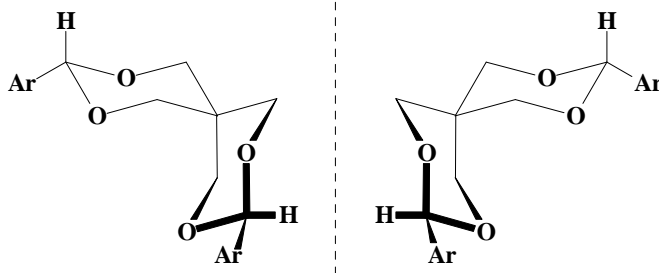
* Babeș-Bolyai" University, Organic Chemistry Department and CCOCCAN, 11 Arany Janos str., 400028, Cluj-Napoca, Romania



Scheme 1

The structural analysis was carried out using NMR investigations. The spectra of compounds **1-4** exhibit different signals for the axial and equatorial protons of the 1,3-dioxane rings (Table 2) and prove the anancomeric structure of these compounds. On the other side positions 1(11) and 5(7) are diastereotopic as a consequence of the chirality of the spirane skeleton.

The conformational equilibrium involving the heterocycles is shifted toward the conformer exhibiting the aryl group in equatorial orientation and the stable enantiomers of the compound are shown in Scheme 2.



Scheme 2

The equatorial preference of the naphthyl groups is in agreement with the high conformational enthalpy of the aromatic substituents located at the position 2 of the 1,3-dioxane rings¹⁴⁻¹⁶.

Table 2.

NMR data for compounds 1-4

Compound/Solvent	1(11)-H		5(7)-H	
	ax.	eq.	ax.	eq.
1/ CDCl₃	3,91	4,93	3,71	3,88
2/ (CD₃)₂SO	3,80	4,18	3,65	3,80
3/ (CD₃)₂SO	4,25	4,80	3,98	3,98
4/ (CD₃)₂SO	3,96	4,88	3,80	3,96

CONCLUSIONS

Spiranes with aromatic substituents at the extremities of the spirane skeleton exhibit anancomeric structures. The aromatic groups prefer the equatorial orientation. Despite the size of the naphthalene ring and of the substituents located on it, the rotation of the naphthalene unit is not hindered.

EXPERIMENTAL

¹H-NMR (300 MHz) spectra were recorded at *rt* in CDCl₃ or in (CD₃)₂SO on a Bruker 300 MHz / 400MHz spectrometer, using the solvent line as reference.

Melting points were measured with a Kleinfeld melting point apparatus and are uncorrected. Chemicals were purchased from Aldrich or Acros and were used without further purification.

General procedure for the synthesis of compounds 1-4

(25 mmol) pentaerythritol and (50 mmol) aromatic aldehyde with catalytic amounts of *p*-toluenesulphonic acid (0.1 g) were solved in 150 mL benzene. The mixture was refluxed and the water produced in the reaction removed using a Dean-Stark trap. When 80 % of the water had been separated, the mixture was cooled to room temperature and the catalyst was neutralized (under stirring 0.5 h) with Na₂CO₃ powder in excess (1 g). After filtration, the solvent was removed and the crude products were purified by crystallization from ethanol or methanol.

3,9-Bis-(biphenyl)-2,4,8,10-tetraoxaspiro[5.5]undecane 1

White solid, m.p.=217-219°C, yield 47.3%. C₃₁H₂₈O₄ (464.56), calc. 80.15 C, 6.08 H, found 80.04 C, 6.27 H. ¹H-NMR (300 MHz, CDCl₃, δ ppm): 3.71 (2H, d, J = 11.5 Hz, 5,7-H_{ax}), 3.88 (2H, dd, J = 11.5 Hz, J = 2.4 Hz, 5,7-H_{eq}),

3.91 (2H, d, J = 10.4 Hz, 1,11-H_{ax}), 4.93 (2H, dd, J = 10.4 Hz, J = 2.4 Hz, 1,11-H_{eq}), 5.55 (2H, s, 3,9-H), 7.20-7.80 (18 aromatic H, overlapped peaks)

3,9-Bis-(5-nitro-1-naphthyl)-2,4,8,10-tetraoxaspiro[5.5]undecane 2

Yellow solid, m.p.=255-258°C, yield 55.2%. C₂₉H₃₀N₂O₈ (534.56), calc. 65.16 C, 5.66 H, 5.24 N, found 64.70 C, 5.90 H, 4.90 N. ¹H-NMR (300 MHz, (CD₃)₂SO, δ ppm): 3.65 (2H, d, J = 11.0 Hz, 5,7-H_{ax}), 3.80 (4H, overlapped peaks, 1,11-H_{ax}, 5,7-H_{eq}), 4.80 (2H, d, J = 11.0 Hz, 1,11-H_{eq}), 5.60 (2H, s, 3,9-H), 7.50-8.40 (12 aromatic H, overlapped peaks)

3,9-Bis-(8-nitro-1-naphthyl)-2,4,8,10-tetraoxaspiro[5.5]undecane 3

Yellow solid, m.p.=178-180°C, yield 60.8%. C₂₉H₃₀N₂O₈ (534.56), calc. 65.16 C, 5.66 H, 5.24 N, found 65.30 C, 5.70 H, 5.10 N. ¹H-NMR (300 MHz, (CD₃)₂SO, δ ppm): 3.98 (4H, overlapped peaks, 5,7-H_{ax}, 5,7-H_{eq}), 4.25 (2H, d, J = 10.4 Hz, 1,11-H_{ax}), 4.80 (2H, d, J = 10,4 Hz, 1,11-H_{eq}), 6.25 (2H, s, 3,9-H), 7.70-7.80 (12 aromatic H, overlapped peaks).

3,9-Bis-(5-nitro-2-naphthyl)-2,4,8,10-tetraoxaspiro[5.5]undecane 4

White-yellow solid, m.p.=210-212°C, yield 48.8%. C₂₉H₃₀N₂O₈ (534.56), calc. 65.16 C, 5.66 H, 5.24 N, found 65.20 C, 5.50 H, 5.10 N. ¹H-NMR (400 MHz, (CD₃)₂SO, δ ppm): 3.80 (2H, d, J = 11.2 Hz, 5,7-H_{ax}), 3.96 (4H, overlapped peaks, 1,11-H_{ax}, 5,7-H_{eq}), 4.88 (2H, d, J = 11.4 Hz, 1,11-H_{eq}), 5.71 (2H, s, 3,9-H), 7.75 – 8.78 (12 H, overlapped peaks).

REFERENCES

1. Grosu I., Mager S., Plé G., Horn M., *J. Chem. Soc. Chem. Commun.* **1995**, 167-168
2. Grosu I., Mager S., Plé G., *J. Chem. Soc. Perkin Trans. 2* **1995**, 1351-1357
3. Grosu I., Mager S., Plé G., Mesaroș E., Gegö C., Dulău A., *Rev. Roum. Chim.* **1999**, *44*, 467-473
4. Grosu I., Mager S., Plé G., Mesaros E., *Tetrahedron* **1996**, *52*, 12783-12798
5. Grosu I., Plé G., Mager S., Martinez R., Mesaros C., Camacho B., *Tetrahedron* **1997**, *53*, 6215-6232
6. Grosu I., Mager S., Plé G., Turos I., Mesaros E., Schirger I., *Monatsh. Chem.* **1998**, *129*, 59-68
7. Opris D., Grosu I., Toupet L., Plé G., Terec A., Mager S., Muntean L., *J. Chem. Soc. Perkin Trans. 1* **2001**, 2413-2420
8. Grosu I., Bogdan E., Plé G., Toupet L., Ramondenc Y., Condamine E., Peulon- Agasse V., Balog M., *Eur. J. Org. Chem.* **2003**, 3153-3161

9. Balog, M., Grosu, I., Plé, G., Ramondenc Y., Toupet, L., Condamine, E., Lange, C., Loutelier, C., Peulon-Agasse, V., Bogdan, E., *Tetrahedron* **2004**, *60* (22), 4789-4799
10. Cismaş, C., Terec, A, Mager, S., Grosu, I., *Curr. Org. Chem.* **2005**, *9*, 14, 1287-1314
11. Lemcoff, N. G., Fuchs, B., *Org. Lett.* **2002**, *4*, 731-734
12. Böhm, U., Voss, G., Möller, G., Gerlach, H., *Tetrahedron: Asymmetry* **1994**, *5*, 1281-1290
13. Séller, J., Barr, J., Ng, S. Y., Shen, H. -R., Schwach-Abdellaoui, K., Gurny, R., Vivien-Castioni, N., Loup, P. J., Baehni, P., Mombelli, A., *Biomaterials* **2002**, *23*, 4397-4404
14. Anteunis M.J.O., Tavernier D., Borremans F., *Heterocycles* **1976**, *4*, 293-371
15. Kleinpeter E., *Adv. Heterocycl. Chem.* **1998**, *69*, 217-269
16. Kleinpeter E., *Adv. Heterocycl. Chem.* **2004**, *86*, 41-127